Molecular explanations for gating in simple model K^+ channels

Vom Fachbereich Biologie der Technischen Universität Darmstadt

zur Erlangung des akademischen Grades

eines *Doctor rerum naturalium*

genehmigte Dissertation von

M.Sc. Oliver Rauh

aus Görlitz

1. Referentin: Dr. Indra Schröder

2. Referent: Prof. Dr. Gerhard Thiel

Tag der Einreichung: 16.04.2018

Tag der mündlichen Prüfung: 22.05.2018

Darmstadt 2018

D17

Rauh, Oliver: Molecular explanations for gating in simple model K^+ channels

Darmstadt, Technische Universität Darmstadt

Jahr der Veröffentlichung der Dissertation auf TUPrints: 2018

URN: urn:nbn:de:tuda-tuprints-74372

Tag der mündlichen Prüfung: 22.05.2018

Seht ihr den Mond dort stehen?
Er ist nur halb zu sehen,
Und ist doch rund und schön!
So sind wohl manche Sachen,
Die wir getrost belachen,
Weil unsre Augen sie nicht sehn.

Matthias Claudius

Table of Contents

Summary

Potassium channels are transmembrane proteins that facilitate the passive and selective flux of K^+ ions across biological membranes in cells of virtually all species. They are involved in a broad variety of cellular and physiological processes such as neuronal excitability, muscle contraction, volume regulation and secretion. Consequently, the understanding of these processes and their pathological dysfunctions requires insights into the molecular mechanisms underlying the functions of potassium channels. The focus of the present thesis is placed on the investigation of gating mechanisms in potassium channels. For this purpose, I used small viral encoded $Kcv_{ATCV\text{-}1}$-like potassium channels, which resemble with a monomer size of only 82 amino acids, the pore module of all complex potassium channels in terms of structure and function.

In the first part of this work two members of the $Kcv_{ATCV\text{-}1}$-family, Kcv_S and Kcv_{NTS}, are used in a comparative experimental and computational analysis to examine the mechanistical and chemical explanation of a particular gating process. Even though both proteins share about 90% amino acid sequence identity they exhibit different open probabilities with ~90% in Kcv_{NTS} and ~40% in Kcv_S. Single-channel analysis, mutational studies and molecular dynamics simulations show that the difference in open probability is the result of a single long-lasting closed state in Kcv_S. This closed state is caused by the formation of a transient, intrahelical hydrogen-bond between the side chain of a serine located in the pore-lining transmembrane helix and a carbonyl oxygen in the preceding helix turn. This hydrogen-bond induces a kink, which promotes an interaction of aromatic groups from downstream phenylalanine residues at the intracellular pore entrance that blocks ion flux.

The second part deals with the investigation of the kinetics and molecular causes of a voltage-dependent gating process in $Kcv_{NH\,S77G}$. This channel exhibits in multi-channel bilayer experiments in response to membrane hyperpolarization a time-dependent, ultra-slow inactivation, resulting in an outwardly-rectifying current-voltage relationship. Single-channel measurements demonstrate that this inactivation is caused by the voltage-dependent transition from an active state, in which the channel exhibits an open probability of about 90%, to an ultra-long-lasting, voltage-insensitive inactive state. The transition into the inactive state is sensitive to both the external potassium concentration and the electrochemical driving force. The electrophysiological experiments, the kinetic information extracted from these and the agreement of model-based predictions with experimentally obtained data support the hypothesis that inactivation is directly coupled to the permeation of ions through the channel

pore. These results provide a plausible mechanistic explanation on how ion channels without a VSD in general can sense a change in membrane voltage.

Zusammenfassung

Kaliumkanäle sind Transmembranproteine, die Kaliumionen den passiven und selektiven Durchtritt durch biologische Membranen ermöglichen und in den Zellen nahezu aller Organismen zu finden sind. In diesen sind sie an einer Vielzahl zellulärer und physiologischer Prozesse beteiligt, zu denen die Generierung und Weiterleitung von Aktionspotentialen in neuronalen Zellen, die Kontraktion von Muskelzellen, die Regulation des Zellvolumens sowie Sekretionsvorgänge gehören. Das Verständnis dieser Prozesse sowie ihrer pathologischen Störungen muss daher zwangsläufig auch das Verständnis der molekularen Mechanismen umfassen, die der Funktion von Kaliumkanälen zugrunde liegen. Zu diesem Zweck verwende ich in der vorliegenden Arbeit viral kodierte $Kcv_{ATCV\text{-}1}$-ähnliche Kaliumkanäle, die mit einer Größe von lediglich 82 Aminosäuren je Monomer strukturell und funktionell dem Porenmodul komplexerer Kaliumkanäle entsprechen.

Im ersten Teil der vorliegenden Thesis werden zwei Mitglieder der $Kcv_{ATCV\text{-}1}$-Familie, Kcv_S und Kcv_{NTS}, verwendet, um unter Verwendung experimenteller und simulationsbasierter Methoden die mechanistischen und chemischen Ursachen eines bestimmten *Gating*-Prozesses zu untersuchen. Trotz einer Sequenzübereinstimmung von annähernd 90%, weist Kcv_S mit etwa 40% eine deutlich niedrigere Offenwahrscheinlichkeit auf als Kcv_{NTS}, der mit einer Offenwahrscheinlichkeit von etwa 90% als konstitutiv offen betrachtet werden kann. Durch Kombination von Einzelkanalmessungen, Mutationsstudien und Moleküldynamiksimulationen kann gezeigt werden, dass die niedrigere Offenwahrscheinlichkeit des Kcv_S durch das Auftreten eines zusätzlichen, langlebigen Geschlossenzustandes hervorgerufen wird. Dieser Geschlossenzustand kann wiederum auf eine transiente, intrahelikale Wasserstoffbrücke zurückgeführt werden, die sich innerhalb der inneren Transmembranhelix zwischen der Seitengruppe eines Serins und einem Carbonylsauerstoff des Peptidrückgrates ausbildet. Diese Wasserstoffbrücke bedingt eine Änderung der Helixgeometrie und dadurch eine Änderung in der Orientierung eines unterhalb des Serins gelegenen Phenylalanins. Die Interaktion der vier Phenylalaninseitengruppen innerhalb der Pore des tetrameren Kaliumkanals führt schließlich zur Blockierung des Ionenstroms.

Der zweite Teil befasst sich mit der Untersuchung der molekularen Ursachen eines spannungsabhängigen *Gating*-Prozesses im viralen Kaliumkanal $Kcv_{NH\ S77G}$. Dieser Kanal zeigt in Multikanal-Experimenten nach Hyperpolarisation der Lipidmembran eine zeitabhängige, ultra-langsame Inaktivierung. Diese verleiht dem $Kcv_{NH\ S77G}$ eine für Auswärtsgleichrichter charakteristische Strom-Spannungsbeziehung. Durch Einzelkanalmessungen kann gezeigt

werden, dass die Inaktivierung das Resultat eines spannungsabhängigen Übergangs von einem aktiven Zustand, in dem der Kanal eine Offenwahrscheinlichkeit von etwa 90% aufweist, in einen ultra-langlebigen, spannungsunabhängigen inaktiven Zustand widerspiegelt. Der Übergang in den inaktiven Zustand ist sowohl von der externen Kaliumkonzentration als auch von der elektrochemischen Triebkraft abhängig. Die durchgeführten Experimente, die aus diesen extrahierten kinetischen Informationen sowie die Übereinstimmung modellbasierter Voraussagen mit experimentell gewonnenen Daten unterstützen die Hypothese, dass die Inaktivierung eine direkte Folge der Ionenpermeation darstellt. Die Ergebnisse dieser Untersuchungen liefern eine schlüssige mechanistische Erklärung, wie Ionenkanäle, die über keine Spannungssensordomäne verfügen, Änderungen in der Membranspannung sensieren und in das Öffnen oder Schließen der Kanalpore übersetzen können.

1. General Introduction

1.1. Ion channels

Cells are separated from their environment by a lipid membrane, which prevents the unregulated exchange of molecules and ions between an intra- and extracellular space. This distinction between 'inside' and 'outside' is the basic principle of life. However, the continuity of a living system requires a constant and highly regulated exchange of energy, matter and information with the environment. This exchange is in part facilitated by integral membrane proteins, which can be divided into transporter and channel proteins (Hille 2001). Briefly, transporters transfer soluble molecules by a mechanism that is similar to an enzyme-substrate reaction: the protein binds the solute on one side of the membrane, undergoes a conformational change that transports the solute through the hydrophobic core of the membrane and releases it on the other side. Transporters allow the transport of a solute "uphill" against its electrochemical gradient by coupling this transport to an energy-supplying process such as the hydrolysis of ATP or the "downhill" transport of a second substrate (Alberts et al. 2002). Transport processes facilitated by the use of chemical energy are referred to as active. The corresponding proteins are also called pumps. Accordingly, the coupling of the "uphill" transport of one solute to the "downhill" transport of a second solute is referred to as secondary active transport, since the energy stored in the electrochemical gradient of the second solute must be provided by an active process. Thus, secondary active transport processes are actually passive.

In contrast, channel proteins facilitate the transport of ions 'downhill' their electrochemical gradient by providing a continuous aqueous pore (Hille 2001). While the selectivity of transporters and pumps is guaranteed by the specific binding of the substrate to a solvent-exposed binding site, the specificity of ion channels is provided by a selectivity filter. Since the transfer of ions through an ion channel pore is not coupled to a conformational change, ion channel mediated transport can occur with a rate of 10^6-10^8 ions per second. This is two to six orders of magnitude faster than transport via transporters and pumps (Lodish et al. 2000). In spite of this huge difference in transport velocity, there is increasing evidence that the structural differences between channels and transporters are much smaller than previously assumed (DeFelice 2004). For example, it has been shown that a member of the Cl^- channel (CLC) family, CLC-ec1, works as a H^+-coupled Cl^--antiporter (Arcadi & Miller 2004). Remarkably, a single point mutation near the Cl^--binding site reconverts the antiporter into a Cl^--selective channel.

Since ion channels allow the selective and regulated passage of ions through the outer cell membrane or membranes of internal compartments, they play a crucial role in a tremendous variety of physiological processes in both prokaryotic and eukaryotic cells (Hille 2001). Their known functions comprise the setting and regulation of the resting membrane potential, the shaping of action potentials in electrically excitable cells, the control and regulation of the cell volume, and the flux of ions and water across epithelial cells. Therefore, ion channels are involved in physiological processes such as muscle contraction, electrical signal propagation, cell motility, fluid secretion in exocrine glands, and many more (e.g. Hille 2001, Schwab et al. 2012, Stojilkovic et al. 2010).

Apart from ion selectivity, another important property of ion channels is their ability to switch between an open and closed state. The probability of switching is altered in response to stimuli such as a change in membrane voltage or binding of a ligand (Hille 2001). This property is referred to as *gating*. The coordinated interplay between different ion channels in time and space is particularly important for the transmission of electrical messages by means of action potentials. Briefly, in nerve cells the resting potential of about -60 mV is mainly maintained by the action of Na^+/K^+-ATPases and a large number of open K^+ channels in the plasma membrane. An action potential is caused by the initial opening of voltage-gated Na^+ channels that conduct Na^+ ions into the cell, resulting in a fast and large depolarization of the membrane segment. After about 1 ms the Na^+ channels inactivate for several milliseconds, preventing further influx of Na^+. The depolarization leads to the transient opening of voltage-gated K^+ channels that cause a rapid efflux of K^+ ions and thus a hyperpolarization of the membrane. After closing of these K^+ channels, the membrane voltage returns to the resting potential (Lodish et al. 2000). It is obvious that even small changes in ion selectivity or gating can cause serious consequences for the function of a cell and thus the vitality of an entire organism. It is thus not surprising that the dysfunction of ion channels is the underlying cause of a large number of diseases. These diseases, referred to as channelopathies, include for instance disorders of the nervous system (e.g. epilepsy), the cardiovascular system (e.g. long QT syndrome) and the respiratory system (e.g. cystic fibrosis) (Dworakowska & Dołowy 2000). Moreover, there is increasing evidence that a wide variety of ion channels is also implicated in tumor growth and metastasis (Lang & Stournaras 2014). Due to the increasing knowledge about the involvement of ion channels in the manifestation of various diseases, ion channels become increasingly recognized as important therapeutic targets (Kaczorowski et al. 2008).

1.2. Potassium channels

In the course of evolution, organisms developed selective channels for all physiologically important ions, namely Ca^{2+}, Na^{+}, K^{+} and Cl^{-} (Hille 2001). K^{+} channels were originally identified as essential entities in the membrane of nerve cells facilitating the efflux of potassium ions during action potential generation and propagation (Hodgkin & Huxley 1952). With the ongoing investigation of living cells at the molecular level, it became clear that K^{+} channels are involved in a wide variety of processes in the cells of virtually all species (Miller 2000). These processes include electrical impulse formation (Pongs 1999), volume regulation (Deutsch & Chen 1993), secretion (Stojilkovic et al. 2010), and muscle contraction (Nelson & Quayle 1995). K^{+} channels are mainly found in the plasma membrane, but they are also present in the membranes of intracellular organelles such as mitochondria (Szewczyk et al. 2009), endoplasmic reticulum (Salari et al. 2015) and lysosomes (Wang et al. 2017).

1.2.1. Structure of potassium channels

All known potassium channels are members of a single protein family and therefore share a universal architecture: they are usually composed of four identical membrane-spanning subunits that form a central water-filled pore with four-fold symmetry (MacKinnon 2003).

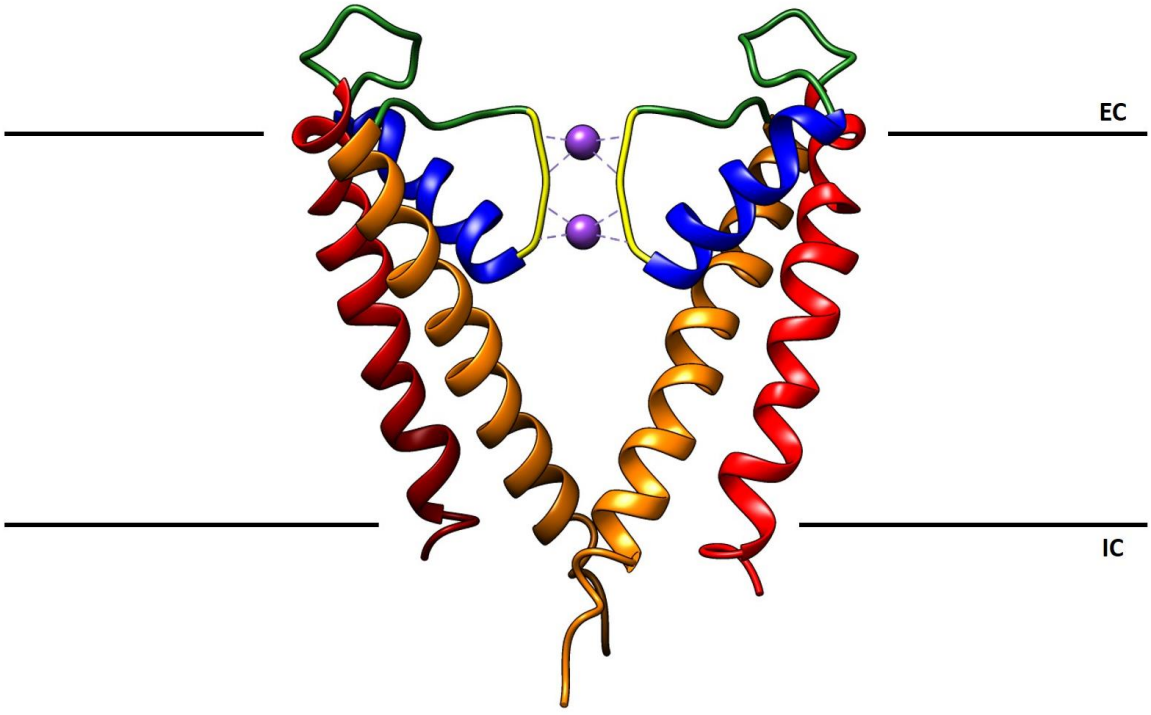

Figure 1-1: Transmembrane part of the prototypical potassium channel KcsA from *Streptomyces lividans*. Shown are two opposing subunits of the KcsA in the closed state (PDB: 1BL8, Doyle et al. 1998) viewed along the membrane plane. The pore-forming domain comprises of the outer helix (red), inner helix (orange), loop regions (green), pore helix (blue), and selectivity filter (yellow). Potassium ions are represented as purple spheres. EC and IC indicate the extracellular and intracellular space, respectively.

The pore-forming domain of a prototypical K^+ channel subunit comprises of two α-helical transmembrane segments and a tilted pore helix that spans about half of the membrane, pointing with its C-terminal end towards the ion conduction pathway (Doyle et al. 1998) (**Figure 1-1**). The pore helix is part of a structure called P-loop, which connects the outer (N-terminal) transmembrane helix with the inner (C-terminal) transmembrane helix. The P-loop contains apart from the pore helix a highly conserved 'signature sequence', TVGYG, that lines together with the inner transmembrane helix the ion conduction pore. The signature sequences of all four pore-forming domains form together the selectivity filter, which is the crucial structural element that facilitates the selective passage of K^+ ions through the channel pore at rates close to the diffusion limit (Sansom et al. 2002). In the conductive state, the selectivity filter forms with a diameter of about 3 Å the narrowest part of the pore (Doyle et al. 1998). The selectivity filter originates on the extracellular pore entrance and opens after 10 to 15 Å into a central, water-filled cavity (**Figure 1-1**) (Miller 2000).

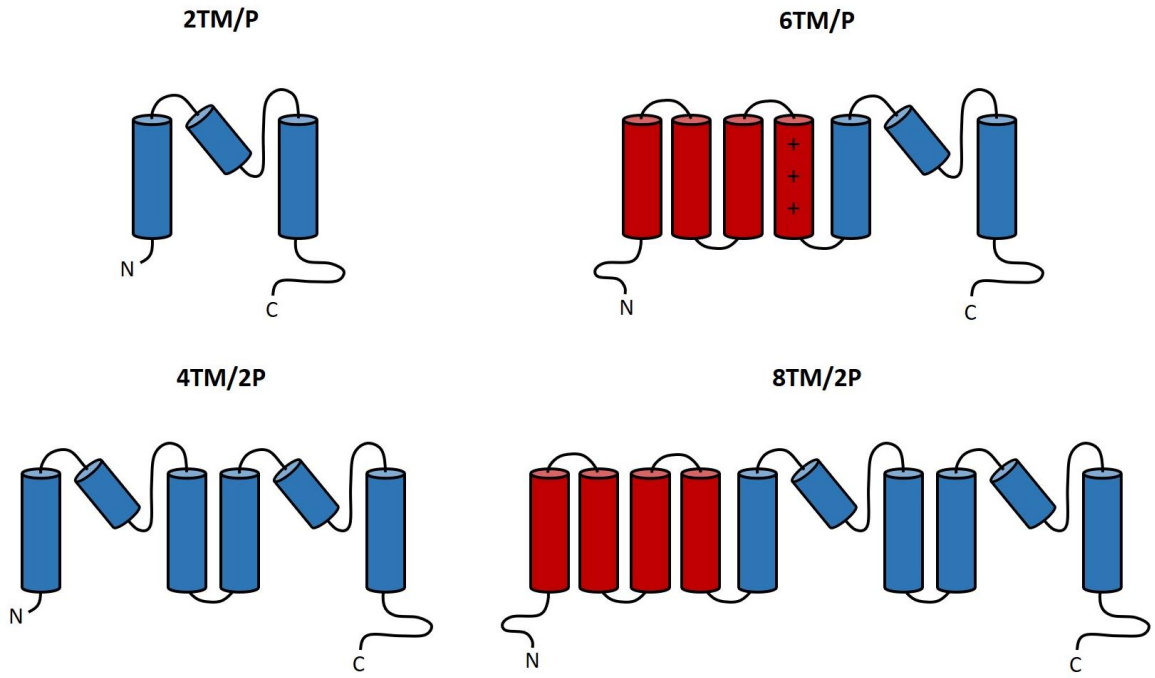

Figure 1-2: Topologies of K^+ channel subunits. The pore-forming domains (colored in blue) are composed of two transmembrane helices (TM) and a P-loop (P). Additional transmembrane helices are shown in red. N and C indicate the amino- and carboxy-terminus of the subunit.

According to their transmembrane topology, potassium channels can be categorized into three major classes: the two transmembrane helices/one P-loop (2TM/P), six transmembrane helices/one P-loop (6TM/P), and tandem pore domain (K2P) subtypes (**Figure 1-2**) (Kuang et al. 2015). The 2TM/P channel family includes the mammalian inwardly rectifying (Kir) (Hibino et al. 2010) and prokaryotic inwardly rectifying (KirBac) channels (Bavro et al. 2012), the bacterial KcsA channel (Doyle et al. 1998) as well as the viral K^+ channels of the

Kcv family (Thiel et al. 2013). The most diverse group, the 6TM/P family, is represented by the voltage-gated Kv channels (Yu et al. 2005). Kv channels are composed of the canonical pore-domain and a C-terminal voltage-sensing domain (VSD), which is formed by four transmembrane segments (S1-S4). The S4 helix possesses a series of positively charged residues that act as actual gating charges (Gandhi & Isacoff 2002). While active 2TM/P and 6TM/P channels are composed of four subunits, K2P channels are dimers. The subunits of most K2P channels consist of two linked Kir-like sequences, resulting in a four transmembrane helices/two P-loops (4TM/2P) topology. This subfamily includes, for example, the weakly inwardly rectifying K^+ (TWIK) channels (Lesage & Lazdunski 2000). However, a few K2P channels are composed of a Kv-like and a Kir-like sequence, resulting in an eight transmembrane helices/two P-loops (8TM/2P) topology (**Figure 1-2**). A prominent member of the 8TM/2P subfamily is the outwardly rectifying TOK1 from *Saccharomyces cerevisiae* (Ketchum et al. 1995).

Independent of their transmembrane topology, the K^+ channels have a modular structure that can be divided into the pore-forming domain and regulatory domains (Kuang et al. 2015). The regulatory domains of different potassium channels sense diverse stimuli including voltage, temperature, mechanical stretch or pressure, ions, small molecules and pH (Hille 2001, Pongs 1999). As for Kv channels, the transmembrane helices can be part of the regulatory domain (Gandhi & Isacoff 2002). For other K^+ channels such as Kir or KCNH channels, the regulatory domain is present in the cytoplasm and attached to the pore-forming domain via a peptide linker (Hibino et al. 2010, Haitin et al. 2013). Moreover, some potassium channels interact with auxiliary subunits. For example, the mammalian K_{ATP} channels are composed of four Kir6.1 or Kir6.2 subunits and four regulatory sulfonylurea receptors (SURs) (Inagaki & Seino 1998).

An incoming stimulus leads to a conformational change of the regulatory domain, which is transferred to the pore domain and thus causes the opening or closing of the ion permeation pathway. The structural entity that occludes the channel pore is called *gate*. Accordingly, the stimulus-induced opening or closing of this gate is called *gating* (Hille 2001). Therefore, the structural elements of potassium channels correspond to three functional aspects: conductivity, selectivity, and gating.

1.2.2. Ion conductivity and selectivity

The most striking feature of potassium channels is their ability to conduct K^+ ions selectively at near diffusion-limited rates of about 10^7 ions per second (Sansom et al. 2002). Sodium ions, which are also physiologically important, are conducted at least 1,000 times less efficient than potassium, although sodium ions even have a smaller atomic radius (0.95 Å for Na^+ compared to 1.33 Å for K^+) (MacKinnon 2003). This remarkable feature already illustrates that the selectivity of K^+ channels cannot be explained by a simple size-exclusion mechanism. Electrophysiological experiments already provided a detailed view of the pore structure before the first crystal structure of a potassium channel was available. For example, the examination of the influence of different internal monovalent cations on the outward current of K^+ channels in voltage clamped squid axons led Bezanilla and Armstrong (1972) to the conclusion that the potassium channel has a wide inner mouth followed by a narrow tunnel that is specific for dehydrated K^+ and lined by carbonyl oxygens of the peptide backbone. In 1988, Neyton and Miller identified four different ion binding sites inside the channel pore. This result supported the idea of a single-file, multi-ion translocation mechanism. Furthermore, mutational studies allowed the identification of the signature sequence, i.e. the amino acids that form the selectivity filter (Heginbotham et al. 1994). However, the breakthrough was achieved with the crystallization of the bacterial potassium channel KcsA from *Streptomyces lividans* by Doyle et al. (1998). The crystal structure of KcsA provided a direct answer to the question how K^+ channels manage the effective and selective conduction of potassium. The ion binding sites within the selectivity filter are formed by the main chain carbonyl oxygens of the signature sequence TVGYG together with the hydroxyl oxygen atoms of the conserved threonine groups (Doyle et al. 1998). These oxygen atoms create a stack of oxygen rings that form four discrete ion binding sites (S1-S4) within the selectivity filter and an additional ion binding site (S0) in the extracellular entryway (**Figure 1-3**) (Doyle et al. 1998, Alam & Jiang 2011). Potassium ions must enter the selectivity filter from the water-filled cavity or the extracellular space in a dehydrated form (Doyle et al. 1998). The energetic costs of the dehydration process are compensated by the stabilization of the potassium ion by the eight oxygen ligands arranged in a square antiprism geometry at each ion binding site (**Figure 1-3**) (Alam & Jiang 2011). The high K^+ over Na^+ selectivity of potassium channels is classically explained by a snug-fit mechanism as previously proposed by Bezanilla and Armstrong (1972). According to the snug-fit mechanism, the rigid geometry of the ion binding sites provides a good fit for dehydrated K^+ ions but not for smaller and more strongly solvated Na^+ ions (Doyle et al. 1998). Therefore, the entry and transfer of Na^+ ions into and through the selectivity filter is thermodynamically unfavorable due to a higher dehydration energy and

a higher coulombic energy within the selectivity filter (Bezanilla & Armstrong 1972, Doyle et al. 1998).

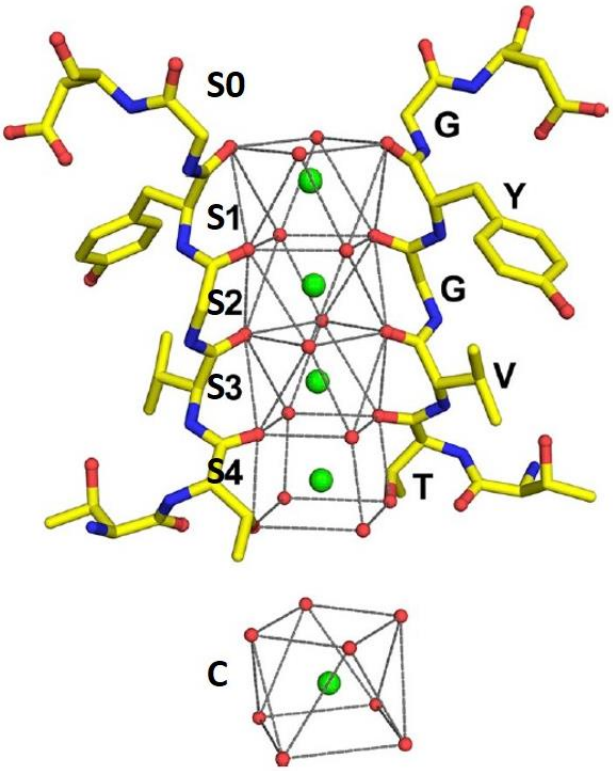

Figure 1-3: Structure of the selectivity filter of the bacterial K^+ channel KcsA. The five ion binding sites within the filter are labeled S0-S4 from top to bottom. The amino acids of the signature sequence are labeled with their single-letter abbreviations. Potassium ions are shown as green spheres, oxygen atoms as red balls. The potassium ion in the cavity (C) is surrounded by eight water molecules (from Alam & Jiang 2011).

However, additional theoretical studies have suggested that a simple energetic explanation as provided by the snug-fit mechanism is not sufficient to explain the high K^+ over Na^+ selectivity. The thermal B-factors, which could be obtained from the data of the KcsA X-ray structure (Zhou et al. 2001), argue against a simple snug-fit mechanism: these data show that the structural fluctuations are in the range of 0.75 Å and thus larger than the difference between the atomic radii of K^+ and Na^+ (0.38 Å) (Pauling 1960). Molecular dynamics (MD) simulations performed by Noskov et al. (2004) have suggested that the selectivity of K^+ channels is mainly determined by the electrostatic and dynamic properties of the carbonyl ligands rather than a sub-Ångstrom precision of the selectivity filter. The characterization of multi-ion energy landscapes has further shown that the free energy minima for the main ion configurations are similar, regardless of whether Na^+ and K^+ enters the K^+ occupied selectivity filter (Egwolf & Roux 2010). However, the free energy barriers between the stable ion locations are significantly higher for Na^+ than for K^+, suggesting that the selectivity of K^+ channels is basically kinetically rather than thermodynamically controlled. Since the basics of

ion conduction in K^+ channels are still in the focus of intensive research efforts, it is likely that ion selectivity reflects a combination of both energetic and kinetic contributions.

Another aspect that is still under intense debate even after decades of experimental and theoretical efforts is the mechanism of ion translocation: How do K^+ channels realize the selective transport of K^+ ions at rates close to the diffusion limit? Two different permeation mechanisms are in the focus of current discussions, referred to as *soft knock-on* and *hard knock-on* mechanisms (Hummer 2014). The soft knock-on mechanism posits that the four ion binding sites (S1-S4) within the selectivity filter are alternatingly occupied by two K^+ ions and two water molecules in single file. Thereby, the K^+ ions occupy either the binding sites S1 and S3 or the sites S2 and S4 (Bernèche & Roux 2001). Accordingly, an ion approaching on one side of the filter pushes the entire chain of water molecules and K^+ ions forward to the other side (**Figure 1-4A**).

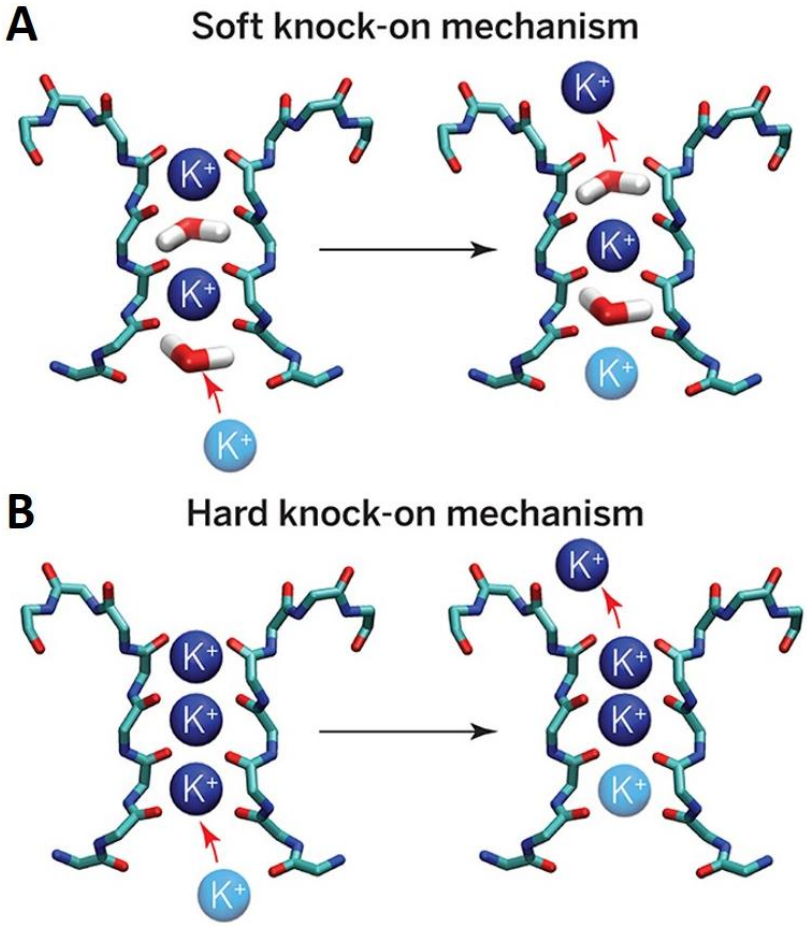

Figure 1-4: Ion permeation mechanisms in potassium channels. A In the soft knock-on model the selectivity filter is alternatingly occupied by water molecules and K^+ ions. Accordingly, approaching K^+ ions knock-out water and K^+ ions. **B** According to the hard knock-on mechanism, the selectivity filter is densely packed with K^+ ions in direct contact (from Hummer 2014).

The hard knock-on mechanism postulated by Köpfer et al. (2014) on the basis of extensive MD simulations posits that the K^+ ions within the selectivity filter have direct contact with

each other, i.e. they are not separated by water molecules. Accordingly, the conductance of K^+ channels is caused by direct ion-ion collisions inside the filter (**Figure 1-4B**). Even though this model provides some correct predictions, for example the diffusion limitation of ion conduction, the soft knock-on mechanism is the preferred permeation mechanism in the potassium channel community. A strong argument against the hard knock-on model was provided by electrophysiological measurements of streaming potentials performed by Iwamoto and Oiki (2011). The results of these experiments suggest that the translocation of a K^+ ion through the channel pore is accompanied by the cotransport of at least one water molecule. Further support for the soft knock-on model was provided by Kratochvil et al. (2016) by combining experimental and computational methods: they could show that the experimentally obtained two-dimensional infrared spectra of a semisynthetic KcsA channel can be reproduced by MD simulations of the KcsA channel with water molecules separating two potassium ions in the selectivity filter binding sites. However, the truth is perhaps more complicated, so that both mechanisms may contribute to ion conduction depending on the experimental conditions.

1.2.3. Pore gating and regulation

The permeation pathway of potassium channels can dynamically switch between conductive (open) and non-conductive (closed) states in response to external stimuli such as voltage, temperature, mechanical stretch or pressure, ions, small molecules and pH (Hille 2001, Pongs 1999). The stimuli-induced transition from a closed to an open state or *vis versa* is called *gating* (Hille 2001). Whereas the alteration of gene expression or membrane protein turn-over allows the regulation of membrane permeability on a timescale of minutes to hours, pore gating enables a very fast reaction to external stimuli in a time range of seconds or milliseconds (Yellen 2002).

Of particular importance is a fast pore gating mechanism in the context of electrical excitability of neurons and muscle cells. As briefly discussed in **section 1.1**, voltage-dependent potassium (Kv) channels play an essential role in generation, propagation and shaping of action potentials (Lodish et al. 2000). During the course of an action potential, Kv channels run through three different states: resting, activated and inactivated (Kuang et al. 2015). In the resting state the ion permeation pathway is closed by the so-called activation gate. The primary activation gate is formed by the C-termini of the S6 helices, that intersect near the intracellular membrane surface preventing hydrated potassium ions to enter/leave into/from the cavity. The S6 helices of Kv channels correspond to the inner transmembrane

helices of the bacterial KcsA channel (orange in **Figure 1-1**). The resulting constriction is referred to as *bundle crossing* (Kuang et al. 2015). The bundle-crossing gate acts in its closed conformation as a hydrophobic barrier for K^+ ions. As determined by mutation studies, in the voltage-dependent *Shaker* channel valine and phenylalanine residues act as effective blocking groups (Hackos et al. 2002). The S6 transmembrane helix and its cytoplasmic extension exhibit a high sequence similarity throughout the family of voltage-gated potassium channels and a conserved proline motif (PxP or PxG) close to the C-terminal end of the S6 transmembrane region (Labro & Snyders 2012). During opening and closing of the bundle-crossing gate in Kv channels, this proline motif acts as a flexible hinge that enables tilting or swiveling motions of the post-hinge portion of the S6 helix (Bright & Sansom 2003, Labro & Snyders 2012) (**Figure 1-5**). In contrast, in prokaryotic potassium channels such as KcsA and MthK the bending point of the inner pore helix is located at a highly conserved glycine residue in the middle of the transmembrane region (Labro & Snyders 2012).

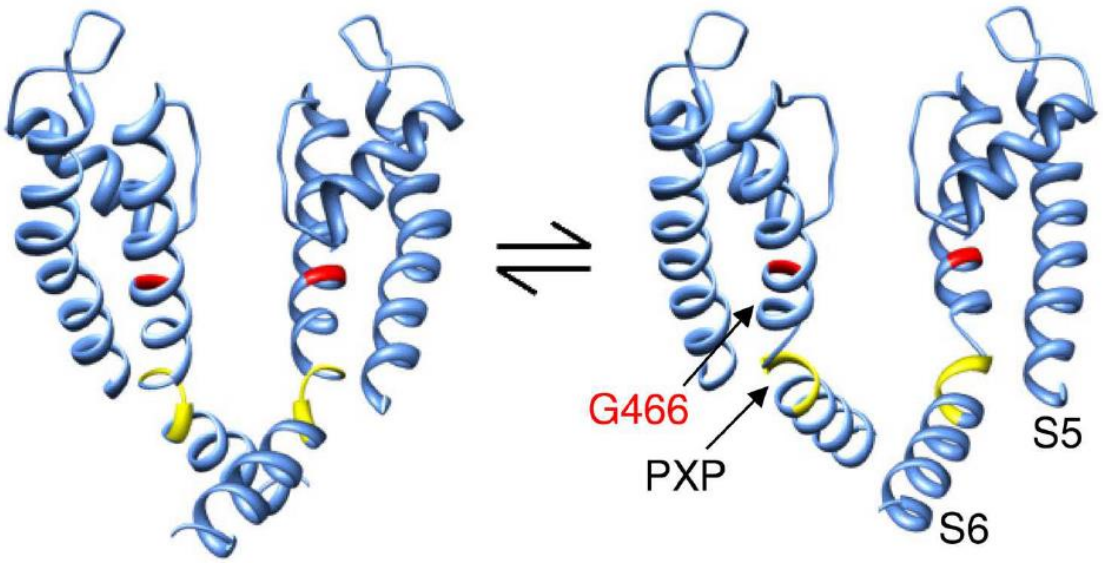

Figure 1-5: Opening and closing of the activation gate (bundle-crossing gate) in Shaker-type Kv channels. The S6 helix is bended at the conserved PxP motif (yellow) in both the closed (left) and open state (right). The bundle-crossing gate opens by reorientation of the post-hinge S6 helix portion. The location of the glycine residue that forms the hinge in KcsA is indicated in red (from Labro & Snyders 2012).

The activation gate of the majority of Kv channels opens in response to a membrane depolarization (Kuang et al. 2015). The voltage-dependent activation is controlled by the voltage-sensing domain (VSD), which is composed of the transmembrane segments S1-S4 (Gandhi & Isacoff 2002). The actual voltage sensor is constituted by the S4 helix, that contains 4 - 8 repeats of a conserved three residue sequence (+, *X1*, *X2*), where (+) denotes a positively charged amino acid (arginine or lysine), while *X1* and *X2* are hydrophobic residues. Depolarization of the membrane leads to a displacement of ~3.2 - 3.4 charges per subunit in

the *Shaker* potassium channel (Grizel et al. 2014). These gating charges are carried by four arginine residues and potentially one lysine residue of the conserved repeated three residue sequence (Gandhi & Isacoff 2002). Consequently, not all positively charged residues of the S4 helix are directly involved in voltage sensing. Furthermore, accessibility scanning experiments have shown that only 10 residues of the S4 segment span the membrane (Larson et al. 1996, Baker et al. 1998). This portion of the S4 helix corresponds to a length of 13.5 Å, which is considerably shorter than the hydrophobic core of the membrane, indicating that the S4 helix moves inside a short gating channel with a water-filled cavity on both sides of the membrane (**Figure 1-6**). It is assumed that in this way the electric transmembrane field is focused on the gating charges of the S4 helix (Gandhi & Isacoff 2002). In the last two decades, a variety of activation models have been postulated that try to combine the vast amount of experimental results. Currently it is generally accepted that the movement of the S4 helix caused by membrane depolarization is the result of an inclination of the S4 segment in the membrane, rotation on its axis, and a vertical and radial translocation (Grizel et al. 2014).

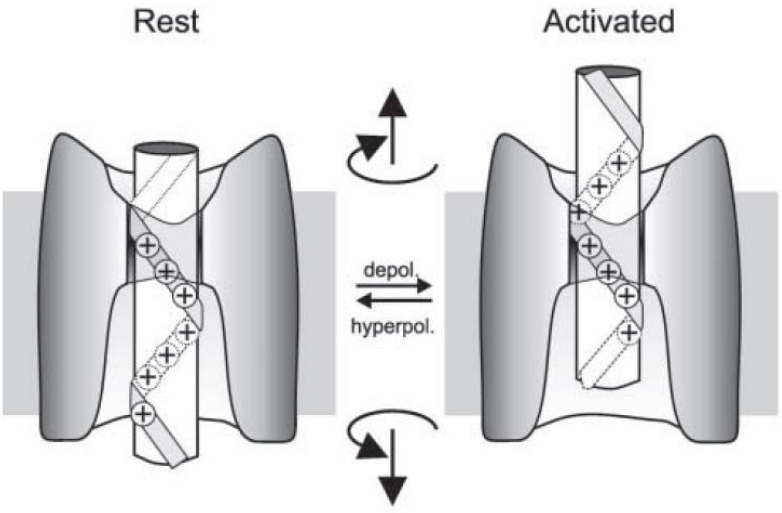

Figure 1-6: Schematic representation of Kv channel activation. Membrane depolarization causes a screw rotation and motion of the S4 helix inside the gating channel of the voltage-sensing domain (from Gandhi & Isacoff 2002).

The movement of the S4 helix is electromechanically coupled to the pore-forming domain via the S4-S5 linker, which interacts with the C-terminus of the pore-lining S6 helix. In this way, the energy of the S4 helix movement is transferred to the pore, resulting in an opening of the activation gate and a rapid efflux of potassium ions (Blunck & Batulan 2012, Jensen et al. 2012).

Activation is followed by an inactivation process that can be caused by at least two different mechanisms: N-type or C-type inactivation (Kuang et al. 2015). N-type inactivation has been described for *Shaker* channels and some mammalian Kv channels and is the result of an

interaction between a N-terminal particle (inactivation ball) and the open channel (Hoshi et al. 1990) (**Figure 1-7A**).

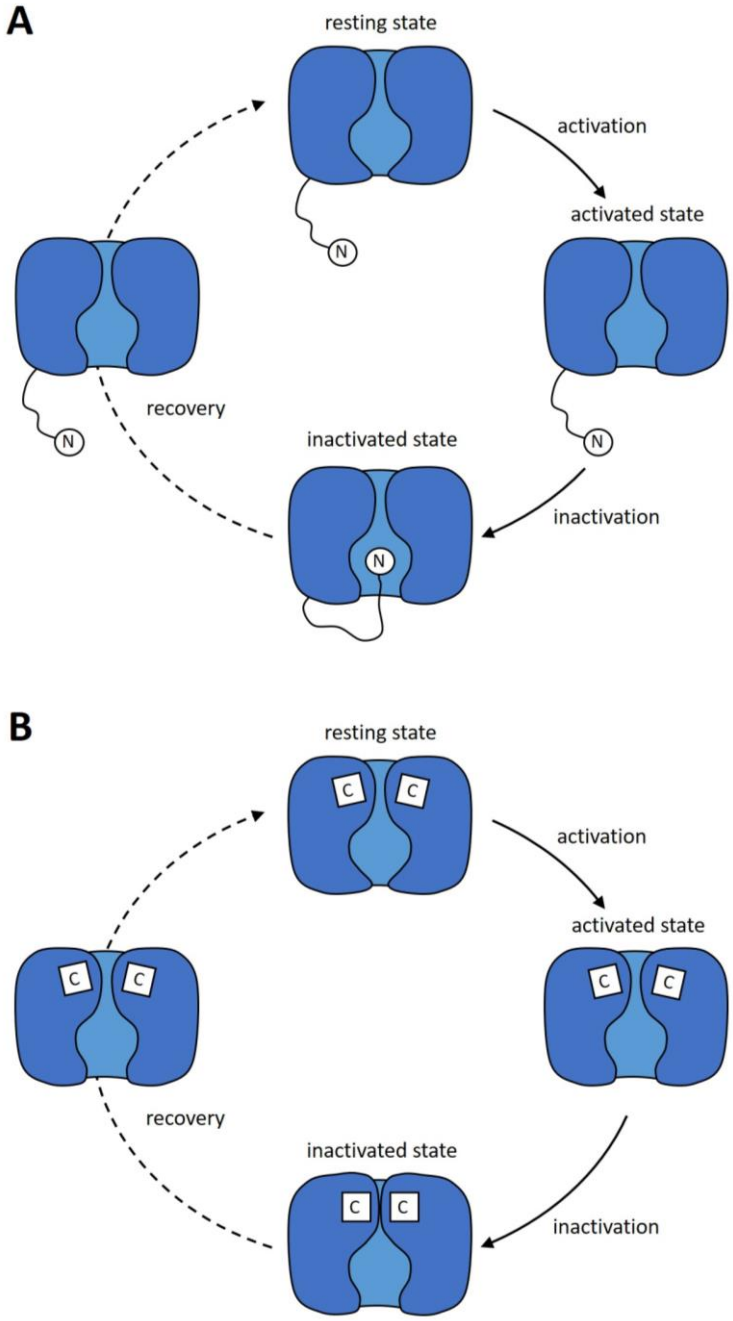

Figure 1-7: Schematic representation of conformational changes that gate the K^+ channel pore. A N-type inactivation: after voltage-dependent activation, i.e. opening of the intracellular bundle-crossing gate, a N-terminal inactivation peptide (ball) enters the permeation pathway and thereby inactivates the channel. **B** C-type inactivation: channel inactivation involves conformational changes in the selectivity filter or the extracellular pore mouth, which render the permeation pathway non-conductive. Recovery from both types of inactivation is voltage-dependent.

The N-terminal inactivation particle consists of about 10 hydrophobic residues, followed by a series of amino acids with a net positive charge (Kurata & Fedidia 2006). Basically, the inactivation ball acts as an open channel blocker: upon opening of the intracellular activation

gate, the inactivation ball can penetrate the channel pore and thereby block the efflux of K^+ ions. The blockage is caused by interactions between the hydrophobic residues of the inactivation ball and hydrophobic regions within the pore (Murrell-Lagnado & Aldrich 1993). The positively charged residues in the inactivation particle interact electrostatically with negatively charged residues in the linker between the S1 transmembrane segment and the cytosolic T1 domain. These linkers form four fenestrations that likely serve as passage way for the inactivation particle (Gulbis et al. 2000).

The second and usually slower inactivation process is called C-type inactivation. This inactivation process results from conformational changes in the selectivity filter or the extracellular pore region of voltage-gated channels (Hoshi & Armstrong 2013) (**Figure 1-7B**) and is also present in 2TM/P channels like MthK (Thomson et al. 2014) or KcsA (Bernèche & Roux 2005). An important example of a C-type inactivating channel is the human ERG (HERG or Kv11) channel, which is responsible for terminating the plateau phase of action potentials in cardiac ventricular cells (Keating & Sanguinetti 2001). The molecular causes of C-type inactivation are still under discussion. It is even not clear, if all inactivation processes, that have been referred to as C-type inactivation, are indeed caused by the same mechanism (Kurata & Fedida 2006, Hoshi & Armstrong 2013). A common feature of C-type inactivation is its sensitivity to external K^+: elevation of the extracellular K^+ concentration causes an inhibition or deceleration of the inactivation process (Hoshi et al. 1990). The same effect on the C-type inactivation rate has been observed for extracellular TEA^+ (Molina et al. 1997). These findings have been explained by a 'foot in the door' mechanism, that posits that binding of K^+ or TEA^+ to an ion binding site at the extracellular pore entrance prevents the conformational changes underlying C-type inactivation (Baukrowitz & Yellen 1996). Kiss and Korn (1998) could demonstrate that this binding site is located inside the selectivity filter. On the basis of Cd^{2+} binding experiments performed with an engineered *Shaker* channel, Yellen et al. (1994) postulated that C-type inactivation goes along with a constriction of the outer pore entrance. In addition, simulations and crystallographic studies performed with the prokaryotic potassium channel KcsA suggested that C-type inactivation reflects the transition from a conductive to a partially collapsed selectivity filter conformation (Cordero-Morales et al. 2007, Zhou et al. 2001). In contrast, Hoshi and Armstrong (2013) hypothesized that C-type inactivation in Kv channels may reflect a pore dilation, rather than a pore constriction.

Inwardly rectifying (Kir) channels do not possess a canonical VSD nor do they show Kv-like C-type inactivation (McCoy & Nimigean 2012). The characteristic inward rectification, i.e. the ability to allow greater influx than efflux of ions, is caused by cytosolic ions such as Mg^{2+} and polyamines, which block K^+ efflux at membrane voltages that are more positive than the

resting potential (Bichet et al. 2003). In addition to the blockage of the permeation pathway by cytosolic ions, Kir channels and their prokaryotic homologs (KirBac) are gated by several cytosolic factors such as G-proteins, phosphatidylinositol-4,5-bisphosphate (PIP_2), arachidonic acid, pH, Na^+ and ATP (Bichet et al. 2003). The interaction of these regulatory factors mainly occurs at the cytoplasmic domains, which are formed by the C- and N-termini of the four Kir subunits (Hibino et al. 2010). For instance, PIP_2 enhances the currents of Kir channels by interaction with positively charged residues in the cytoplasmic domains and a region just below the inner TM helix (Hibino et al. 2010). It is assumed that the interaction of regulatory factors with the cytoplasmic domain is transferred into gating movements, which predominantly take place at the bundle crossing (Bichet et al. 2003). Several mutation studies suggest that the inner TM helix bends around a glycine hinge point during opening and closing of the bundle-crossing gate (e.g. Jin et al. 2002, Sadja et al. 2001). The actual gate in Kir and KirBac channels is probably formed by bulky hydrophobic residues (e.g. phenylalanine and leucine) at the bundle-crossing point (Sadja et al. 2001, Meng et al. 2016). In addition, there is ample evidence that the selectivity filter of Kir channels acts as a second gate, which corresponds to fast gating events (flickering) within bursts of activity (Guo & Kubo 1998, Proks et al. 2001). However, it is believed that the majority of regulatory factors affect the slow bundle-crossing gate, rather than the fast selectivity-filter gate (Bichet et al. 2003).

Voltage-dependent gating has also been described for two-pore domain (K2P) potassium channels such as TREK-3 and TREK-1 (Bockenhauer et al. 2001, Brickley et al. 2007, Schewe et al. 2016). Like Kir channels, K2P channels do not possess a canonical VSD. However, in contrast to the inward rectification of Kir channels, voltage-dependent gating in K2P channels is not caused by internal or external blockers such as Mg^{2+}, but represents an intrinsic and common property of nearly all members of the K2P channel family (Schewe et al. 2016). However, the underlying mechanism is still poorly understood. Mutational studies performed by Schewe et al. (2016) suggest that the voltage-dependent gate resides within or close to the selectivity filter and not at the intracellular pore entrance as in Kv channels. Consequently, the voltage-dependent activation/inactivation of K2P channels is likely caused by an ion-flux mechanism, which is directly powered by the electrochemical gradient for K^+ (Schewe et al. 2016). K2P channels have been mainly recognized as “background” K^+-selective channels, that establish and maintain in a highly regulated way the hyperpolarized resting membrane potential in excitable cells (O'Connell et al. 2002). This inevitably raises the question whether the voltage-dependence is merely an oddity or a physiologically important property of K2P channels. The latter is supported by a study published by Bockenhauer et al. (2001). They could demonstrate that the native hippocampal TREK-1 (KCNK2) channel can be reversibly

converted from a leak to a voltage-dependent phenotype by phosphorylation of a single serine residue. This mechanism provides a possible pathway for dynamic regulation of excitability (Bockenhauer et al. 2001). In another study the authors could show that the voltage-dependent activation of a particular K2P channel, TASK-3, increases the excitability of cerebellar granule neurons by supporting high-frequency firing (Brickley et al. 2007).

Voltage-dependent gating as found in K2P channels is of particular importance for the present work, since similar processes can also occur in members of the Kcv family.

1.3. Viral Kcv channels

Prokaryotic and eukaryotic potassium channels are usually composed of several hundred amino acids per monomer. For example, a subunit of the relatively small bacterial potassium channel KirBac1.1 is composed of 333 amino acids (Kuo et al. 2003). Highly regulated channels, such as the human ERG (hERG) channel (**Figure 1-8**), are with more than 1000 amino acids per monomer truly gigantic (Vandenberg et al. 2012). In contrast, dsDNA viruses of the *Phycodnaviridae* family encode for miniature potassium channels with usually less than 100 amino acids per monomer (Thiel et al. 2011). These potassium channels, referred to as Kcv channels, consist of four identical subunits with a highly reduced architecture: each subunit is composed of two TM helices linked by a pore loop. The latter contains a pore helix and the canonical signature sequence TVGY/FGD (Thiel et al. 2011). In contrast to prokaryotic or eukaryotic potassium channels, Kcv channels do not possess cytosolic N- or C-terminal domains. In spite of their small size, Kcv channels exhibit many of the properties typical for more complex potassium channels: they show a high K^+ over Na^+ selectivity, fluctuate stochastically between open and closed states and can be inhibited by classical potassium channel blockers such as Ba^{2+} (Gazzarini et al. 2009, 2003, Braun et al. 2014, Rauh et al. 2017a,b).

The prototypical viral potassium channel Kcv_{PBCV-1} was found in the chlorella virus PBCV-1 (*Paramecium bursaria Chlorella virus*-1) that infects the eukaryotic *Chlorella*-like green algae NC64A (Thiel et al. 2010). Kcv_{PBCV-1} has a size of 94 amino acids per monomer and is presumably part of the internal membrane of the PBCV-1 virion (Thiel et al. 2010). As such, it plays an important role in the early phase of infection. It is assumed that the internal PBCV-1 membrane physically fuses with the host plasma membrane during infection, thereby allowing Kcv_{PBCV-1} channels to enter the plasma membrane (Neupärtl et al. 2008). Due to the Kcv-mediated efflux of K^+ ions, a rapid membrane depolarization is initiated, which leads via

secondary events to the loss of water and thus to a reduction of the high internal pressure. This finally enables the injection of viral DNA into the host cell (Neupärtl et al. 2008, Agarkova et al. 2008).

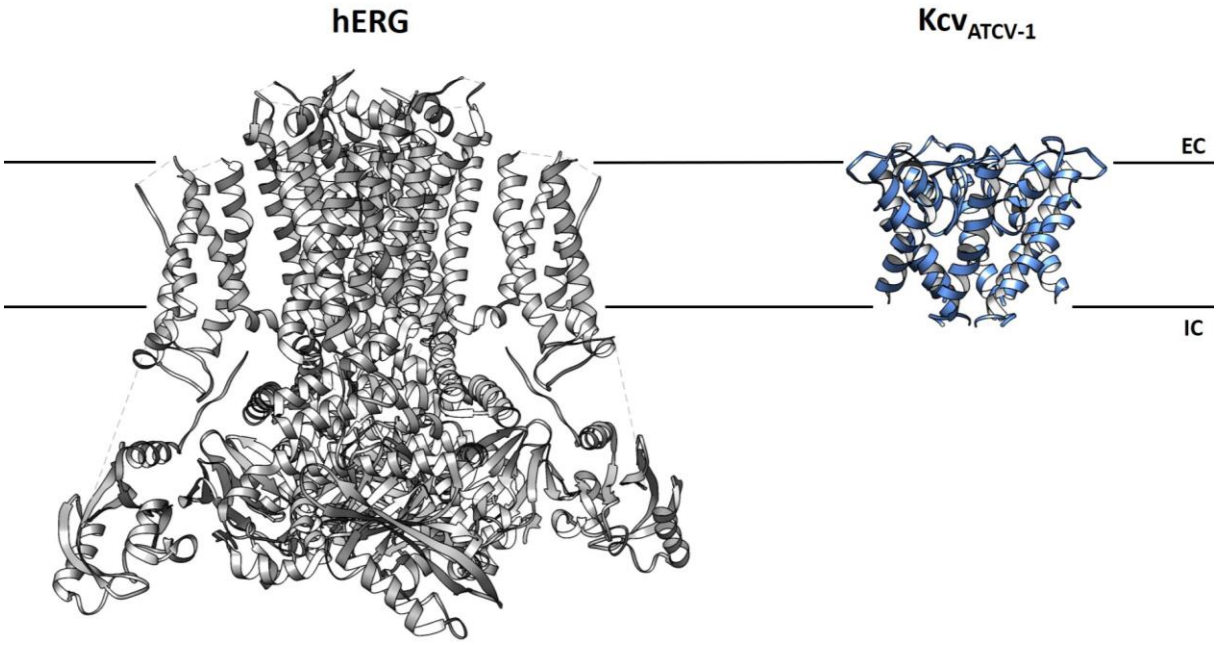

Figure 1-8: Comparison between the structures of the voltage-dependent hERG channel and the viral potassium channel Kcv$_{NTS}$. Left: cryo-EM structure of the human hERG channel (PDB: 5VA1, Wang & MacKinnon 2017). Right: homology model of the potassium channel Kcv$_{NTS}$. The homology model was calculated with Swissmodel (Arnold et al. 2006) using structural KirBac1.1 data (PDB code 1P7B, Kuo et al. 2003). EC and IC indicate the extracellular and intracellular space, respectively.

Kcv-type potassium channels are also found in other members of the *Phycodnaviridae* family (Thiel et al. 2010). Of particular importance for the present work are the so-called Kcv$_{ATCV-1}$-like viral potassium channels. These channels are encoded by Phycodnaviruses, which infect unicellular SAG type Chlorella algae (Bubeck & Pfitzner 2005). The prototype of this group of channels, Kcv$_{ATCV-1}$, is encoded by the chlorella virus ATCV-1 (*Acanthocystis turfacea Chlorella virus-1*) (Fitzgerald et al. 2007). The subunits of nearly all Kcv$_{ATCV-1}$-like channels known so far consist of 82 amino acids and share a high sequence identity (Siotto 2017). Since they lack any cytosolic or extracellular domains, Kcv$_{ATCV-1}$-like channels are fully embedded in the lipid membrane (Braun et al. 2014) (**Figure 1-8**). For more details see **section 3.2.**

Due to their simple architecture, which is identical to the architecture of the pore module of more complex K^+ channels (Kang et al. 2004), their easy handling (Winterstein et al. 2018) and the large variety of homologous sequences, Kcv$_{ATCV-1}$-like channels provide an ideal system for investigating the molecular causes of basic channel properties such as selectivity, conductivity and gating.

1.4. References

Alam & Jiang (2011) Structural studies of ion selectivity in tetrameric cation channels. J Gen Physiol 137(5):397-403

Alberts et al. (2002) Carrier proteins and active membrane transport. Molecular Biology of the Cell. 4th edition. New York: Garland Science

Agarkova et al. (2008) Chlorovirus-mediated membrane depolarization of Chlorella alters secondary active transport of solutes. J Virol 82(24):12181-90

Arcadi & Miller (2004) Secondary active transport mediated by a prokaryotic homologue of ClC Cl^- channels. Nature 427(6977):803-7

Arnold et al. (2006) The SWISS-MODEL workspace: a web-based environment for protein structure homology modelling. Bioinformatics 22(2):195-201

Baker et al. (1998) Three transmembrane conformations and sequence-dependent displacement of the S4 domain in shaker K^+ channel gating. Neuron 20:1283–1294.

Baukrowitz & Yellen (1996) Use-dependent blockers and exit rate of the last ion from the multi-ion pore of a K^+ channel. Science 271(5249):653-6.

Bavro et al. (2012) Structure of a KirBac potassium channel with an open bundle-crossing indicates a mechanism of channel gating. Nat Struct Mol Biol 19(2):158–163

Bernèche & Roux (2001) Energetics of ion conduction through the K^+ channel. Nature 414(6859):73-7

Bernèche & Roux (2005) A gate in the selectivity filter of potassium channels. Structure 13:591-600

Bezanilla & Armstrong (1972) Negative conductance caused by entry of sodium and cesium ions into the potassium channels of squid axons. J Gen Physiol 60(5):588-608

Bichet et al. (2003) Merging functional studies with structures of inward-rectifier K^+ channels. Nature Reviews 4(12):957-67

Blunck & Batulan (2012) Mechanism of electromechanical coupling in voltage-gated potassium channels. Front Pharmacol 3:166

Bockenhauer et al. (2001) KCNK2: reversible conversion of a hippocampal potassium leak into a voltage-dependent channel. Nat Neurosci 4(5):486-91

Braun et al. (2014) Viral potassium channels as a robust model system for studies of membrane-protein interaction. Biochim Biophys Acta 1838(4):1096-103

Brickley et al. (2007) TASK-3 two-pore domain potassium channels enable sustained high-frequency firing in cerebellar granule neurons. J Neurosci 27(35):9329-40

Bright & Sansom (2003) The flexing/twirling Helix: exploring the flexibility about molecular hinges formed by proline and glycine motifs in transmembrane helices. J. Phys. Chem. B 107 (2):627–636

Bubeck & Pfitzner (2005) Isolation and characterization of a new type of chlorovirus that infects an endosymbiotic Chlorella strain of the heliozoon Acanthocystis turfacea. J Gen Virol 86(Pt 10):2871-7

Cordero-Morales et al. (2007) Molecular driving forces determining potassium channel slow inactivation. Nat Struct Mol Biol. 14(11):1062-9

DeFelice (2004) Transporter structure and mechanism. Trends Neurosci 27(6):352-9

Deutsch & Chen (1993) Heterologous expression of specific K^+ channels in T lymphocytes: functional consequences for volume regulation. Proc Natl Acad Sci USA 90(21): 10036–10040

Doyle et al. (1998) The structure of a potassium channel: molecular basis of K^+ conduction and selectivity. *Science* **280**:69–77

Dworakowska & Dołowy (2000) Ion channels-related diseases. Acta Biochim Pol 47(3):685-703

Egwolf & Roux (2010) Ion selectivity of the KcsA channel: A perspective from multi-ion free energy landscapes. J Mol Biol 401(5): 831–842.

Fitzgerald et al. (2007) Sequence and annotation of the 288-kb ATCV-1 virus that infects an endosymbiotic chlorella strain of the heliozoon Acanthocystis turfacea. Virology 362(2): 350–361

Gandhi & Isacoff (2002) Molecular models of voltage sensing. J Gen Physiol. 120(4): 455–463

Gazzarini et al. (2003) The viral potassium channel Kcv: structural and functional features. FEBS Lett. 2003 Sep 18;552(1):12-6

Gazzarini et al. (2009) Chlorella virus ATCV-1 encodes a functional potassium channel of 82 amino acids. Biochemical Journal 420:295-303

Grizel et al. (2014) Mechanisms of activation of voltage-gated potassium channels. Acta Naturae 6(4): 10–26

Gulbis et al. (2000) Structure of the cytoplasmic beta subunit-T1 assembly of voltage-dependent K^+ channels. Science 289(5476):123-7

Guo & Kubo (1998) Comparison of the open-close kinetics of the cloned inward rectifier K^+ channel IRK1 and its point mutant (Q140E) in the pore region. Receptors Channels 5(5):273-89

Hackos et al. (2002) Scanning the intracellular S6 activation gate in the Shaker K^+ channel. J Gen Physiol 119(6): 521–531

Haitin et al. (2013) The structural mechanism of KCNH-channel regulation by the eag domain. Nature 501(7467):444-8

Heginbotham et al. (1994) Mutations in the K^+ channel signature sequence. Biophys J 66(4): 1061–1067

Hibino et al. (2010) Inwardly rectifying potassium channels: their structure, function, and physiological roles. Physiol Rev 90(1):291-366

Hille (2001) Ion channels of excitable membranes. Sinauer Associates, Inc.

Hodgkin & Huxley (1952) Currents carried by sodium and potassium ions through the membrane of the giant axon of *Loligo*. J Physiol 116(4): 449–472

Hoshi et al. (1990) Biophysical and molecular mechanisms of shaker potassium channel inactivation. Science 250(4980):533-538

Hoshi & Armstrong (2013) C-type inactivation of voltage-gated K^+ channels: Pore constriction or dilation? JGP 141(2):151-160

Hummer (2014) Biochemistry. Potassium ions line up. Science 346(6207):303

Inagaki & Seino (1998) ATP-sensitive potassium channels: structures, functions, and pathophysiology. Jpn J Physiol 48(6):397-412

Iwamoto & Oiki (2011) Counting ion and water molecules in a streaming file through the open-filter structure of the K channel. J Neurosci 31(34):12180-8

Jensen et al. (2012) Mechanism of voltage gating in potassium channels. Science 336(6078):229-33

Jin et al. (2002) The (beta)gamma subunits of G proteins gate a K^+ channel by pivoted bending of a transmembrane segment. Mol Cell 10(3):469-81

Kaczorowski et al. (2008) Ion channels as drug targets: the next GPCRs. J Gen Physiol 131(5):399–405

Kang et al. (2004) Small potassium ion channel proteins encoded by chlorella viruses. Proc Natl Acad Sci USA. 101(15):5318-24

Keating & Sanguinetti (2001) Molecular and cellular mechanisms of cardiac arrhythmias. Cell 104(4):569-80

Ketchum et al. (1995) A new family of outwardly rectifying potassium channel proteins with two pore domains in tandem, Nature 376:690-695

Kiss & Korn (1998) Modulation of C-type inactivation by K^+ at the potassium channel selectivity filter. Biophys J. 74(4): 1840–1849

Kratochvil et al. (2016) Instantaneous ion configurations in the K^+ ion channel selectivity filter revealed by 2D IR spectroscopy. Science 353(6303):1040-1044

Kuang et al. (2015) Structure of potassium channels. Cell. Mol. Life Sci. 72:3677-3693

Kuo et al. (2003) Crystal structure of the potassium channel KirBac1.1 in the closed state. Science 300(5627):1922-6

Kurata & Fedida (2006) A structural interpretation of voltage-gated potassium channel inactivation. Progress in Biophysics and Molecular Biology 92(2):185-208

Labro & Snyders (2012) Being flexible: The voltage-controllable activation gate of Kv channels. Front Pharmacol 3:168

Lang & Stournaras (2014) Ion channels in cancer: future perspectives and clinical potential. Philos Trans R Soc Lond B Biol Sci 369(1638):20130108

Larsson et al. (1996) Transmembrane movement of the shaker K^+ channel S4. Neuron 16:387–397.

Lesage & Lazdunski (2000) Molecular and functional properties of two-pore-domain potassium channels. Am J Physiol Renal Physiol 279(5):F793-801

Lodish et al. (2000) Overview of membrane transport proteins. Molecular Cell Biology. 4th edition. New York: W. H. Freeman

MacKinnon (2003) Potassium channels. FEBS Lett. 555(1):62-5

McCoy & Nimigean (2012) Structural correlates of selectivity and inactivation in potassium channels. Biochim Biophys Acta 1818(2):272-85

Meng et al. (2016) The molecular mechanism of opening the helix bundle crossing (HBC) Gate of a Kir Channel. Sci Rep 6: 29399

Miller (2000) An overview of the potassium channel family. Genome Biol 1(4): reviews0004.1–reviews0004.5

Molina et al. (1997) Pore mutations in Shaker K^+ channels distinguish between the sites of tetraethylammonium blockade and C-type inactivation. J Physiol 499 (Pt 2):361-7

Murrell-Lagnado & Aldrich (1993) Energetics of Shaker K^+ channels block by inactivation peptides. J Gen Physiol 102(6):977-1003

Nelson & Quayle (1995) Physiological roles and properties of potassium channels in arterial smooth muscle. Am J Physiol. 268(4 Pt 1):C799-822

Neupärtl et al. (2008) Chlorella viruses evoke a rapid release of K+ from host cells during the early phase of infection. Virology 372(2):340-8

Noskov et al. (2004) Control of ion selectivity in potassium channels by electrostatic and dynamic properties of carbonyl ligands. Nature 431(7010):830-4

O'Connell et al. (2002) Two-pore domain K^+ channels-molecular sensors. Biochim Biophys Acta 1566(1-2):152-61

Pauling (1960) The nature of the chemical bond and the structure of molecules and crystals. Cornell Univ Press 3rd edn

Pongs (1999) Voltage-gated potassium channels: from hyperexcitability to excitement. FEBS Lett. 452(1-2):31-5

Proks et al. (2001) Mutations within the P-Loop of Kir6.2 Modulate the Intraburst Kinetics of the ATP-Sensitive Potassium Channel. J Gen Physiol 118(4): 341–353

Rauh et al. (2017a) Identification of intrahelical bifurcated H-bonds as a new type of gate in K^+ channels. J. Am. Chem. Soc. 139 (22):7494–7503

Rauh et al. (2017b) Extended beta distributions open the access to fast gating in bilayer experiments-assigning the voltage-dependent gating to the selectivity filter. FEBS Lett. 2017 591(23):3850-3860

Sadja et al. (2001) Coupling Gβγ-dependent activation to channel opening via pore elements in inwardly rectifying potassium channels. Neuron 29(3):669-80

Salari et al. (2015) Evidence for a KATP channel in rough endoplasmic reticulum (rerKATP Channel) of rat hepatocytes. PLoS One 10(5):e0125798

Sansom et al. (2002) Potassium channels: structures, models, simulations. Biochim Biophys Acta 1565(2):294–307

Schewe et al. (2016) A non-canonical voltage-sensing mechanism controls gating in K2P K^+ channels. Cell 164(5): 937–949

Schwab et al. (2012) Role of ion channels and transporters in cell migration. Physiol Rev. 92(4):1865-913

Siotto (2017) Mining and analysis of new viral potassium channel proteins. Dissertation at the Technische Universität Darmstadt.

Stojilkovic et al. (2010) Ion channels and signaling in the pituitary gland. Endocr Rev. 31(6):845-915

Szewczyk et al. (2009) Mitochondrial potassium channels. IUBMB Life 61(2):134-43

Thiel et al. (2010) Initial events associated with virus PBCV-1 infection of chlorella NC64A. Prog Bot 71(3):169-183

Thiel et al. (2011) Minimal art: or why small viral K^+ channels are good tools for understanding basic structure and function relations. Biochim. Biophys. Acta. 1808:580-588

Thiel et al. (2013) Potassium ion channels: could they have evolved from viruses? Plant Physiology 162: 1215–1224

Thomson et al. (2014) Initial steps of inactivation at the K^+ channel selectivity filter. PNAS 111(17):E1713-22

Vandenberg et al. (2012) hERG K^+ channels: structure, function, and clinical significance. Physiol Rev 92(3):1393-478

Wang et al. (2017) A voltage-dependent K^+ channel in the lysosome is required for refilling lysosomal Ca^{2+} stores. J Cell Biol 216(6):1715-1730

Wang & MacKinnon (2017) Cryo-EM Structure of the Open Human Ether-à-go-go-Related K^+ Channel hERG. Cell 169(3):422-430

Winterstein et al. (2018) Reconstitution and functional characterization of ion channels from nanodiscs in lipid bilayers. J Gen Physiol. 150 (4): 637

Yellen et al. (1994) An engineered cysteine in the external mouth of a K^+ channel allows inactivation to be modulated by metal binding. Biophys J 66(4):1068-75

Yellen (2002) The voltage-gated potassium channels and their relatives. Nature 419(6902):35-42

Yu et al. (2005) Overview of molecular relationships in the voltage-gated ion channel superfamily. Pharmacol Rev 57(4):387-95

Zhou et al. (2001) Chemistry of ion coordination and hydration revealed by a K^+ channel-Fab complex at 2.0 Å resolution. Nature 414(6859):43-8

2. Identification of intrahelical bifurcated H-bonds as a new type of gate in K^+ channels

This chapter was published with small modifications in Rauh O, Urban M, Henkes LM, Winterstein T, Greiner T, Van Etten JL, Moroni A, Kast SM, Thiel G, Schroeder I. (2017) Identification of Intrahelical Bifurcated H-Bonds as a New Type of Gate in K^+ Channels. J Am Chem Soc. 139(22):7494-7503

2.1. Abstract

Gating of ion channels is based on structural transitions between open and closed states. To uncover the chemical basis of individual gates, a comparative experimental and computational analysis between two K^+ channels, Kcv_S and Kcv_{NTS}, was performed. These small viral encoded K^+ channel proteins, with a monomer size of only 82 amino acids, resemble the pore module of all complex K^+ channels in terms of structure and function. Even though both proteins share about 90% amino acid sequence identity they exhibit different open probabilities with ca. 90% in Kcv_{NTS} and 40% in Kcv_S. Single channel analysis, mutational studies and molecular dynamics simulations show that the difference in open probability is caused by one long closed state in Kcv_S. This state is structurally created in the tetrameric channel by a transient, serine-mediated, intrahelical hydrogen bond. The resulting kink in the inner transmembrane domain promotes an interaction of aromatic rings from downstream phenylalanine residues in the cavity of the channel that blocks ion flux. The frequent occurrence of Ser or Thr based helical kinks in membrane proteins suggests that a similar mechanism could also occur in the gating of other ion channels.

2.2. Introduction

Ion channels fluctuate stochastically between conductive “open” states and non-conductive “closed” states (Hille 2001). This process of gating determines the flux of ions across membranes and is therefore a crucial parameter for the regulation of channel activity in the physiological context. Many physical factors like voltage or mechanical stretch and chemical factors like ligands or signaling molecules can modulate the stability of individual closed or open states and as a consequence regulate ion fluxes across membranes. The recent availability of high-resolution structures from channel proteins makes it possible to correlate

experimentally measured gating events from single channel recordings with dynamic structural phenomena in channel proteins (Cordero-Morales et al. 2006, Thompson et al. 2008). Well documented correlations between channel gating and structural modifications are known from the model K^+ channel KscA. Two gates have been identified in this channel. One gate is located at the inner bundle crossing and is activated by H^+ (Thompson et al. 2008). The second gate is in the selectivity filter (Cordero-Morales et al. 2006). Additional structure/function studies have uncovered some electrostatic interactions among amino acid side chains, which are involved in gating and which are presumably responsible for the stochastic switching between open and closed states of the channel. For the H^+ dependent gating in the KcsA channel a complex network of inter- and intra-subunit salt bridges and hydrogen bonds was identified near the bundle crossing; these are stabilized or de-stabilized according to pH (Thompson et al. 2008). In the case of the KscA filter gate a network of amino acid (AA) side chains surrounding the selectivity filter together with the ions in the filter and water behind the filter affect the stability of the conformational states of the pore. A key role in this network is played by a single carboxyl-carboxylate interaction between a Glu (E71) in the pore helix and an Asp (D80) in the signature sequence. Substitution of E71 with Ala (E71A) led to a complete disappearance of inactivation and a constitutively open channel at low pH (Cordero-Morales et al. 2006).

Here I use small chlorovirus encoded K^+ channels to search for additional structural motives for ion channel gating. These channels, which represent the pore module of complex K^+ channels (Tayefeh et al. 2009), have the advantage of being truly minimal because they consist of two transmembrane domains, a pore loop with short N- and C-termini and small extracellular loops (**Figure 2-1**). Like other K^+ channels they form functional tetramers and have many functional properties present in more complex K^+ channels. This includes K^+ selectivity, a susceptibility to blockers and, important for this study, stochastic gating between defined open and closed states (Thiel et al. 2011, Abenavoli et al. 2009). By using K^+ channel genes from chloroviruses isolated from different environments a large library of structural orthologs, which exhibit distinct functional differences, has been created (e.g. Kang et al. 2004, Gazzarrini et al. 2004). In the present study two small K^+ channel orthologs were analyzed, which differ in the presence or absence of a long-lived closed state, even though they have high amino acid identity. Comparative analysis of the two channels identified a phenylalanine in the inner transmembrane domain as a gate, which can obstruct the ion pathway in the cavity. The stochastic insertion and removal of the aromatic barrier must be achieved by the formation of H-bonds between an adjacent serine with upstream-positioned amino acids in the transmembrane domain. Hence stochastic gating of this long-lived closed

state presumably reflects the formation of a kink in the inner transmembrane domain and its subsequent effect on the orientation of the phenylalanine barrier.

2.3. Results and Discussion

2.3.1. The viral K^+ channels Kcv_{NTS} and Kcv_S exhibit different open probabilities

The viral encoded proteins Kcv_{NTS} and Kcv_S are small K^+ channels with only 82 amino acids per monomer. The two proteins differ in 11 amino acids of which 8 are conservative and 3 are semi-conservative exchanges (**Figure 2-1B**). The difference between Kcv_{NTS} and a third channel Kcv_{ATCV-1}, which was analyzed previously (Gazzarini et al. 2009), is only four amino acids.

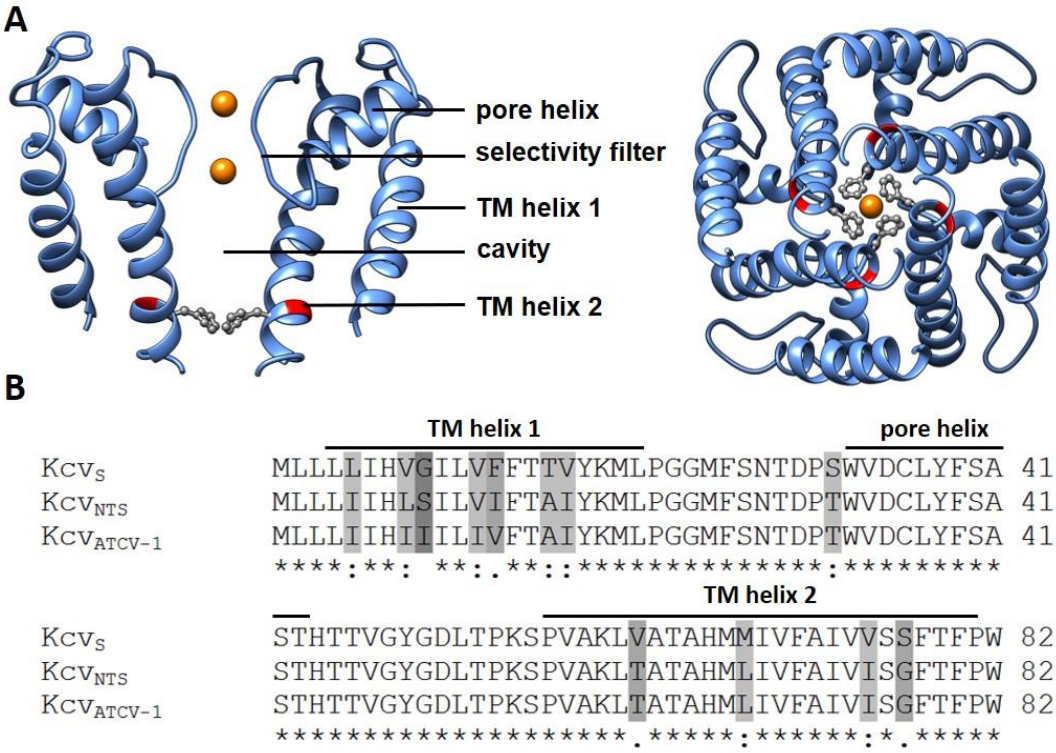

Figure 2-1: Chlorovirus encoded K^+ channels. A Cartoon representations of a homology model of Kcv_S. Left: Side view of the channel (two opposing monomer units). Right: view from bottom to top of the full tetrameric channel. Potassium ions are shown as orange spheres, the position of S77 in red, and F78 as explicit side chains in gray. The homology model was calculated with Swissmodel (Arnold et al. 2006) using structural KirBac1.1 data (PDB code 1P7B, Kuo et al. 2003). **B** Sequence alignment of three viral encoded K^+ channels. The position of the transmembrane (TM) helices 1 and 2 as well as the pore helix are indicated by bars. The sequences are 86% identical; amino acid differences are highlighted in gray.

When reconstituted in planar lipid bilayers, Kcv_{NTS} and Kcv_S generate channel fluctuations with a similar unitary conductance (86.8 ± 1.4 pS (N = 6) and 93.6 ± 3.6 (N = 8) for Kcv_{NTS}

and Kcv_S, respectively) and the same characteristic i/V relation (**Figure 2-2A-C**). The latter is characterized by an Ohmic conductance at positive voltages and a negative slope conductance at negative voltages. The decrease in channel amplitude at negative voltages is caused by a rapid flickering of the channel, which results in unresolved channel openings (**Figure 2-2A,B**) (Abenavoli et al. 2009, Rauh et al. 2017b). These recordings imply that the sequence deviations between the two channels have no large impact on the unitary conductance and on fast gating, which is presumably dominated by a pore gate (Abenavoli et al. 2009, Rauh et al. 2017b).

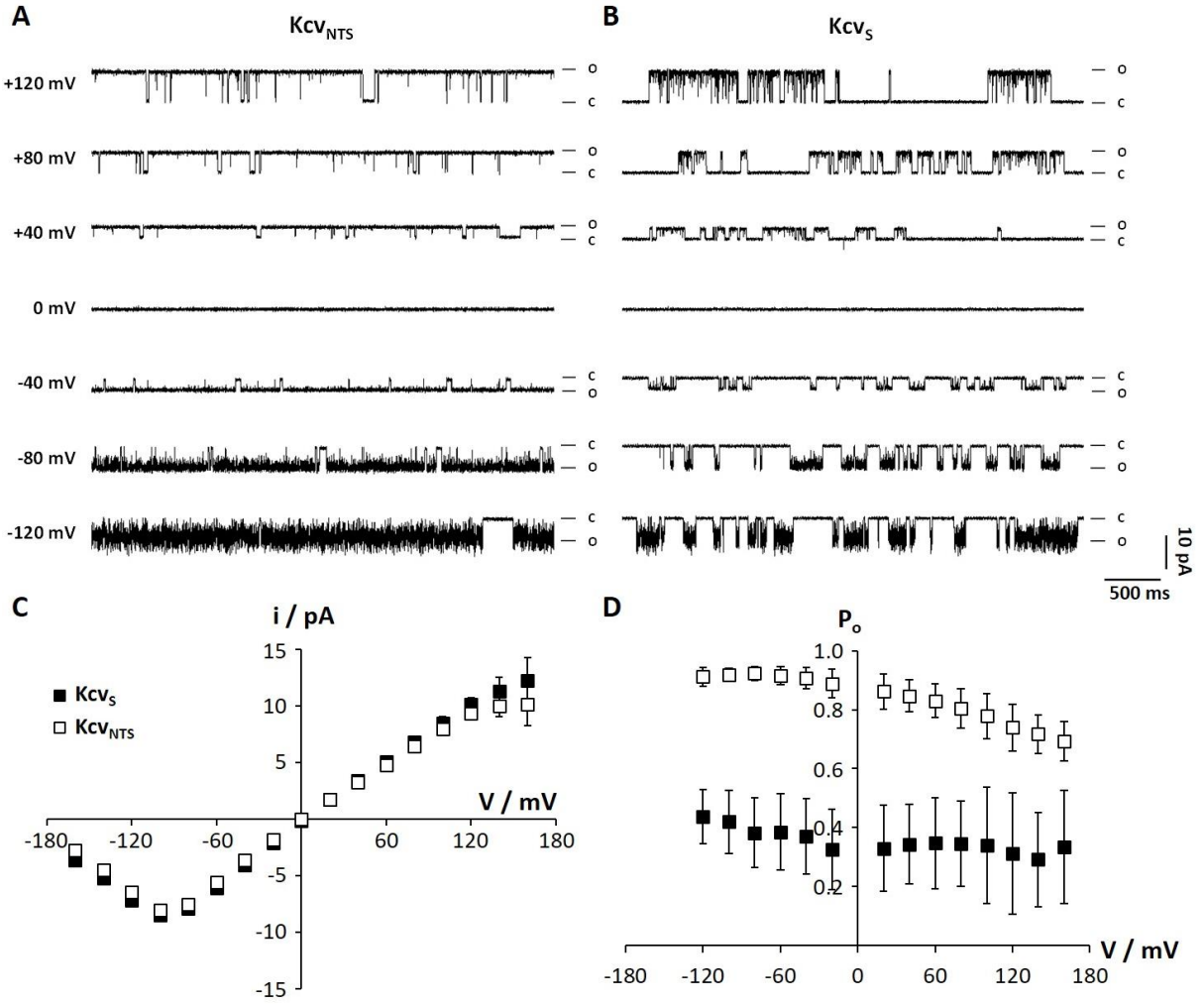

Figure 2-2: Kcv_{NTS} and Kcv_S differ in their open probability. A,B Characteristic single channel fluctuations of Kcv_{NTS} and at different voltages in a planar lipid bilayer. The closed (C) and open (O) levels are indicated along the current traces. **C** Mean single channel i/V relations (± standard deviation) of Kcv_{NTS} and Kcv_S from 6 and 9 independent recordings, respectively. **D** Mean open probabilities (± standard deviation) of the two channels from 6 and 9 independent recordings. The symbols in **D** correspond to those in **C**.

In spite of the sequence similarity, the two channels differ significantly in their open probability (P_o) (**Figure 2-2D**). While Kcv_{NTS} shows robust high P_o values of 0.84 ± 0.08 (N = 6) over the entire voltage window, Kcv_S exhibits a much lower open probability of only

0.35 ± 0.04 (N = 9). A comparative analysis of the open and closed dwell-times shows that the two channels differ mainly in one distinct parameter namely a long closed time τ_3, which is absent in Kcv_{NTS} (**Figure 2-3C,E**) and present and frequently occupied in Kcv_S (**Figure 2-3A,E**).

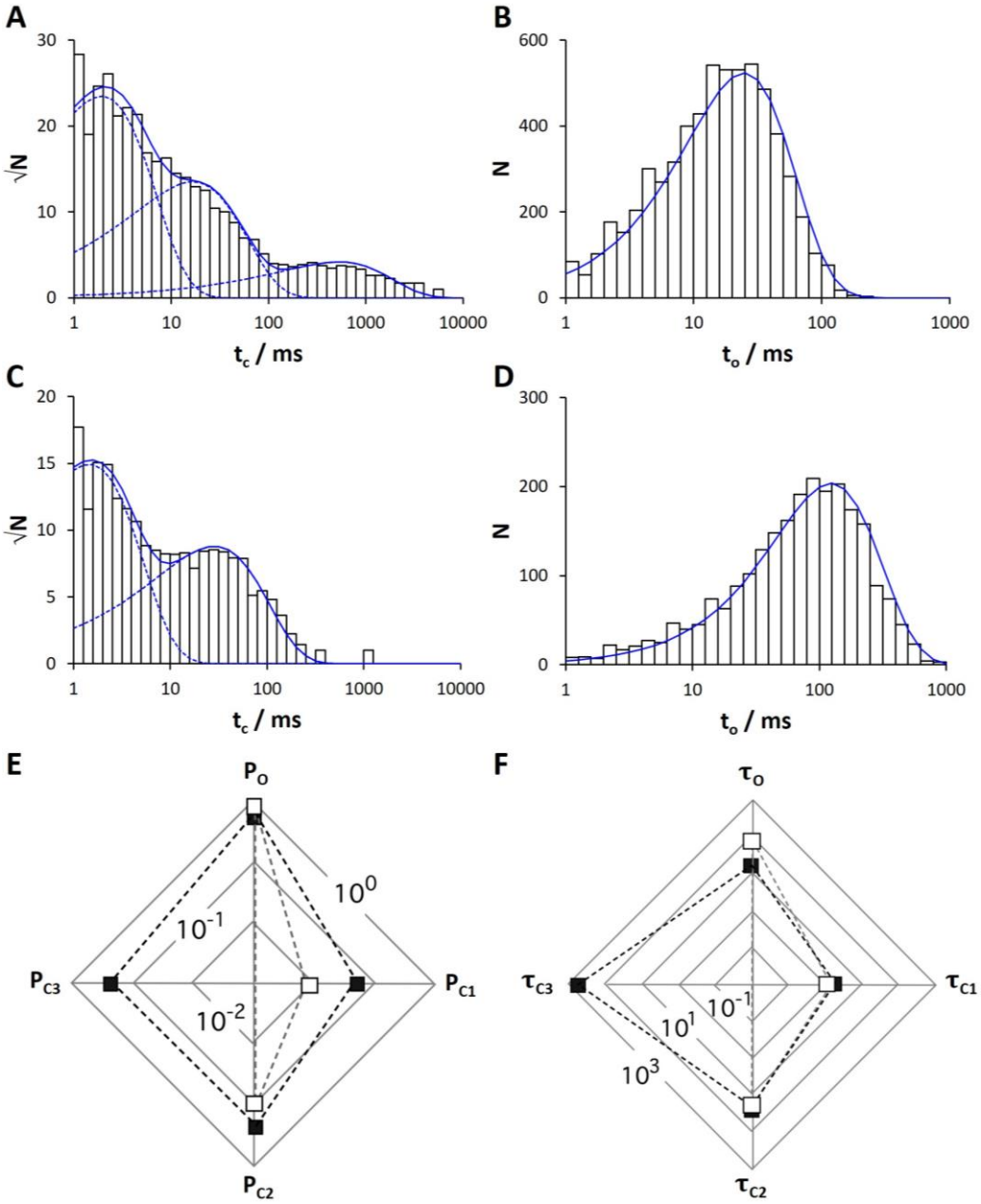

Figure 2-3: The difference in open probability of two similar K^+ channels originates from a long closed time, which is absent in Kcv_{NTS} and present in Kcv_S. A,C Exemplary closed-time histograms at +120 mV for Kcv_S (**A**) and Kcv_{NTS} (**C**). The data in **C** can be fitted with two exponential functions while the data in **A** require a third exponential function. The long-lived closed state in **A** is absent in **C**. **B,D** Exemplary open-time histograms at +120 mV for Kcv_S (**B**) and Kcv_{NTS} (**D**). Both open-time histograms can be fitted with a single exponential function. **E** Probabilities (P) of Kcv_S (filled squares) and Kcv_{NTS} (open squares) for occupying the open state (O) and the closed states (C1-C3) at +120 mV. **F** Mean lifetimes (in ms) of the open state (τ_O) and of the three closed states (τ_{C1}-τ_{C3}) at +120 mV. The probabilities of occupancy and mean lifetimes were calculated from three independent 5 min recordings. The symbols in **F** correspond to those in **E**.

The two channels also exhibit a difference in the mean open dwell-times, which are at +120 mV 79.1 ± 18.6 ms (N = 3) and 15.1 ± 2.5 ms (N = 3) for Kcv_{NTS} and Kcv_S, respectively (**Figure 2-3B,D,F**). This difference, which is not sufficient as an explanation for the different P_o values, is caused by variable rate constants for the transition from the open state to the first, short closed state (C1). The associated closing frequency has little effect on P_O because of the short mean life time τ_1 of the first closed state (1.3 ± 0.2 ms and 1.8 ± 0.8 ms at +120 mV for Kcv_{NTS} and Kcv_S, respectively) (**Figure 2-3F**). The low open probability of Kcv_S is hence primarily the result of the long-lasting closed events with a mean lifetime τ_3 of 480 ± 145 ms (N = 3) at +120 mV (**Figure 2-3F**).

2.3.2. The inner transmembrane helix of Kcv_S causes the long lasting closed events

From the data discussed above I concluded that the high sequence similarity and the fact that the two channels differ in one defined closed state make their comparative analysis an ideal system for studying the molecular basis of the responsible channel gate. Since the different amino acids are distributed over the two transmembrane (TM) helices (**Figure 2-1B**) I first tackled the location of the gate, which is responsible for the long-closed time, by generating chimeras in which the TM helices are swapped (**Figure 2-4A**). Hereinafter, the first chimera, which consists of TM helix 1 (outer TM helix) of Kcv_S and TM helix 2 (inner TM helix) of Kcv_{NTS}, is referred to as $Kcv_{S/NTS}$. Correspondingly, the second chimera is referred to as $Kcv_{NTS/S}$. **Figure 2-4B** shows that both chimeras produce channel activity after reconstitution in artificial DPhPC membranes. Interestingly, the slope conductance of $Kcv_{S/NTS}$ between ±60 mV is with 100.0 ± 6.5 pS (N = 9) about 28% higher than the unitary conductance of $Kcv_{NTS/S}$ (77.9 ± 5.9 pS, N = 3) (**Figure 2-4C**). Therefore, $Kcv_{S/NTS}$ exhibts a higher and $Kcv_{NTS/S}$ a lower unitary conductance than the wild-type channels. This finding already indicates that the outer and inner TM helices cannot be considered as independent entities. However, the molecular origin of this difference in unitary conductance remains unclear and will not be further investigated here.

More interesting, the mutual exchange of the inner TM helix of Kcv_{NTS} and Kcv_S results in a remarkable change in gating kinetics. The chimeric channel $Kcv_{S/NTS}$, which possesses the TM helix 2 of Kcv_{NTS}, shows with 0.74 ± 0.09 (N = 9) a only slightly lower mean open probability than the wild-type channel Kcv_{NTS} (0.84 ± 0.08) (**Figure 2-4B,D**). On the other hand, the second chimera $Kcv_{NTS/S}$, which possesses the TM helix 2 of Kcv_S, exhibits with 0.27 ± 0.09 (N = 3) a similarly low mean open probability as Kcv_S (0.35 ± 0.04) (**Figure 2-4B,D**).

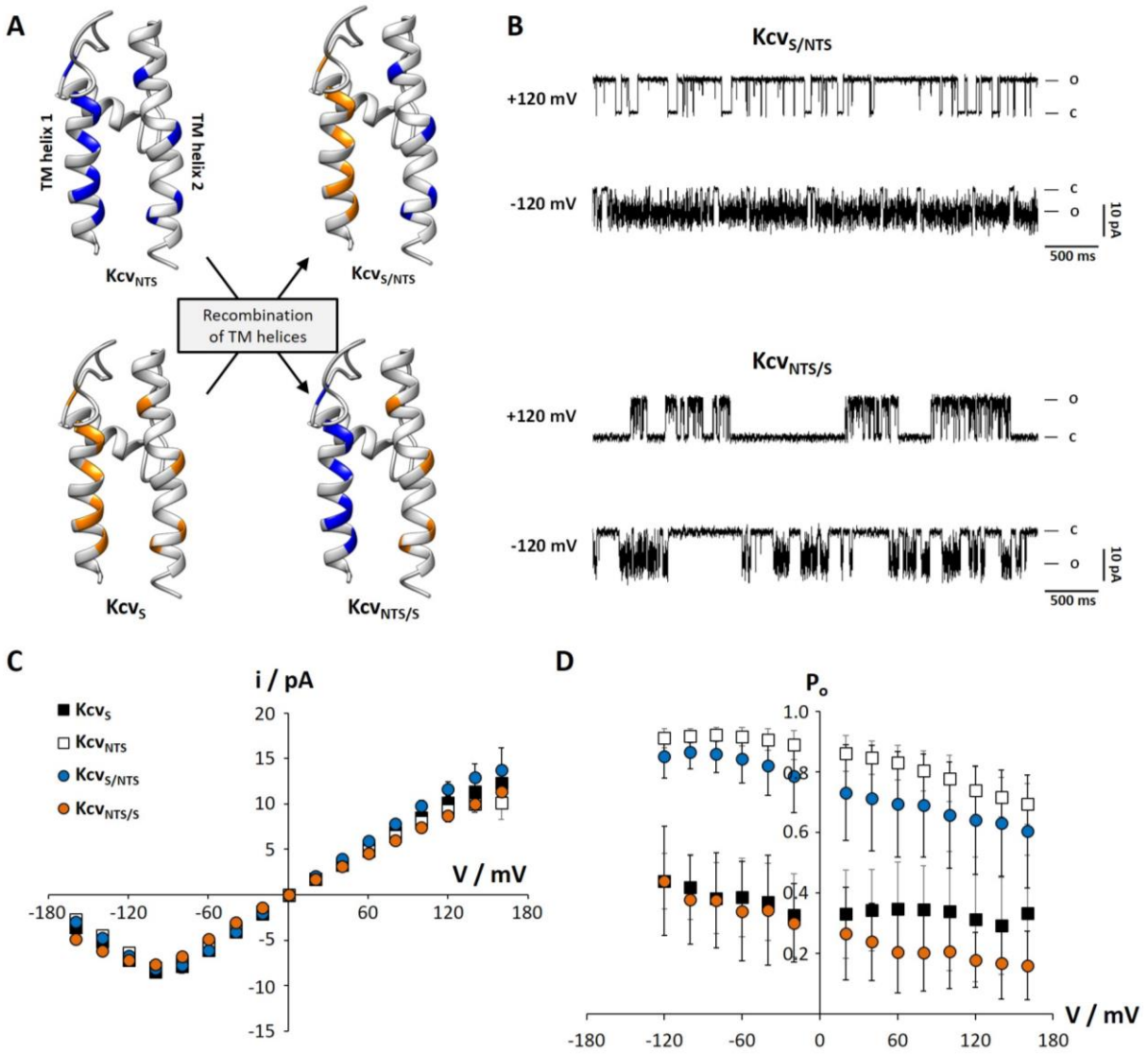

Figure 2-4: Swapping of the inner TM helices causes an inversion of the electrophysiological properties. A Chimeras were constructed by swapping transmembrane helices between Kcv_{NTS} (non-conserved amino acids in blue) and Kcv_S (non-conserved amino acids in orange). **B** Characteristic single-channel fluctuations of chimeras $Kcv_{S/NTS}$ and $Kcv_{NTS/S}$ at ±120 mV in planar lipid bilayers. **C** Mean single-channel i/V relations (± standard deviation) of Kcv_{NTS}, Kcv_S, $Kcv_{S/NTS}$ (N = 9) and $Kcv_{NTS/S}$ (N = 3). **D** Mean open probabilities (± standard deviation) of wt channels and chimeras (N = 9 and N = 3 for $Kcv_{S/NTS}$ and $Kcv_{NTS/S}$, respectively). The symbols in **D** correspond to those in **C**.

The analysis of open and closed dwell-times shows that the low open probability of $Kcv_{NTS/S}$ is caused by the appearance of the same long-lived closed state (C3) that could be observed for Kcv_S (**Figure 2-5B-D**). This closed state exhibits a mean lifetime τ_3 of 1070 ± 118 ms (N = 3) and an occupation probability P_{C3} of 0.65 ± 0.03 (N = 3) at +120 mV. $Kcv_{S/NTS}$ exhibits only two closed states with virtually the same mean lifetimes as Kcv_{NTS} and no long-lasting closed events (**Figure 2-5A,C,D, Table S 2-1**). The slightly lower P_O of $Kcv_{S/NTS}$ compared to Kcv_{NTS} (**Figure 2-4C**) is caused by a higher probability for an occupation of closed state C2 (**Figure 2-5C, Table S 2-1**). From the results of these experiments I conclude that the structural information, which is responsible for the long-closed time, must be located on TM helix 2.

Nevertheless, as indicated by the higher occupation probability P_{C2} of chimera $Kcv_{S/NTS}$, also TM helix 1 must have some impact on channel gating, but this contribution is not relevant for the long closed time.

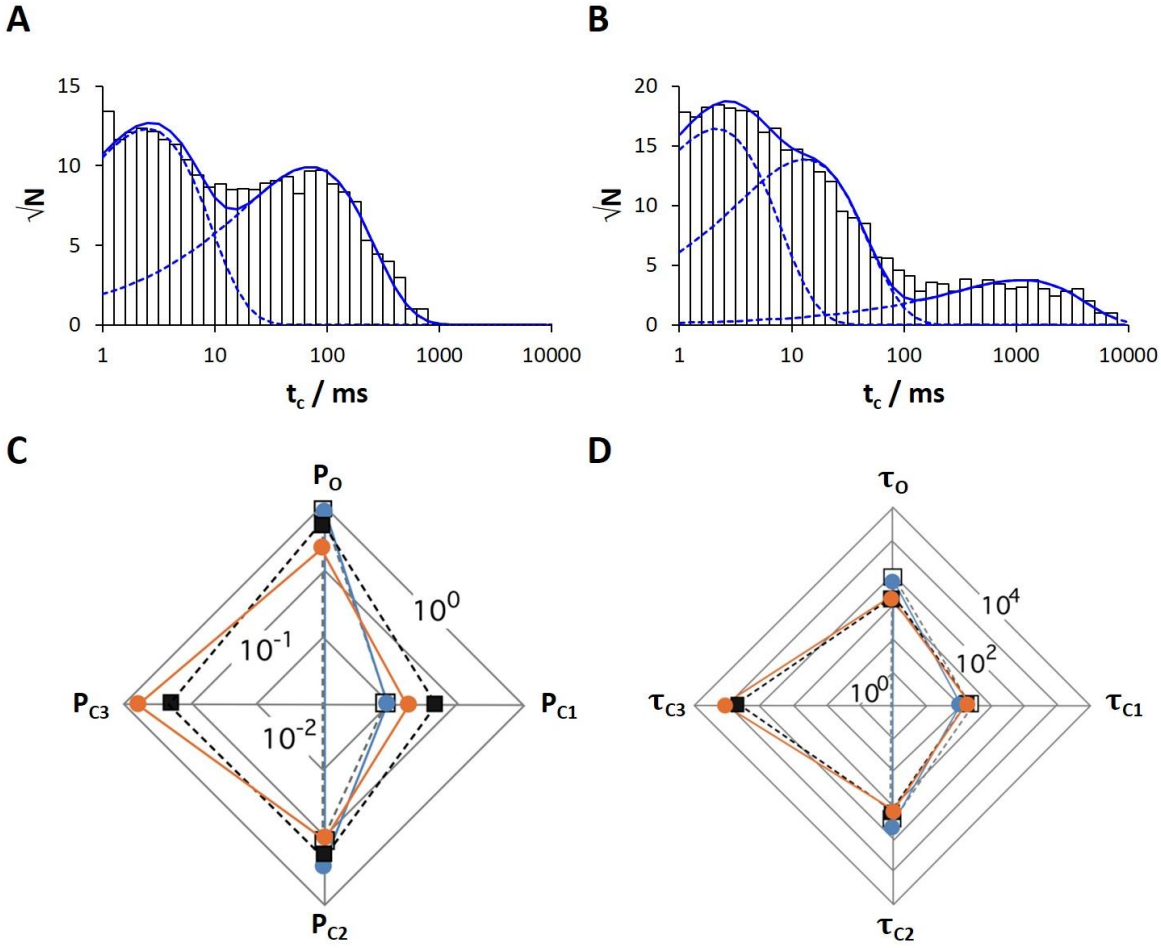

Figure 2-5: The Kcv_S long closed time is related to TM helix 2. **A,B** Exemplary closed-time histograms at +120 mV for chimeras $Kcv_{S/NTS}$ and $Kcv_{NTS/S}$, respectively. The data in **A** can be fitted with two exponential functions while the data in **B** require a third exponential function. **C** Probabilities (P) of the wt channels Kcv_{NTS} (open squares) and Kcv_S (filled squares) and the chimeras $Kcv_{S/NTS}$ (blue circles) and $Kcv_{NTS/S}$ (orange circles) for occupying the open state (O) and the closed states (C1-C3) at +120 mV. **D** Mean lifetimes (in ms) of the open state (τ_O) and of the three closed states (τ_{C1}-τ_{C3}) at +120 mV. The probabilities of occupancy and mean lifetimes were calculated from three independent 5 min recordings. The symbols in **D** correspond to those in **C**.

2.3.3. The amino acid difference at position 77 exclusively causes the occurrence of the long-lived closed state

There are only four amino acid differences between the TM helix 2 of Kcv_{NTS} and Kcv_S (**Figure 2-1B**). To identify the relevant amino acid in TM helix 2 for gating all four candidates in Kcv_{NTS} were mutated into the respective residue of Kcv_S. A functional analysis of the mutants shows that mutations T62V, L68M, and I75V in Kcv_{NTS} have no impact on gating (**Figure S**

2-1). Only the mutual exchange of serine and glycine at position 77 in Kcv_{NTS} and Kcv_S completely inverts the gating properties of the two channels: the Kcv_S S77G mutant acquires with a mean value of 0.88 ± 0.05 (N = 3) the high open probability of Kcv_{NTS} while the mean open probability of Kcv_{NTS} G77S decreases to 0.32 ± 0.10 (N = 5), which is similar to the low open probability of Kcv_S (**Figure 2-6A,B,D**). Interestingly, the substitution of serine with glycine in Kcv_S results in an increase of the unitary conductance in the Ohmic range between ±60 mV from 93.6 ± 3.6 to 104.4 ± 2.4 pS (N = 3) (**Figure 2-6C**). As described above, a similar change in the unitary conductance was achieved by exchanging the TM helix 2 of Kcv_S with the TM helix 2 of Kcv_{NTS} (**Figure 2-4C**). Therefore, both experiments suggest that position 77 is somehow involved in the modulation of ion conduction through the channel pore. However, since the unitary conductance of the wild-type channels, Kcv_{NTS} and Kcv_S, barely differ, the influence of the amino acid at position 77 on ion conduction must also depend on the amino acid differences in TM helix 1 and thus the interaction between both TM helices.

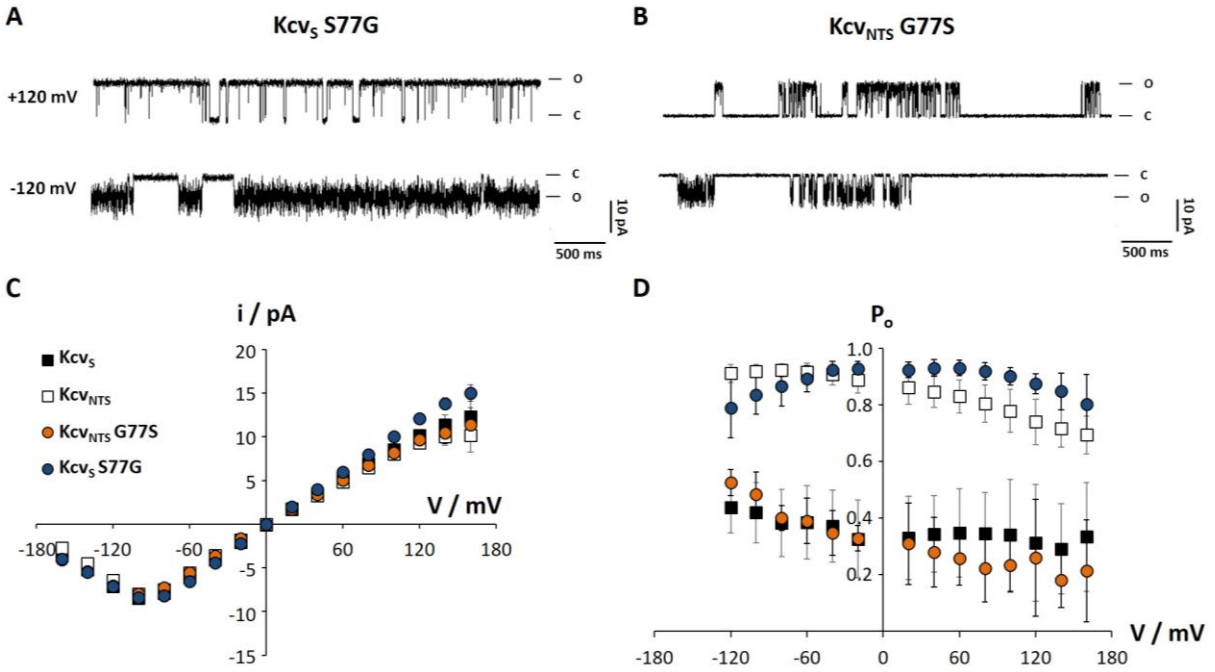

Figure 2-6: The difference of Kcv_{NTS} and Kcv_S in position 77 is responsible for the high or low open probability. Characteristic single channel fluctuations of mutant Kcv_S S77G (**A**) and Kcv_{NTS} G77S (**B**) at ±120 mV in planar lipid bilayers. **C** Mean single channel i/V relations (± standard deviation) of Kcv_{NTS} (open squares), Kcv_S (filled squares), Kcv_{NTS} G77S (orange circles, N = 5) and Kcv_S S77G (blue circles, N = 3). **D** Mean open probabilities (± standard deviation) of wt channels and mutants (N = 5 and N = 3 for Kcv_{NTS} G77S and Kcv_S S77G, respectively). The symbols in **D** correspond to those in **C**.

A comparative analysis of the mean open and closed dwell-times shows that the impact of the mutations on the open probability can be explained by the disappearance of the long-lasting closed state C3 in Kcv_S S77G and its appearance in Kcv_{NTS} G77S with a mean lifetime τ_3 of

354 ± 220 ms (N = 3) (**Figure 2-7**). Moreover, the mutual exchange of the amino acid at position 77 also causes an inversion of the open dwell-time characteristics (**Figure 2-7C,D**): Kcv_S S77G acquires a mean open lifetime of 79.7 ± 15.7 ms (N = 3), while the mean open lifetime of Kcv_{NTS} G77S drops to 11.2 ± 0.4 ms (N = 5). Exemplary open dwell-time histograms are shown in **Figure S 2-1C,D**.

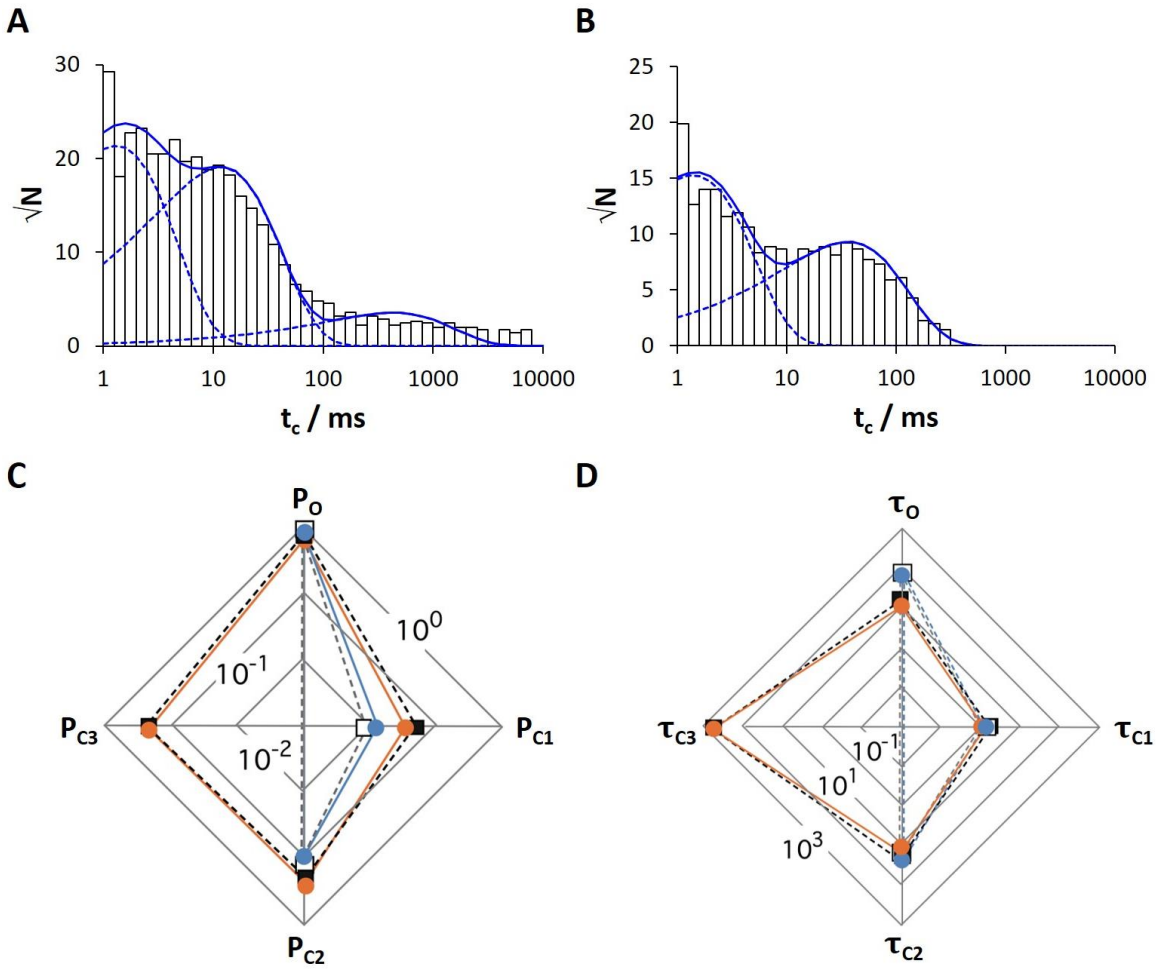

Figure 2-7: The mutual exchange of serine and glycine at position 77 in Kcv_{NTS} and Kcv_S completely inverts the gating properties of the two channels. Exemplary closed-time histograms at +120 mV for Kcv_{NTS} G77S (**A**) and Kcv_S S77G (**B**). The data in **B** can be fitted with two exponential functions while the data in **A** again require a third exponential function. **C** Probabilities (P) of the wt channels Kcv_{NTS} (open squares) and Kcv_S (filled squares) and mutants Kcv_S S77G (blue circles) and Kcv_{NTS} G77S (orange circles) for occupying the open state (O) and the closed states (C1-C3) +120 mV. **D** Mean lifetimes (in ms) of the open state (τ_O) and of the three closed states (τ_{C1}-τ_{C3}) +120 mV. The probabilities of occupancy and mean lifetimes were calculated from three independent 5 min recordings. The symbols in **D** correspond to those in **C**.

In summary, the experiments discussed here reveal that the presence or absence of the long-lasting closed state C3 in Kcv_S and Kcv_{NTS} is exclusively caused by the amino acid difference at position 77.

2.3.4. The long-lasting closed state reflects the obstruction of the channel pore by the side chain of F78

Due to the predicted position of S77 in the inner TM helix of Kcv_S, turned away from the pore (**Figure 2-1A**), I reasoned that the amino acid at position 77 cannot be the actual gate, which could by itself obstruct the flow of ions. Scrutiny of the channel sequences however reveals that the next position downstream of position 77 is occupied by the aromatic amino acid phenylalanine (F78) in both channels (**Figure 2-1**A,**B**). It is therefore conceivable that the F78 aromatic side chain could be positioned in or out of the ion pathway, depending on the nature of the adjacent amino acid. To test if F78 has any influence on the gating of the two channels it was mutated to an alanine in Kcv_S. The data show that the removal of the aromatic side chain in the Kcv_S channel results in a drastic increase in the mean open probability from 0.35 ± 0.04 to 0.93 ± 0.03 (N = 4) (**Figure 2-8A,D**), which is even higher than the open probability of Kcv_{NTS}.

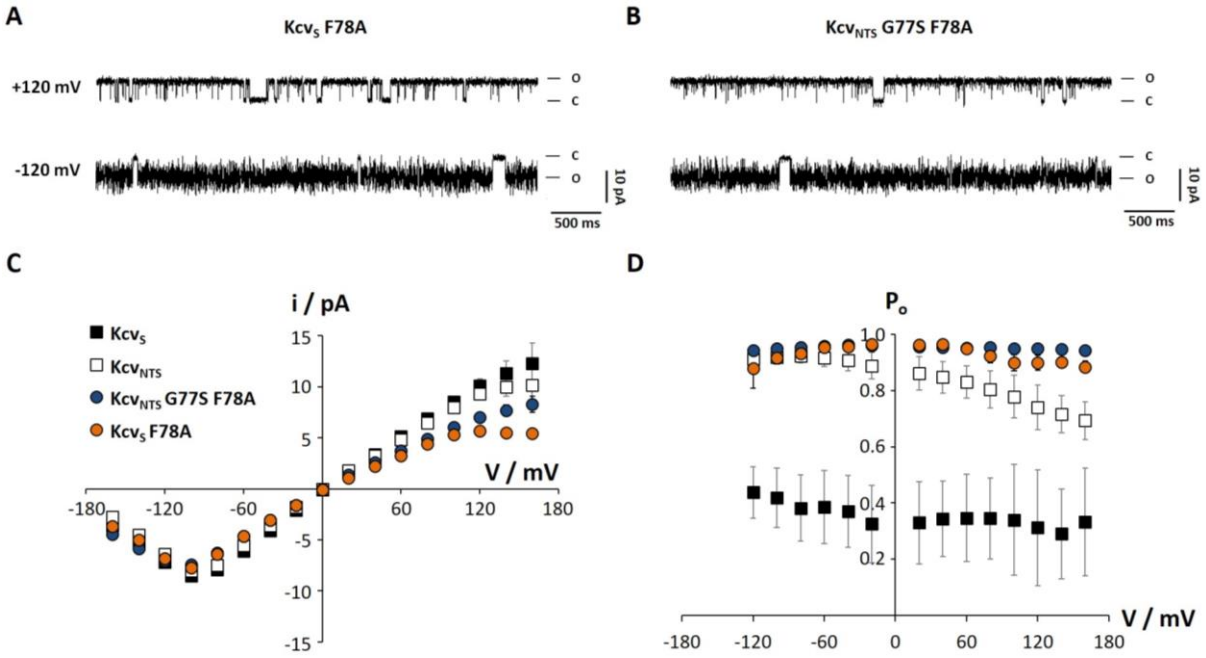

Figure 2-8: Removal of the F78 side chain results in a drastic increase in open probability. Characteristic single channel fluctuations of mutant Kcv_S F78A (**A**) and Kcv_{NTS} G77S F78A (**B**) at ±120 mV in planar lipid bilayers. **C** Mean single channel i/V relations (± standard deviation) of Kcv_{NTS}, Kcv_S, Kcv_S F78A (N = 4) and Kcv_{NTS} G77S F78A (N = 7). **D** Mean open probabilities (± standard deviation) of wt channels and mutants (N = 4 and N = 7 for Kcv_S F78A and Kcv_{NTS} G77S F78A, respectively).

The increase in open probability is caused by a complete disappearance of the long closed state C3 and a decrease of the probability to find the channel in closed state C2 (**Figure 2-9A,C,D**, **Table S 2-1**).

To further test the hypothesis that F78 is a gate in combination with the adjacent amino acid the double mutant Kcv_{NTS} G77S F78A was constructed. The experimental data reveal that the replacement of the aromatic amino acid neutralizes the effect of the G77S mutation (**Figure 2-9B,D**, **Table S 2-1**), which alone causes a decrease in P_O (**Figure 2-6B,D**, **Table S 2-1**). The Kcv_{NTS} G77S F78A mutant has with 0.95 ± 0.01 (N = 7) a similarly high mean open probability as Kcv_S F78A and an even higher open probability than Kcv_{NTS} (**Figure 2-8D**). As obtained by dwell-time analysis, this remarkable increase in open probability is again the result of a disappearance of the long-lasting closed state C3 and an drop in the occupation probability of P_{C2} (**Figure 2-9B-D**, **Table S 2-1**).

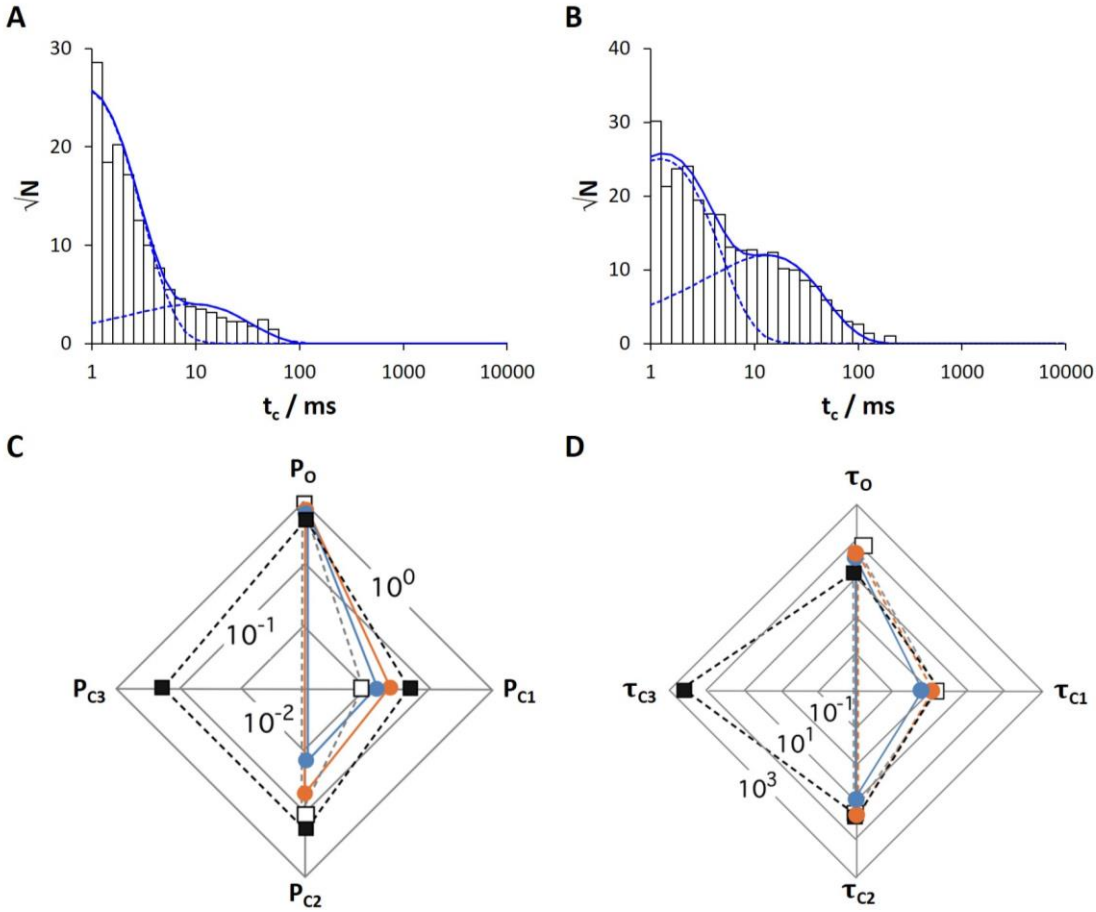

Figure 2-9: The aromatic amino acid F78 functions in combination with the upstream amino acid as a gate for the long closed time. Exemplary closed-time histograms at +120 mV for Kcv_S F78A (**A**) and Kcv_{NTS} G77S F78A (**B**). The data in **A** and **B** can now be fitted with two exponential functions. **C** Probabilities (P) of the wt channels Kcv_{NTS} (open squares) and Kcv_S (filled squares) and the mutant channels Kcv_S F78A (orange circles) and Kcv_{NTS} G77S F78A (blue circles) for occupying the open state (O) and the closed states (C1-C3) +120 mV. **D** Mean lifetimes (in ms) of the open state (τ_O) and of the three closed states (τ_{C1}-τ_{C3}) +120 mV. The mean lifetimes were calculated from three independent 5 min recordings. The symbols **D** correspond to those in **C**.

The change in P_O is accompanied by a striking decrease of the open-channel conductance: the unitary conductance between ±60 mV drops to 65.9 ± 3.2 pS (N = 4) and to 68.5 ± 3.8 pS

(N = 7) by substituting F78 with an alanine in Kcv_S and Kcv_{NTS} G77S, respectively (**Figure 2-8A-C**). Consequently, the amino acid F78 does not only function as a gate, but also seems to be of importance for the structure of the channel pore and thus for the passage of potassium ions.

In a nutshell, the gate, which is responsible for the occurrence of the long-lasting closed state, is formed by the aromatic side chain of the phenylalanine at position 78 and modulated by the amino acid one position upstream.

2.3.5. The F78 side chains create a hydrophobic barrier at the cytosolic entrance to the cavity

To understand the nature of the gate, i.e. whether the aromatic rings form a barrier by π:π interactions or whether the side chains are only steric hindrances, F78 in Kcv_S was replaced with either leucine or tyrosine. The analysis of single-channel recordings shows that the substitution of F78 with leucine - a large, non-aromatic and hydrophobic amino acid - causes a mean open probability of 0.23 ± 0.05 (N = 3), which is significantly lower than that in the F78A mutant and even lower than in the Kcv_S wild-type channel.

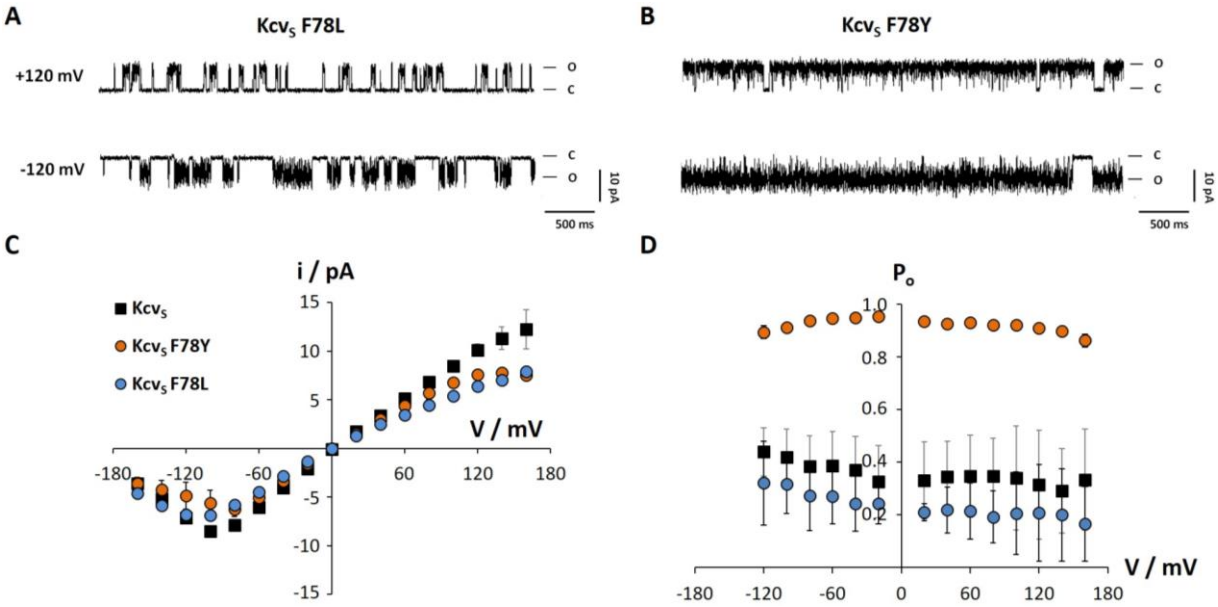

Figure 2-10: The gating function of the aromatic side chain of F78 can be substituted by the hydrophobic amino acid leucine but not by the aromatic side chain of tyrosine. Characteristic single channel fluctuations of mutant Kcv_S F78L (**A**) and Kcv_S F78Y (**B**) at ±120 mV in planar lipid bilayers. **C** Mean single channel i/V relations (± standard deviation) and (**D**) mean open probabilities (± standard deviation) of Kcv_S, Kcv_S F78Y (N = 3) and Kcv_S F78L (N = 3). The symbols in **D** correspond to those in **C**.

The single-channel traces shown in **Figure 2-10A** as well as the analyzed dwell-time histograms (**Figure 2-11A**) reveal that the low open probability of Kcv_S F78L is caused by transitions into the long-lasting closed state C3, which is absent in the F78A mutant. The

lower P_O of Kcv_S F78L compared to that of Kcv_S is the result of a higher probability of occupancy P_{C3} (0.436 ± 0.305, N = 3) and a longer mean lifetime τ_3 (983 ± 419 ms, N = 3) of the third, long lasting closed state (**Figure 2-11C,D**, **Table S 2-1**). This closed state must be caused by the concerted action of the leucine side chain with the upstream amino acid serine because a F78L substitution in Kcv_{NTS} had no effect on gating (**Table S 2-1**).

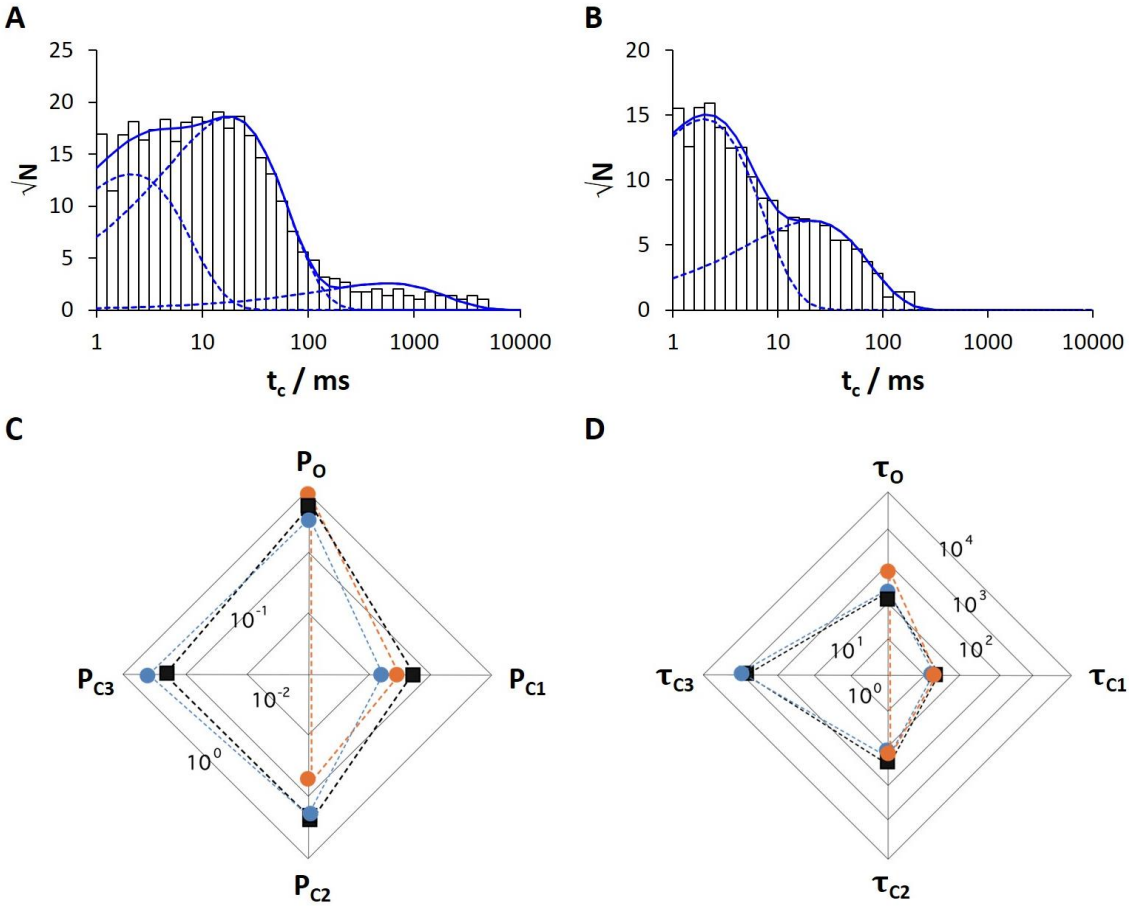

Figure 2-11: The hydrophobic, non-aromatic amino acid leucine can functionally replace F78, but the aromatic amino acid tyrosine cannot. Exemplary closed-time histograms at +120 mV for Kcv_S F78L (**A**) and Kcv_S F78Y (**B**). The data in **B** can be fitted with two exponential functions while the data in **A** require a third exponential function. **C** Probabilities (P) of the wt channel Kcv_S (filled squares) and the mutant channels Kcv_S F78Y (orange circles) and Kcv_S F78L (blue circles) for occupying the open state (O) and the closed states (C1-C3). **D** Mean lifetimes (in ms) of the open state (τ_O) and of the three closed states (τ_{C1}-τ_{C3}). The probabilities of occupancy and mean lifetimes were calculated from three independent 5 min recordings. The symbols in **D** correspond to those in **C**.

F78 in Kcv_S was also substituted with the polar aromatic amino acid tyrosine. This causes the disappearance of the long-lasting closed state C3 (**Figure 2-11B-D**) and thus a significant increase in P_O (**Figure 2-10B,D**).

The results of these experiments establish that F78 is a gate, which is responsible for the long closed events in Kcv_S. It obstructs the flow of ions by creating a hydrophobic barrier in the cavity of the channel.

2.3.6. The long-lasting closed state in Kcv_S is caused by a specific interaction between the Ser77 side chain and the peptide backbone

The dynamics of the gate, which is responsible for the occurrence of the long-lasting closed state C3, are apparently determined by the adjacent amino acids glycine in Kcv_{NTS} and serine in Kcv_S. It was previously proposed in other channels that the flexible amino acid glycine could create a hinge in the inner TM helix of Kir channels and that this hinge might be essential for gating (Jiang et al. 2002, Shrivastava & Bahar 2006). In analogy to this model it may be possible that a flexible G77 favors the removal of F78 from the ion pathway while the small serine does not. To test the relevance of a potential glycine hinge for gating in Kcv_{NTS} and Kcv_S position 77 were mutated into several other small amino acids namely alanine, asparagine, serine, proline and threonine.

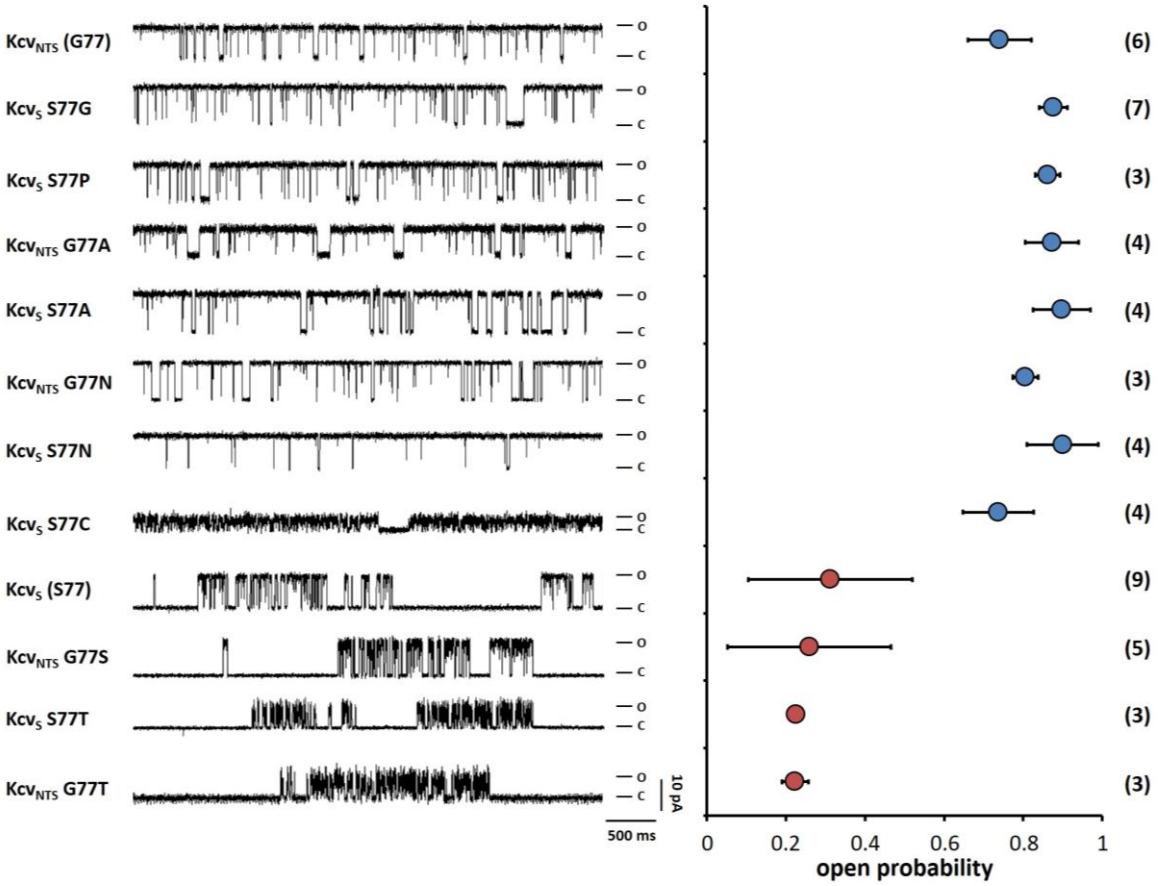

Figure 2-12: The amino acid S77 is responsible for the gate with the long closed time. A Characteristic single-channel fluctuations at +120 mV of Kcv_S and Kcv_{NTS} and mutants in which the position 77 in both channels was exchanged with an amino acid with different physicochemical properties. **B** Open probabilities (± standard deviation) of wt channels and mutants at +120 mV. The number of independent measurements is shown in brackets. Data in **B** correspond to the constructs on the left in **A**. Only the amino acids serine and threonine in position 77 generate a low open probability with a long-lasting closed time.

The resulting mutant channels were expressed *in vitro* and subsequently examined in artificial DPhPC membranes. However, the results of these experiments do not support the hypothesis

of a glycine hinge; they show that G77 in Kcv_{NTS} can be replaced by other amino acids like the strong helix former alanine, which provide no flexibility in an α-helix (Chou & Fasman 1974), while still preserving the high open probability (**Figure 2-12**). The results of these experiments suggest that glycine is not essential for the high open probability in Kcv_{NTS} but that serine is important for the low open probability in Kcv_S. The data in **Figure 2-12** show that S77 can be replaced in Kcv_S by different amino acids and that these changes result in an increase in open probability. The only replacement of S77, which conserves the low open probability of Kcv_S, is S77T (**Figure 2-12**). In agreement, only G77S and G77T in Kcv_{NTS} cause a low, Kcv_S-like open probability. These experimental results refute the hypothesis that a Gly mediated hinge plays a crucial role in gating. Instead the data support a gating mechanism, which depends on the hydroxy group of either serine or threonine.

Serines and threonines are known for forming hydrogen bonds. Since serine has no apparent interaction partner for such a bond within TM helix 1 (**Figure 2-1**) it is reasonable to assume that the relevant gating entities must be located solely within TM helix 2. This is consistent with the fact that also Kcv_{ATCV-1} exhibits a high open probability (Gazzarini et al. 2009) in spite of some sequence variability with Kcv_{NTS} in TM helix 1 (**Figure 2-1A**). Potential intra- or interhelical interacting partners of S77 in TM helix 2 could be the side chains of S76 or T79 (**Figure 2-13**).

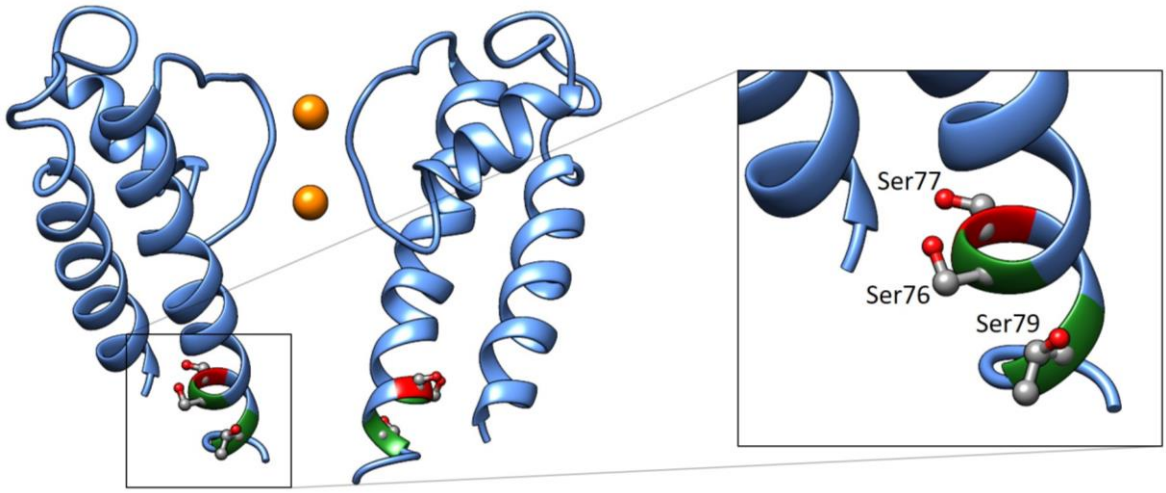

Figure 2-13: Possible interaction partners in the proximity of S77. Left: Side view of the channel (two opposing monomer units). Right: enlarged section of the C-terminal part of the inner TM helix. Potassium ions are shown as orange spheres, the position of S77 in red, the positions S76 and T79 in green. The side chains of S76, S77 and T79 are shown as balls and sticks. The homology model was calculated with Swissmodel (Arnold et al. 2006) using structural KirBac1.1 data (PDB code 1P7B, Kuo et al. 2003).

If one of these amino acids is involved in the formation of a hydrogen bond with S77, one would expect that substitution with alanine in Kcv_S would lead to a significant increase in open probability and the disappearance of the long closed events. However, the functional

tests show that both mutants, Kcv_S S76A and Kcv_S T79A, still exhibit the typical gating of the wild-type channel Kcv_S (**Figure 2-14**). Therefore, S76 and T79 are not part of the gating mechanism.

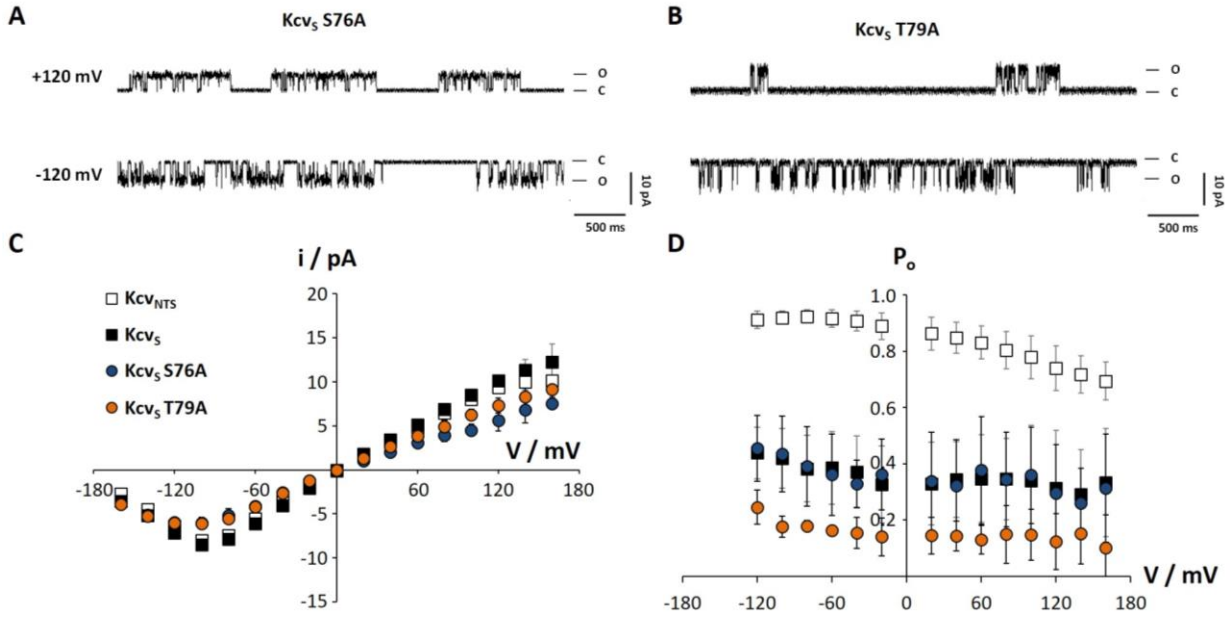

Figure 2-14: The amino acids S76 and T79 in Kcv_S do not contribute to the long-lived closed time. Characteristic single channel fluctuations of mutant Kcv_S S76A (**A**) and Kcv_S T79A (**B**) at ±120 mV in planar lipid bilayers. **C** Mean single channel i/V relations (± standard deviation). **D** Mean open probabilities (± standard deviation) of Kcv_{NTS}, Kcv_S, Kcv_S T79A (N = 4) and Kcv_S S76A F78A (N = 3). The symbols in **D** correspond to those in **C**.

What remains as an explanation for the gating mechanism, in which S77 plays the crucial role, are interactions of the S77 side chain with the peptide backbone. In this context, it is interesting to note that serine and threonine were found as important structural amino acids in α-helices (Ballesteros et al. 2000, Hall et al. 2009). They can form hydrogen-bonds with a carbonyl oxygen in the preceding helix turn and such an intrahelical interaction can generate a kink in the α-helix. I reasoned that such a transient serine interaction in the TM helix 2 of Kcv_S could generate a kink in TM helix 2 in a stochastic manner and that this structural modulation could affect the positioning of F78 in the ion pathway. This hypothesis is consistent with the experimental data. As shown in **Figure 2-12**, S77 can be functionally replaced in Kcv_S by threonine but not by cysteine. While serine and threonine are able to form an intrahelical hydrogen-bond, cysteine cannot reach the required side chain conformation because of the steric hindrance between the thiol group and the carbonyl oxygen of the amino acid three positions upstream inside the α-helix (McGregor et al. 1987).

2.3.7. Molecular dynamics simulations disclose intrahelical hydrogen bond

The following section, including text, figures and supplemental material (section 2.6.6, section 2.6.7 and Figs. S2-3 and S2-4), was included in the present work for reasons of completeness and kindly provided by Prof. Dr. Stefan M. Kast, Dr. Leonhard M. Henkes and Martin Urban from the department of physical chemistry III, Technische Universität Dortmund.

To quantify the structural and dynamical implications of differing sequences between Kcv_S and Kcv_{NTS} on the putative gate in the absence of experimental structural information, a computational model of the two variants was developed. They were examined by molecular dynamics (MD) simulations to determine the angle φ between normal vectors placed on the centers of the F78 phenyl rings along with the respective distance *d* between phenyl centers (see **Figure S 2-3**). Distributions of these coordinate pairs were averaged over neighboring and opposite monomers for both channel variants, as shown in **Figure 2-15**.

Kcv_S shows a densely populated area of opposite monomer residues with an angle less than 20° and around 3-8 Å distance, and another area with less population at around 50-60° and more than 18 Å distance (**Figure 2-15C**). The area with the smaller angle/distance pairs can be identified with π-stack geometries. Kcv_{NTS} has similar areas of likely monomer distances at 3-8 Å and about 20 Å, but with on average larger angles between the phenyl residues (**Figure 2-15A**). The angles of the area at around 3-8 Å distance fall in the range between 20° and 40°, implying much weaker π:π interactions. The angle of the area around 20 Å is also much larger with angles between 60° and 100°. Angle/distance pairs between phenyl rings in neighboring monomers of Kcv_S occur with high probability at 8-13 Å and 20°-40° (**Figure 2-15D**) whereas in the Kcv_{NTS} channel a substantially less focused area is found covering a wider angle range (**Figure 2-15B**). In summary, the results indicate more pronounced structural rigidity for Kcv_S over Kcv_{NTS}, combined with a slightly larger propensity of the Kcv_S variant to form π-stack pairs between opposite monomers that could potentially block the translocation pathway. This structural and dynamical observation can be correlated with the functional differences between both variants expressed by the larger open probability of Kcv_{NTS}. Kcv_S shows a densely populated area of opposite monomer residues with an angle less than 20° and around 3-8 Å distance, and another area with less population at around 50-60° and more than 18 Å distance (**Figure 2-15C**). The area with the smaller angle/distance pairs can be identified with π-stack geometries. Kcv_{NTS} has similar areas of likely monomer distances at 3-8 Å and about 20 Å, but with on average larger angles between the phenyl residues (**Figure 2-15A**). The angles of the area at around 3-8 Å distance fall in the range between 20° and 40°,

implying much weaker π:π interactions. The angle of the area around 20 Å is also much larger with angles between 60° and 100°. Angle/distance pairs between phenyl rings in neighboring monomers of Kcv_S occur with high probability at 8-13 Å and 20°-40° (**Figure 2-15D**) whereas in the Kcv_{NTS} channel a substantially less focused area is found covering a wider angle range (**Figure 2-15B**). In summary, the results indicate more pronounced structural rigidity for Kcv_S over Kcv_{NTS}, combined with a slightly larger propensity of the Kcv_S variant to form π-stack pairs between opposite monomers that could potentially block the translocation pathway. This structural and dynamical observation can be correlated with the functional differences between both variants expressed by the larger open probability of Kcv_{NTS}.

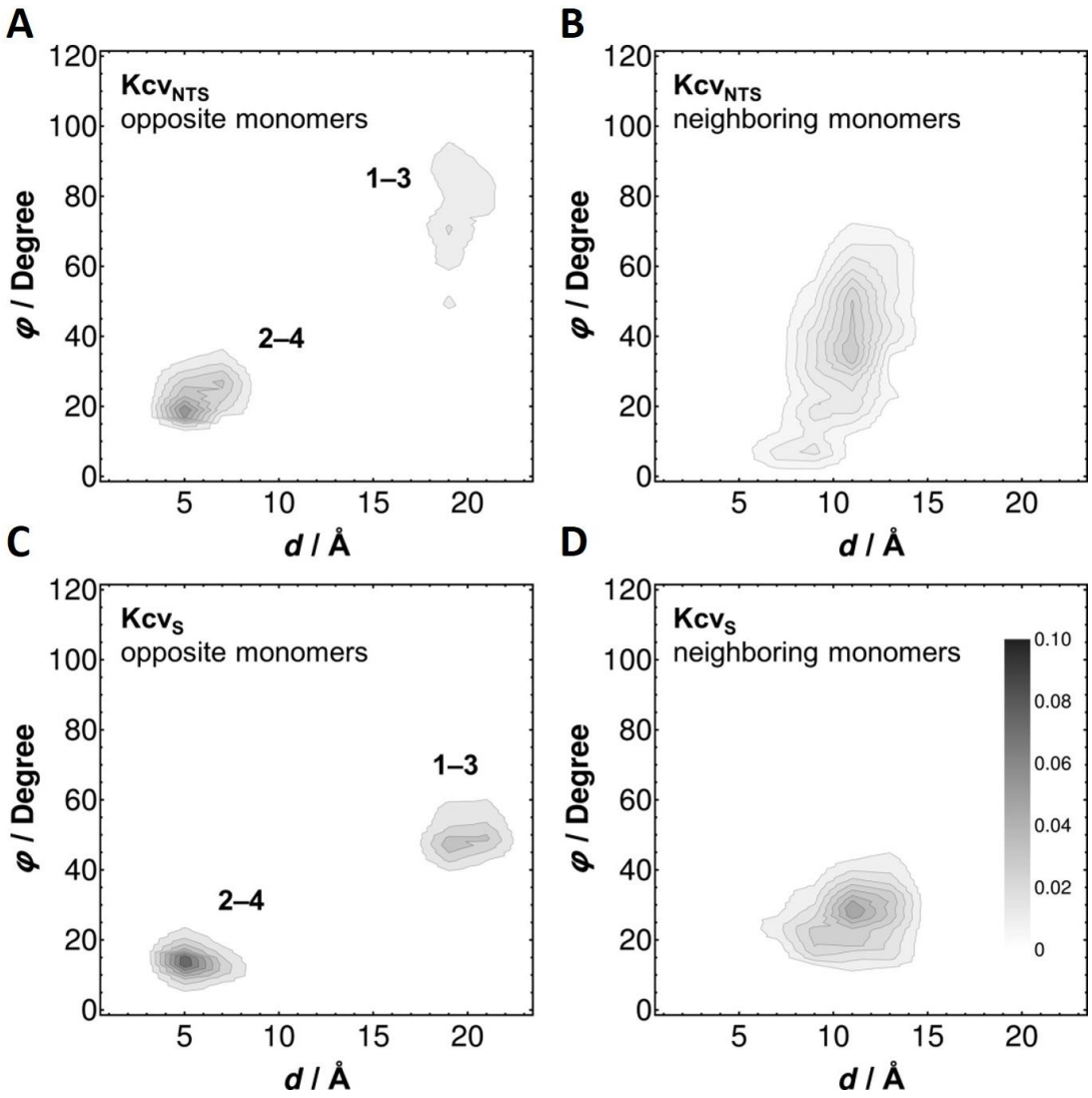

Figure 2-15: Dynamics of TM helix 2 in Kcv_S and Kcv_{NTS}. Distribution of distance-angle pairs characterizing π-stack geometries in Kcv_{NTS} (**A,B**) and Kcv_S (**C,D**) averaged over all F78 pairs in opposite (left column) and neighboring (right column) monomers. The geometric criteria are shown **Figure S 2-3**. Numbers in the left panel denote different monomers.

MD simulations were also used to test the hypothesis that the functional gate hinges upon possible hydrogen-bond interactions between S77 and the helix backbone at the I73 position in Kcv_S (**Figure 2-16B**).

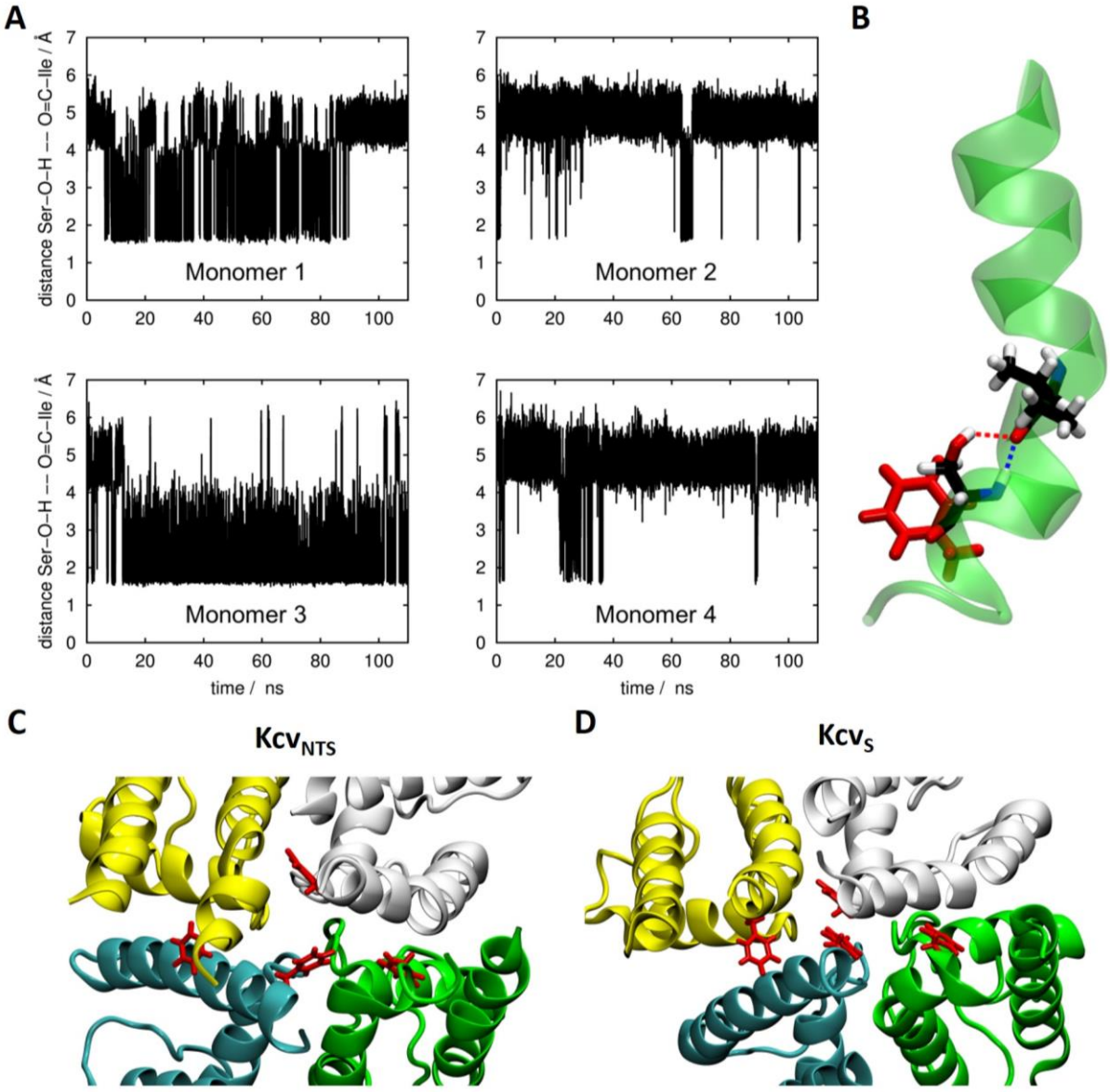

Figure 2-16: A Time series of the distances between the carbonyl oxygen of I73 and the hydroxyl hydrogen of S77 for all four monomers. **B** Schematic representation of a hydrogen-bond formed between the amide oxygen of I73 and the hydroxyl hydrogen of S77 within monomer 3 of Kcv_S supplemented by orientation of F78 (snapshot taken at 80 ns). **C,D** Snapshots of F78 (red) in tetramer of Kcv_{NTS} (**C**) and Kcv_S (**D**) representing a narrow and a wider translocation pathway corresponding to statistics shown in **Figure 2-15**.

Therefore, the distances between the S77 hydroxyl hydrogens and the I73 backbone amide oxygens were calculated as a measure for hydrogen-bonding patterns for all monomers, as depicted in **Figure 2-16A**. Two distinct states can be identified, one of which with a smaller distance at about 2 Å corresponds to a hydrogen-bonded situation. Remarkably, oppositely

placed and neighboring residues behave differently, at least on the observed simulation time scale. Monomers 1 and 3 (opposite) show predominantly the hydrogen-bond, whereas in the other pair of opposite monomers (2 and 4), it occurs much less frequently. This inherent asymmetry is likely inherited from the KirBac1.1 template structure that can be interpreted as a "dimer of dimers" pairwise asymmetric state, which also explains the 1-3/2-4 difference found for the π-stack statistics (**Figure 2-15A,C**). Deeper analysis for separate monomer units (**Figure 2-16A**) reveals that monomers 2 and 4 (broken hydrogen-bonds) are more likely to form π-stack geometries (not shown). In other words, the formation of hydrogen bonds within a monomer is correlated with the phenyl-ring motion by bending them away from the translocation pathway, allowing oppositely placed phenyl groups to interact more strongly, thereby blocking ion translocation as a signature of a closed channel.

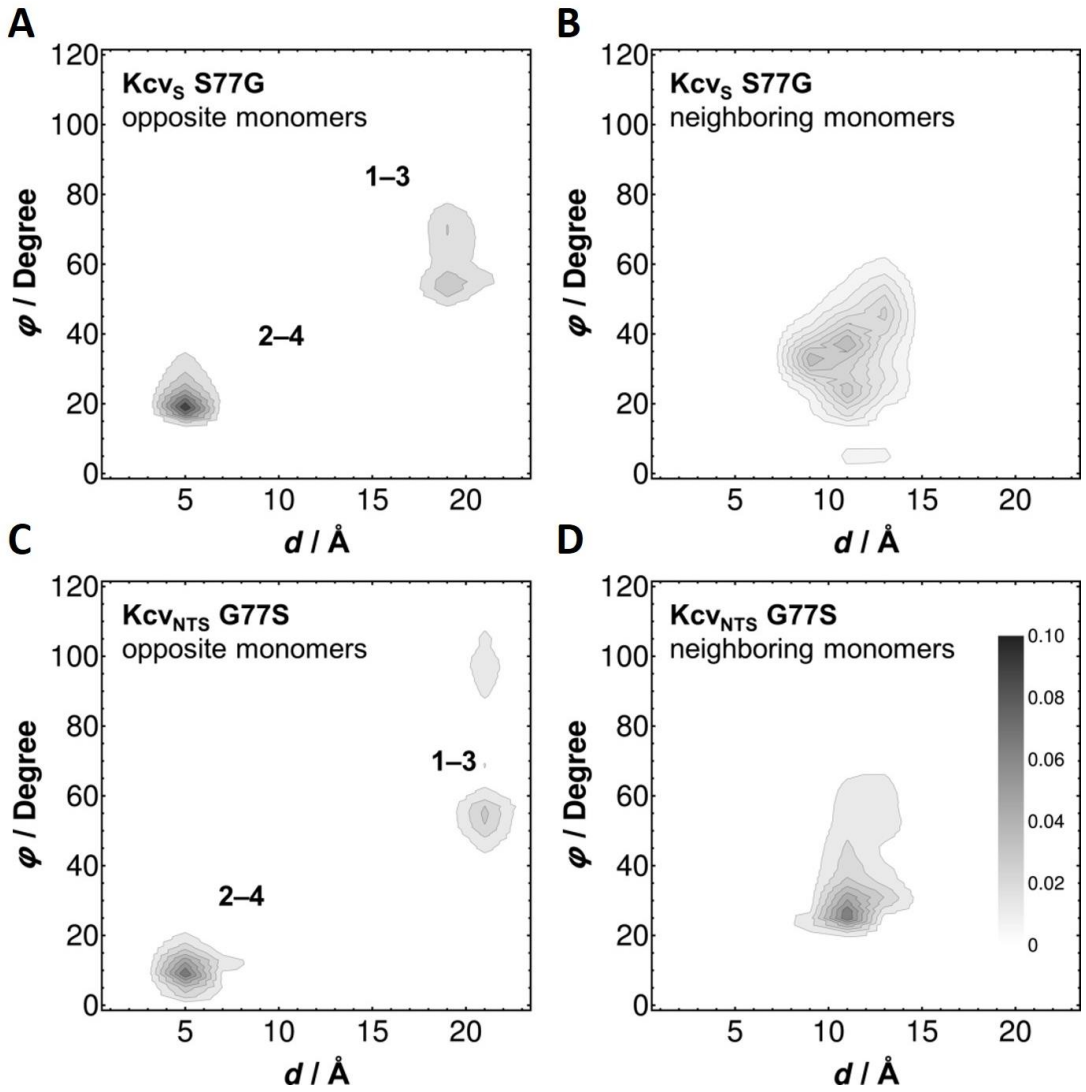

Figure 2-17: Dynamics of TM helix 2 in Kcv$_S$ S77G and Kcv$_{NTS}$ G77S. Distribution of distance-angle pairs characterizing π-stack geometries in Kcv$_S$ S77G (**A,B**) and Kcv$_{NTS}$ G77S (**C,D**) averaged over all F78 pairs in opposite (left column) and neighboring (right column) monomers. The geometric criteria are shown **Figure S 2-3**. Numbers in the left panel denote different monomers.

In order to test the hypothesis that the chosen geometric π-stack definitions represent valid descriptors that correlate with functional states, two computational control experiments were designed. Following the experimental strategy, Kcv_S S77G and Kcv_{NTS} G77S mutants were created based on the respective last frames of the Kcv_S and Kcv_{NTS} runs. As discussed in section **2.3.3**, the mutual exchange of the amino acid at position 77 in Kcv_S and Kcv_{NTS} gives rise to an inversion of the gating properties. As hoped for, the angle/distance distributions of Kcv_S can also be reproduced by Kcv_{NTS} G77S and those of Kcv_{NTS} by Kcv_S S77G (**Figure 2-17**). Hence, it can be concluded that the π-stack descriptor (angle/distance pairs) indeed correlates with open/closed state propensities even in the absence of a functionally open, conductive simulation system.

2.3.8. Absence or presence of Ser77 alters orientation of C-terminal part of TM helix 2

The experimental and computational data agree with the view that the gating differences between the two channels are determined by the presence or absence of a kink in TM helix 2. The modeling data further suggest that this could result in an altered orientation of the TM helix 2 downstream of F78.

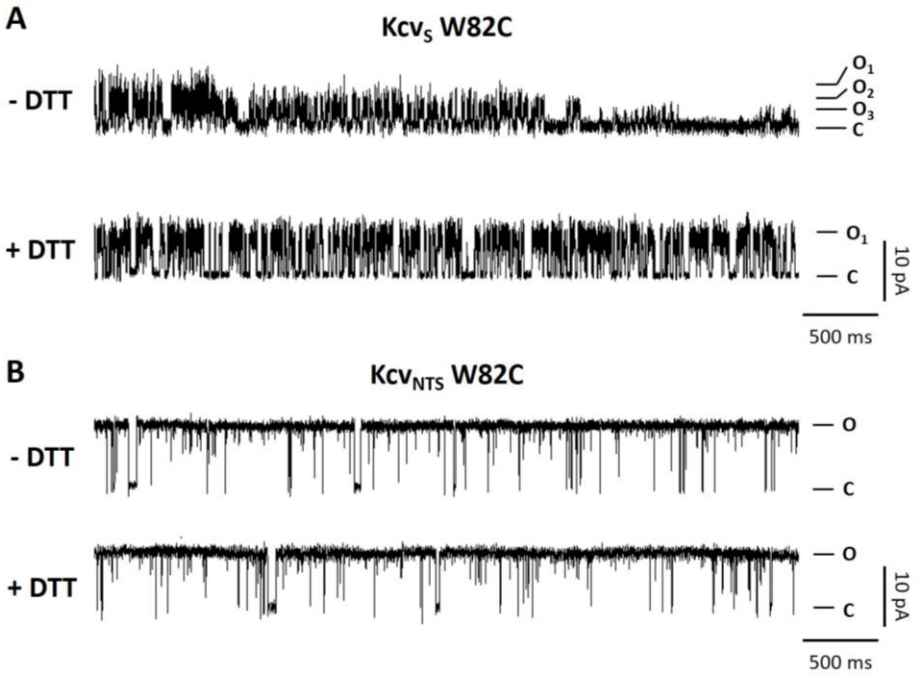

Figure 2-18: The two channels Kcv_S and Kcv_{NTS} have a different orientation of the C-terminus. Characteristic single channel fluctuations at +120 mV of Kcv_S W82C (**A**) and Kcv_{NTS} W82C (**B**) in absence (-DTT) and presence of 5 mM DTT (+DTT) in the bath solution. The prevailing open (O) and closed (C) levels are indicated along the traces.

In order to test the hypothesis that a helix kink has an effect on the orientation of the last part of TM helix 2 mutants were created in which the amino acid W82 in Kcv_{NTS} and Kcv_S was replaced with a cysteine. We reasoned that a different orientation of the TM helixes in the mutant channels should affect the propensity of forming sulfhydryl bridges between the terminal cysteines. The functional data of the mutant channels strongly supports this hypothesis. The exemplary current traces of the Kcv_S W82C mutant show that this channel has a reduced unitary conductance with different conductance levels (**Figure 2-18A**). The low unitary conductance was partially rescued by adding dithiothreitol (DTT). This finding suggests that the terminal cysteine forms sulfhydryl bridges, which lowers the conductance at the cytosolic exit of this mutant channel. The Kcv_{NTS} W82C mutant on the other hand functions like the wild-type Kcv_{NTS} channel and does not respond to DTT (**Figure 2-18B**). The terminal cysteine must be oriented in the Kcv_{NTS} W82C mutant in such a way that it is unable to form sulfhydryl bridges.

2.4. Conclusion

Ion channels typically exhibit open and closed states with different lifetimes in single channel recordings. It is generally believed that each of these closed dwell-times reflects the dynamics of a distinct gate. In the present study one long-lived closed state in the Kcv_S channel could be causally linked to a simple electrostatic interaction in the channel protein. The presence of a serine (or threonine) in the inner TM helix of the Kcv_S channel promotes formation of an intrahelical hydrogen-bond and a consequent kink in this helix. The kink, which according to the data in **Figure 2-18** also generates a twist in the lower part of the helix, has by itself no impact on gating. The channel only acquires a long-lived closed state when the amino acid downstream of the critical serine has an aromatic or a long hydrophobic side chain. The computational data suggest the following scenario: the formation of hydrogen-bonds within a transmembrane domain moves the phenyl ring of this domain out of the cavity giving room for a movement of the adjacent phenyl groups towards the pore center (**Figure 2-19**). These structural changes in the ns time window trigger a long-lived conformation, which closes the ion pathway. Hence the closing of the pore reflects a close interplay between all four monomers.

A similar gate, in which hydrophobic aromatic or aliphatic side chains serves as an obstruction of ion flow, has previously been proposed for other ion channels including complex K^+ channels (Zhou & McCammon 2010). From the crystal structure of KirBac channels it was deduced that the aromatic side chain of a phenylalanine within the intracellular half of the

inner helix could project into the channel pore and close it. Opening of the channels was presumably promoted by an upstream glycine kink in the inner helix with a simultaneous retraction of the aromatic ring from the ion pathway (Kuo et al. 2003, Kuo et al. 2005, Nishida et al. 2007, Clayton et al. 2008). Since many Kir channels have a hydrophobic aromatic phenylalanine or aliphatic leucine at this position (Rojas et al. 2007), it was proposed that they may constitute a general gate in the Kir family. In the case of Kir6.2 and Kir1.1 it was already experimentally confirmed that the respective phenylalanine and leucine are involved in a pH sensitive gating of these channels (Rojas et al. 2007, Sackin et al. 2005).

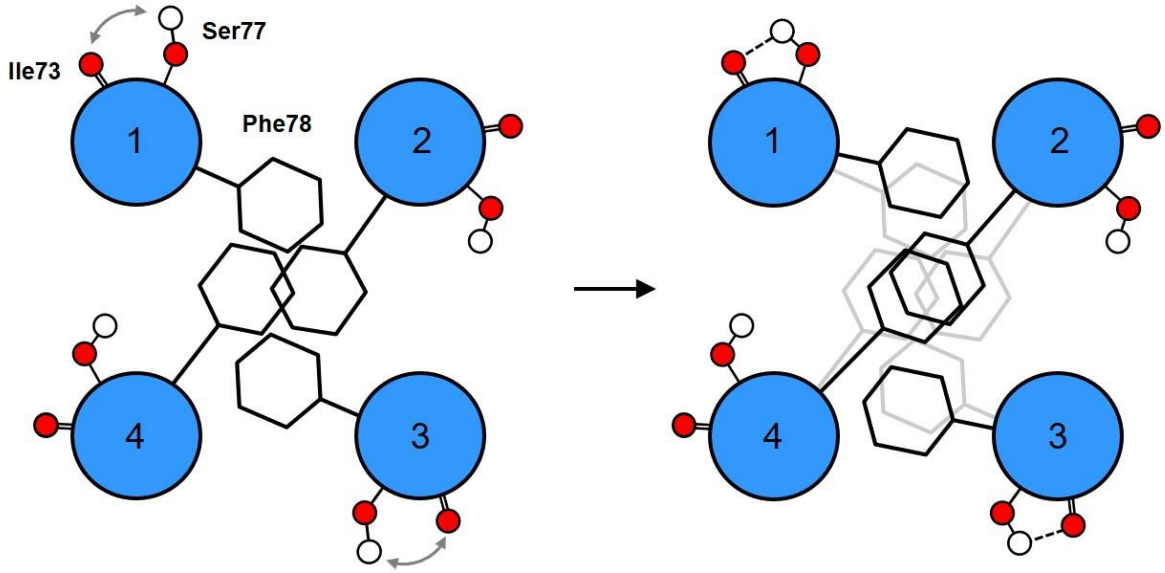

Figure 2-19: Proposed mechanism of channel closure in Kcv_S. The formation of an intrahelical hydrogen-bond between the hydroxyl group of Ser77 and the amid oxygen of Ile73 moves the aromatic side chain of F78 out of the channel pore giving room for a movement of the adjacent phenyl groups towards the pore center. The inner TM helices are shown in blue, hydrogen atoms and oxygen atoms are represented as filled white and red circles. Hydrogen-bonds are indicated as black dashed lines.

The present data further underscore the relevance of phenylalanine and leucine in gating. But different from Kir channels their function as a gate is not connected to a flexible glycine hinge. Both the Kcv_S and the Kcv_{NTS} channels have a phenylalanine in the same position in the inner helix. This phenylalanine serves as a gate only in combination with an adjacent serine. Placing a glycine in this position, which occurs in many Kcv channels, does not affect gating. The phenylalanine side chain only becomes relevant as a gate in combination with an upstream amino acid like serine or threonine, which is able to form an intrahelical hydrogen-bond. In this scenario phenylalanine serves as the door and serine as the hinge of the door in the Kcv_S channel.

The detailed analysis of single channel data shows that the Ser/Phe gate at the entry to the Kcv_S channel functions autonomously. The presence or absence of this gate has no appreciable impact on the two remaining closed dwell-times. This is different from other studies in which

channel gating was examined in the context of an individual gate. In the case of the KcsA channel it was reported that any modification of the filter gate or of the pH sensitive gate always resulted in a complex modulation of several open and/or closed dwell-times (Cordero-Morales et al. 2006, Thompson et al. 2008). In Kir6.2 channels, removal of the critical phenylalanine at the inner gate affects the stability of both open and closed states (Rojas et al. 2007). This is consistent with the idea that the dynamics of the Ser/Phe gate in Kcv_S is governed only by a single conformational alteration. The filter gate or the pH sensitive gate in KcsA in contrast may involve a network of electrostatic interactions, which include more than one defined conformational state.

While the MD simulation data provided a detailed insight into the structural components of the gate they do not completely describe the dynamics of the gating process due to the simulation time restriction. MD provides structural/dynamical correlates with function, not the complete microscopic picture. However, the MD simulations confirm that the intrahelical hydrogen-bond promotes a positioning of the phenylalanine side chain in the ionic pathway; this can generate π:π stacking interactions between aromatic rings from different monomers. Computational mutation tests confirmed the relevance of π:π stacking for understanding the gating transition, in line with the experimental finding that switching serine and glycine at position 77 inverts the open/closed propensities of Kcv_{NTS} and Kcv_S. The results of the simulations suggest that the α-helix can dynamically fluctuate between a straight and bended conformation, correlating with switching hydrogen-bond patterns. A similar observation was reported from long MD simulations in which the backbone structure of an α -helix in the pore domain of a voltage gated Na^+ channel undergoes dynamic deformation in response to the formation and breaking of intrahelical hydrogen-bonds (Boiteux et al. 2014). All of these events occur in the time window of ns (**Figure 2-15A**) or μs (Boiteux et al. 2014) while the lifetime of the closed state is in the range of hundreds of ms. Hence it is still not possible to directly correlate the lifetime of the closed state with the lifetime of an interaction or a conformational state of the channel protein. The only possibility that can be ruled out is that the respective long-lived close state reflects the lifetime of π:π stacking between the aromatic rings of opposite phenylalanine residues; notably a similar long close time is also observed when the phenylalanine residues are replaced by leucine.

The importance of intrahelical hydrogen-bonds and their potential role in channel gating have not been reported previously. However, it is reasonable to assume that similar mechanisms, which are relevant in the simple Kcv channels, could be important in the gating of complex eukaryotic channels. Extensive structural studies have shown that either serine or threonine induce either alone or in combination with proline distinct distortions in transmembrane

domains of many proteins including ion channels (Deupi et al. 2010, Deupi et al. 2004, Perea et al. 2015). Some isolated data already suggest that such serine or threonine mediated intrahelical hydrogen-bonds have an effect on protein function (Deupi et al. 2004, Sansuk et al. 2011). Notably, pairs of serine or threonine together with aromatic or large hydrophobic amino acids are also frequently present in the inner TM helices of K^+ channels. The BK channel for example has a SFF338-340 motive at the cytosolic end of the pore lining TM helix in which serine and both phenylalanine residues are involved in channel gating (Strutz-Seebohm et al. 2011, Panaghie et al. 2008).

2.5. Outlook

The experimental and computational results discussed above suggest a close interplay between all four monomers. In order to further examine the proposed mechanism of channel closure, Kcv_{NTS} concatemers were constructed by fusing two adjacent monomers with various short peptide linkers namely $(GGGGS)_2$, $E(GGGGS)_2K$, $E(GGGGS)_3K$, $EG(AGS)_4K$ and $EGGS(EAAAK)_2GGSK$. All constructs were expressed in HEK293 cells and tested for functionality using the patch-clamp technique in on-cell configuration. Surprisingly, all constructs generate a K^+ conductance with Kcv_{NTS}-like single-channel fluctuations. Exemplary single-channel traces of the Kcv_{NTS} concatemer with the peptide linker $E(GGGGS)_3K$ are shown in **Figure 2-20A**. This concatemer exhibits a high open probability and a wild-type like i/V relationship.

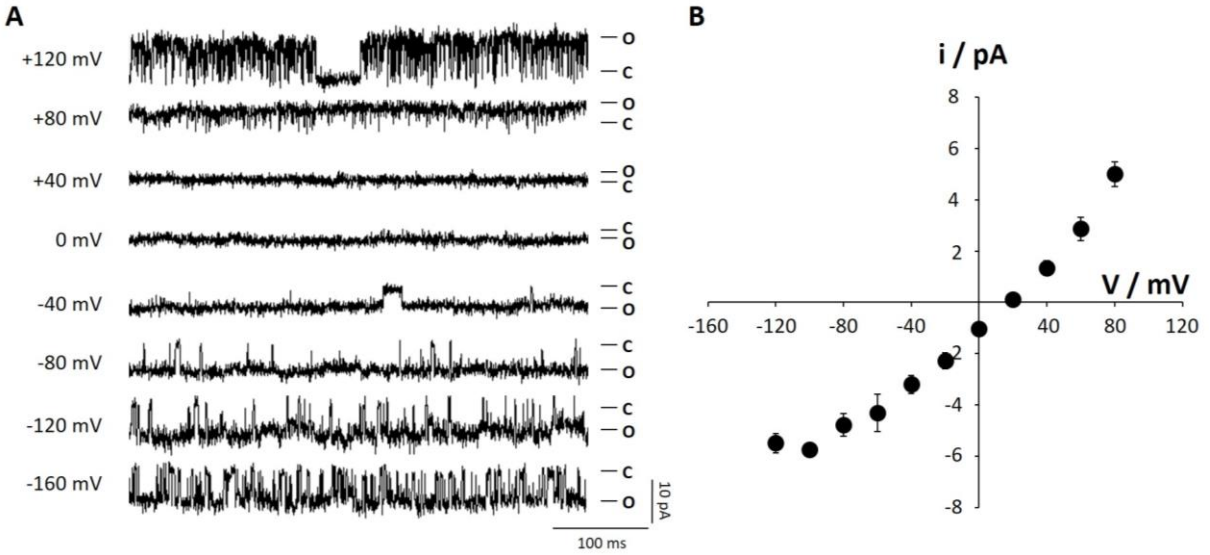

Figure 2-20: The Kcv_{NTS} concatemer with the linker $E(GGGGS)_3K$ can be functionally expressed in HEK293 cells. A Single-channel fluctuations recorded with the patch-clamp technique in the on-cell configuration at various applied voltages. **B** Mean single-channel i/V relation. Mean and standard deviation of three experiments.

Since the coding sequences of the fused monomers are different, these concatemers can be used to introduce mutations separately into the monomer pairs 1/3 and 2/4 allowing a closer examination of the gating mechanism. For instance, the substitution of glycine with serine in only one of the pore-forming Kcv_{NTS} subunits of a concatemeric monomer could answer the question whether the closure of the inner gate is indeed caused by the formation of intrahelical hydrogen-bonds in only one of both pairs of opposite monomers as predicted by the molecular dynamics simulations.

2.6. Material and Methods

2.6.1. Cloning, mutagenesis, protein expression and purification

The two viruses encoding the Kcv_{NTS} and Kcv_{S} channels were originally isolated from alkaline lakes in western Nebraska. For cell-free protein expression the coding sequences of Kcv_{NTS} and Kcv_{S} as well as their chimeras ($Kcv_{NTS/S}$, $Kcv_{S/NTS}$) were cloned into the pEXP5-CT/TOPO-vector with the pEXP5-CT/TOPO TA Expression Kit (Invitrogen, Karlsbad, CA, USA). To express the channel proteins in their native form, a stop-codon was inserted directly upstream of the coding sequence of a 6xHis-tag. The sequences of $Kcv_{NTS/S}$ and $Kcv_{S/NTS}$ were generated by fusion-PCR (Horton et al. 1989). All mutations were introduced by site-directed mutagenesis using a protocol based on the method described in30. The coding regions of all constructs were sequenced. *In vitro* expression of the channel proteins was performed with the MembraneMax HN Protein Expression Kit (Invitrogen, Karlsbad, CA, USA) following the manufacturer's instructions. The *in vitro* expression takes place in the presence of nano-lipoproteins (NLPs) (Katzen 2008) fused with multiple His-tags. This allows the purification of the native channel proteins by metal chelate affinity chromatography. For purification the crude reaction mixture was loaded on a 0.2 mL HisPur Ni-NTA spin column (ThermoFisher Scientific, Waltham, MA, USA). All steps were performed ac-cording to the manufacturer's instructions, with the exception of the elution step. To elute the NLP/channel conjugates the spin column was washed three times with two resin-bed volumes of 250 mM imidazole.

2.6.2. Planar lipid bilayer experiments

All planar lipid bilayer experiments were performed at room temperature (20-25°C) with a conventional bilayer setup (IonoVation, Osnabrück, Germany). The preparation of the recording chambers was done as described earlier32. Both chambers were connected with Ag/AgCl electrodes to the head-stage of a patch-clamp amplifier (L/M-EPC-7, List-Medical, Darmstadt). Membrane potentials were referred to the cis compartment. Current traces were filtered at 1 kHz with a 4-pole Bessel filter and digitized with a sampling frequency of 5 kHz by an A/D-converter (LIH 1600, HEKA Elektronik, Lambrecht, Germany). 1,2-diphytanoyl-sn-glycero-3-phosphocholine (DPhPC, Avanti Polar Lipids, Alabaster, AL, USA) bilayers were formed by the Pseudo painting/air bubble technique (Braun et al. 2014b) in symmetrical 100 mM KCl solution (pH 7, buffered with 10 mM HEPES). For reconstitution of channel proteins, a small amount (1-3 μL) of the purified NLP/channel-conjugates diluted in 250 mM imidazole

solution was added directly below the bilayer in the trans compartment with a bent Hamilton syringe. After successful incorporation of a single channel in the DPhPC bilayer, constant voltages were applied for 1 to 5 min. Voltage was changed in steps of 20 mV between +160 mV and -160 mV. Single-channel current traces were recorded with Patchmaster (HEKA) and analyzed with the custom-made program Kielpatch (http://www.zbm.uni-kiel.de/aghansen/software.html). Single channel amplitudes were measured visually. For determination of open probabilities an automated Hinkley jump detector (Schultze & Draber 1993) was used. Dwell-time histograms were fitted with sums of 1 to 3 exponential functions (for details see section **3.5.4**). Because of the limited temporal resolution of the experimental setup a notable number of sub-ms closed events were not detected. The number of missed events that belong to the observed closed-time populations was calculated from the obtained fitting parameters. The calculated number of missed closed-events was used to correct the mean lifetimes of the open state, which were obtained by fitting the open dwell time histograms. For this we assumed (i) that the missed closed events were randomly distributed over the open events and (ii) the missed closed events have a negligible effect on the total time that the channel spent in the open state. For calculating the mean lifetimes and probabilities of occupancy, a simple Markov model was assumed in which all closed states are directly coupled to the open state with no unobservable closed-closed transitions. If additional information on the state transitions will become available in the future, which require a modification of this model topology, algorithms are available to transform equivalent models into each other (Kienker 1989).

2.6.3. Construction of Kcv_{NTS} concatemers

For construction of Kcv_{NTS} concatemers, synthetic double-stranded DNA fragments were ordered (IDT Inc., San Diego, CA, USA) containing two alternative sequences coding for Kcv_{NTS} monomers. Both coding sequences were connected by a BspOI restriction site and flanked by overlapping ends for subsequent cloning into pIRES2-EGFP. DNA fragments were amplified via PCR, electrophoretically separated in an agarose gel and then purified by gel extraction using the GenElute™ Gel Extraction Kit (Sigma-Aldrich, St. Louis, MO, USA). 1 μg pIRES-EGFP DNA was linearized in a double digest reaction with EcoRI and BspOI (NEB, Ipswich, MA, USA), blunted with a T4 DNA polymerase (Sigma-Aldrich, St. Louis, MO, USA) and then purified using the GenElute™ Gel Extraction Kit. The synthetic double-stranded DNA fragments were inserted into the linearized pIRES2-EGFP vector using the Gibson Assembly Cloning Kit (NEB, Ipswich, MA, USA). 50 μL α-Select Silver Competent Cells (Bioloine,

London, United Kingdom) were transformed with 2 μL of the reaction mix by heat shock at 42°C for 30 seconds and subsequent transfer on ice. Positive colonies were selected after incubation at 37°C over night from LB (10 g/L tryptone, 5 g/L yeast extract, 5 g/L NaCl, 20 g/L agar, pH 7 adjusted with 1M NaOH) agar plates containing 50 μg/mL kanamycin and grown in LB medium at 37°C. The plasmid DNA were purified using a GenElute™ Plasmid Miniprep Kit (Sigma-Aldrich, St. Louis, MO, USA).

The coding sequences of various peptide linkers (**Table S 2-2**), which were flanked by overhanging ends, were ordered as double-stranded DNA fragments (IDT Inc., San Diego, CA, USA) and amplified via PCR. 1 µg of the pIRES2-EGFP vector containing the two alternative Kcv_{NTS} coding sequences was linearized with the restriction enzyme BspOI (NEB, Ipswich, MA, USA), blunted with a T4 DNA polymerase (Sigma-Aldrich, St. Louis, MO, USA) and purified using the GenElute™ Gel Extraction Kit. Cloning was performed using the Gibson Assembly Cloning Kit. Plasmids containing the correct insert were selected and purified as described above. The coding region of all constructs were sequenced.

2.6.4. Transfection of HEK293 cells

HEK293 cells were transiently transfected with 1-5 μg of the bicistronic pIRES2-EGFP vector coding for one of five Kcv_{NTS} concatemers. The transfection procedure was done according to an established calcium phosphate protocol (Liu et al. 2010). Cells were washed with PBS 6-8 hours after transfection and then incubated in a water-saturated 5% CO_2 incubator for 24 to 48 hours at 37°C in 60 mm dishes. In order to prepare transfected cells for patch-clamp measurements, they were washed with PBS and then treated with 250 μL trypsin for about one minute to separate the cells. The trypsin reaction was stopped by adding 1 mL supplemented DMEM. Subsequently, cells were transferred into 5 mL Falcon tubes and pelleted at 1000 rpm for 1 min. The supernatant was removed, cells were resuspended in 1 mL supplemented DMEM and then distributed on poly-D-lysine coated coverslips. In order to allow cells to adhere to the coverslips, cells were incubated for 45 min to 2 hours at 37°C.

2.6.5. Patch-clamp experiments

Patch-clamp experiments were performed at room temperature (25°C) with a EPC-10 amplifier (HEKA Elektronik, Lambrecht, Germany). Patch-pipettes were pulled with borosilicate capillaries by a programmable puller (P-1000, Sutter Insyruments, Novato, CA,

USA) and heat-polished by a microforge (MF-830, Narishige, Japan) resulting in 1-2 MOhm resistances. The internal solutions contained: 1 mM $CaCL_2$, 2 mM $MgCl_2$, 10 mM HEPES, 1 mM EGTA, 130 mM KCl, adjusted to 330 mOsm with mannitol and pH 7.4 with KOH. The external solutions contained: 50 mM KCl, 1.8 mM $CaCl_2$, 1 mM $MgCl_2$, 5 mM HEPES, adjusted to 340 mOsm and pH 7.4 with KOH. On-cell currents were generated by a voltage step protocol from -160 mV to +120 mV in 20 mV steps for 5 seconds each. Currents were recorded with a 2kH low-pass filter and sampled with a frequency of 5 kHz. Data were memorized with Pulse (HEKA Elektronik, Lambrecht, Germany) and analyzed with Pulse Fit (HEKA Elektronik, Lambrecht, Germany).

2.6.6. Homology modeling

The closed KirBac1.1 structure (PDB code: 1P7B16) was chosen as template for initial homology modeling of the Kcv_S and Kcv_{NTS} geometries, following closely the methodology for developing Kcv_{PBCV-1} (Tayefeh et al. 2009) and Kcv_{ATCV-1} (Braun et al. 2014a) models. The template tetramer was constructed from the KirBac1.1 monomer by applying the provided symmetry operations using VMD 1.9.1 (Humphrey et al. 1996). Deletion of the cytosolic domain resulted in a truncated KirBac1.1 tertiary structure sharing the same total number of 82 residues. Sequence alignments using CLUSTAL (version 2.1) (Larkin et al. 2007) revealed large gaps, which would lead to helix breaks. These were circumvented by restraining residues 10-15 and 75-82 to an α-helical structure during model preparation using Papwoth (version 9.10) (Web & Sali 2014, Shen & Sali 2006) with default settings for optimization cycles.

The energetically most favored model out of ten was identified by its DOPE score and further processed. Hydrogen atoms were added by CHARMM's HBUILD tool (Brünger & Karplus 1988), keeping all titratable residues in their standard protonation state at neutral pH; C-terminal residues remained deprotonated and the N-termini residues were protonated; His residues were protonated at their δ-nitrogen. The resulting models were minimized in the presence of two ions (selectivity filter binding sites S2 and S4) and two water molecules (sites S1 and S3) introduced at the filter positions by adapting the available information from the KirBac1.1 structure. PROCHECK was utilized in its online version (http://www.ebi.ac.uk/pdbsum/) (Laskowski et al. 1993) to assess the model quality, ignoring hydrogen atoms.

2.6.7. Molecular dynamics simulations

Again following the methodology for simulating the Kcv_{ATCV-1} wild type system (Braun et al. 2014a) the KirBac1.1-based homology models of Kcv_S and Kcv_{NTS} were inserted into a pre-equilibrated DMPC bilayer membrane utilizing the CHARMM-GUI tools (Jo et al. 2008) by deletion of lipid molecules colliding with any protein residues within a sharp radius of 0.5 Å of the protein, resulting in a membrane comprising 192 lipid species in total with 90 molecules in the upper and 102 in the lower layer induced by the conic protein shape. 16726 water molecules (TIP3P model) (Jorgensen et al. 1983) were added, removing water molecules inside the membrane. By random exchange with 60 water molecules 31 Cl^- and 29 K^+ ions were introduced into the bulk solution creating a concentration of approximately 100 mM KCl. With the two K^+ ions already located inside the selectivity filter electroneutrality of the entire system was achieved. The initial system dimensions were ca. 90 Å x 90 Å x 115 Å along x, y and z dimensions, with the latter representing the channel axis. Periodic boundary conditions were employed by treating electrostatics with the particle mesh Ewald algorithm (Darden et al. 1993) using a spacing of 0.1 Å between grid points and a real-space short range cutoff of 12 Å. The temperature was set to 300 K for production runs, controlled by a Langevin thermostat with a damping coefficient of 1 ps^{-1} (Kubo et al. 1991), and a pressure of 1 atm was applied by a Langevin-piston Nose-Hoover barostat (Feller et al. 1995). The CHARMM22* force field for proteins and CHARMM27 for lipids were applied throughout the simulations (Buck et al. 2006, McKerell et al. 1998) with ion parameters as used earlier (Tayefeh et al. 2009, Braun et al. 2014a). NAMD (version 2.9) was used for performing simulations (Phillips et al. 2005). After minimization and equilibration with gradually removing restraints over 12.7 ns, production runs were performed over 110 ns for each variant, sampled at each ps for further evaluation. The quality of the MD simulations is demonstrated in Supplementary **Figure S 2-4**, where the root mean square displacements (RMSD) indicate long-time stability.

2.7. Supplemental Material

2.7.1. Tables

Table S 2-1: Mean lifetimes and probabilities of occupancy of Kcv_{NTS}, Kcv_S and some selected mutants. The probabilities of occupancy P (± standard deviation) and mean lifetimes τ (± standard deviation) of the open state O and the three closed states C1, C2 and C3 were calculated from three independent 5 min recordings at +120 mV.

	τ_O / ms	τ_{C1} / ms	τ_{C2} / ms	τ_{C3} / ms	P_O	P_{C1}	P_{C2}	P_{C3}
Kcv_{NTS}	79.1 ± 18.6	1.3 ± 0.2	24.0 ± 3.9	-	0.874 ± 0.073	0.008 ± 0.002	0.117 ± 0.075	0
Kcv_S	15.1 ± 2.5	1.8 ± 0.8	23.8 ± 9.4	480 ± 145	0.525 ± 0.101	0.047 ± 0.029	0.208 ± 0.095	0.220 ± 0.152
$Kcv_{S/NTS}$	63.5 ± 28.4	1.1 ± 0.5	47.6 ± 12.2	-	0.704 ± 0.171	0.008 ± 0.003	0.252 ± 0.171	0
$Kcv_{NTS/S}$	15.4 ± 6.4	2.1 ± 1.1	17.0 ± 3.4	1070 ± 118	0.227 ± 0.053	0.018 ± 0.011	0.109 ± 0.028	0.647 ± 0.028
Kcv_S S77G	79.7 ± 15.7	1.3 ± 0.1	28.4 ± 3.6	-	0.904 ± 0.029	0.012 ± 0.004	0.084 ± 0.031	0
Kcv_{NTS} G77S	11.2 ± 0.4	1.2 ± 0.2	15.1 ± 4.4	354 ± 220	0.540 ± 0.032	0.036 ± 0.007	0.245 ± 0.035	0.179 ± 0.074
Kcv_S F78A	42.1 ± 17.2	0.6 ± 0.1	7.9 ± 4.2	-	0.971 ± 0.014	0.014 ± 0.005	0.015 ± 0.017	0
Kcv_{NTS} G77S F78A	63.7 ± 60.1	1.3 ± 0.5	27.8 ± 16.5	-	0.926 ± 0.026	0.026 ± 0.010	0.051 ± 0.018	0
Kcv_S F78L	21.8 ± 13.9	1.7 ± 0.6	13.5 ± 5.0	983 ± 419	0.348 ± 0.126	0.017 ± 0.011	0.199 ± 0.171	0.436 ± 0.305
Kcv_S F78Y	56.4 ± 6.0	1.9 ± 0.2	16.9 ± 2.1	-	0.922 ± 0.012	0.025 ± 0.002	0.052 ± 0.013	0
Kcv_{NTS} F78L	108.8 ± 16.4	1.3 ± 0.2	27.3 ± 3.8	-	0.916 ± 0.024	0.008 ± 0.001	0.077 ± 0.024	0

Table S 2-2: Linker sequences and corresponding coding sequences used for the construction of Kcv_{NTS} concatemers.

linker sequence	coding sequence
$(GGGGS)_2$	GGAGGTGGTGGAAGTGGGGGGGGTGGGTCC
$E(GGGGS)_2K$	GAAGGAGGAGGTGGTAGTGGGGGCGGTGGCTCTAAG
$E(GGGGS)_3K$	GAAGGCGGCGGCGGCTCAGGGGGCGGTGGCTCTGGTGGTGGCGGTAGCAAG
$EG(AGS)_4K$	GAAGGGGCCGGGAGTGCGGGTAGTGCTGGATCAGCGGGAAGCAAA
$EGGS(EAAAK)_2GGSK$	GAGGGTGGCAGCGAGGCTGCGGCAAAAGAAGCCGCAGCAAAGGGCGGAAGCAAG

2.7.2. Additional figures

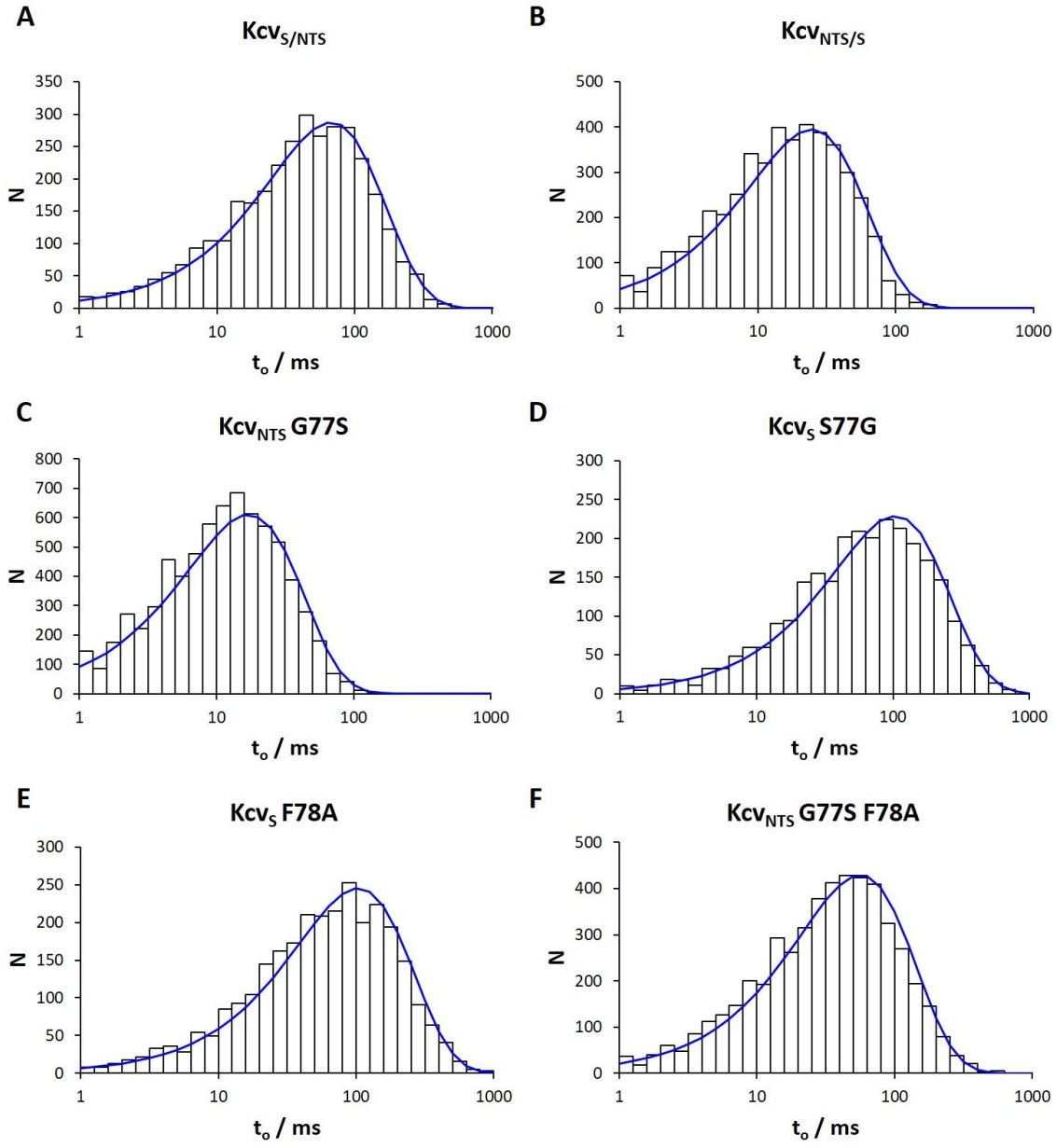

Figure S 2-1: Open and closed dwell times of Kcv channels. Exemplary open dwell time histograms from single channel recordings at +120 mV for indicated chimeras and mutants. All open dwell time histograms can be fitted with a single exponential.

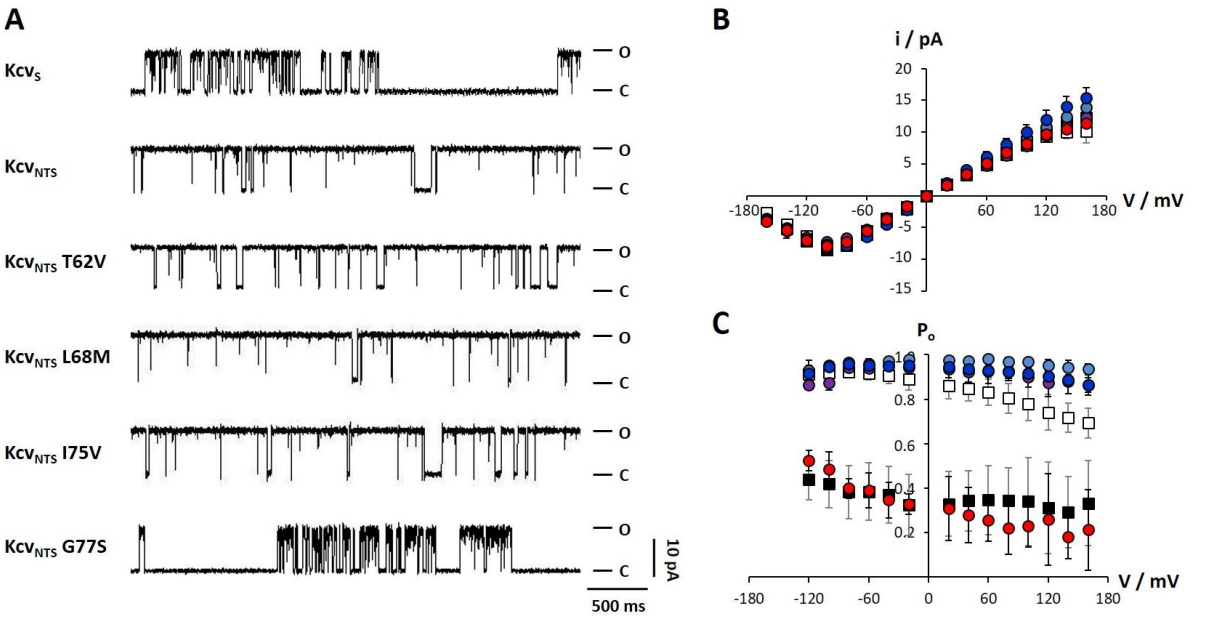

Figure S 2-2: Only the exchange G77S in Kcv$_{NTS}$ results in the electrophysiological phenotype of Kcv$_S$. To identify the relevant amino acid in TM heix 2 for gating all 4 candidates in Kcv$_{NTS}$ were mutated into the respective residue of Kcv$_S$. **A** Characteristic single-channel fluctuations of the wt channels Kcv$_S$ and Kcv$_{NTS}$ as well as the Kcv$_{NTS}$ mutants T62V, L68M, I75V and G77S at +120 mV in planar DPhPC bilayers. **B** Mean single channel i/V relations (± standard deviation) and **C** mean open probabilities (± standard deviation) of Kcv$_{NTS}$ (open squares, n = 6), Kcv$_S$ (filled squares, n = 9), Kcv$_{NTS}$ T62V (purple circles, n = 4), Kcv$_{NTS}$ L68M (light blue circles, n = 3), Kcv$_{NTS}$ I75V (blue circles, n = 4) and Kcv$_{NTS}$ G77S (red circles, n = 5).

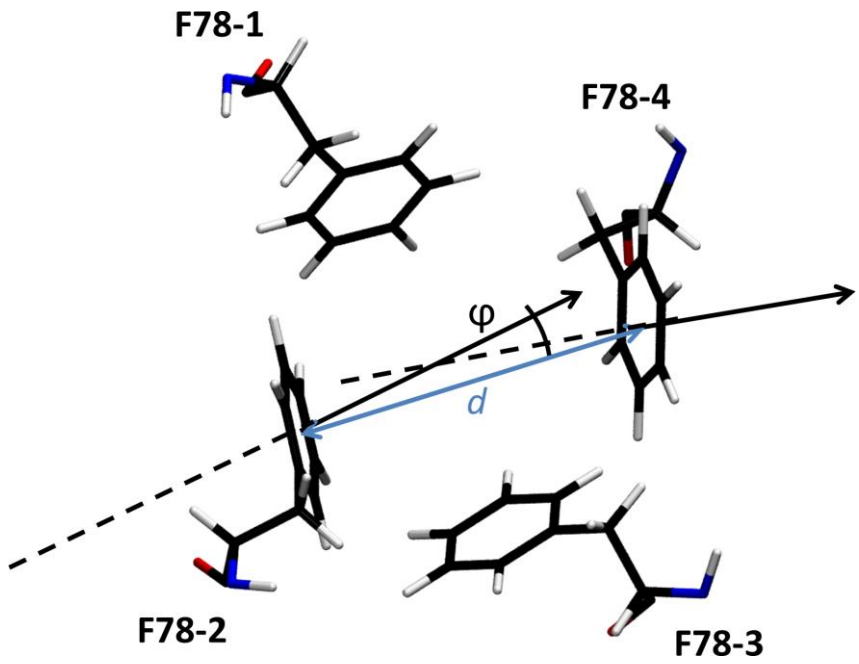

Figure S 2-3: Definition of distance-angle pairs of F77 in Kcv$_{NTS}$ and Kcv$_S$ tetramers. The image illustrates the geometric criteria with distance *d* and angle φ for characterizing π-stack geometries in **Figure 2-15** and **Figure 2-17**.

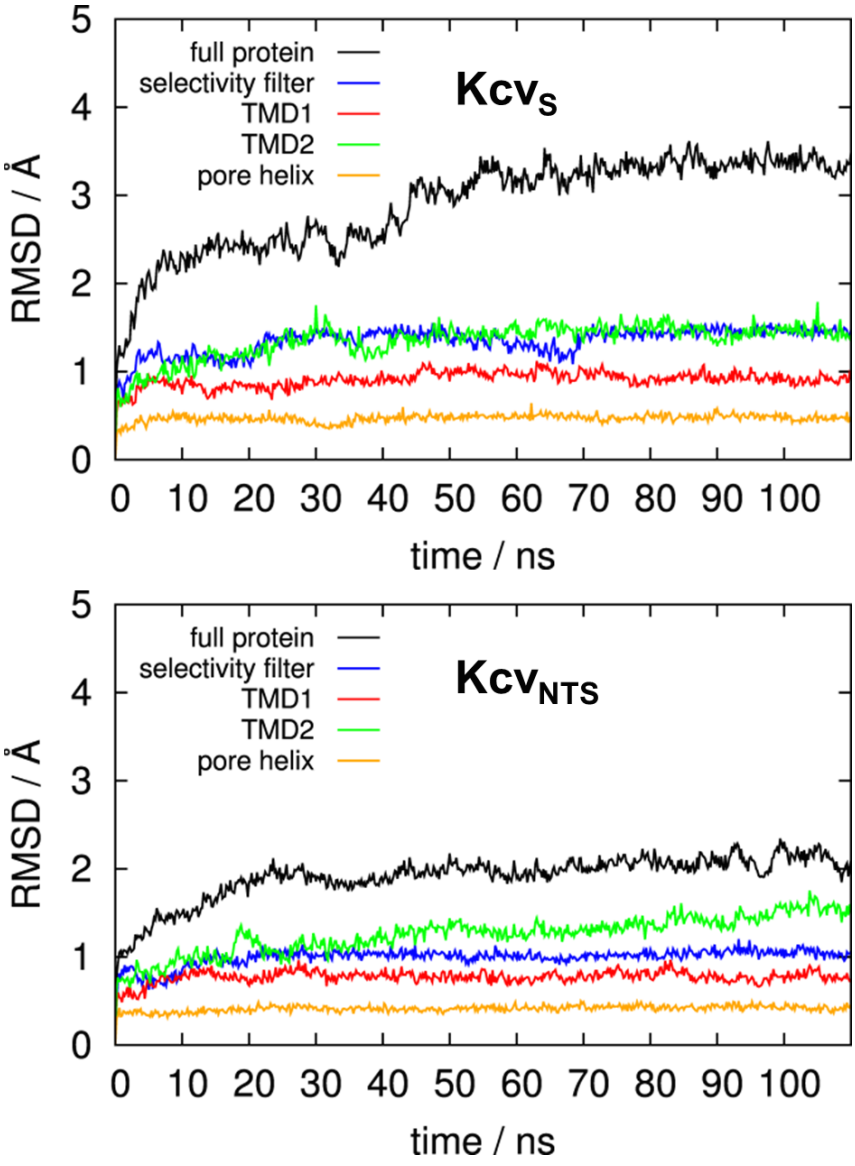

Figure S 2-4: Demonstration of MD simulation stability for Kcv$_S$ (top) and Kcv$_{NTS}$ (bottom) models as measured by the root mean square deviations (RMSD) for various protein structure components with respect to the start of production runs.

2.8. References

Abenavoli et al. (2009) Fast and slow gating are inherent properties of the pore module of the K^+ channel Kcv. J Gen Physiol. 134(3):219-29

Arnold et al. (2006) The SWISS-MODEL workspace: a web-based environment for protein structure homology modelling. Bioinformatics 22(2):195-201

Ballesteros et al. (2000) Serine and threonine residues bend alpha-helices in the chi(1)=g(-) conformation. Biophys J. 79(5):2754-60

Boiteux et al. (2014) Ion conduction and conformational flexibility of a bacterial voltage-gated sodium channel. Proc Natl Acad Sci USA 111(9):3454-9

Braun et al. (2014a) Viral potassium channels as a robust model system for studies of membrane-protein interaction. Biochim Biophys Acta 1838(4):1096-103

Braun et al. (2014b) Pseudo painting/air bubble technique for planar lipid bilayers. J Neurosci Methods 233:13-7

Brünger & Karplus (1988) Polar hydrogen positions in proteins: empirical energy placement and neutron diffraction comparison. Proteins 4(2):148-56

Buck et al. (2006) Importance of the CMAP correction to the CHARMM22 protein force field: dynamics of hen lysozyme. Biophys J. 90(4):L36-8

Clayton et al. (2008) Structure of the transmembrane regions of a bacterial cyclic nucleotide-regulated channel. Proc Natl Acad Sci USA 105(5):1511-5

Cordero-Morales et al. (2006) Molecular determinants of gating at the potassium-channel selectivity filter. Nat. Struct. Mol. Biol. 13:311–318

Chou & Fasman (1974) Conformational parameters for amino acids in helical, beta-sheet, and random coil regions calculated from proteins. Biochemistry 13(2):211-22

Darden et al. (1993) Particle mesh Ewald: An N·log(N) method for Ewald sums in large systems. J. Chem. Phys. 98:10089

Deupi et al. (2010) Tryptophan scanning mutagenesis reveals distortions in the helical structure of the δM4 transmembrane domain of the Torpedo californica nicotinic acetylcholine receptor. Channels (Austin) 6(2): 111–123

Deupi et al. (2004) Ser and Thr residues modulate the conformation of pro-kinked transmembrane alpha-helices. Biophys J 86(1 Pt 1):105-15

Feller et al. (1995) Constant pressure molecular dynamics simulation: The Langevin piston method. J. Chem. Phys. 103:4613

Gazzarini et al. (2004) Long-distance interactions within the potassium channel pore are revealed by molecular diversity of viral proteins. J. Biol. Chem. 279:28443-28449

Gazzarini et al. (2009) Chlorella virus ATCV-1 encodes a functional potassium channel of 82 amino acids. Biochemical Journal 420:295-303

Hall et al. (2009) Position of helical kinks in membrane protein crystal structures and the accuracy of computational prediction. J Mol Graph Model 27(8):944-50

Hille (2001) Ion channels of excitable membranes. Sinauer Associates, Inc.

Horton et al. (1989) Engineering hybrid genes without the use of restriction enzymes: gene splicing by overlap extension. Gene 1989 77(1):61-8

Humphrey et al. (1996) VMD: visual molecular dynamics. J Mol Graph 14(1):33-8, 27-8

Jiang et al. (2002) The open pore conformation of potassium channels. Nature 417(6888): 523-6

Jo et al. (2008) CHARMM-GUI: a web-based graphical user interface for CHARMM. J Comput Chem 29(11):1859-65

Jorgensen et al. (1983) Comparison of simple potential functions for simulating liquid water. J. Chem. Phys. 79:926

Kang et al. (2004) Small potassium ion channel proteins encoded by chlorella viruses. Proc Natl Acad Sci USA. 101(15):5318-24

Katzen (2008) Cell-free protein expression of membrane proteins using nanolipoprotein particles. Biotechniques 45(2):190

Kienker (1989) Equivalence of aggregated Markov-models of ion-channel gating. Proc R Soc Lond B Biol Sci 236(1284):269-309

Kubo et al. (1991) Statistical Physics II: Non equilibrium statistical mechanics, Springer

Kuo et al. (2003) Crystal structure of the potassium channel KirBac1.1 in the closed state. Science 300(5627):1922-6

Kuo et al. (2005) Two different conformational states of the KirBac3.1 potassium channel revealed by electron crystallography. Structure 13(10):1463-72

Larkin et al. (2007) Clustal W and Clustal X version 2.0. Bioinformatics 23(21):2947-8

Laskowski et al. (1993) Main-chain bond lengths and bond angles in protein structures. J Mol Biol 231(4):1049-67

Liu et al. (2010) Enzyme-inhibitor-like tuning of Ca^{2+} channel connectivity with calmodulin. Nature 463:968–972.

McGregor et al. (1987) Analysis of the relationship between side-chain conformation and secondary structure in globular proteins. J Mol Biol. 198(2):295-310

McKerell et al. (1998) All-atom empirical potential for molecular modeling and dynamics studies of proteins. J Phys Chem B. 102(18):3586-616

Nishida et al. (2007) Crystal structure of a Kir3.1-prokaryotic Kir channel chimera. EMBO J. 26(17):4005-15

Panaghie et al. (2008) Voltage-dependent C-type inactivation in a constitutively open K^+ channel. Biophys J 95(6):2759-78

Perea et al. (2015) TMalphaDB and TMbetaDB: web servers to study the structural role of sequence motifs in α-helix and β-barrel domains of membrane proteins. BMC Bioinformatics 16(1): 266

Phillips et al. (2005) Scalable molecular dynamics with NAMD. J. Comput. Chem 26:1781

Rauh et al. (2017a) Identification of intrahelical bifurcated H-bonds as a new type of gate in K^+ channels. J. Am. Chem. Soc. 139 (22):7494–7503

Rauh et al. (2017b) Extended beta distributions open the access to fast gating in bilayer experiments-assigning the voltage-dependent gating to the selectivity filter. FEBS Lett. 2017 591(23):3850-3860

Rojas et al. (2007) Gating of the ATP-sensitive K^+ channel by a pore-lining phenylalanine residue. Biochim Biophys Acta 1768(1):39-51

Sackin et al. (2005) Structural locus of the pH gate in the Kir1.1 inward rectifier channel. Biophys J 88(4):2597-606

Sansuk et al. (2011) A structural insight into the reorientation of transmembrane domains 3 and 5 during family A G protein-coupled receptor activation. Mol Pharmacol 79(2):262-9

Schultze & Draber (1993) A nonlinear filter algorithm for the detection of jumps in patch-clamp data. J Membr Biol. 132(1):41-52

Shen & Sali (2006) Statistical potential for assessment and prediction of protein structures. Protein Sci 15(11):2507-24

Shrivastava & Bahar (2006) Common mechanism of pore opening shared by five different potassium channels. Biophys J. 90(11):3929-40

Strutz-Seebohm et al. (2011) Structural basis of slow activation gating in the cardiac I Ks channel complex. Cell Physiol Biochem 27(5):443-52

Tayefeh et al. (2009) Model development for the viral Kcv potassium channel. Biophys. J. 96:485-498

Thiel et al. (2011) Minimal art: or why small viral K^+ channels are good tools for understanding basic structure and function relations. Biochim. Biophys. Acta. 1808:580-588

Thompson et al. (2008) Molecular mechanism of pH sensing in KcsA potassium channels. Proc. Natl. Acad. Sci. U.S.A. 105:6900-6905

Web & Sali (2014) Protein structure modeling with MODELLER. Methods Mol Biol 1137:1-15

Zhou & McCammon (2010) The gates of ion channels and enzymes. Trends Biochem Sci. 35(3):179-85

3. Outward rectification in a viral potassium channel is based on ion depletion of the selectivity filter

3.1. Abstract

Voltage-dependence is an important property of potassium channels in a variety of physiological processes such as neuronal excitability and muscle contraction. Canonically, voltage-sensitivity is attributed to conformational changes in a specialized transmembrane voltage-sensing domain (VSD), which is covalently linked to the pore module. However, there is increasing evidence that voltage-sensitivity is also an intrinsic property of potassium channels lacking any canonical VSD. Here, I investigate the kinetics and mechanism of a pronounced voltage-dependent gating process in a member of the family of viral pore-only Kcv channels. $Kcv_{NH\ S77G}$ exhibits in multi-channel bilayer experiments in response to membrane hyperpolarization a time-dependent, ultra-slow inactivation, resulting in an outwardly-rectifying current-voltage relationship. Single-channel measurements demonstrate that this inactivation is caused by the voltage-dependent transition from an active state, in which the channel exhibits an open probability of about 90%, to an ultra-long-lasting, voltage-insensitive inactive state. The transition into the inactive state is sensitive to both the external potassium concentration and the electrochemical driving force, supporting the idea that inactivation is directly linked to the permeation of potassium ions through the channel pore. These results provide a plausible mechanistic explanation on how ion channels without a VSD can sense a change in membrane voltage.

3.2. Introduction

Potassium channels are dynamic structures that can be gated by diverse physiologically relevant stimuli including for instance temperature, mechanical stretch or pressure, ions, small molecules and pH (Hille 2001, Pongs 1999). One of the most important and extensively studied gating stimuli is membrane voltage. The respective voltage-gated ion channels play an important regulatory role in a vast number of cellular processes like neuronal excitability (Pongs 1999), muscle contraction (Nelson & Quayle 1995), secretion (Stojilkovic et al. 2010) as well as cell volume regulation (Deutsch & Chen 1993).

In Kv channels, which form with 12 families the most diverse group of potassium channels (Yu et al. 2005), the voltage-dependent activation is controlled by the voltage-sensing domain (VSD), which is composed of the transmembrane segments S1-S4 (Gandhi & Isacoff 2002).

The actual voltage sensor is constituted by the S4 helix, that contains a motif of positively charged amino acids. Depolarization of the membrane voltage leads to a complex movement of the S4 helix inside the VSD and subsequently to the opening of the activation gate. Even though the mechanism is still in the focus of ongoing debates, it is widely accepted that the S4-S5 linker plays a key role in the electromechanical coupling between the VSD and the pore (Pischalnikova & Sokolova 2009, Jensen et al. 2012). The primary activation gate is formed by the S6 helices, that intersect near the intracellular membrane surface. The resulting hydrophobic constriction is referred to as bundle crossing (Kuang et al. 2015). In the resting state the bundle crossing constricts the ion permeation pathway and hence prevents hydrated potassium ions to enter/leave into/from the cavity. A voltage-driven conformational change in the VSD activates the channel by opening the bundle crossing gate (Long et al. 2005). The activation is followed by an inactivation process that can be caused by at least two different mechanisms (Kuang et al. 2015). The so-called N-type inactivation that has been described for some Kv channels is the result of an interaction between a N-terminal particle (inactivation ball) and the open channel (Hoshi et al. 1990). The second and usually slower inactivation process is called C-type inactivation. This inactivation process results from conformational changes in the selectivity filter or the extracellular pore region (Hoshi & Armstrong 2013) and is also present in pore-only channels like MthK (Thomson et al. 2014) or KcsA (Bernèche & Roux 2005). The molecular causes of C-type inactivation are still under discussion. It is even not clear, if all inactivation processes, that have been referred to as C-type inactivation, are indeed caused by the same mechanism (Kurata & Fedida 2006, Hoshi & Armstrong 2013).

Another major class of rectifying potassium channels are the inwardly rectifying (Kir) channels, that play a crucial role in diverse physiological processes such as glucose homeostasis and membrane excitability (Bichet et al. 2003). Inward rectification, that means the ability to allow greater influx than efflux of potassium ions, is not caused by the conformational change of a VSD, but by intracellular ions such as Mg^{2+} and polyamines, which block the ion permeation pathway due to membrane depolarization (Matsuda 1991, Nichols & Lopatin 1997, Oliver et al. 2000). Consequently, the voltage-dependent ion flux through Kir channels is not an intrinsic voltage-dependence.

However, there is increasing evidence that also channels that do not possess a canonical VSD or sensitivity to Mg^{2+}/polyamines can exhibit intrinsic voltage-dependence. For example, it has been shown that voltage-dependent gating is a common property of nearly all members of the two-pore domain K^+ (K2P) channel family (Schewe et al. 2016). Moreover, intrinsic voltage-dependent gating behavior has also been reported for some modified inwardly rectifying K^+ (Kir) channels. As an example, a single point mutation in the inner, pore-lining helix turns the two-transmembrane domain inwardly rectifying K^+ channel Kir6.2 into a

channel that exhibits voltage-dependent gating in the absence of blockers, resulting in a slow outwardly rectifying current-voltage relationship (Kurata et al. 2010). In another study performed by Yeh et al. (2005) it has been shown that the substitution of a negatively charged glutamate residue with a glycine in the cytosolic entryway of Kir2.1 generates intrinsic inward rectification in the absence of intracellular blockers. Single-channel experiments revealed that this inward rectification is the result of both voltage-dependent ion conductance and a voltage-dependent gating mechanism (Chang et al. 2007).

Intrinsic voltage-dependent gating has also been reported for viral potassium channels of the Kcv family (Pagliuca et al. 2007, Abenavoli et al. 2009, Gazzarini et al. 2009). This sub-millisecond gating process, which is referred to as flicker gating, occurs at hyperpolarized membrane voltages and causes an apparent decrease in the single-channel conductance as well as an increase in the open-channel noise. Mutational studies in combination with extended beta distribution analysis of single-channel recordings revealed that this fast voltage-dependent gating process originates from the selectivity filter (Rauh et al. 2017b). In addition, a second slow voltage-dependent gating process could be established in Kcv_{PBCV-1} by extending the outer transmembrane domain by one alanine (Baumeister et al. 2017). This mutation converted the instantaneous activating Kcv_{PBCV-1} into a slow activating inward rectifier. The authors attributed the voltage-dependent activation to the voltage-sensitive formation of salt bridges between cationic amino acids on the N-terminal helix and the negatively charged C-terminus. Accordingly, channel closure is presumably caused by a voltage-dependent disruption of these salt bridges and subsequent strong interaction of the free C-terminus with K^+ ions.

This brief overview shows that voltage-dependence is not only limited to canonical voltage-sensing Kv channels but is also an intrinsic property of channels that lack a canonical VSD. The investigation of these gating processes will support a comprehensive understanding of the functionality of potassium channels as well as of the coupling between fundamental channel properties such as selectivity, conductivity and gating.

Here I investigate the mechanism of a voltage-dependent, outward rectifying gating process in a mutant of the viral pore-only K^+ channel Kcv_{NH}. Kcv_{NH} was isolated from a water sample collected from Lake Winnipesaukee in New Hampshire (USA) and belongs to the family of Kcv_{ATCV-1}-like potassium channels (Siotto 2017). These channels are encoded by Phycodnaviruses, which infect unicellular SAG type *Chlorella* algae (Bubeck & Pfitzner 2005). Several electrophysiological studies have already shown that Kcv_{ATCV-1}-like proteins form functional tetrameric channels, which exhibit many properties that are typical for more complex K^+ channels. This comprises a high selectivity for K^+, sensitivity to typical K^+ channel

blockers like Ba^{2+}, and stochastic fluctuations between open and closed states (Gazzarini et al. 2009, Braun et al. 2014a, Rauh et al. 2017a,b). Kcv_{ATCV-1}-like channels have been functionally studied in heterologous expression systems like *Saccharomyces cerevisiae* (Gazzarini et al. 2009), mammalian HEK293 cells (Greiner 2011, Siotto 2017) and *Xenopus laevis* oocytes (Gazzarini et al. 2009). In addition, and important for this study, Kcv_{ATCV-1}-like channels can be easily expressed *in vitro* and subsequently reconstituted into artificial planar lipid bilayers (Braun et al. 2014a, Winterstein et al. 2018). This allows the recording of single-channel fluctuations (Braun et al. 2014a) and macroscopic multi-channel current responses (Winterstein et al. 2018) in a well-defined and readily controllable system.

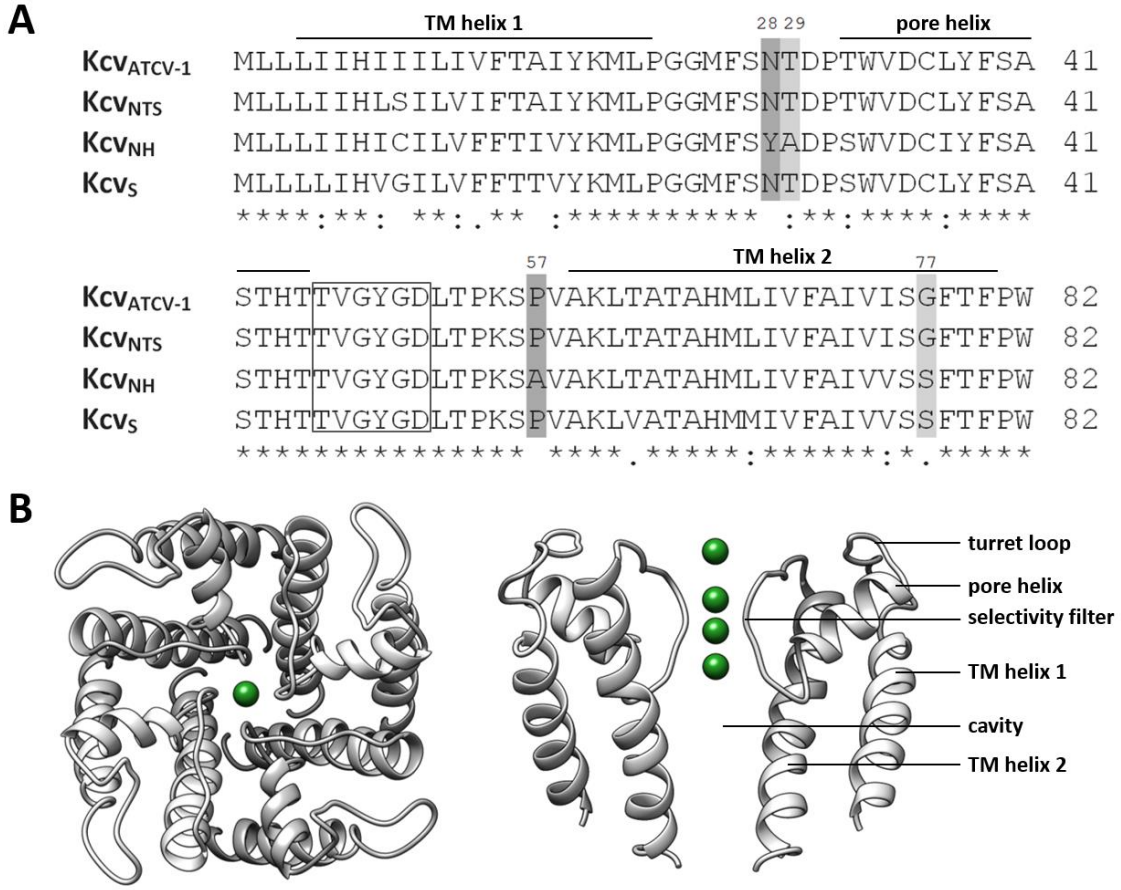

Figure 3-1: Kcv_{ATCV-1}-like viral potassium channels show a high sequence identity and represent the pore module of more complex potassium channels. A Sequence alignment of four Kcv_{ATCV-1}-like viral potassium channels. The predicted transmembrane (TM) helices 1 and 2 as well as the pore helix are highlighted by black lines. The selectivity filter sequences are shown in a gray rectangle. Amino acids of interest are highlighted in gray. Asterisks, colons and points indicate identical, conserved and semi-conserved residues, respectively. **B,C** Structural model of the viral potassium channel Kcv_{NTS}. Left: view from the extracellular side of the full tetrameric channel. Right: Side view of two opposing monomer units. Potassium ions are shown as green spheres. The homology model was calculated with Swissmodel (Arnold et al. 2006) using structural KirBac1.1 data (PDB code 1P7B, Kuo et al. 2003).

The subunits of the homotetrameric Kcv_{NH} consist of 82 amino acids and share a high sequence identity with other members of the Kcv_{ATCV-1}-family (**Figure 3-1A**). Each subunit is built from of two transmembrane (TM) helices and a pore loop. The latter contains beside the

pore helix the selectivity filter motive (TVGYGD), which is conserved in all functional K^+ channels (Doyle et al. 1998). The N-terminal TM helix (TM helix 1) directly interacts with the surrounding lipid membrane (Braun et al. 2014a) (**Figure 3-1B**). In contrast, the C-terminal TM helix (TM helix 2) is located inside the channel and forms together with the pore loop the ion permeation pathway (**Figure 3-1B**). With this simple architecture, Kcv_{NH} represents, like all members of the Kcv family, the pore module of more complex K^+ channels (Kang et al. 2004).

In the present study I analyze the kinetics and the structural causes for the outward rectification of the viral potassium channel $Kcv_{NH\,S77G}$ by means of biomolecular and electrophysiological techniques. Comparative analysis of channel orthologs with different electrical properties but high sequence identity identifies two amino acids in the extracellular turret loop as crucial structural determinants of the voltage-dependence in $Kcv_{NH\,S77G}$. These residues are presumably involved in the formation of the outer pore entrance. Single- and multi-channel experiments performed in artificial lipid membranes reveal that the voltage-dependent inactivation is sensitive to the driving force for potassium as well as the external potassium concentration. These findings, together with the observation that the recovery from the inactive state is voltage-insensitive, support the hypothesis that the voltage-dependence is a direct consequence of ion permeation. Based on the electrophysiological data a mechanistic working model is developed that provides a quantitative explanation for both the inactivation and activation process. Accordingly, the closure of the channel is caused by ion depletion of the channel pore and a subsequent conformational change within the selectivity filter. The rate determining step is the refilling of an outer, non-selective binding site with K^+ during the ion translocation process. If this binding site remains empty while the ions within the filter are moved towards the intracellular space, the selectivity filter becomes inactive. The inactive state is voltage-independent, but stabilized by the occupation of a second, K^+-selective binding site, which is presumably located inside the selectivity filter.

3.3. Results and Discussion

3.3.1. Switching off the inner gate in Kcv_{NH} uncovers a voltage-dependent, outward-rectifying gating process

The wild type potassium channel Kcv_{NH} exhibits in single-channel planar lipid bilayer experiments a low and slightly voltage-dependent open probability. The open probability decreases from ~0.4 at -160 mV to ~0.1 at +160 mV (**Figure 3-2D**). The low open probability at negative voltages is mainly caused by rare closed events with dwell times in the range of several seconds (**Figure 3-2A**). In contrast, the even lower open probability at positive voltages is the result of shorter, but more frequent closed events. The single-channel current-voltage relationship (iV curve) of Kcv_{NH} (**Figure 3-2C**) shows the Kcv-typical negative slope conductance at negative membrane voltages (Pagliuca et al. 2007, Abenavoli et al. 2009, Gazzarini et al. 2009), which is caused by an unresolved voltage-dependent fast gating process (Abenavoli et al. 2009, Rauh et al. 2017b). In addition to the reduced apparent single-channel amplitude, the fast gating process induces an increase in the excess open-channel noise (**Figure 3-2A**). The asymmetry of the iV relationship allows the precise determination of the channel orientation in the bilayer since it is known from patch-clamp measurements (Abenavoli et al. 2009, Gazzarini et al. 2009) that the negative slope conductance is linked to the flux of ions from the extracellular to the intracellular space. Therefore, the orientation of the channels in the bilayer must be the same as in a cell: The N- and C-termini are facing the *cis* compartment (intracellular space), whereas the selectivity filter is oriented towards the *trans* compartment (extracellular space).

When compared with other channels of the Kcv_{ATCV-1}-family, Kcv_{NH} exhibits in symmetrical 100 mM KCl with 70 ± 3 pS (N = 3) a relatively small slope conductance between -80 mV and +80 mV (ohmic range of the iV curve in **Figure 3-2C**). The homologous channels Kcv_{NTS} and Kcv_S, for instance, show in the same voltage range a slope conductance of 87 ± 2 pS (N = 6) and 94 ± 4 pS (N = 8), respectively (see section **2.3.1**). As proven by extended beta distribution analysis of single-channel recordings, the smaller slope conductance of Kcv_{NH} is caused by an additional fast gating process that cannot be fully resolved. This analysis revealed that the true slope conductance is indeed in the same range as for Kcv_{NTS} and Kcv_S (personal communication Dr. Indra Schröder).

Kcv_{NH} exhibits with a value of about 0.25 a mean open probability quite similar to the homologous channel Kcv_S (~0.35). It has been shown that the low open probability of Kcv_S arises from a long-lived closed state with a voltage-independent mean lifetime of about

500 ms (Rauh et al. 2017a). This closed state is caused by the temporary obstruction of the ion pathway by phenylalanine side chains (Phe78) at the cytosolic entrance to the pore (Rauh et al. 2017a and section **2.3.5**).

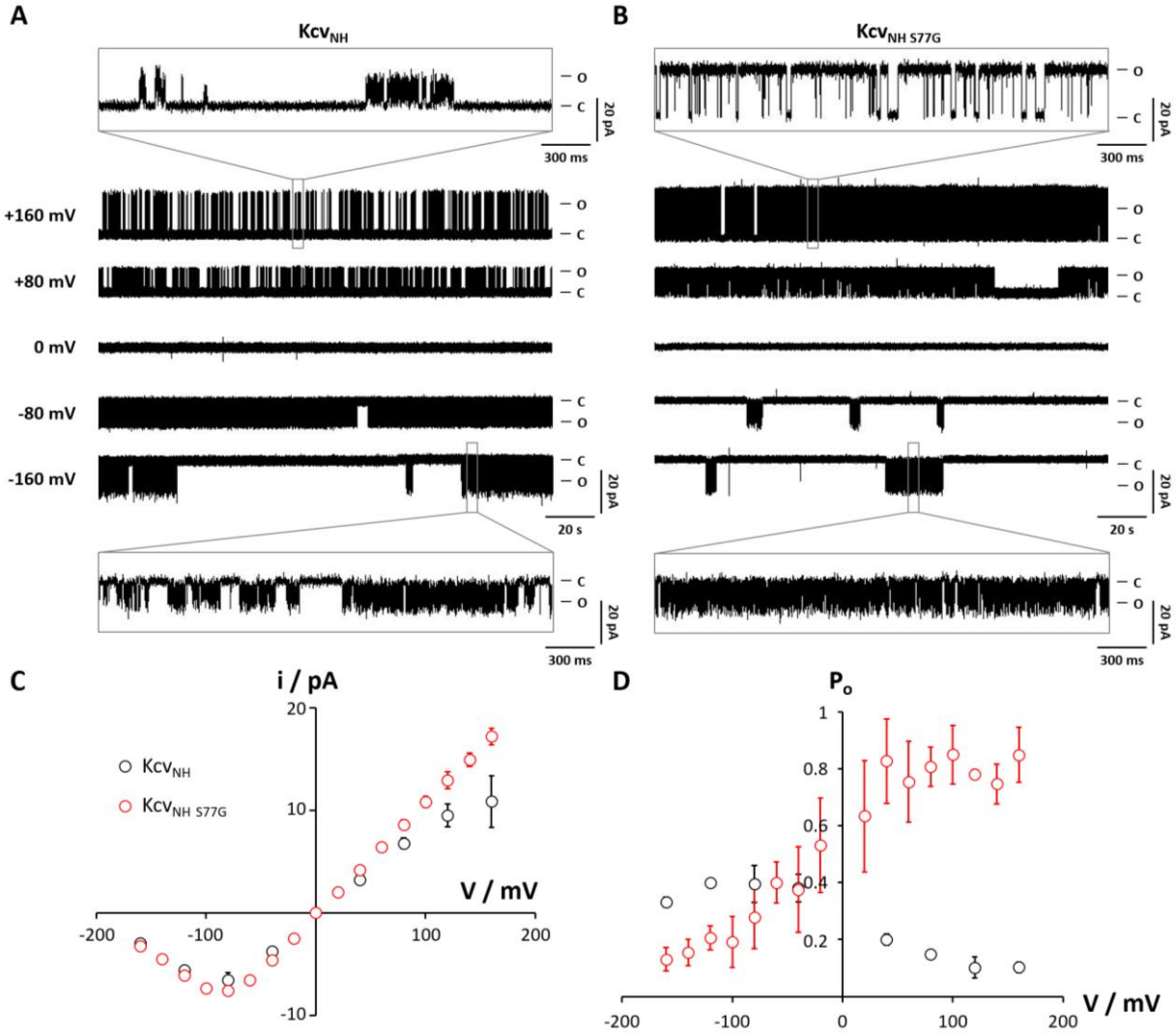

Figure 3-2: The mutation S77G uncovers a voltage-dependent, outward rectifying gating process in the viral potassium channel Kcv$_{NH}$. A,B Representative single-channel recordings in symmetrical 100 mM KCl of Kcv$_{NH}$ and Kcv$_{NH\ S77G}$. The membrane potentials are given on the left-hand side of the traces in **A**. Traces in gray boxes show the gating behavior on a smaller time-scale. C and O indicate the closed and open state. **C** Apparent single-channel amplitudes. **D** Open probabilities calculated from 5- to 30-minutes steady-state measurements. Mean and standard deviation of three and four experiments for Kcv$_{NH}$ and Kcv$_{NH\ S77G}$, respectively. Symbols in **D** cross-reference to symbols in **C**.

A requirement for the activity of this so called 'inner gate' is the presence of a serine one position upstream of Phe78. Substitution of this serine with another amino acid like glycine prevents the formation of an intrahelical hydrogen-bond and thereby the obstruction of the ion pathway by Phe78. Interestingly, Kcv$_{NH}$ also possesses a serine at position 77 (**Figure 3-1A**). Even though the gating behavior of Kcv$_{NH}$ and Kcv$_S$ is quite different, I reasoned that the low open probability of Kcv$_{NH}$ could be caused by the action of the inner gate. To test this hypothesis, Ser77 in Kcv$_{NH}$ was substituted with a glycine. Indeed, this mutation has a

dramatic effect on both the iV relationship and the open probability. First of all, the mutation causes the disappearance of the afore-mentioned flickering at positive membrane voltages (**Figure 3-2B**) and, probably as a consequence, an increase of the single-channel conductance between -80 mV and +80 mV to 109 ± 3 pS (N = 4) (**Figure 3-2C**). This result suggests that the inner gate is also involved in a sub-millisecond gating process. Similar results were obtained by analyzing fast-gating events of the homologous channels Kcv_{NTS} and Kcv_{S} by means of extended beta distributions (Rauh et al. 2017b).

The most striking effect of the introduced mutation is related to the slow gating events: the long-lived closed events, which cause the low open probability of Kcv_{NH} at positive voltages, are absent in $Kcv_{NH\ S77G}$ (**Figure 3-2B**). In contrast, the rare but very long closed events, which are responsible for the low open probability of Kcv_{NH} in the negative voltage range, are not affected by the S77G mutation. Consequently, the open probability decreases from positive to negative voltages (**Figure 3-2D**). Thus, by switching off the inner gate in Kcv_{NH}, an outward-rectifying gating process was uncovered.

3.3.2. The outward-rectification is exclusively caused by the voltage-dependent appearance of ultra-long-lasting closed events

The single-channel current traces presented in **Figure 3-2B** suggest that the outward rectification of $Kcv_{NH\ S77G}$ mainly results from ultra-long-lasting closed events at negative membrane voltages, hereinafter referred to as interbursts or periods of inactivity (I). However, it cannot yet be ruled out that the voltage-dependence is partly due to a voltage-dependent change in the gating behavior within the bursts of activity (A), i. e. within the sections separated from each other by interbursts. To test this possibility, the gating events within bursts of activity were analyzed by means of dwell-time analysis. **Figure 3-3** shows representative open- and closed-time histograms obtained by analyzing 5- to 30-minutes of steady-state single-channel measurements in symmetrical 100 mM KCl. The open-time histograms (**Figure 3-3B,D**) show a single population of open events, indicating a single conformationally stable open state. In order to obtain the mean lifetime of the open state (τ_0), the open-time histograms were fitted with a single exponential function. This analysis reveals a nearly voltage-independent mean open lifetime for moderate positive and negative membrane voltages (between -60 mV and +80 mV) (**Figure 3-3E**). At extreme positive and negative membrane voltages the mean open lifetime decreases from 109 ms at +20 mV to 40 ms and 14 ms at +160 mV and -160 mV, respectively.

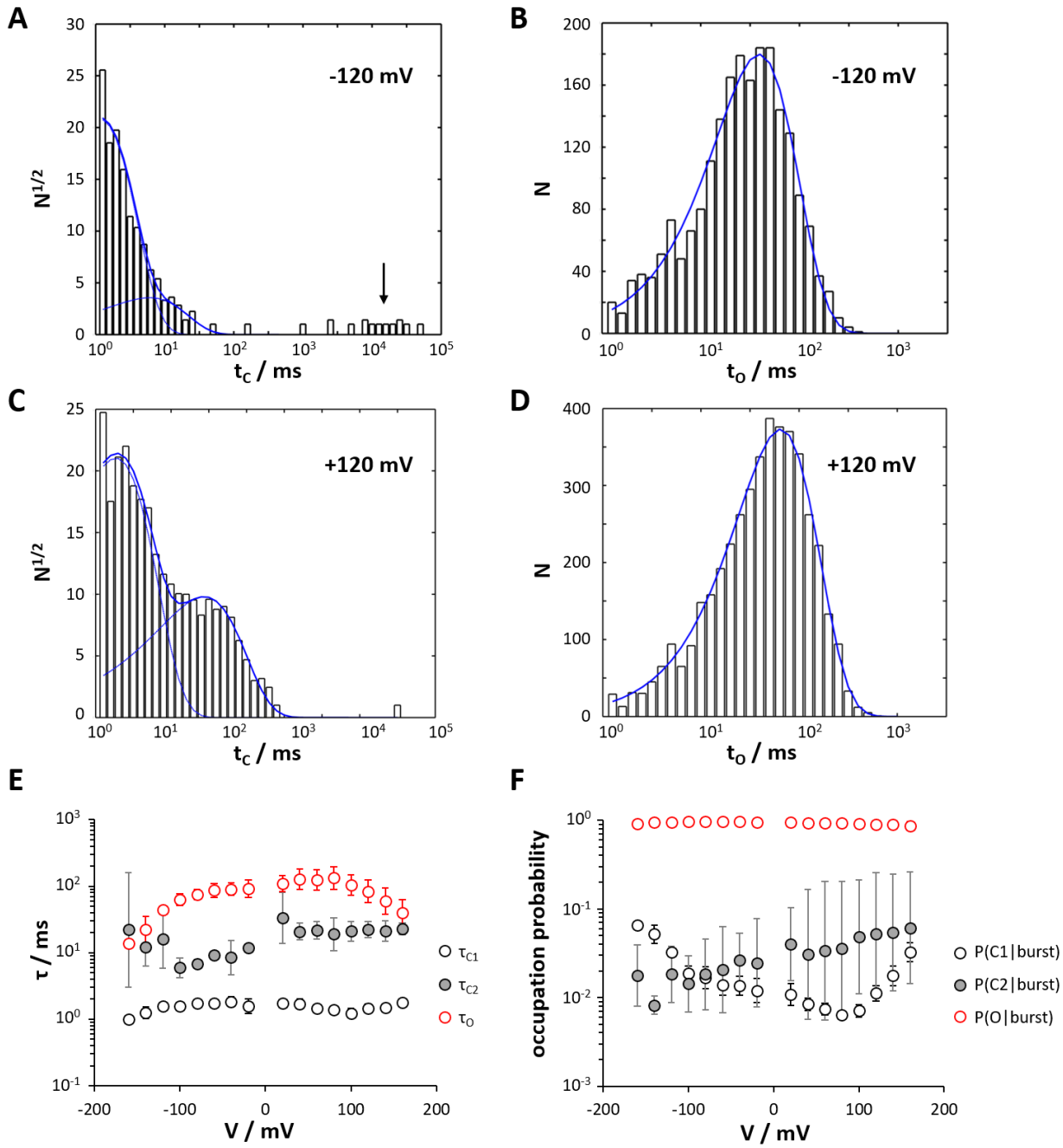

Figure 3-3: The conditional open probability inside a burst of activity is voltage-independent. A,C Representative closed-time histograms for -120 mV and +120 mV, respectively. **B,D** Representative open-time histograms for -120 mV and +120 mV, respectively. The dwell-times were calculated from 5- to 30-minutes steady-state measurements. The closed-time histograms were fitted with two exponential functions, open-time histograms with one exponential function. To obtain the gating characteristics within the bursts of activity, the population of ultra-long-lasting closed events (interbursts, highlighted with an arrow in A) were ignored. **E** Mean lifetimes of the two short-lived closed states (τ_{C1} and τ_{C2}) and the open state (τ_O). **F** Probabilities to find the channel within a burst of activity (burst) in the open state O (P(O|burst)) or in the closed states C1 (P(C1|burst)) and C2 (P(C2|burst)). Geometric mean and geometric standard deviation of three experiments.

The closed-time histograms exhibit for all membrane voltages two overlapping populations of closed events (C1 and C2) in the time window between 1 ms and 1 s (**Figure 3-3A,C**). With increasing negative voltages, a third population of closed events with dwell-times longer than

1 s appears (highlighted with a black arrow in **Figure 3-3A**). This population represents the interbursts that are present in the single-channel traces at negative membrane voltages (**Figure 3-2**B).

To obtain information about gating within the burst of activity solely, all closed-time histograms are fitted with only two exponential functions deliberately ignoring the population of interbursts. The mean lifetimes of C1 (τ_{C1}) and C2 (τ_{C2}) are with mean values of respectively 1.5 ± 0.2 ms (N = 3) and 15.5 ± 7.5 ms (N = 3) virtually voltage-independent (**Figure 3-3E**). Assuming that each population of closed events represents a discrete closed state that can be reached exclusively from the open state, the conditional probability to find an active channel in closed state Ci is given by

$$P\left(Ci\middle|burst\right)=\frac{N_{Ci}\cdot\tau_{Ci}}{\sum_{j=1}^{2}N_{Cj}\cdot\tau_{Cj}+N_{O}\cdot\tau_{O}} \qquad (3\text{-}1)$$

where N_{Ci} and N_{Cj} are the numbers of closed events, τ_{Ci} and τ_{Cj} the mean lifetimes of the corresponding closed states, and N_O and τ_O the number of open events and the mean lifetime of the open state, respectively. According to **equation (3-1)**, the conditional open probability $P\left(O\middle|burst\right)$ is given by

$$P\left(O\middle|burst\right)=\frac{N_{O}\cdot\tau_{O}}{\sum_{j=1}^{2}N_{Cj}\cdot\tau_{Cj}+N_{O}\cdot\tau_{O}}. \qquad (3\text{-}2)$$

For more details see chapter **3.5.4**.

The calculated conditional open probabilities are shown in **Figure 3-3F**. Even though the conditional occupation probabilities for the closed states C1 and C2 vary by about one order of magnitude throughout the examined voltage range, their sum is quite constant, resulting in a fairly voltage-independent conditional open probability with a mean value of 0.92 ± 0.03 (N = 3).

This strongly suggests that the voltage-dependent change in open probability in **Figure 3-2D** is exclusively caused by ultra-long-lasting closed events at negative membrane voltages. To confirm this conclusion, it was necessary to perform long-term steady-state measurements in order to increase the number of inactivation events. As compromise between statistical demands and experimental feasibility, constant voltages were applied for two hours each. The recorded current traces were subsequently analyzed by dwell-time analysis. The exemplary current traces in **Figure 3-4A** as well as the corresponding closed-time histograms in **Figure**

3-4B,C already reveal an increase in the number of inactivation events with increasing negative voltages. Consequently, this increase in the number of inactivation events is accompanied by a shortening of the bursts of channel activity.

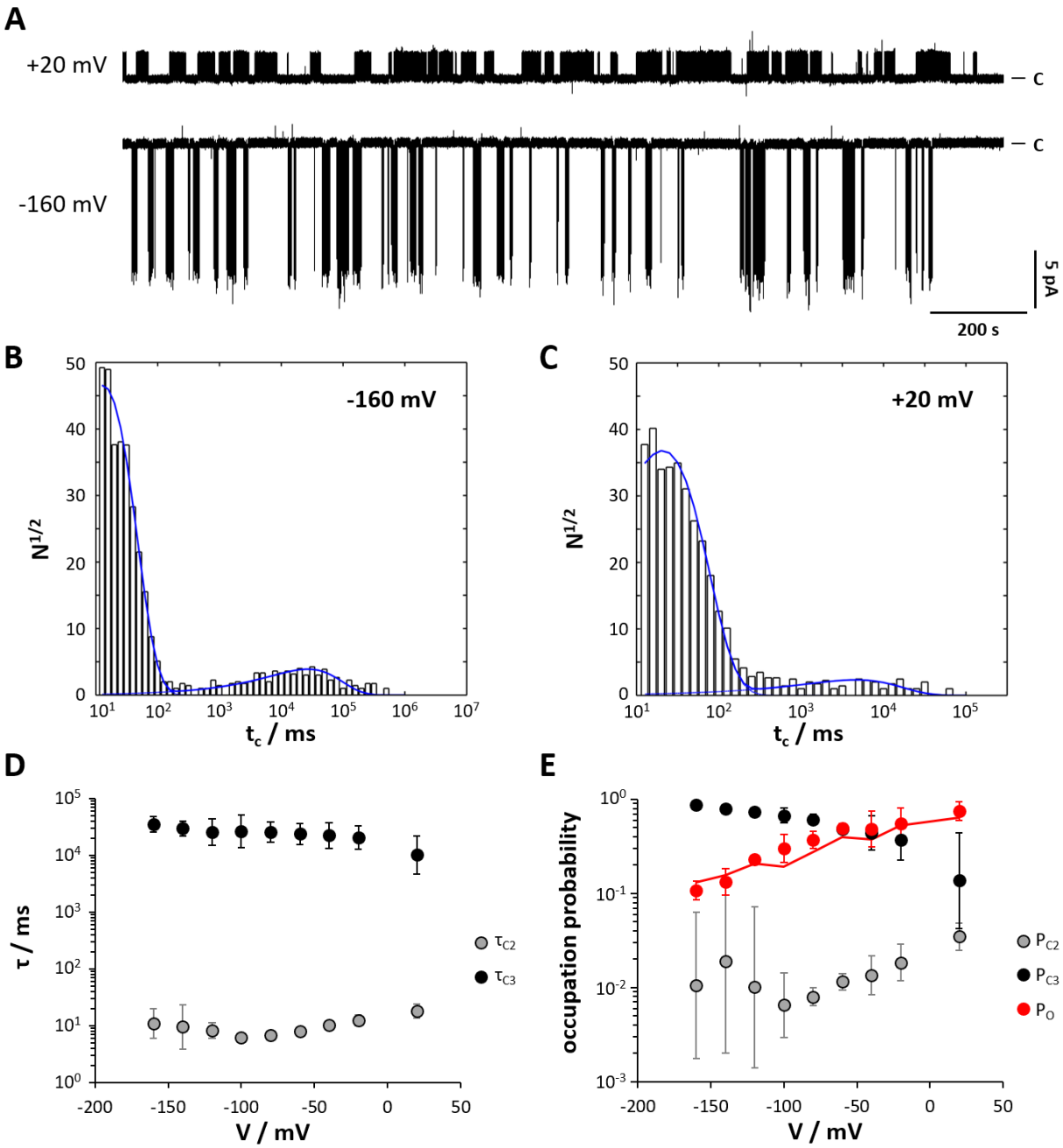

Figure 3-4: The voltage-dependence of P_O can exclusively be attributed to the voltage-dependent occurrence probability of the long-lasting closed (inactivated) state. A 30 minutes section of 2 hours steady-state recordings at +20 mV and -160 mV. The experiments were performed in symmetrical 100 mM KCl. C indicates the baseline (closed state). **B,C** Exemplary closed-time histograms for -160 mV and +20 mV, respectively. The dwell-time histograms were fitted with two exponential functions to obtain the mean lifetimes of the closed states (**D**) and the occupation probabilities (**E**). The red smooth line in **E** shows the open probability as obtained by short-term measurements, the symbols the occupation probability of the open and closed states as calculated by the dwell-time analysis of the long-term measurements. (**Figure 3-2D**). Because of the lower temporal resolution of the long-term measurements is the closed state C1 not resolved or partially merged into C2. Geometric mean and geometric standard deviation of three experiments.

Particularly in the closed-time histograms from current traces recorded at negative voltages (**Figure 3-4B**) one can nicely see, that the population of ultra-long-lasting closed events can be fitted with a single exponential function. Due to the reduced sampling rate, closed events with dwell-times shorter than 10 ms could not be detected in these experiments. Consequently, the first population of closed events (C1), which is present in the dwell-time histograms in **Figure 3-3A,C**, cannot be distinguished from the second population of closed events (C2). As a result, the calculated open probability is slightly overestimated. Nevertheless, because of the small contribution of the first population of closed events to the open probability within a burst of activity (**Figure 3-3E**), it is reasonable to assume that the values of occupation probabilities (**Figure 3-4E**) are very similar to the values one would obtain from measurements with a higher sampling rate. This is supported by the superimposition of the open probability curves obtained by long- and short-term measurements (red circles and red smooth line in **Figure 3-4E**).

Finally, the probability to find the channel in an ultra-long-lasting closed event (P_{C3}) and the open probability P_O obtained from dwell-time analysis show an exactly opposite trend (**Figure 3-4E**). This confirms the conclusion made above that the voltage-dependent change in P_O is exclusively caused by a change in P_{C3}. The dwell-time analysis discloses a second interesting fact: the mean lifetime of the ultra-long-lasting closed events (τ_{C3}) is with an averaged value of 23.1 ± 6.7 s virtually voltage-independent (**Figure 3-4D**). This means that the stability of the inactivated state is not sensitive to the membrane voltage and hence the observed increase in P_{C3} is solely the result of an increase in the inactivation rate.

3.3.3. The transition between the active and inactive state can be described by a simple 2-state reaction scheme

The experiments and analysis described above revealed a voltage-dependent inactivation process and a voltage-insensitive inactive state. Nevertheless, the nature of the inactivation process, or in other words, the kinetic characteristics of the transition from the active to the inactive state remain unclear. To fill this gap, the recorded long-term single-channel recordings are analyzed by burst-analysis. To provide a more detailed description of the voltage-dependent kinetics of the slow inactivation process, a burst analysis based on a kinetic model was performed on the long-term single-channel recordings. A burst of activity includes open as well as short closed events. These closed events exhibit, as shown above, mean lifetimes of about 1.5 ± 0.2 ms (N = 3) for C1 and 15.5 ± 7.5 ms (N = 3) for C2. The mean lifetime of the inactive state is with an averaged value of 23.1 ± 6.7 s (N = 3) three orders of

magnitude longer than the mean lifetime of C2. Therefore, the overlap between the closed-time populations of C2 and C3 (inactive state) is negligible (**Figure 3-4**). In order to analyze the voltage-dependence of the active state, closed events with dwell-times shorter than 1 s were automatically removed from the reconstructed time series provided by a Hinkley detector, effectively merging O, C1 and C2 into the active state A. The new time series, which are obtained in this manner, contain only the events of interest: bursts of activity (A) and interbursts (I) (red in **Figure 3-5A**).

Figure 3-5B-E show exemplary histograms obtained by analyzing the reconstructed time series for -160 mV and -80 mV. Both the burst-time (**Figure 3-5B,D**) as well as the interburst-time histograms (**Figure 3-5C,E**) exhibit only one population of events, that can be fitted with a single exponential function. The simplest model that sufficiently explains single populations of events in the is a two-state reaction scheme:

$$I \underset{k_{AI}}{\overset{k_{IA}}{\rightleftharpoons}} A \tag{3-3}$$

where I and A represent the inactive and active state, respectively. The transitions between both states are characterized by the rate constants k_{IA} and k_{AI}. The probability P, that a channel stays in state I (or A) throughout the time from 0 to t, is given by a simple exponential function (Colquhoun & Hawkes 1983):

$$P(lifetime > t) = e^{-k \cdot t} \tag{3-4}$$

where k is the rate constant. Therefore, the probability, that a channel undergoes a state transition in the time interval from 0 to t, is given by

$$P(lifetime \le t) = 1 - P(lifetime > t) = 1 - e^{-k \cdot t} \ . \tag{3-5}$$

This function is identical to the cumulative distribution of lifetimes. Therefore, the first derivative of **equation (3-5)** represents the probability density function of lifetimes (*pdf*):

$$pdf = k \cdot e^{-k \cdot t} \tag{3-6}$$

The area under this curve in the time interval from 0 to t represents the probability, that the lifetime is equal or less than t. Therefore, the mean life time is given by

$$\tau = \frac{\int_0^\infty t \cdot pdf(t)dt}{\int_0^\infty pdf(t)dt} = \frac{\int_0^\infty t \cdot e^{-k \cdot t}dt}{\int_0^\infty e^{-k \cdot t}dt}$$

Because of $\int_0^\infty pdf(t)dt = 1$, the mean lifetime is equal to

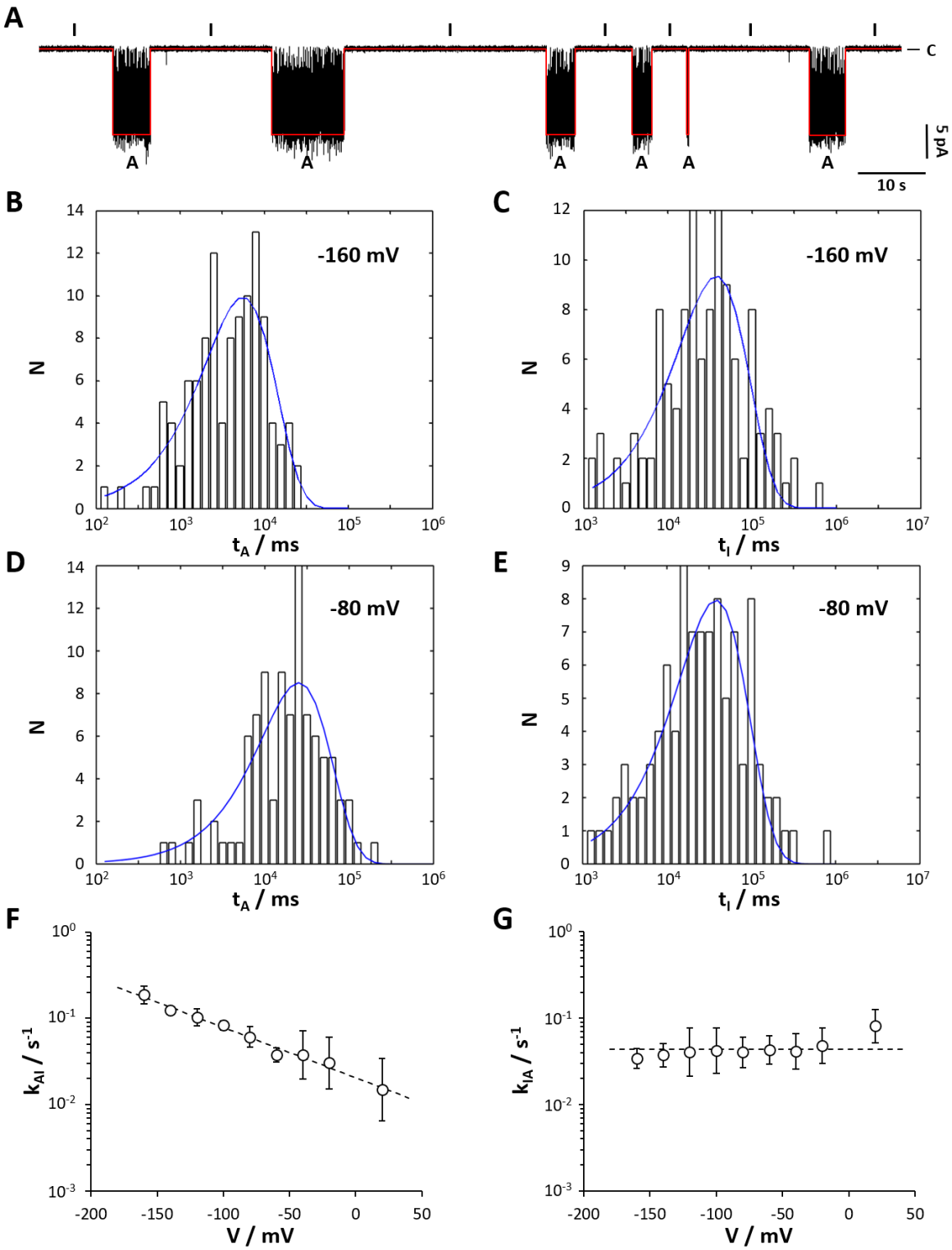

Figure 3-5: Only the transition from the active to the inactive state is voltage-dependent. A Representative section of a 2 hours single channel steady-state measurement at -120 mV and symmetrical 100 mM KCl. The red line gives the reconstructed transitions between the inactive (I) and active state (A) as obtained by a Hinkley detector after removal of closed events with a dwell-time shorter than 1 s. **B,D** Dwell-time histograms for the activated state (bursts of activity) at -160 mV and -80 mV, respectively. **C,E** Dwell-time histograms for the inactive state (interbursts) at -160 mV and -80 mV, respectively. The dwell-time histograms in **B-E** were fitted with one exponential function. **F** Rate constants of the transition from the active to the inactive state for symmetrical 100 mM KCl. **G** Rate constants of the transition from the inactive to the active state. Geometric mean and geometric standard deviation of three experiments.

$$\tau = \int_0^\infty t \cdot e^{-k \cdot t} dt \,.$$

Integration yields

$$\tau = \frac{1}{k} \,. \tag{3-7}$$

Hence, the rate constants k_{AI} and k_{IA} of the transitions in reaction scheme **(3-3)** are given by the inverse mean lifetimes of the burst and interburst events, respectively:

$$k_{AI} = \frac{1}{\tau_A} \tag{3-8}$$

$$k_{IA} = \frac{1}{\tau_I} \tag{3-9}$$

The thus calculated rate constants are shown in **Figure 3-5F,G**. k_{IA}, the transition from the inactive to the active state is voltage-independent, confirming the observations made above. The dashed horizontal line in **Figure 3-5G** represents the mean value of 0.044 s^{-1}. In contrast, the mean lifetime of the active state and thus the rate constant of the transition from the active to the inactive state (k_{AI}) show a distinct voltage-dependence (**Figure 3-5B,D,F**), that can be described in a good approximation with a simple exponential function:

$$k_{AI} = k_{AI}(0) \cdot e^{-\frac{z\delta F}{RT} \cdot V} = k_{AI}(0) \cdot e^{-\frac{V}{V_{AI}}} \tag{3-10}$$

with $k_{AI}(0)$ being the rate constant at 0 mV, z the valence of the ion ($z = +1$ for K^+), δ the fraction of the membrane potential seen when the ion is at the location of energy barrier, F the Faraday constant, R the gas constant, T the absolute temperature, and V_{AI} the characteristic voltage. Fitting of the rate constants from **Figure 3-5F** with **equation (3-10)** yields $k_{AI}(0) = 0.019\ s^{-1}$ and $V_{AI} = 70.5$ mV. The latter corresponds to the movement of one elementary charge through about one third of the entire electric field ($z\delta = 0.36$) (Atkins & dePaula 2014).

In summary, the voltage-dependence of $Kcv_{NH\,S77G}$ is caused by a voltage-dependent inactivation process, that can be described with a simple two-state reaction scheme. The dwell-time and burst analysis revealed that the voltage-dependence of P_O can exclusively be attributed to the transition from the active to the inactive state, whereas the inactive state and therefore the rate constant k_{IA} is virtually voltage-insensitive.

3.3.4. The outward-rectification is triggered by a pair of amino acids in the turret loop

In order to unravel the molecular origin of the outward-rectification of $Kcv_{NH\ S77G}$, mutagenesis experiments were performed. First of all, it was tested if Phe78, the blocking amino acid of the inner gate (Rauh et al. 2017a), is involved in the voltage-dependent inactivation of $Kcv_{NH\ S77G}$. For this reason, Phe78 was substituted with alanine. The experimental data show that the removal of the aromatic side chain in $Kcv_{NH\ S77G}$ has no influence on the outward-rectification: The single-channel current responses of $Kcv_{NH\ S77G}$ F78A still exhibit at negative voltages ultra-long-lasting closed events (**Figure 3-6A**). This causes the same voltage-dependent decrease in the open probability as observed for $Kcv_{NH\ S77G}$ (**Figure 3-6C**). This confirms the above assumption that the inner gate is indeed not responsible for the voltage-dependence. The only mutation-related effect is a small decrease in the open-channel amplitude (**Figure 3-6B**) which results in a smaller single-channel conductance. In the mutant the slope conductance between ±80 mV drops from 109 ± 3 pS (N = 4) to 87 ± 29 pS (N = 4) in symmetrical 100 mM KCl. A similar effect of the F78A mutation on the single-channel conductance could be observed for the orthologs Kcv_{NTS} and Kcv_S (Rauh et al. 2017a). This side-effect will not be further investigated here.

The next step was to examine differences in the amino acid sequences between Kcv_{NH} and other already characterized orthologs. Scrutiny of the multiple sequence alignment shown in **Figure 3-1A** reveals three striking amino acid differences between Kcv_{NH} and the voltage-independent orthologs Kcv_{ATCV-1}, Kcv_{NTS} and Kcv_S at positions 28, 29 and 57. The adjacent positions 28 and 29 are located in the turret loop, which is exposed to the extracellular space. In Kcv_{ATCV-1}, Kcv_{NTS} and Kcv_S these positions are occupied by asparagine and threonine, whereas in Kcv_{NH} these amino acids are replaced by tyrosine and alanine, respectively. Position 57 is located at the very beginning of TM 2 and is occupied by proline in Kcv_{ATCV-1}, Kcv_{NTS} and Kcv_S. However, in Kcv_{NH} this proline is replaced by an alanine. Position 57 seemed to be the most promising candidate for two reasons: First, among the proteinogenic amino acid proline is unique because its side chain is covalently bound to the nitrogen atom of the peptide bond. Consequently, rotation around the N-C^{α} bond is highly restricted and the backbone of proline cannot take part in hydrogen bonding to proton acceptors; this is why proline is referred to as helix-breaking residue (Piela et al. 1987). Second, due to these unique structural features proline is frequently found at the N-terminus of α-helices, where it probably supports their folding (Morgen & Rubenstein 2013) and stability by lowering the conformational entropy (Thompson & Eisenberg 1999). In this context it is worth mentioning

that a second proline at the beginning of the pore helix is conserved throughout the members of the Kcv_{ATCV-1}-family (**Figure 3-1A**).

Surprisingly, the substitution of Ala57 in $Kcv_{NH\ S77G}$ with proline has no effect on the electrophysiological properties at all. The open probability remains voltage-dependent due to ultra-long-lasting closed events at negative voltages (**Figure 3-6A,C**). Also the iV relationship was not affected by the A57P mutation (**Figure 3-6B**).

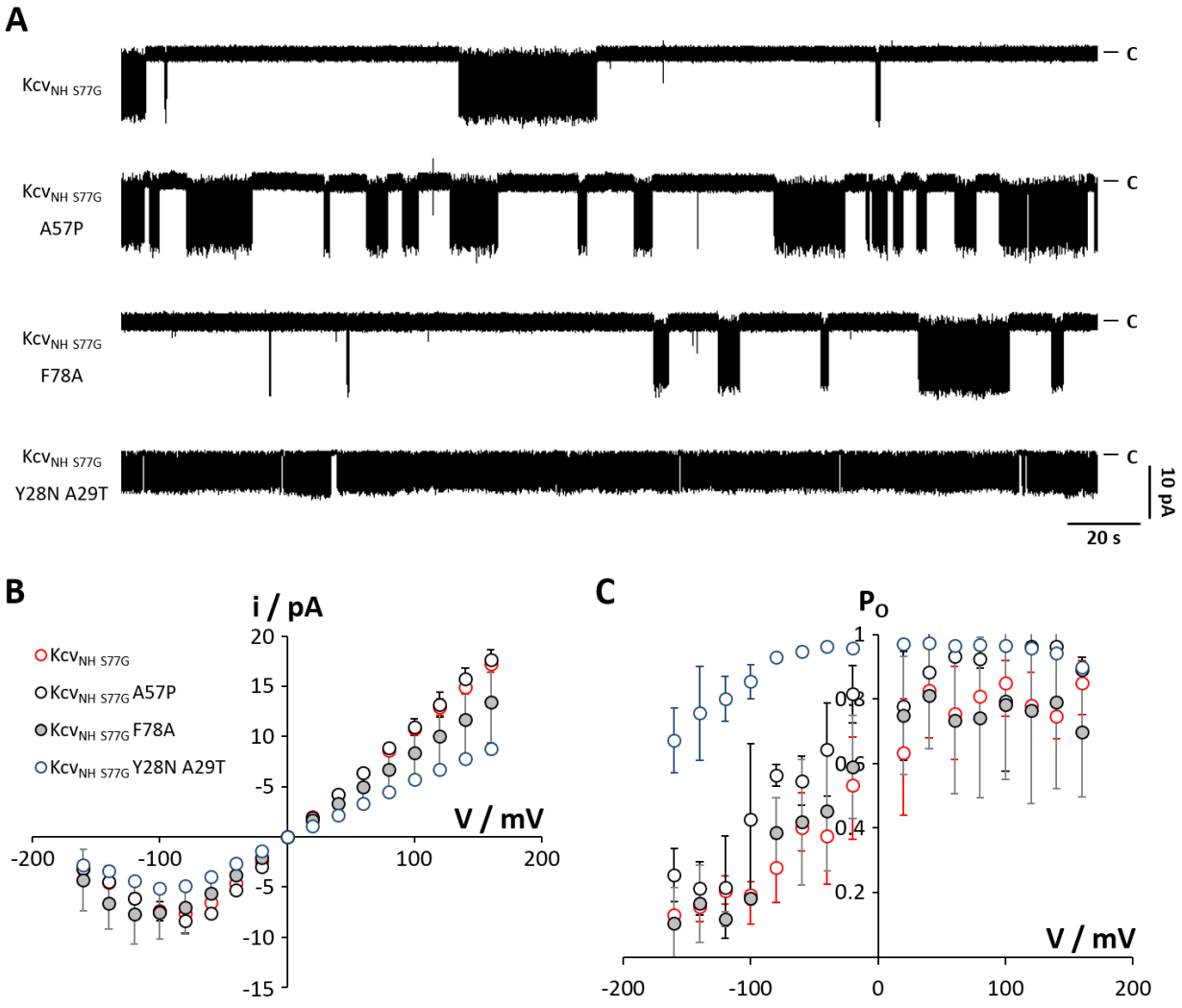

Figure 3-6: The double mutation Y28N A29T causes a loss of the voltage-dependence in $Kcv_{NH\ S77G}$. A Exemplary single-channel recordings of $Kcv_{NH\ S77G}$ and three $Kcv_{NH\ S77G}$ mutants in symmetrical 100 mM KCl at -120 mV. C indicates the baseline (closed state). **B** Apparent single-channel amplitudes of the mutants shown in **A**. **C** Open probabilities calculated from 5- to 30-minutes steady-state measurements. Mean and standard deviation of at least three experiments. Symbols in **C** cross-reference to symbols in **B**.

Next, the amino acids Tyr28 and Ala29 in $Kcv_{NH\ S77G}$ were simultaneously replaced by asparagine and threonine, e.g. the corresponding amino acids in Kcv_{NTS}. This double mutation induces in fact a loss of the voltage-dependent gating and the concomitant disappearance of the ultra-long-lasting closed events in the entire range of examined voltages (**Figure 3-6A,C**).

Additionally, the double mutation induces a remarkable decrease in the open-channel amplitude and hence a reduced single-channel conductance of 59 ± 4 pS (N = 4) between -80 mV and +80 mV in symmetrical 100 mM KCl (**Figure 3-6B**). The origin of this reduction remains elusive and will not be further investigated here. However, it is reasonable to speculate that the decrease in single-channel conductance is caused by an interference of the double amino acid exchange with the influence of other Kcv_{NH}-specific amino acids on the structural and functional properties of $Kcv_{NH\ S77G}$.

In order to confirm that the residues at positions 28 and 29 are causally responsible for the voltage-dependent gating in $Kcv_{NH\ S77G}$, the amino acids Asn28 and Thr29 in the voltage-independent ortholog Kcv_{NTS} were simultaneously replaced by tyrosine and alanine, respectively. The mutant channel was produced *in vitro* and subsequently measured in artificial DPhPC membranes. The experimental data show that Kcv_{NTS} N28Y T29A exhibits in fact the same electrophysiological features as $Kcv_{NH\ S77G}$. In contrast to the wild type channel, which only shows voltage-independent closed events with mean lifetimes in the sub-second range (**Figure 3-7A**), Kcv_{NTS} N29Y T29A exhibits ultra-long-lasting closed events at negative membrane voltages (**Figure 3-7B**). Consequently, the open probability decreases from about 0.86 at +120 mV to about 0.2 at -160 mV. The course of the open probability curves of $Kcv_{NH\ S77G}$ and Kcv_{NTS} N28Y T29A match almost perfectly (**Figure 3-7D**). Interestingly, the double mutation also increases the open-channel amplitude, resulting in an increase of the single-channel conductance between -80 mV and +80 mV in symmetrical 100 mM KCl from 87 ± 2 pS (N = 6) to 101 ± 8 pS (N = 3). This means Kcv_{NTS} N28Y T29A has a similar conductance like $Kcv_{NH\ S77G}$ (109 ± 3 pS, N = 4) (**Figure 3-7C**).

Surprisingly, apart from the voltage-dependent phenotype, a second, voltage-independent phenotype could be observed in Kcv_{NTS} N29Y T29A. This phenotype exhibited a wild type-like high open probability and occurred in 6 (35%) out of 17 independent single-channel measurements. A transition from one phenotype to the other was not observed. That means that the double mutation N28Y T29A is necessary to induce the voltage-dependence in Kcv_{NTS} but is not sufficient in every case. Consequently, it can be concluded that other amino acids in $Kcv_{NH\ S77G}$ participate in the stabilization of the voltage-dependent channel conformation.

To further examine the properties of the mutation-induced outward-rectification in Kcv_{NTS} N28Y T29A, long-term single-channel measurements were performed and subsequently analyzed as in **Figure 3-5**. The burst-time and interburst-time histograms exhibit for all examined membrane voltages only one population of events that can be fitted with a single exponential function (**supplemental material, Figure S 3-1**). Hence, the transition between

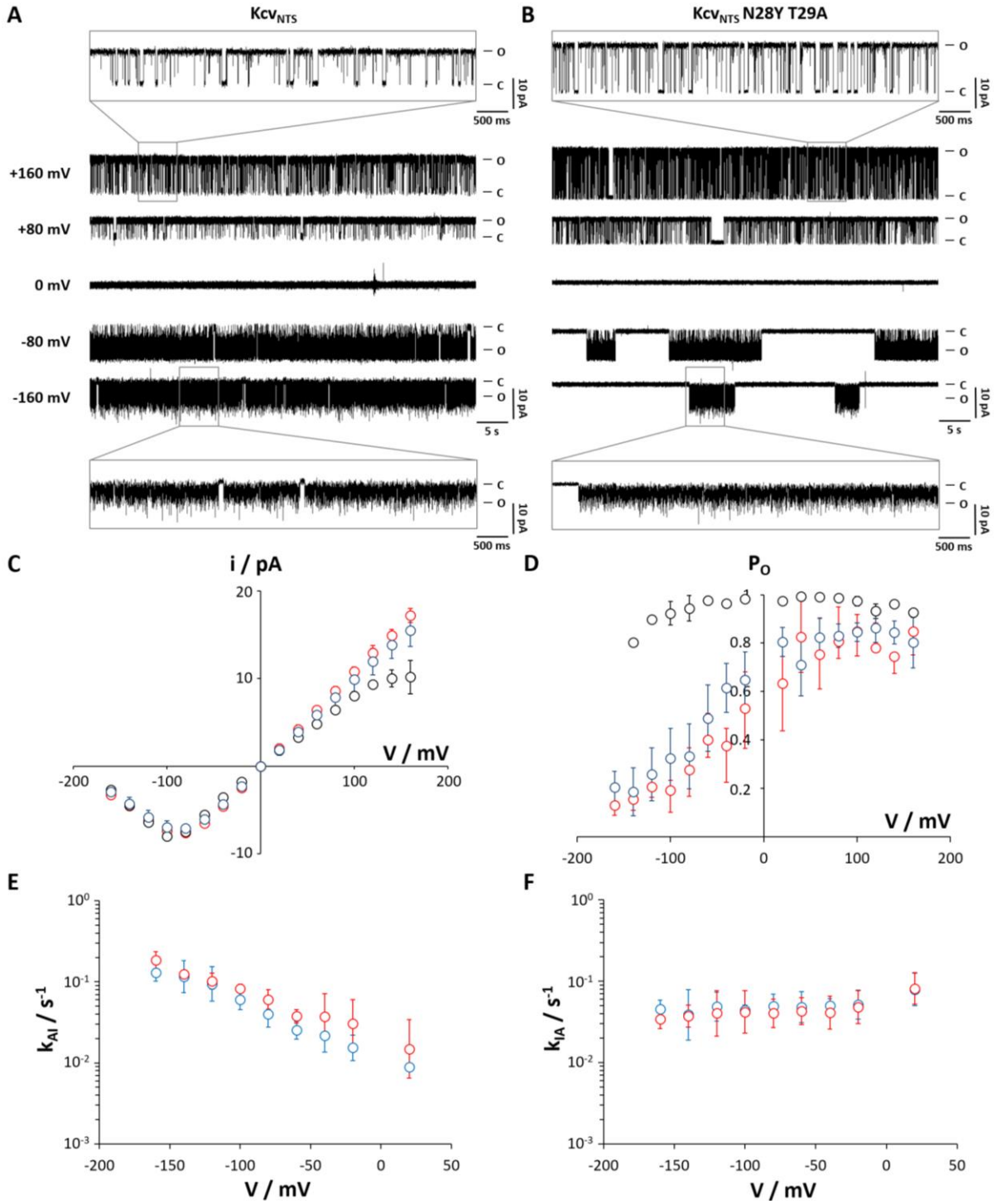

Figure 3-7: The double mutation N28Y T29A converts the voltage-independent, constitutively active channel Kcv$_{NTS}$ into an outward-rectifier. A,B Exemplary single-channel recordings in symmetrical 100 mM KCl of Kcv$_{NTS}$ and Kcv$_{NTS}$ N28Y T29A. The membrane potentials are depicted to the left of the traces in **A**. Traces in gray boxes show the gating behavior on a smaller time-scale. C and O indicate the closed and open state. **C** Apparent single-channel amplitudes of Kcv$_{NH\ S77G}$ (red circles), Kcv$_{NTS}$ (black circles) and Kcv$_{NTS}$ N28Y T29A (blue circles). **D** Open probabilities calculated from 1-minute steady-state measurements for Kcv$_{NTS}$ (N = 3) and 5- to 30-minutes steady-state measurements for Kcv$_{NTS}$ N28Y T29A (N = 5) and Kcv$_{NH\ S77G}$ (N = 4). **E** Comparison between the rate constants of the transition from the active to the inactive state for Kcv$_{NTS}$ N28Y T29A and Kcv$_{NH\ S77G}$ as obtained by burst-analysis. **F** Comparison between the rate constants of the transition from the inactive to the active state as obtained by burst-analysis. Symbols in **D-F** cross-reference to the symbols in **C**. Data points in **E** and **F** represent geometric mean and geometric standard deviation of three experiments.

the active and inactive state can be described with the two-state reaction scheme **(3-3)**. The mean lifetimes of the burst and interburst events were converted into the corresponding rate constants k_{AI} and k_{IA} by means of **equations (3-8)** and **(3-9)**.

The rate constant of the transition from the active to the inactive state (k_{AI}) shows the same voltage-dependence as the equivalent rate constant of $Kcv_{NH\,S77G}$ (**Figure 3-7E**). In addition, the rate constant of the transition from the inactive to the active state (k_{IA}) can be considered as voltage-independent (**Figure 3-7F**). Consequently, it can be noted, that the gating of the mutant channel Kcv_{NTS} N28Y T29A is identical to the gating of $Kcv_{NH\,S77G}$. Hence, the outward-rectification is causally linked to the residues Tyr28 and Ala29.

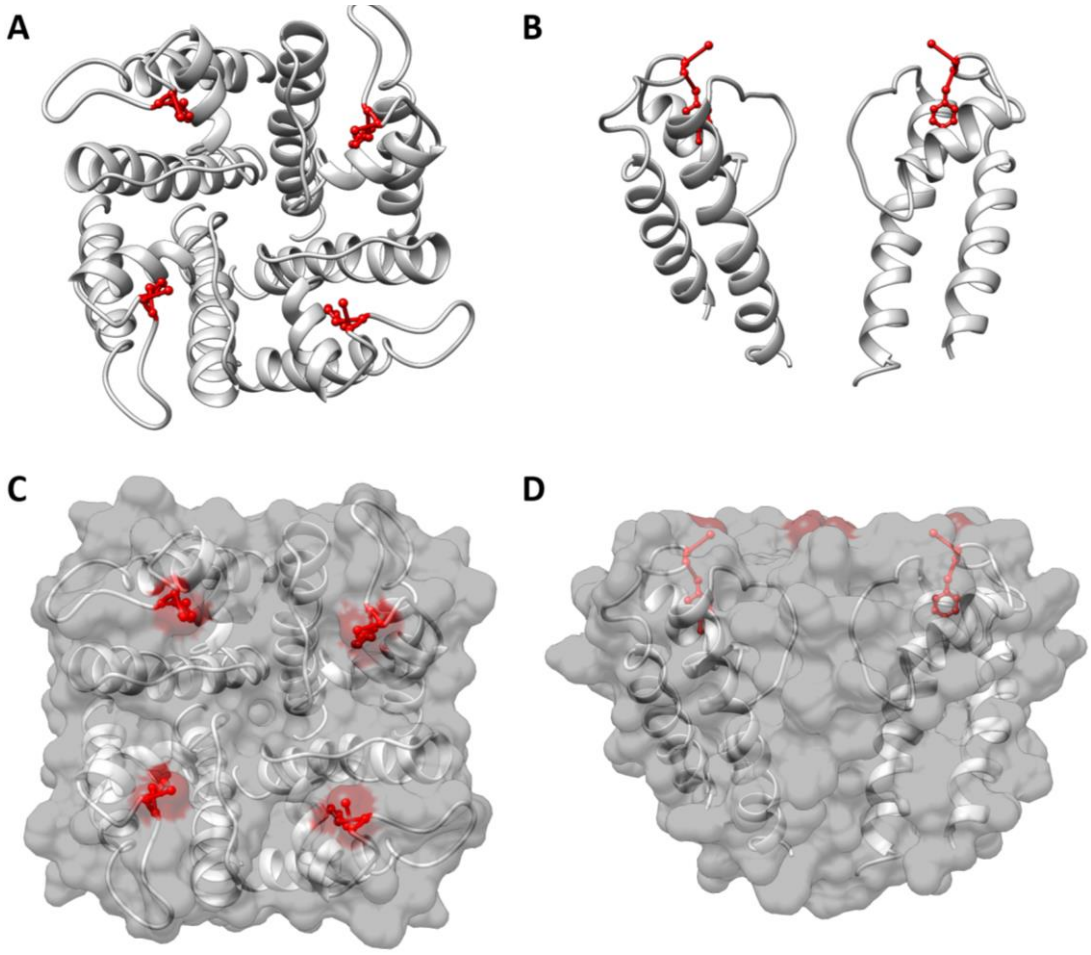

Figure 3-8: The crucial amino acids Y28 and A29 are located at the extracellular protein surface and in the proximity of the entrance to the selectivity filter. A View from the extracellular side of the full tetrameric $Kcv_{NH\ S77G}$ channel. The residues Y28 and A29 are highlighted in red. **B** Side view of two opposing monomer units. **C,D** Surface representation of the structures shown in **A** and **B**. The homology model was calculated with Swissmodel (Arnold et al. 2006) using structural KirBac1.1 data (PDB code 1P7B, Kuo et al. 2003).

The amino acids Tyr28 and Ala29 are located in the turret loop, which connects the transmembrane helix 1 with the pore helix (**Figure 3-8A,B**). Hence, both amino acids are involved in the formation of the outer pore mouth (**Figure 3-8C,D**) and probably in the

shaping of the extracellular entrance to the selectivity filter. It is reasonable to assume that any structural change in the outer pore region can affect the accessibility of the channel pore for potassium. Since the stability of the selectivity filter depends on the occupation of the potassium binding sites within the filter (e.g. Kiss & Korn 1998, Miloshevsky & Jordan 2008, Zhou et al. 2001), reduced accessibility of the channel pore could lead to ion depletion and consequently to a collapse of the permeation pathway. This supports the idea, that the inactivation at negative membrane voltages is directly linked to the permeation of potassium ions through the channel pore. Based on these considerations, one would expect, that a change in the potassium concentration should result in a change of the inactivation and/or activation kinetics.

3.3.5. Elevated potassium concentrations affect the inactivation and activation kinetics

In order to test the effect of elevated potassium concentrations on the voltage-dependent gating of $Kcv_{NH\,S77G}$, single-channel experiments in artificial DPhPC membranes and symmetrical 250 mM KCl were performed. As expected, the increase of the potassium concentration from 100 mM to 250 mM leads to an increase of the open-channel amplitude and thus to an increase of the single-channel conductance between -80 mV and +80 mV from 109 ± 3 pS (N = 4) to 159 ± 8 pS (N = 3) (**Figure 3-9A,B**). However, much more interesting is the finding, that the increase of the potassium concentration causes a dramatic change in the gating of $Kcv_{NH\,S77G}$ by increasing the lifetimes of both burst and interburst events (**Figure 3-9A**). This results in a shift of the open probability curve by about 30 mV towards more negative voltages (**Figure 3-9C**).

To quantify the effect of the elevated potassium concentration on the activation and inactivation kinetics, long-term single-channel measurements were performed and subsequently analyzed by burst analysis as described above. The burst-time and interburst-time histograms still exhibit only one population of events, which can be fitted with a single exponential function (**supplemental material, Figure S 3-2**). Compared to the histograms obtained for symmetrical 100 mM KCl the distributions are clearly shifted to longer dwell-times. Consequently, the rate constants k_{AI} and k_{IA} (**equations (3-8)** and **(3-9)**) are smaller than in 100 mM KCl (**Figure 3-9D,E**). Interestingly, the voltage-dependence of the rate of inactivation, k_{AI}, is not affected by the elevated potassium concentration. It can be described with the same characteristic voltage V_{AI} = 70.5 mV for both 100 mM and 250 mM KCl in a

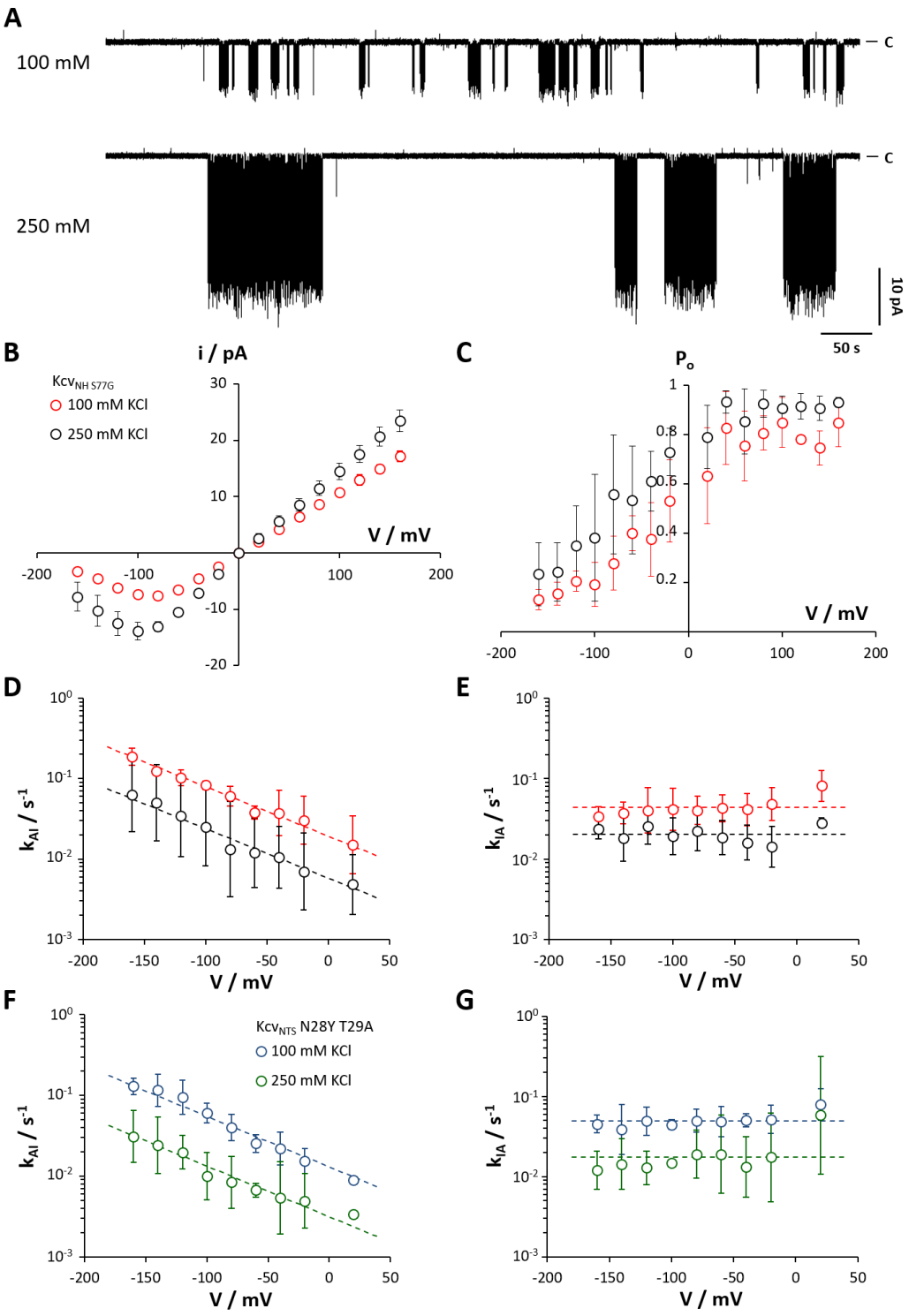

Figure 3-9: The voltage-dependent gating of $Kcv_{NH\ S77G}$ is affected by changing the potassium concentration. A Exemplary single channel recordings in symmetrical 100 mM KCl and 250 mM KCl at -160 mV. C indicates the baseline (closed state). **B** Apparent single-channel amplitudes. **C** Open probabilities calculated from 5- to 30-minutes steady-state measurements. Data points in **B** and **C** represent mean and standard deviation of three and four experiments for symmetrical 100 mM and 250 mM KCl, respectively. **D** Rate constants of the transition from the active to the inactive state. **E** Rate constants of the transition from the inactive to the active state. Symbols in **C-E** cross-reference to symbols in **B**. **F** Rate constants of the transition from the active to the inactive state for Kcv_{NTS} N28Y T29A in symmetrical 100 mM and 250 mM KCl. **G** Rate constants of the transition from the inactive to the active state for Kcv_{NTS} N28Y T29A. Symbols in **G** cross-reference to the symbols in **F**. Data points in **D-G** represent geometric mean and geometric standard deviation of three experiments.

joint fit with **equation (3-10)**. However, the rate constant at 0 mV $k_{AI}(0)$ decreases from 0.019 s^{-1} to 0.006 s^{-1} for 100 mM and 250 mM KCl, respectively. For the rate of activation, even though the mean value of k_{IA} decreases from 0.044 s^{-1} for 100 mM KCl to 0.020 s^{-1} for 250 mM KCl, the voltage-insensitivity remains unchanged.

In order to test whether an increase of the potassium concentration also affects the mutation-induced voltage-dependent gating of Kcv_{NTS} N28Y T29A, experiments as in **Figure 3-9A-E** were repeated with this mutant channel. Indeed, the calculated rate constants k_{AI} and k_{IA} show the same potassium-dependence as for $Kcv_{NH\ S77G}$ (**Figure 3-9F,G**). The joint fit of the k_{AI} values (**Figure 3-9F**) with **equation (3-10)** yields a characteristic voltage V_{AI} of 69.3 mV and a scaling factor $k_{AI}(0)$ of 0.013 s^{-1} and 0.003 s^{-1} for 100 mM KCl and 250 mM KCl, respectively. In addition, the increase of the potassium concentration shifts the mean value of the voltage-insensitive rate constant k_{IA} from 0.050 s^{-1} to 0.018 s^{-1} (**Figure 3-9G**). Hence, these experiments confirm that the double mutant Kcv_{NTS} N28Y T29A responds to a change of the potassium concentration in the same way as $Kcv_{NH\ S77G}$.

In summary, both the inactivation as well as the activation rates slow down as a function of the potassium concentration, supporting the idea that this voltage-dependent gating is directly coupled to the ion permeation through the channel pore.

3.3.6. Multi-channel bilayer experiments can substitute the time-consuming single-channel measurements

The single-channel experiments described above provide direct access to a wide range of parameters such as single-channel amplitudes, open probabilities and mean lifetimes of open and closed states. However, because of the slowness of the gating process of interest, single-channel experiments are not suitable for a comprehensive study of the underlying mechanism. To achieve adequate statistics, the recordings need to be at least two hours long per voltage, i.e. 20 hours long for one single experiment from -160 mV to +20 mV. Furthermore, the membranes often did not stay stable for such long recording times at high voltages.
Thus, to further investigate the effect of different ionic conditions on the voltage-dependence of $Kcv_{NH\ S77G}$ it was necessary to replace the time-consuming single-channel measurements with a more effective method, which gives access to the same kinetic parameters. Fortunately, $Kcv_{ATCV\text{-}1}$-like channels in nanodics, as used here, insert with a strong directional bias into the membrane, namely with the N- and C-termini oriented towards the *cis*-compartment (Winterstein et al. 2018). Actually, not a single case is known so far where a $Kcv_{ATCV\text{-}1}$-like

channel inserted in the opposite direction into an intact artificial lipid bilayer. This opens up the possibility to perform multi-channel measurements in artificial lipid membranes (Winterstein et al. 2018). While these multi-channel measurements reduce the recording time, which is necessary to obtain kinetic parameters and a statistical support, they no longer provide single-channel information.

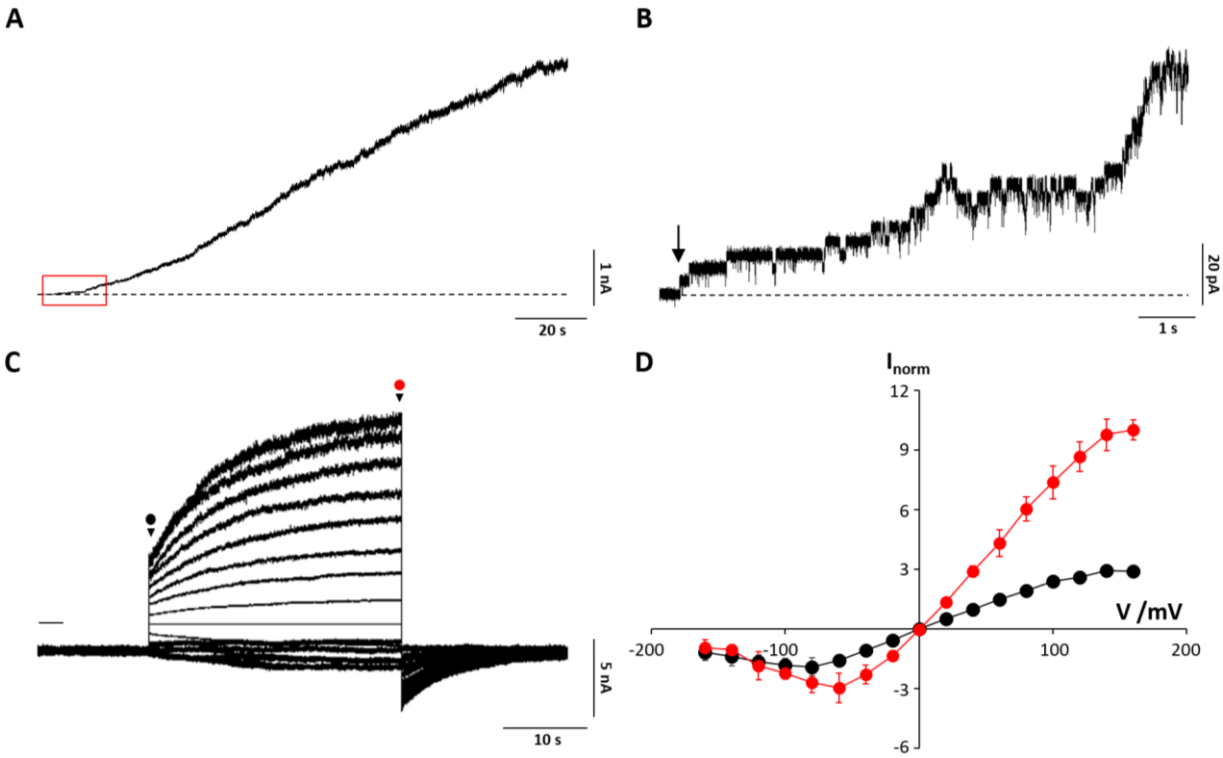

Figure 3-10: The unidirectional insertion of a large number of channels in artificial membranes enables multi-channel recordings. A Exemplary recording of successive insertion of $Kcv_{NH\ S77G}$ channels at +60 mV in symmetrical 100 mM KCl. The section highlighted in red is shown in **B**. The black arrow in **B** highlights the insertion of the first channel. **C** Representative multi-channel current response evoked by 30 s pulses from -160 mV to +160 mV applied in 20 mV steps from the holding potential of -120 mV in symmetrical 100 mM KCl. The zero-current level is indicated by a black bar. **D** Normalized instantaneous (black filled circles) and steady-state (red filled circles) currents. The current values of each measurement were normalized to the corresponding instantaneous current at +40 mV. Mean and standard deviation of three experiments.

For the single-channel recordings above, the purified channel-nanodisc conjugates were diluted to 1:100,000 in 250 mM imidazole. To incorporate a large number of channels into a DPhPC membrane, a small amount (~ 1μL) of a 1:100 or 1:1000 dilution was directly administered to the bilayer in the *trans*-compartment. The successive insertion of $Kcv_{NH\ S77G}$ channels was monitored at a membrane voltage of +60 mV until the current had reached a relatively stable level. **Figure 3-10A** shows exemplarily the rise of the macroscopic current due to the successive insertion of channel proteins at a constant voltage of +60 mV. The increase of the current is accompanied by an increase of the current noise, which is caused by the gain of channel fluctuations. The current noise generated by channel fluctuations is

referred to as excess noise to distinguish it from the background noise (Heinemann & Conti 1992). The causal connection between current and excess noise can be nicely seen in the enlarged section in **Figure 3-10B**: The insertion of each additional channel results in a stepwise increase of the current and a gain of fluctuations due to the independent stochastic opening and closing of the reconstituted channels.

To demonstrate the outward-rectification of $Kcv_{NH\,S77G}$, the membrane voltage was clamped to a holing potential of -120 mV and then stepped to test pulses between -160 mV and +160 mV for 30 seconds in symmetrical 100 mM KCl. The recorded macroscopic currents nicely show an ultra-slow activation for all test pulses more positive than the holding potential as well as slowly inactivating tail currents (**Figure 3-10C**). As illustrated by the normalized IV curves in **Figure 3-10D**, the degree of channel activation increases with increasing positive voltages.

It is worth noting that the normalized macroscopic steady-state IV relation, as obtained from multi-channel current recordings, can be well reproduced by the time-averaged single-channel IV curve (**Figure 3-11D**). The latter were obtained by multiplying the unitary open-channel amplitudes with the corresponding open probabilities. This result underscores the assumption that all channels insert with the same orientation into the membrane.

In the next step, an experimental and analytical procedure had to be developed that provides the same kinetic parameters as the single-channel experiments. The simplest strategy is to measure the time constant of inactivation as well as the fraction of active channels at different test pulses. To get access to these parameters, multi-channel current responses to the pulse protocol shown in **Figure 3-11A** were recorded. In this pulse protocol the holding potentials as well as the post pulse were set to +100 mV to ensure that all channels stay in the active state. **Figure 3-11B** shows an exemplary current response of about 600 $Kcv_{NH\,S77G}$ channels in symmetrical 100 mM KCl. As expected, the hyperpolarizing test pulses elicit an instantaneous current jump followed by a slow inactivation. Consequently, the measured steady-state currents are smaller than the corresponding instantaneous currents for all examined test voltages (**Figure 3-11C**). With more positive membrane voltages the fraction of inactive channels decreases as illustrated by the increasing instantaneous tail current (**Figure 3-11B**).

The reaction scheme **(3-3)** predicts that the activation and inactivation kinetics should follow a simple exponential time course, which can be described by

$$I(t) = I(\infty) - \big(I(\infty) - I(0)\big) \cdot e^{-t/\tau} \qquad (3\text{-}11)$$

with $I(t)$ being the macroscopic current measured at time t after a voltage step, $I(0)$ the instantaneous current at $t = 0$, $I(\infty)$ the steady-state current, and τ the time constant. The time constant τ is given by

$$\tau = \frac{1}{k_{AI} + k_{IA}}. \qquad (3\text{-}12)$$

Figure 3-12 shows examples in which the time course of both inactivation and activation can be adequately described by **equation (3-11)**, supporting the assumption that the voltage-dependent transition between the active and inactive state can be represented by a simple two-state reaction scheme. Fitting of **equation (3-11)** to the currents elicited by the test pulses provides the time constant τ and thus, according to **equation (3-12)**, the sum of the rate constants k_{AI} and k_{IA}.

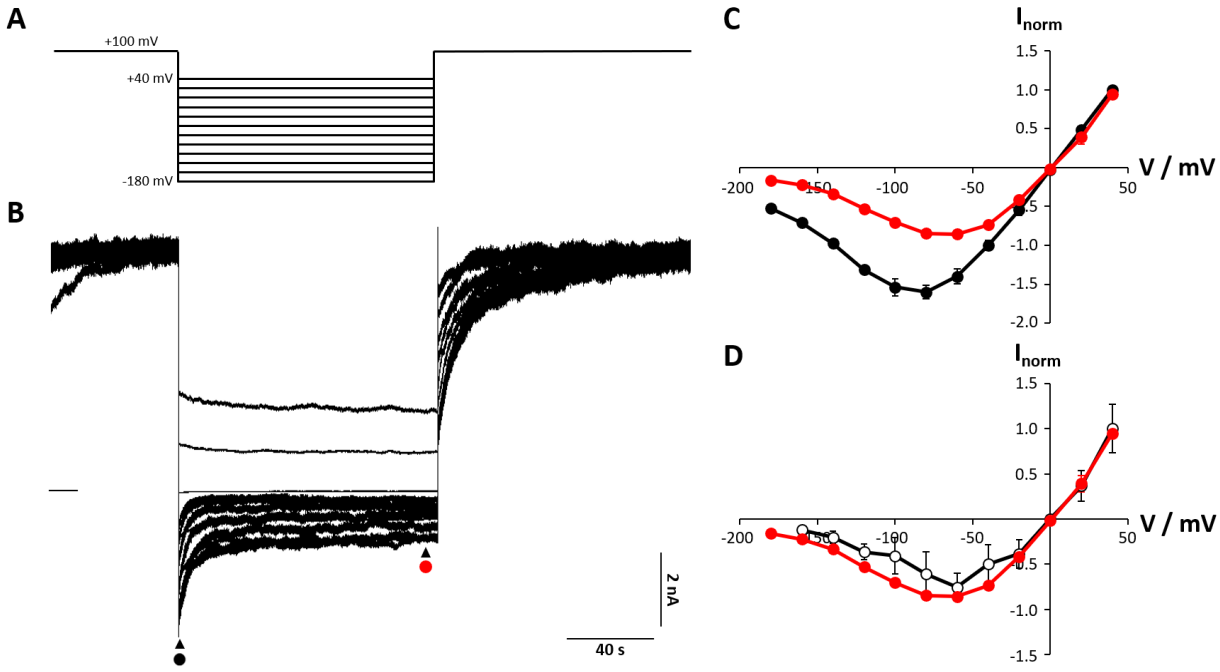

Figure 3-11: Multi-channel bilayer experiments enable access to inactivation kinetics of $Kcv_{NH\ S77G}$. A Voltage pulse protocol used to investigate the voltage-dependence of $Kcv_{NH\ S77G}$. **B** Representative multi-channel current response in symmetrical 100 mM KCl to the voltage pulse protocol shown in **A**. Black and red filled circles indicate the time points at which the instantaneous and steady-state currents were measured. **C** Normalized initial (black filled circles) and steady-state (red filled circles) currents. The current values of each measurement were normalized to the corresponding instantaneous current at +40 mV. **D** Comparison between the normalized multi-channel steady-state current (red filled circles) and the time-averaged single-channel current (open black circles) as calculated by multiplication of the single channel amplitude i and the open probability P_O. The time-averaged single-channel currents were normalized to the value at +40 mV. Data points in **C** and **D** represent mean and standard deviation of three experiments.

The fraction of channels, which is found in the active state at the end of a test pulse, is given by the quotient of the instantaneous and steady-state tail current, as shown below.

The instantaneous tail current I_i is given by

$$I_i = i(V_{PP}) \cdot N \cdot P_{Burst}(V_{TP}) \cdot P\left(O \middle| Burst\right) \tag{3-13}$$

with $i(V_{PP})$ being the open-channel amplitude during the post pulse, N the total number of channels in the membrane, $P_{Burst}(V_{TP})$ the probability to find a channel in a burst of activity at the end of the preceding test pulse, and $P(O|Burst)$ the conditional probability to find a channel open during a burst of activity. Accordingly, the steady-state current I_{ss} is given by

$$I_{ss} = i(V_{PP}) \cdot N \cdot P_{Burst}(V_{PP}) \cdot P\left(O \middle| Burst\right) \tag{3-14}$$

with $P_{Burst}(V_{PP})$ being the probability to find a channel in a burst of activity at the end of the post pulse. Because V_{PP} was set to +100 mV, $P_{Burst}(V_{PP})$ is approximately equal to 1. In addition, the conditional open probability $P(O|Burst)$ can be considered as a voltage-independent constant, as shown above (**Figure 3-3F**). Therefore, the quotient of I_i and I_{ss} gives

$$\frac{I_i}{I_{ss}} = P_{Burst}(V_{TP}) \tag{3-15}$$

Furthermore, reaction scheme **(3-3)** implies the following relation between P_{Burst} and the rate constants k_{AI} and k_{IA}:

$$P_{Burst} = \frac{k_{IA}}{k_{IA} + k_{AI}} \tag{3-16}$$

Combination of **equations (3-12)**, **(3-15)** and **(3-16)** gives the following relations for determining the rate constants k_{AI} and k_{IA}:

$$k_{IA} = \frac{P_{Burst}}{\tau} = \frac{1}{\tau} \cdot \frac{I_i}{I_{ss}} \tag{3-17}$$

$$k_{AI} = \frac{1 - P_{Burst}}{\tau} = \frac{1}{\tau} \cdot \left(1 - \frac{I_i}{I_{ss}}\right) \tag{3-18}$$

Therefore, the rate constants k_{AI} and k_{IA} can be directly calculated from the currents provided from multi-channel experiments in **Figure 3-11**.

In a first series of experiments it was tested whether multi-channel measurements provide the same results as the single-channel experiments with $Kcv_{NH\,S77G}$. For that reason, multi-channel current responses to the pulse protocol shown in **Figure 3-11A** were recorded in symmetrical

100 mM and 250 mM KCl. From the recorded tail currents, the burst probabilities were calculated from equation **(3-15)**. The values are shown in **Figure 3-12B**.

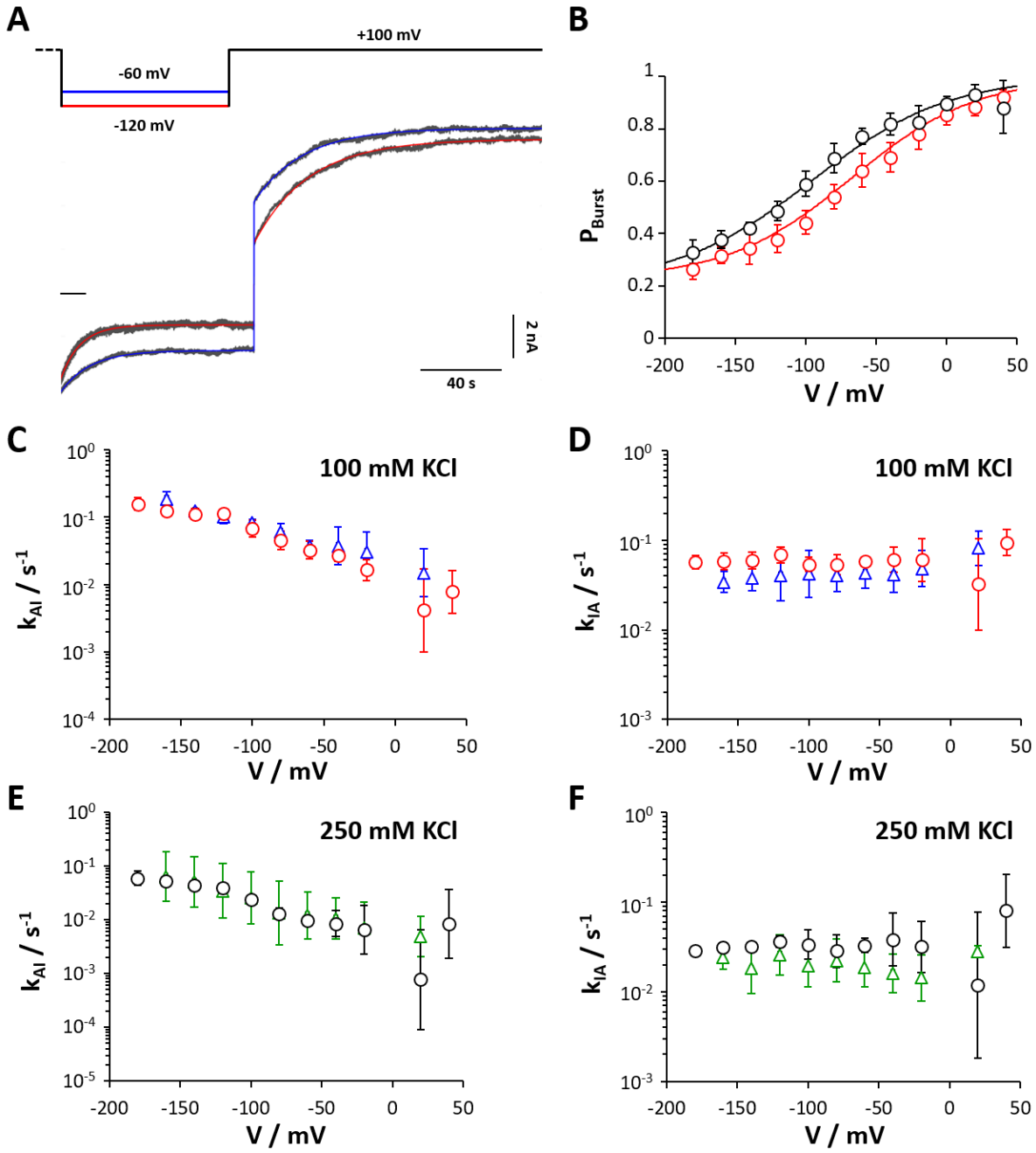

Figure 3-12: The analysis of multi- and single-channel experiments provide the same results. A Exemplary fits of two current responses in symmetrical 100 mM KCl to test-pulses of -120 mV (red line) and -60 mV (blue line) and subsequent post-pulses of +100 mV. The responses to test- and post-pulses were separately fitted with Eqn (3-11). The zero-current level is indicated by a black bar. **B** Burst probabilities for symmetrical 100 mM (red circles) and 250 mM KCl (black circles) as calculated from multi-channel recordings. Red and black lines show the best fits with the Boltzmann-equation (3-19). **C,D** Rate constants for the transition from the active to the inactive state (**C**) and for the transition from the inactive to the active state (**D**) as obtained by single-channel (blue triangles) and multi-channel recordings (red circles) in symmetrical 100 mM KCl. **E,F** Rate constants for the transition from the active to the inactive state (**E**) and for the transition from the inactive to the active state (**F**) as obtained by single-channel (green triangles) and multi-channel recordings (black circles) in symmetrical 250 mM KCl. Data points in **B-F** represent geometric mean and geometric standard deviation of three experiments.

As expected, the burst probability decreases for both conditions with increasing negative voltages in a similar manner as the open probability calculated from single-channel measurements (**Figure 3-9C**). In addition, both the single-channel open probability and the burst probability curves shift to more negative membrane voltages due to an increase in the potassium concentration (**Figure 3-9C, Figure 3-12B**).

In order to quantify the voltage-dependence of P_{Burst} as well as the effect of the elevated potassium concentration, the P_{Burst} curves were fitted separately with the Boltzmann equation

$$P_{Burst} = \frac{1 - P_{Burst,\min}}{1 + e^{\left(z \cdot \frac{F}{RT} \cdot (V_{1/2} - V)\right)}} + P_{Burst,\min} \qquad (3\text{-}19)$$

with $P_{Burst,min}$ being the lower plateau, z the equivalent gating charge, F the Faraday constant, R the gas constant, T the absolute temperature, V the test potential and $V_{1/2}$ the half-activation potential.

The best fit of **equation (3-19)** with the P_{Burst} curve obtained for symmetrical 100 mM KCl was achieved with z = 0.58, $P_{Burst,min}$ = 0.23, and $V_{1/2}$ = -67.3 mV. Increasing the potassium concentration to 250 mM shifted $V_{1/2}$ by almost 30 mV to -95.1 mV, whereas the parameters z and $P_{Burst,min}$ remained with 0.53 and 0.21, respectively, nearly unchanged.

The time constants τ and the calculated P_{Burst} values were subsequently converted into the corresponding rate constants k_{AI} and k_{IA} with **equations (3-17)** and **(3-18)**. As illustrated by **Figure 3-12C-F**, these values are in good agreement with the rate constants from single-channel experiments. The results of the multi-channel experiments confirm that the voltage-dependence of $Kcv_{NH\ S77G}$ originates from the inactivation rate constant k_{AI}, whereas the rate constant for the transition from the inactive to active state k_{IA} is voltage-independent. This is true for both potassium concentrations tested. In addition, an increase of the potassium concentration from symmetrical 100 mM to 250 mM shifts both rate constants to smaller values.

In summary, the multi-channel measurements performed in symmetrical 100 mM and 250 mM KCl satisfyingly reproduce the results which had been obtained by single-channel experiments. In addition, multi-channel experiments reduce the measurement time by a factor of at least 20. On the basis of these results the time-consuming single-channel measurements will be replaced in the following experiments by multi-channel recordings.

3.3.7. Increasing potassium concentrations shift the activation curve to more negative voltages

To examine the effect of potassium over a wider concentration range, the KCl concentration on either side of the artificial bilayer membrane was stepwise increased from 10 mM to 750 mM. At each potassium concentration, a pulse protocol as in **Figure 3-11A** was applied. The resulting multi-channel currents were recorded and subsequently analyzed as in **Figure 3-12**.

The stepwise increase of the potassium concentration on either side of the membrane resulted in a dramatic slowdown of the inactivation time course and furthermore in a decrease of the fraction of inactivating channels at a particular membrane voltage. The slowdown of the inactivation kinetics is illustrated by the normalized current responses in **Figure 3-13A**. The decrease in the fraction of inactivating channels becomes apparent from the increase of the normalized instantaneous tail current in **Figure 3-13B**. This results in a concentration dependent shift of the P_{Burst} curve to more negative membrane voltages (**Figure 3-13C**). In order to quantify the effect of elevated potassium concentrations on the voltage-dependence of the burst probability, the P_{Burst} curves were fitted with the Boltzmann-equation **(3-19)**. **Figure 3-13C** displays the equivalent gating charge z and the half-activation potential $V_{1/2}$ for all examined potassium concentrations. $V_{1/2}$ shifts steadily with increasing potassium concentrations to more negative membrane potentials, whereas z increases barely. This result suggests that an increase of the potassium concentration does not affect the actual mechanism of voltage sensing, but the probability that a channel undergoes an inactivation event. The latter is also reflected in the continuous decrease of the inactivation rate constant k_{AI} with rising potassium concentrations (**Figure 3-13E**). A similar shift is also observed for the rate constant k_{IA}. However, the voltage-insensitivity of k_{IA} remains unaffected. Interestingly, a closer inspection of **Figure 3-13E** reveals that k_{AI} does not exhibit a simple exponential voltage-dependence. With increasing negative membrane voltages, the slope of the k_{AI}/V curve decreases, resulting in a saturation of k_{AI}. This saturation indicates the existence of at least one additional process, that interferes with the transition from the active to the inactive state. This in turn means that k_{AI} does not represent the rate constant of a single transition, but the gross rate constant of at least two coupled processes. The saturation of k_{AI} is also reflected by the lower plateau $P_{Burst,min}$ in equation **(3-19)**. If it were possible to describe k_{AI} with a simple exponential function, the burst probability curves shown in **Figure 3-13C** should reach zero at very negative membrane voltages. Instead, the lower plateau rises with increasing potassium concentrations, indicating the existence of a second KCl-dependent process, that suppresses the voltage-dependent inactivation.

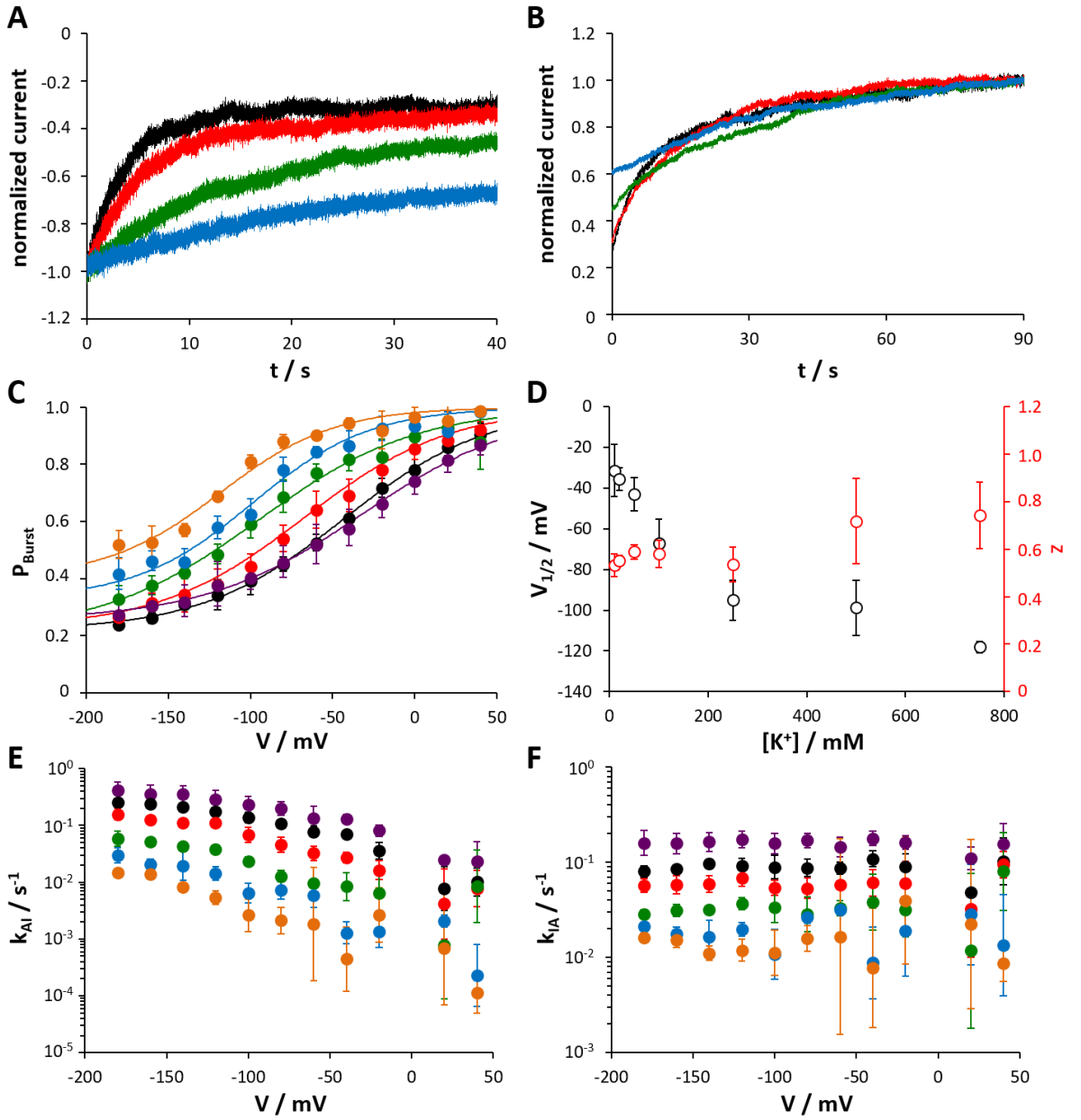

Figure 3-13: Increasing symmetrical potassium concentrations slow down the inactivation and activation kinetics. A Exemplary current responses to a test-pulse of -120 mV in symmetrical 50 mM (black trace), 100 mM (red trace), 250 mM (green trace) and 500 mM KCl (blue trace). For reasons of comparability the instantaneous currents were normalized to a value of -1. **B** Corresponding post-pulses (+100 mV) of the current responses shown in **A**. For reasons of comparability the steady-state currents were normalized to a value of +1. **C** Burst probabilities for symmetrical 10 mM (purple circles), 50 mM (black circles), 100 mM (red circles), 250 mM (green circles), 500 mM (blue circles) and 750 mM KCl (orange circles) as calculated from multi-channel recordings. Smooth lines show the best fit with the Boltzmann-equation (3-19). The obtained values of $V_{1/2}$ and z (mean ± standard deviation) are shown in **D**. **E** Rate constants of the transition from the active to the inactive state for different symmetrical KCl concentrations. **F** Rate constants of the transition from the inactive to the active state for different symmetrical KCl concentrations. Symbols in **E** and **F** cross-reference to the symbols in **C**. Data points in **C-F** represent geometric mean and geometric standard deviation of three experiments.

In summary, the experimental results described here show, that the transition from the active to the inactive state can be suppressed by elevated potassium concentrations, supporting the hypothesis that the inactivation is directly coupled to the flux of potassium ions from the

extracellular (*trans*) to the intracellular space (*cis*). In addition, the shift of the voltage-independent rate constant k_{IA} to smaller values with increasing potassium concentrations suggests that the inactive state is stabilized by potassium ions.

3.3.8. The inactivation is sensitive to the driving force for potassium and the potassium concentration on the extracellular side

The experimental data presented in the preceding section as well as the mutational studies discussed in chapter **3.3.4** support the idea, that the inactivation is linked to the flux of potassium ions from the extracellular to the intracellular space. Nevertheless, the measurements discussed so far were all performed under symmetrical conditions. To decide whether the effects are caused by external or internal potassium ions, multi-channel measurements with asymmetrical potassium concentrations were performed.

Two complementary series of experiments were conducted. In both cases the compartments of the bilayer chamber were initially filled with 10 mM KCl. Subsequently, the concentration in only one of both compartments was increased to 100 mM. In the final step the concentration in the other compartment was also elevated to 100 mM KCl. At each potassium concentration, a pulse protocol as shown in **Figure 3-11A** was applied. The resulting multi-channel currents were recorded and subsequently analyzed as in section **3.3.6**.

In the first series of experiments, the potassium concentration on the extracellular side (*trans* compartment) of the membrane was increased first. The results are shown in **Figure 3-14**. As expected, the increase of the extracellular potassium concentration caused an increase of the potassium influx as well as a shift of the reversal potential E_r from 0 mV to 50.8 ± 3.5 mV (N = 3) (**Figure 3-14B**). The deviation of the measured reversal potential from the theoretical reversal potential ($E_{r,theo}$ = 58.7 mV) remains unclear. Additionally, the shift in the reversal potential is accompanied by a shift of the onset of the negative slope conductance, which is caused by a voltage-dependent fast gating process (Abenavoli et al. 2009, Rauh et al. 2017b), to more positive membrane potentials. This result is in line with the hypothesis, that this so-called flicker-gating originates from the selectivity filter (Rauh et al. 2017b). The final increase of the intracellular potassium concentration to 100 mM causes, as expected, a back shift of the reversal potential to 0 mV.

Furthermore, increasing the extracellular potassium concentration causes a slowdown of the inactivation time course as illustrated by the exemplary current responses recorded at a test pulse of -120 mV (**Figure 3-14A**). However, this slowdown of the inactivation has no effect

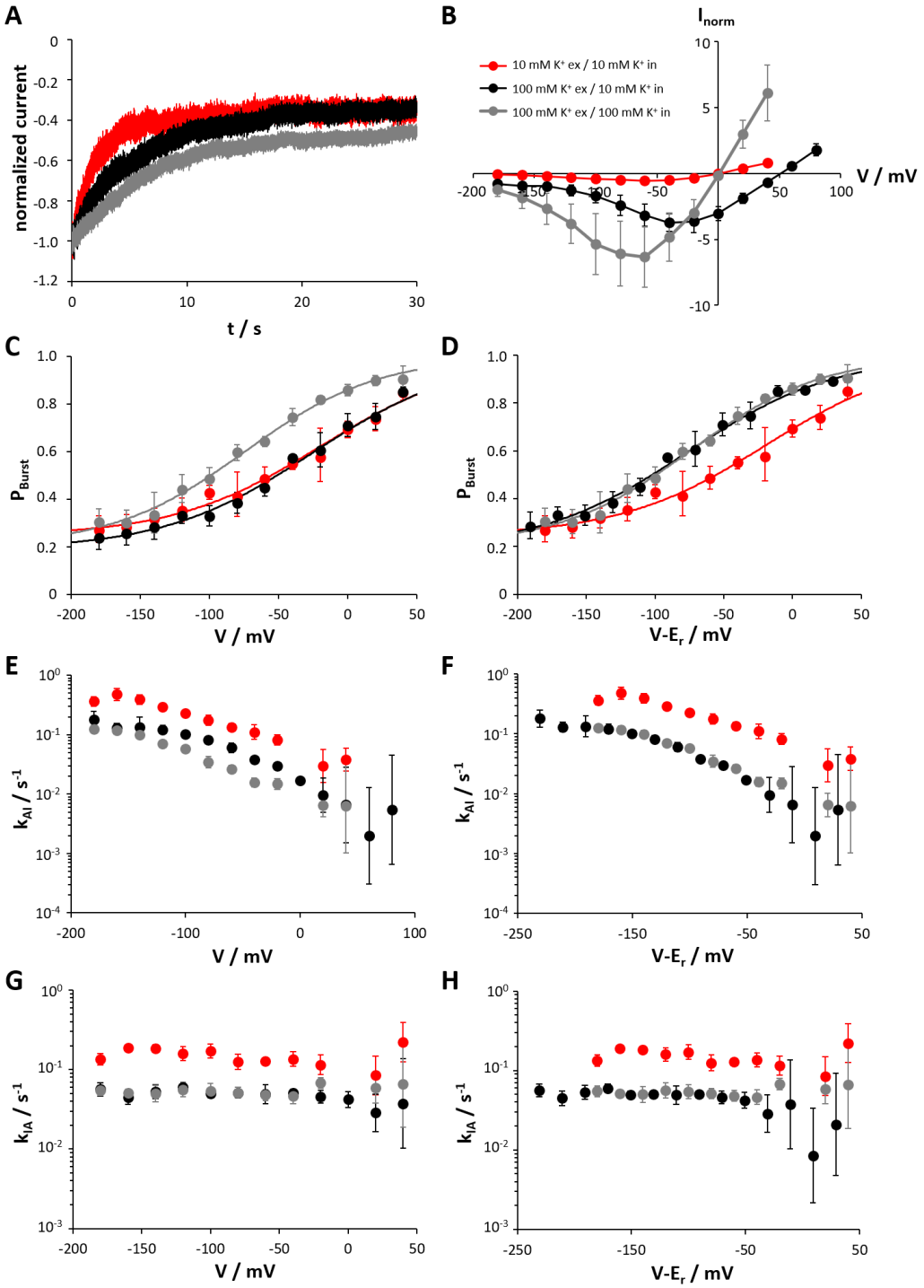

Figure 3-14: The voltage-dependence of $Kcv_{NH\ S77G}$ is affected by the extracellular potassium concentration and the K^+ driving force. A Exemplary current responses to a test-pulse of -120 mV for 10 mM KCl extracellular / 10 mM KCl intracellular (red trace), 100 mM KCl extracellular / 10 mM KCl intracellular (black trace) and 100 mM KCl extracellular / 100 mM KCl intracellular (gray trace). For reasons of comparability the instantaneous currents were normalized to a value of -1. **B** Normalized steady-state currents. The current values of each experiment were normalized to the instantaneous current measured in symmetrical 10 mM KCl at +40 mV. Mean and standard deviation of three experiments. **C** Burst probabilities as calculated from multi-channel recordings. Smooth lines show the best fit with the Boltzmann-equation (3-19). **D** Dependence of burst probabilities on the driving force for K^+. **E** Rate constants k_{AI} of the transition from the active to the inactive state. **F** Dependence of k_{AI} on the driving force for K^+. **G** Rate constants k_{IA} of the transition from the inactive to the active state. **H** Dependence of k_{IA} on the driving force for K^+. Symbols in **C-H** cross-reference to the symbols in **B**. Data points in **C-H** represent geometric mean and geometric standard deviation of three experiments.

on the P_{Burst} curve (**Figure 3-14C**). Only the increase of the potassium concentration on the intracellular side of the membrane causes a shift of the half-activation potential $V_{1/2}$ from -25.7 ± 6.3 mV (N = 3) to -74.1 ± 3.3 mV (N = 3) as determined by fitting the Boltzmann-**equation (3-19)** to the measured P_{Burst} curves. Although the increase of the extracellular potassium concentration does not affect the burst probability, a change in the rate constants k_{AI} and k_{IA} can be observed. The voltage-insensitive rate constant k_{IA} shifts to the same values that can be measured in symmetrical 100 mM KCl (**Figure 3-14G**). Accordingly, the increase of the extracellular potassium concentration from 10 mM to 100 mM has the same effect as the simultaneous increase of the potassium concentration on either side of the membrane.

The one-sided increase of the extracellular potassium concentration also strongly shifts the voltage-dependent rate constant k_{AI} to smaller values. However, compared to the k_{AI} curve obtained for symmetrical 100 mM KCl, this shift seems to be incomplete (**Figure 3-14E**). Consequently, the increase of the extracellular potassium concentration has two apparently contradictory consequences: a shift of the rate constants k_{AI} and k_{IA} to lower values and an almost unchanged P_{burst}/V relationship. This apparent contradiction can be resolved by plotting the P_{burst}, k_{AI} and k_{IA} values as a function of the driving force (V-E_r) for potassium. As shown in **Figure 3-14D,F,H**, this results in a perfect superimposition of the P_{burst}, k_{AI} and k_{IA} curves, which were obtained under asymmetrical conditions (100 mM KCl ex/10 mM KCl in), with the corresponding curves, which were determined in symmetrical 100 mM KCl. Hence, both the inactivation as well as the activation rate constant are directly sensitive to the external potassium concentration. However, the inactivation constant k_{AI} is also dependent on the driving force for potassium.

In order to confirm these results, a second series of experiments was carried out, in which the potassium concentration on the intracellular side of the membrane was increased to 100 mM first. The results are shown in **Figure 3-15**. As expected, the increase of the intracellular potassium concentration results an increase of the potassium efflux and a shift of the reversal potential from 0 mV to -49.0 ± 3.9 mV (N = 3) (**Figure 3-15B**). Also in this case, the measured reversal potential deviates by almost 10 mV from the theoretical reversal potential ($E_{r,theo}$ = -58.7 mV, calculated using the activities of KCl in water). The origin of this deviation remains unclear.

As illustrated by the exemplary current responses recorded at a test pulse of -120 mV (**Figure 3-15A**), increasing the intracellular potassium concentration affects the inactivation time course only slightly. On the other hand, the half-activation potential of the P_{Burst} curve shifts from -24.2 ± 1.6 mV (N = 3) to -69.1 ± 1.2 mV (N = 3) (**Figure 3-15C**). However, plotting

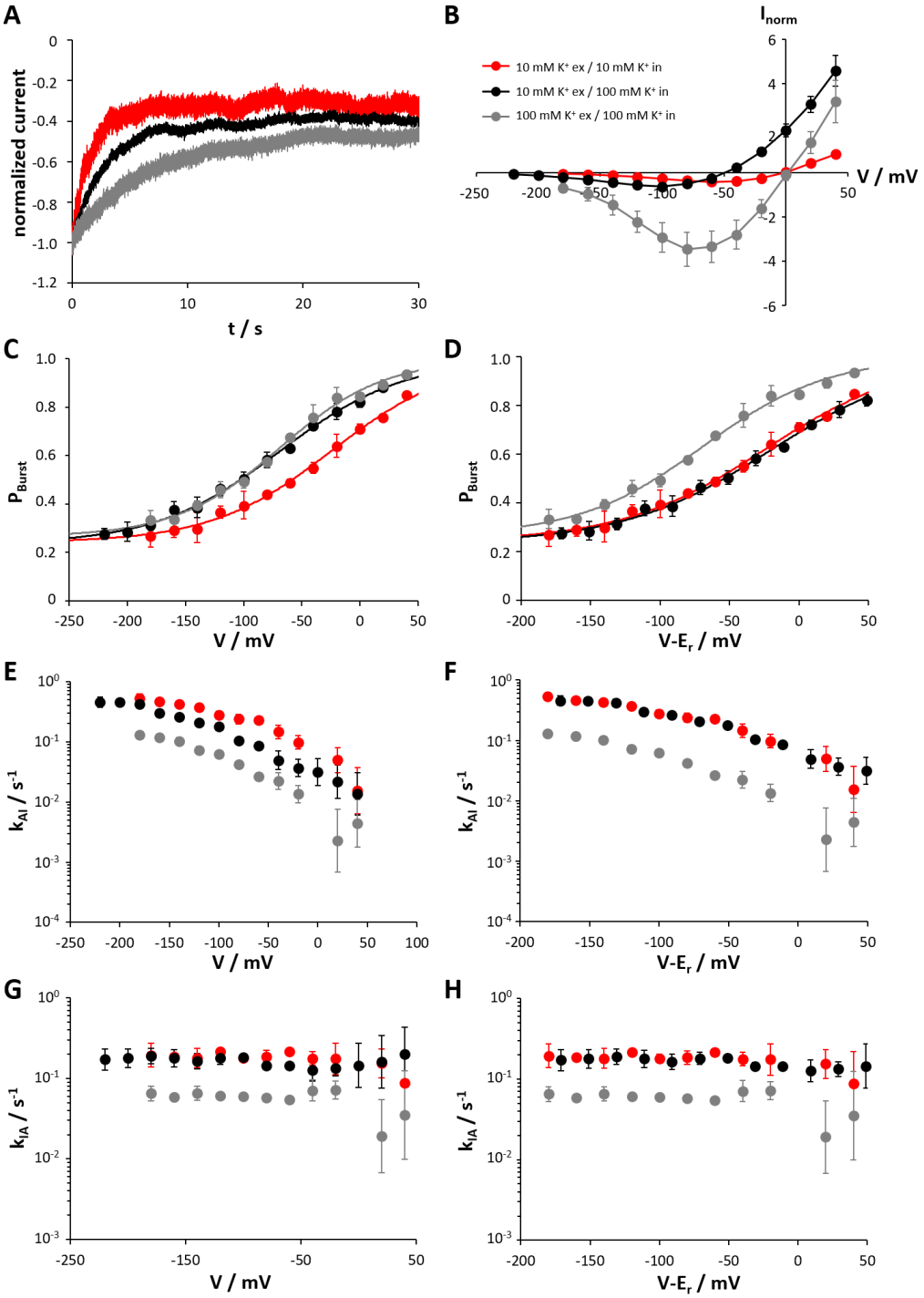

Figure 3-15: The rate constants k_{IA} and k_{AI} are not sensitive to the intracellular KCl concentration. A Exemplary current responses to a test-pulse of -120 mV for 10 mM KCl extracellular / 10 mM KCl intracellular (red trace), 10 mM KCl extracellular / 100 mM KCl intracellular (black trace) and 100 mM KCl extracellular / 100 mM KCl intracellular (gray trace). For reasons of comparability the instantaneous currents were normalized to a value of -1. **B** Normalized steady-state currents. The current values of each experiment were normalized to the instantaneous current measured in symmetrical 10 mM KCl at +40 mV. Mean and standard deviation of three experiments. **C** Burst probabilities as calculated from multi-channel recordings. Smooth lines show the best fit with the Boltzmann-equation (3-19). **D** Dependence of burst probabilities on the driving force for K^+. **E** Rate constants k_{AI} of the transition from the active to the inactive state. **F** Dependence of k_{AI} on the driving force for K^+. **G** Rate constants k_{IA} of the transition from the inactive to the active state. **H** Dependence of k_{IA} on the driving force for K^+. Symbols in **C-H** cross-reference to the symbols in **B**. Data points in **C-H** represent geometric mean and geometric standard deviation of three experiments.

of P_{Burst} against the driving force for potassium reveals that the shift in $V_{1/2}$ is solely caused by the shift of the reversal potential (**Figure 3-15D**), rather than by a direct sensing of the intracellular potassium concentration. This is consistent with the result, that an increase of the intracellular potassium concentration has no effect on the $k_{AI}/(V\text{-}E_r)$ and $k_{IA}/(V\text{-}E_r)$ relationships. Only the subsequent increase of the extracellular potassium concentration to 100 mM causes a decrease of k_{AI} and k_{IA} (**Figure 3-15F,H**), resulting in a shift of the P_{Burst} curve to $V_{1/2}$ = -69.0 ± 2.2 mV (N = 3) (**Figure 3-15D**).

In summary, both series of experiments provide the same picture: the voltage-sensitive inactivation as well as the voltage-insensitive activation depend directly on the extracellular potassium concentration. In addition, the inactivation is sensitive to the driving force for potassium and thus to the flux of potassium ions through the channel pore. These results support the idea, that the inactivation is linked to potassium binding in the outer entry pathway, which is involved in the ion permeation. Furthermore, the inactive state is stabilized by increased potassium concentrations, suggesting the existence of an extracellular binding site. The occupation of this putative binding site seems to prevent the transition from the inactive to the active state. In addition, the observation that the activation rate constant k_{IA} is voltage-independent at all tested potassium concentrations indicates that this binding site is located outside the electric field.

3.3.9. The effect of sodium on the voltage-dependence of $Kcv_{NH\ S77G}$

The experiments discussed so far have been performed exclusively with KCl. To test whether the changes in the activation and inactivation kinetics are indeed linked to the permeable cation, additional experiments with NaCl were performed. It is known that Kcv channels exhibit a negligibly small permeability for sodium (Greiner 2011). Experiments were performed as in **Figure 3-14**: both compartments of the bilayer chamber were initially filled with 10 mM KCl. Subsequently, the cation concentration on the extracellular side were increased to 100 mM by adding 90 mM NaCl. If sodium ions have the same effect on the inactivation and activation kinetics of $Kcv_{NH\ S77G}$ as potassium, the addition of 90 mM NaCl to the extracellular compartment should lead to a shift in the $P_{burst}/(V\text{-}E_r)$ curve to more negative membrane voltages. On the other hand, if the inactivation and activation process is highly selective for potassium, the addition of NaCl should have no effect on the P_{Burst} curve at all.

Figure 3-16A,B show exemplary multi-channel current responses to a pulse protocol as in **Figure 3-11A** before and after addition of 90 mM NaCl to the extracellular compartment. These recordings reveal that the addition of NaCl caused a reduction of both the

instantaneous and steady-state current. As illustrated by the steady-state IV curves shown in **Figure 3-16C**, the sodium mediated current reduction was voltage-dependent and increased with increasing negative voltages.

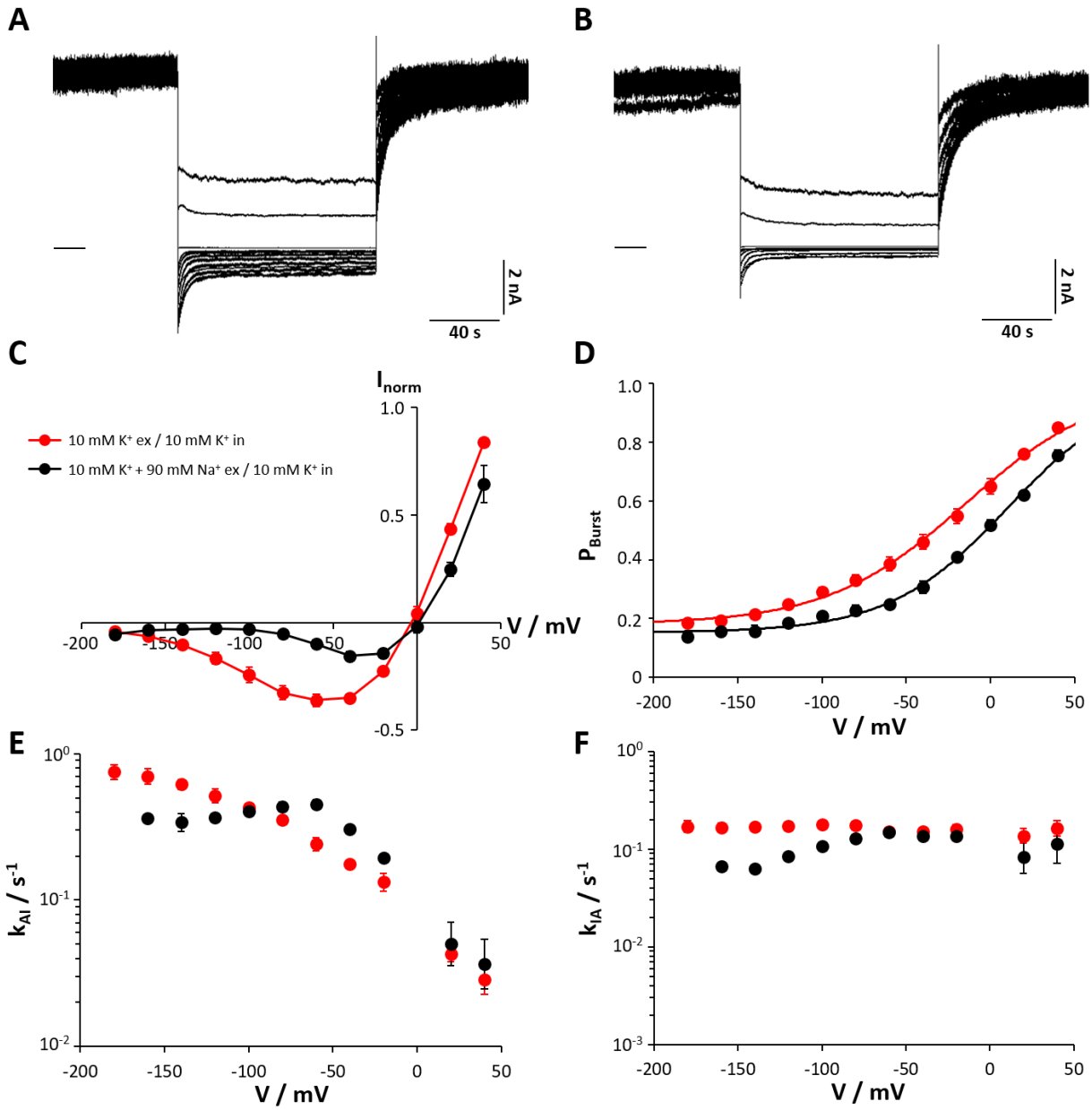

Figure 3-16: Extracellular Na^+ affects the voltage-dependence of $Kcv_{NH\ S77G}$ in a different and more complex manner as compared to K^+. A,B Exemplary multi-channel current responses for 10 mM KCl extracellular / 10 mM KCl intracellular (**A**) and 10 mM KCl + 90 mM NaCl extracellular / 10 mM KCl intracellular (**B**) to a voltage pulse protocol as in **Figure 3-11A**. **C** Normalized steady-state currents. The current values of each experiment were normalized to the instantaneous current measured in symmetrical 10 mM KCl at +40 mV. Mean and standard deviation of three experiments. **D** Burst probabilities as calculated from multi-channel recordings. Smooth lines show the best fit with the Boltzmann-equation (3-19). **E** Rate constants k_{AI} of the transition from the active to the inactive state. **F** Rate constants k_{IA} of the transition from the inactive to the active state. Symbols in **D-F** cross-reference to the symbols in **C**. Data points in **D-F** represent geometric mean and geometric standard deviation of three experiments.

As known from single-channel measurements, this voltage-dependent current reduction was due to a fast Na^+ block (data not shown). As expected, the addition of NaCl to the extracellular compartment did not cause a significant shift in the reversal potential (**Figure 3-16C**), but it does lead to a shift in the P_{burst} curve (**Figure 3-16D**). Important to note is that NaCl did not shift the P_{burst} curve to negative, but to positive membrane voltages. Fitting the P_{Burst} curves with the Boltzmann-equation **(3-19)** uncovers a shift in the half-activation potential of about 25 mV from $V_{1/2}$ = -14.6 ± 5.7 mV (N = 3) to $V_{1/2}$ = 10.3 ± 1.7 mV (N = 3).

The positive shift is caused by a complex effect of sodium ions on the rate constants k_{AI} and k_{IA} (**Figure 3-16E,F**). At positive and moderate negative membrane voltages (V ≥ -60 mV), external sodium shifts the inactivation rate constant k_{AI} to higher values. This means that an inactivation event becomes more likely (**Figure 3-16E**). However, for membrane voltages < -60 mV k_{AI} decreases, resulting in an intersection with the k_{AI} curve in symmetrical 10 mM KCl at around -100 mV. Thus, sodium shows a voltage-dependent effect on the inactivation of $Kcv_{NH\ S77G}$: at positive and moderate negative membrane voltages the addition of sodium has the same effect as a decrease of the potassium concentration. At higher negative membrane potentials, the effect of NaCl seems to be similar to the effect of additional KCl. A comparable voltage-dependent effect of NaCl can be observed for the activation rate constant k_{IA} (**Figure 3-16F**). At positive and moderate negative membrane voltages (V ≥ -60 mV), the addition of 90 mM NaCl has no significant influence on k_{IA}. However, at more negative membrane voltages, NaCl causes a decrease of k_{IA}. This effect is again similar to the effect of additional KCl. It is striking that the transition from one mode to the other occurs for both rate constants at voltages above -60 mV. This may reflect the transition from a conventional voltage-dependent Na^+ block to a punch through mechanism. A similar mechanism has been proposed for the block of potassium permeation in the bacterial potassium channel KcsA by internal Na^+ (Nimigean & Miller 2002). A Na^+ punch through in $Kcv_{NH\ S77G}$ is supported by the fact, that the steady-state current recorded in the presence of 90 mM external NaCl rises again for negative membrane voltages above -120 mV (**Figure 3-16C**).

In addition, the qualitatively different effects of sodium ions on the rate constants k_{AI} and k_{IA} at voltages ≥ -60 mV give rise to the conclusion, that the K^+ binding site involved in the inactivation process does not coincide with the binding site responsible for the stabilization of the inactive conformation. Since external Na^+ increases the inactivation rate k_{AI} at membrane voltages ≥ -60 mV, Na^+ can apparently compete with K^+ for a non-selective binding site in the outer pore entrance, but not enter into the selectivity filter.

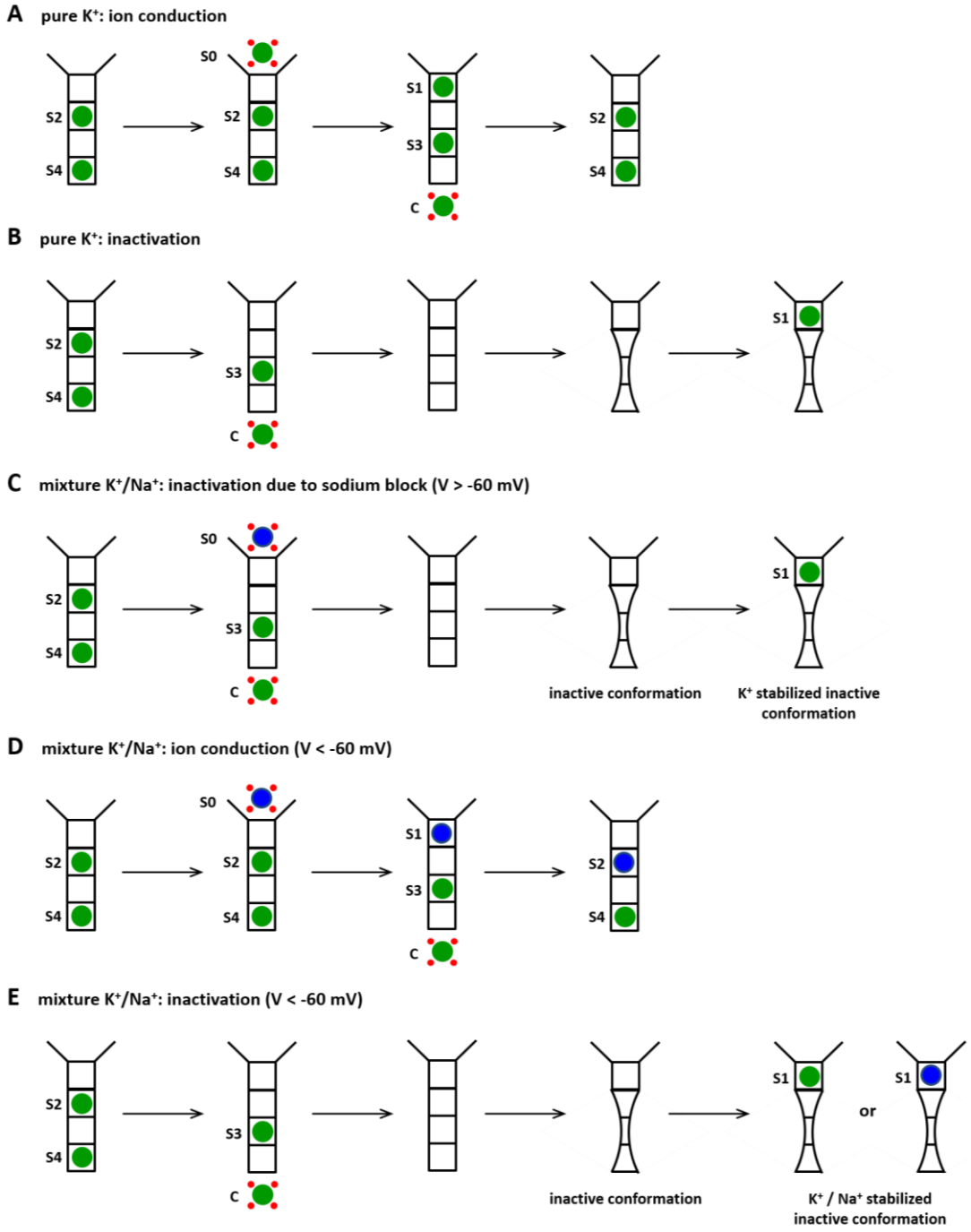

Figure 3-17: Schematic illustration of the effects of Na^+ on ion conduction and channel inactivation in $Kcv_{NH\ S77G}$. The cartoon shows locations of supposed K^+- and Na^+-binding sites in the selectivity filter. Potassium ions, sodium ions and water molecules are indicated as green, blue and red circles, respectively. The binding sites inside the selectivity filter are labeled with S0-S4, the binding site inside the cavity with C. **A** The inward current is generated by a single-file movement of potassium ions towards the intracellular space. The ion binding sites inside the selectivity filter are alternately occupied with water molecules (not shown) and potassium ions. **B** The inactivation of the channel pore is caused by ion depletion of the selectivity filter. The inactive conformation can be stabilized by binding of K^+ at the S1 site. **C** At voltages > -60 mV Na^+ cannot overcome the energy barrier between the S0 and the S1 binding sites due to its higher hydration energy. Therefore, binding of sodium at the S0 site prevents potassium to enter into the selectivity filter, resulting in an inactivation of the channel pore. The inactive conformation can only be stabilized by K^+. **D** At voltages < -60 mV Na^+ can overcome the energy barrier between the S0 and S1 site and thus prevent the channel pore of being inactivated. **E** At voltages < -60 mV K^+ and Na^+ can stabilize the inactive state by binding at the S1 site.

Therefore, the occupation of this putative non-selective binding site by Na^+ seems to increase the inactivation rate by preventing K^+ to enter into the selectivity filter. In the same voltage range the activation rate constant k_{IA} is not influenced by external Na^+, which suggests that the binding site involved in the stabilization of the inactive state is K^+-selective or separated from the extracellular space by an energy barrier which is substantially higher for Na^+ than for K^+. This energy barrier might represent the stripping of the hydration shell when the ion enters from the extracellular space into the selectivity filter. The selectivity filter is lined by carbonyl oxygens of the peptide backbone, which are oriented towards the center of the pore (Doyle et al. 1998). Due to this orientation the carbonyl oxygens coordinate conducted ions by replacing the water molecules of their hydration shell. Computational studies suggest that sodium ions are less stable in the extracellular half of the selectivity filter than potassium ions, reflecting the higher hydration energy of the smaller sodium ion (Biggin et al. 2001). Hence the external entrance to the selectivity filter poses a potential energy barrier for sodium ions that is not seen by potassium. This scenario would provide a consistent explanation for the observation that the accessibility of the binding site responsible for the stabilization of the inactive conformation is voltage-independent for potassium ions, but voltage-dependent for sodium ions (**Figure 3-17B-D**). Therefore, the course of both the k_{AI} and the k_{IA} curves suggests that sodium ions are excluded from entering the selectivity filter at membrane voltages > -60 mV (**Figure 3-17C**). However, for more negative membrane voltages, sodium ions may overcome this energy barrier and enter into the selectivity filter (**Figure 3-17D,E**). According to these considerations, the change in the course of both the k_{AI} and the k_{IA} curves at membrane voltages < -60 mV might reflect the onset of sodium permeation. As illustrated in **Figure 3-17**, the binding site involved in the inactivation might therefore be the same as the S0 binding site, while the binding site responsible for stabilizing the inactive state may coincide with the first binding site within the selectivity filter (S1).

In summary, external Na^+ affects the voltage-dependent gating of $Kcv_{NH\ S77G}$ in a complex way, that seems to reflect the transition from a conventional voltage-dependent Na^+ block to a Na^+ permeation or punch through at high negative membrane voltages. Since the Na^+ block in $Kcv_{ATCV\text{-}1}$-like channels has not been investigated systematically so far, the conclusions drawn here must be regarded as speculative. Nevertheless, the experiments discussed above reveal that the potassium-dependent suppression of inactivation and the stabilization of the inactive conformation are two distinct processes, suggesting two binding sites, which differ in their ability to discriminate between K^+ and Na^+.

3.3.10. Development of a mechanistic working model

The experimental data discussed so far allow the development of a mechanistic working model for the outward-rectification in $Kcv_{NH\ S77G}$. For this purpose, all relevant results and conclusions are briefly summarized:

1) The voltage-dependent decrease in the open probability of $Kcv_{NH\ S77G}$ is caused by the occurrence of ultra-long-lasting closed events (inactivation events). The transition between bursts of activity and ultra-long-lasting closed events can be described with a simple two-state reaction scheme. As shown by dwell-time and burst analyses of single-channel recordings, the voltage-dependence of this ultra-slow gating process can be exclusively attributed to the inactivation rate constant k_{AI}. The activation rate constant k_{IA}, on the other hand, is voltage-insensitive. This result strongly supports the idea that the inactivation is not caused by the voltage-driven movement of charged amino acid residues in the electric field, because such a movement would react to voltage for both activation and inactivation.

2) The increase of the potassium concentration on either side of the membrane results in a slowdown of both the inactivation and activation rate. The K^+-dependent change in the inactivation rate suggests that the inactivation is caused by an interruption of the ion permeation through the channel pore, which finally leads to a complete or partial depletion of the selectivity filter. The latter is supported by the fact, that the activation rate constant is voltage-independent.

3) Mutational experiments revealed that the voltage-dependence of $Kcv_{NH\ S77G}$ originates from a pair of uncharged amino acids located in the turret loop. Replacing these residues with the (also uncharged) amino acids that occur at the corresponding positions in voltage-independent orthologs of $Kcv_{NH\ S77G}$ results in a complete loss of voltage-dependence. The turret loop faces the extracellular space and is involved in the shaping of the outer pore entrance. Therefore, it is reasonable to assume that this region in $Kcv_{NH\ S77G}$ differs conformationally from that in voltage-independent orthologs.

4) Experiments performed with asymmetrical potassium concentrations revealed that the slowdown of both the inactivation as well as the activation rate is due to an increase of the external, rather than the internal potassium concentration, suggesting at least one external K^+ binding site. Since the inactivation is accelerated in the presence of low potassium concentrations, it is reasonable to assume that the vacancy of this external

potassium binding site during a permeation event can lead to an inactivation of the channel. In addition, the inactivation rate k_{AI} is sensitive to the driving force for potassium, resulting in a shift of the k_{AI} curve with the reversal potential E_r. The latter underscores the hypothesis, that the inactivation is directly coupled to the permeation of ions through the channel pore and that the permeating ions are the effective gating charges.

5) Experiments carried out in the presence of external Na^+ suggest that the external binding site involved in inactivation does not coincide with the binding site responsible for the stabilization of the inactive state. The first site seems to be non-selective and easily accessible for external Na^+, suggesting that this binding site is located at the very beginning of the external pore entrance. The second binding site, on the other site, exhibits a strong voltage-dependent accessibility for Na^+, but not for K^+, suggesting that this binding site is located inside the selectivity filter. On the other hand, the voltage-insensitivity of the activation rate constant k_{IA} measured in pure KCl solutions supports the assumption, that this binding site cannot be located very deeply inside the pore. Both the ease and voltage-independent accessibility for K^+ and the voltage-dependent accessibility for Na^+ support the idea that this binding site may be identical with the S1 binding site. In this case, the voltage-dependent accessibility for Na^+ would reflect the substantially higher dehydration energy required to enter into the selectivity filter (e.g. Biggin et al. 2001, Shrivastava et al. 2002).

These results and conclusions have been combined in developing the working model shown in **Figure 3-18**. In this model, the permeation cycle, which produces the open-channel current, is represented by a four-state ion hopping model. This four-state model represents a reduced version of the five-state model proposed by Roux (2005). For the sake of simplicity, the ion permeation pathway is reduced to the extracellular binding site S0, the four binding sites S1-S4 inside the selectivity filter, and the cavity (C). During ion translocation, the selectivity filter is always occupied by two potassium ions located alternatively in the binding sites S1 and S3 or in the binding sites S2 and S4 (Bernèche & Roux 2003). Depending on the state of the permeation cycle, a third potassium ion can occupy either the extracellular binding site S0 or the cavity. The inward current measured at membrane voltages more negative than the reversal potential (E_r) is mainly carried by the sequence of states [S2,S4] → [S0,S2,S4] → [S1,S3,C] → [S1,S3] → [S2,S4]. The active state (A) contains apart from the open state different short-lived closed states, which are depicted as C_1, C_2, …, C_n in **Figure 3-18**.

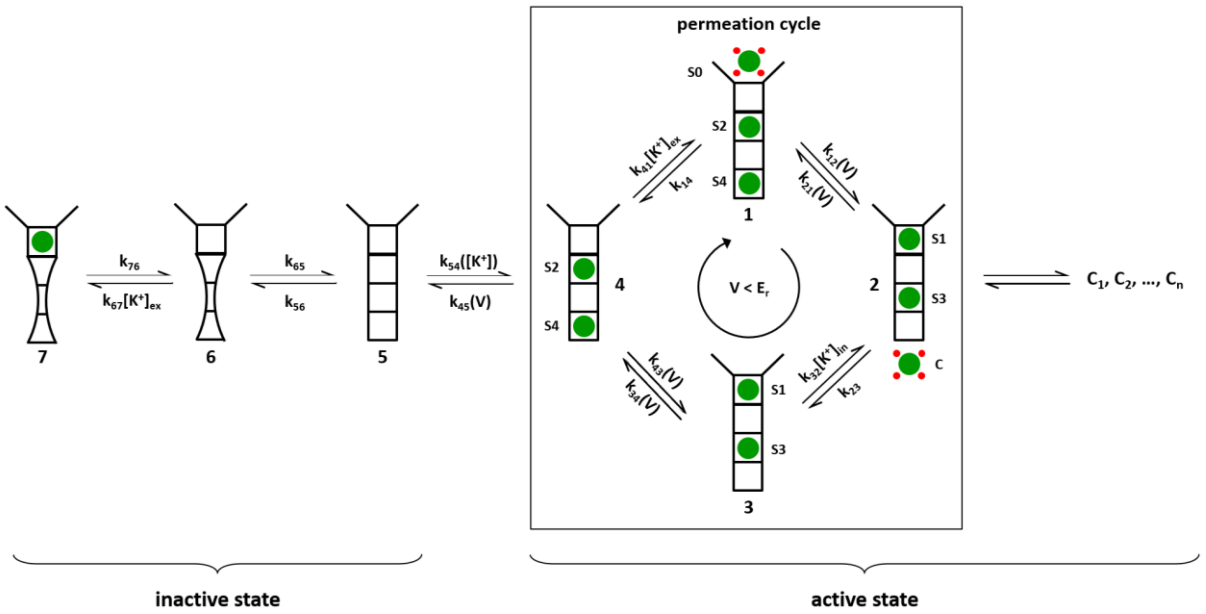

Figure 3-18: Proposed model for the transition between the active and inactive state of $Kcv_{NH\ S77G}$. The cartoon shows locations of supposed K^+-binding sites in the selectivity filter of $Kcv_{NH\ S77G}$. Potassium ions are indicated as green circles, water molecules of the hydration shell as red circles. The ion translocation process in the active state is represented as a four-state model (Roux 2005). The K^+-binding sites inside the selectivity filter are labeled with S0-S4, the binding site inside the cavity with C. Closed states, which occur within a burst of activity, are depicted as C_1, C_2, ..., C_n.

In this model, the non-selective binding site involved in the inactivation is represented by the extracellular binding site S0. Crucial for the prevention of an inactivation event is the successful transition from state 4 to state 1, i.e. the binding of a potassium ion to the S0 site. Conversely, if the dissociation of the potassium ions bound in the selectivity filter occurs before binding of a potassium ion in S0, the selectivity filter will run empty (state 5). As known from various experimental, computational and crystallographic studies on other potassium channels (e.g. Kiss & Korn 1998, Miloshevsky & Jordan 2008, Zhou et al. 2001), the stability of the conductive conformation of the selectivity filter depends on the presence of potassium ions in the filter. Therefore, it is assumed that the inactive state of $Kcv_{NH\ S77G}$ is caused by a conformational change of the selectivity filter, indicated as a constriction of the selectivity filter in **Figure 3-18** (state 6). Of course, this is only one of several possible interpretations. Since the inactive state is stabilized by external K^+, a K^+ binding site between the external solution and the putative constriction inside the selectivity filter must be assumed. As discussed above, this binding site could be the S1 site at the extracellular entrance of the selectivity filter. Therefore, binding of K^+ in this site of the inactivated channel locks the selectivity filter in the non-conductive conformation (state 7). After dissociation of this potassium ion, the selectivity filter can spontaneously and voltage-independently return to the conductive conformation.

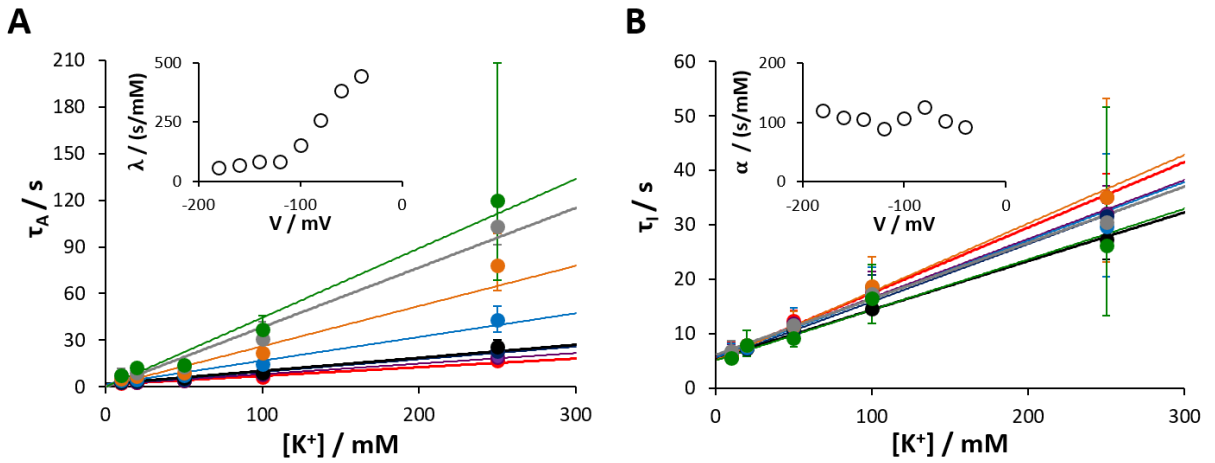

Figure 3-19: The mean lifetimes τ_A and τ_I increase linearly with the potassium concentration. A $[K^+]$-dependence of τ_A for -180 mV (red circles), -160 mV (purple circles), -140 mV (dark blue circles), -120 mV (black circles), -100 mV (light blue circles), -80 mV (orange circles), -60 mV (gray circles) and -40 mV (green circles) as calculated from multi-channel recordings. The measurements were performed with symmetrical KCl solutions. Smooth lines represent the best fit with Eqn (3-24). The inset shows the relation between the slope of Eqn (3-24) and the voltage. **B** $[K^+]$-dependence of τ_I for the same voltages as in **A**. Smooth lines represent the best fit with Eqn (3-27). The inset shows the relation between the slope of Eqn (3-27) and the voltage. Geometric mean and geometric standard deviation of three experiments.

This model provides a qualitative explanation for both the $[K^+]_{ex}$ and the driving-force dependence of the inactivation process. The dependence of the inactivation rate constant k_{AI} on the driving force for potassium reflects the causal connection between the transition to the inactive state and the influx of potassium ions. The more negative the electrochemical driving force for potassium, the higher the probability that the channel undergoes the transition 4 → 5. Consequently, a shift in the reversal potential must lead to a corresponding shift in the k_{AI} curve.

The dependence on the external potassium concentration simply reflects the competition between the transitions 4 → 1 and 4 → 5. On the basis of this model, the probability that the channel moves from state 4 to state 5 can be approximately calculated by

$$P_{4\to5} = \frac{k_{45}}{k_{45} + k_{41} \cdot [K^+]_{ex}} \qquad (3\text{-}20)$$

Because the transition from the active to the inactive state is an extremely rare event, it is reasonable to assume that k_{45} is several orders of magnitude smaller than $k_{41} \cdot [K^+]_{ex}$, resulting in $k_{45} + k_{41} \cdot [K^+]_{ex} \approx k_{41} \cdot [K^+]_{ex}$. Thus, equation **(3-20)** can be simplified as follows:

$$P_{4\to5} = \frac{k_{45}}{k_{41} \cdot [K^+]_{ex}} \qquad (3\text{-}21)$$

The inactivation rate constant k_{AI} should be directly proportional to $P_{4\to5}$:

$$k_{AI} \propto P_{4\rightarrow5} \tag{3-22}$$

Consequently, k_{AI} can be approximated as follows:

$$k_{AI} = c_{AI} \cdot P_{4\rightarrow5} = c_{AI} \cdot \frac{k_{45}}{k_{41} \cdot [K^+]_{ex}} \tag{3-23}$$

with c_{AI} being a scaling factor. Inserting equation **(3-23)** to equation **(3-8)** yields the following relationship between the mean lifetime of the active state τ_A and the external potassium concentration $[K^+]_{ex}$:

$$\tau_A = \lambda \cdot [K^+]_{ex} \tag{3-24}$$

with $\lambda = \frac{k_{41}}{c_{AI} \cdot k_{45}}$.

Accordingly, the working model predicts for a particular membrane voltage a linear relationship between the mean lifetime τ_A and $[K^+]_{ex}$. As shown in **Figure 3-19A**, this is indeed the case for all examined membrane voltage between -40 mV and -180 mV. In addition, the slope λ decreases, as expected, with increasing negative membrane voltages (**Inset Figure 3-19A**).

Similar considerations can also be used to predict the dependence of the mean lifetime of the inactive state τ_I on the external potassium concentration. If the channel can actually be locked in the inactive state by binding a single potassium ion, as assumed in the working model, the activation rate constant k_{IA} should be identical to the gross rate constant $g_{7,4}$:

$$k_{IA} = g_{7,4} \tag{3-25}$$

$g_{7,4}$ can be easily set up by means of the arrow scheme (Hansen et al. 2016) as follows:

$$g_{7,4} = \frac{\begin{matrix}4 & 5 & 6 & 7\end{matrix}}{\begin{bmatrix}\leftarrow & \leftarrow & \leftarrow\end{bmatrix}} \Bigg/ \begin{matrix}4 & 5 & 6 & 7\end{matrix} \begin{bmatrix} & \rightarrow & \rightarrow \\ \leftarrow & & \rightarrow \\ \leftarrow & \leftarrow & \end{bmatrix} = \frac{k_{76} \cdot k_{65} \cdot k_{54}}{k_{56} \cdot k_{67} \cdot [K^+]_{ex} + k_{54} \cdot k_{67} \cdot [K^+]_{ex} + k_{54} \cdot k_{65}} \tag{3-26}$$

Combining **equations (3-9)**, **(3-25)** und **(3-26)** yields the following relation between the mean lifetime of the inactive state τ_I and the external potassium concentration $[K^+]_{ex}$:

$$\tau_I = \alpha \cdot [K^+]_{ex} + \beta \tag{3-27}$$

with $\alpha = \frac{\left(k_{56} \cdot k_{67} + k_{54} \cdot k_{67}\right)}{k_{76} \cdot k_{65} \cdot k_{54}}$ and $\beta = \frac{1}{k_{76}}$.

According to **equation (3-27)**, the mean lifetime of the inactive state should increase linearly with the external potassium concentration, provided that α and β can be considered as $[K^+]_{ex}$-independent. **Figure 3-19B** shows this is indeed the case for all membrane voltage between -40 mV and -180 mV. Since the rate constant k_{IA} is voltage-insensitive for all potassium concentrations, the slope α (**Inset Figure 3-19B**) and the y-axis intersection β (data not shown) also do not exhibit any voltage-dependence.

In summary, the working model correctly predicts the dependence of the mean lifetimes τ_A and τ_I on the potassium concentration. The model also provides a plausible explanation for the dependence of the inactivation on the electrochemical driving force for potassium by interpreting the transition from the active to the inactive state as depletion of the selectivity filter.

3.3.11. The model correctly predicts the influence of external Ba^{2+} on the inactivation rate constant

The working model (**Figure 3-18**) implies that the duration of a burst of activity is not only determined by the permeation cycle, but also by closed states that block the ion translocation. Therefore, the model predicts that either the change in the kinetics of an existing open/closed transition or the artificial creation of an additional closed state should alter the mean lifetime of the active state and therefore the probability to find the channel in a burst of activity. Since the closed states described in section **3.3.2** are insensitive to any external stimulus investigated so far, this prediction was tested by using low concentrations of external Ba^{2+}. The alkaline earth cation Ba^{2+} exhibits a crystal radius equal to that of K^+ (1.35 Å and 1.33 Å for Ba^{2+} and K^+, respectively), but with +2 a higher electrical charge (Lockless et al. 2007). Due to the equal radius, Ba^{2+} can easily enter into the selectivity filter. However, the higher electrical charge results in a strong binding of Ba^{2+} to certain binding sites inside the filter and thus to a temporary and voltage-dependent block of the ion permeation pathway (Neyton & Miller 1988, Lockless et al. 2007). In several studies (e.g. Gazzarini et al. 2009, Greiner 2011) it has been shown, that Kcv_{ATCV-1}-like potassium channels are also sensitive to externally and internally applied Ba^{2+}. A closer examination of the blocking properties of Ba^{2+} has been performed for Kcv_{NTS} (Rauh 2014). The experimental data obtained from this previous work were used to develop a model that allows the computation of the voltage- and concentration

dependent inhibition by external Ba^{2+} (for more details see **Supplemental Material 3.6.2**). Here it is assumed that this model can also be used without modifications to calculate the inhibitory effect of Ba^{2+} on $Kcv_{NH\ S77G}$ channels in the active state, since the selectivity filter sequence of both channels is identical (**Figure 3-1A**).

According to the model in **Figure 3-18**, external Ba^{2+} can enter into the selectivity filter of $Kcv_{NH\ S77G}$ and thus lock the channel temporarily in a blocked active state, referred to as $A_{blocked}$. Therefore, the two-state model **(3-3)** must be extended to a three-state model as follows:

$$I \underset{k_{AI}^0}{\overset{k_{IA}^0}{\rightleftharpoons}} A \underset{k_d}{\overset{k_b \cdot [Ba^{2+}]_{ex}}{\rightleftharpoons}} A_{blocked} \qquad \text{with } k_{AI} \text{ as the direct transition from } A \text{ to } I \tag{3-28}$$

with k^0_{IA} and k^0_{AI} being the activation and inactivation rate constants as measured in the absence of external Ba^{2+}, respectively, k_{AI} the inactivation rate constant as measured in the presence of external Ba^{2+}, k_b the binding rate constant, k_d the dissociation rate constant, and $[Ba^{2+}]_{ex}$ the external Ba^{2+} concentration. Since the channel can only become inactive as long as ion transfer through the channel pore occurs, the Ba^{2+}-mediated blockage should slow down the inactivation rate k_{AI} but keep the activation rate constant k_{IA} unchanged. In the presence of external Ba^{2+} the inactivation rate constant k_{AI} is given by the gross rate constant of the transition from the blocked active state $A_{blocked}$ to the inactive state I. Therefore, k_{AI} is given by

$$k_{AI} = \frac{k_{AI}^0 \cdot k_d}{k_d + k_b \cdot [Ba^{2+}]_{ex}} = k_{AI}^0 \cdot \left(1 - \frac{[Ba^{2+}]_{ex}}{[Ba^{2+}]_{ex} + K_d^{app}}\right) \tag{3-29}$$

with $K_d^{app} = k_d / k_b$ being the apparent dissociation constant. As shown in the **Supplemental Material 3.6.2**, the ratio in the brackets of **equation (3-29)** is identical to the inhibition θ caused by Ba^{2+}. Therefore, **equation (3-29)** can be rewritten as

$$k_{AI} = k_{AI}^0 \cdot (1 - \theta). \tag{3-30}$$

The two-barrier, one-site blocking model used to predict the Ba^{2+} block in Kcv_{NTS} yields the following relation between the inhibition θ, the external barium concentration $[Ba^{2+}]_{ex}$ and the membrane voltage V:

$$\theta = \frac{[Ba^{2+}]_{ex}}{[Ba^{2+}]_{ex} + K_d^{app}(0) \cdot e^{\lambda \cdot zFV/RT} \cdot \left(1 + e^{-(\gamma - \delta) \cdot zFV/RT} \cdot e^{-(G_2 - G_1)/RT}\right)} \tag{3-31}$$

with G_1 and G_2 being the heights of the energy barriers between the Ba^{2+} binding site and the extra- and intracellular solutions, respectively, z the valence of the ion ($z = +2$ for Ba^{2+}), and δ, λ and γ the fractions of the membrane potential seen when the barium ion is at the location of the first energy barrier, the binding site and the second energy barrier, respectively. For more details see **Supplemental Material 3.6.2**. Assuming that k^0_{AI} can be approximated by **equation (3-10)**, the global model and the Ba^{2+} blocking model provide the following equation for calculating the inactivation rate constant k_{AI}:

$$k_{AI} = k_{AI}(0) \cdot e^{-V/V_{AI}} \cdot \left(1 - \frac{[Ba^{2+}]}{[Ba^{2+}] + K_d^{app}(0) \cdot e^{\lambda \cdot zFV/RT} \cdot \left(1 + e^{-(\gamma-\delta)\cdot zFV/RT} \cdot e^{-(G_2-G_1)/RT}\right)} \right) \quad (3\text{-}32)$$

In order to test whether the working model correctly predicts the effect of external Ba^{2+} on the voltage-dependence of $Kcv_{NH\ S77G}$, multi-channel measurements in the presence of external Ba^{2+} were performed. For this purpose, both compartments of the bilayer chamber were initially filled with 100 mM KCl. Subsequently, the external $BaCl_2$ concentration was stepwise increased from 0 μM to 50 μM and 100 μM. At each concentration, a pulse protocol as in **Figure 3-11A** was applied. The resulting multi-channel currents were recorded and subsequently analyzed as in section **3.3.6**.

The exemplary current responses recorded at a test pulse of -100 mV (**Figure 3-20A**), shows that adding of Ba^{2+} to the extracellular solution causes a dramatic decrease of the instantaneous current. This decrease simply reflects the voltage-dependent Ba^{2+} block, which occurs almost immediately after changing the membrane voltage from the holding potential to the test potential. The addition of external Ba^{2+} also leads to a concentration and voltage-dependent decrease of the steady-state current (**Figure 3-20C**). Since the Ba^{2+}-induced reduction of the instantaneous current is much stronger than the reduction of the steady-state current, the time-dependent inactivation becomes less obvious with increasing Ba^{2+} concentrations (**Figure 3-20A**).

Much more interesting, these blocking effects are accompanied by a $[Ba^{2+}]_{ex}$- and voltage-dependent decrease of the fraction of inactive channels. This can be seen from the increase of the instantaneous tail current in **Figure 3-20B** and the change in the course and shape of the P_{Burst} curve (**Figure 3-20C**). Therefore, the blockage of the open channel leads to an increase in the probability to find a channel in the active state. Moreover, this $[Ba^{2+}]_{ex}$- and voltage-dependent increase in P_{Burst} is exclusively caused by a decrease of the inactivation rate constant k_{AI} (**Figure 3-20E**). The activation rate constant k_{IA}, on the other hand, remains unchanged (**Figure 3-20F**).

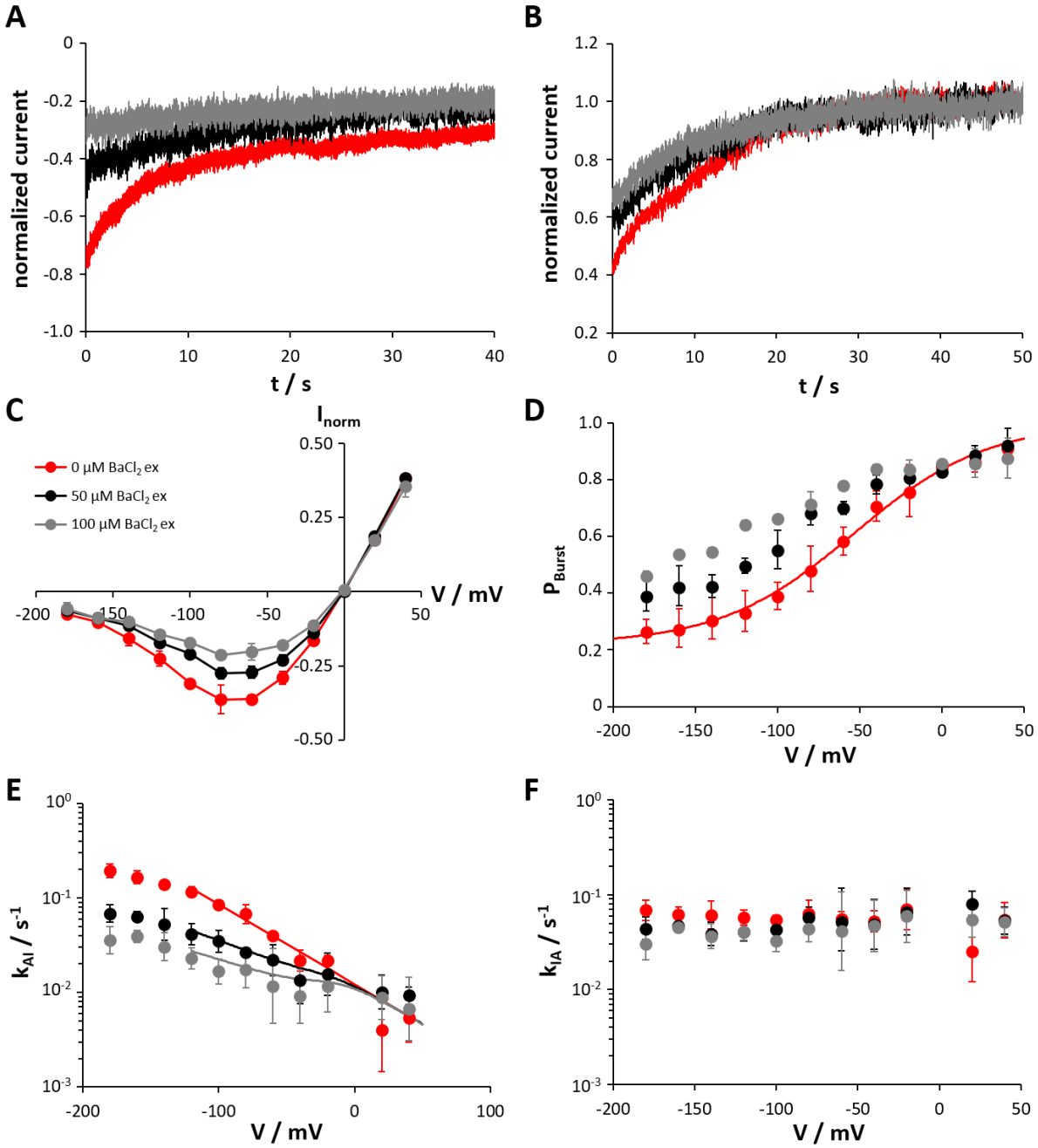

Figure 3-20: External Barium slows down the inactivation rate. A Exemplary current responses to a test-pulse of -100 mV in symmetrical 100 mM KCl (red trace), with additional 50 µM external $BaCl_2$ (black trace), and with additional 100 µM external $BaCl_2$ (gray trace). For reasons of comparability the current values were normalized to the steady-state current at the holding potential of +100 mV. **B** Corresponding post-pulses (+100 mV) of the current responses shown in **A**. For reasons of comparability the current values were normalized to the steady-state current. **C** Normalized steady-state currents. The current values of each experiment were normalized to the steady-state current at the holding potential of +100 mV. Mean and standard deviation of three experiments. **D** Burst probabilities as calculated from multi-channel recordings. The smooth red line shows the best fit with the Boltzmann-equation (3-19). **E** Rate constants k_{AI} of the transition from the active to the inactive state. The red smooth line shows the best fit of the k_{AI} values obtained in the absence of $BaCl_2$ from +40 mV to -120 mV with Eqn (3-10) with $k_{AI}(0) = 0.012\ s^{-1}$ and $V_{AI} = -51.5$ mV. The black and gray smooth lines show the predicted k_{AI} curves for 50 µM and 100 µM external Ba^{2+}, respectively, as calculated with Eqn (3-32) with $K_d^{app}(0) = 696.4$ µM, $\lambda = 0.95$, $(\gamma - \delta) = 0.80$, $(G_2 - G_1)/RT = 1.78$. **F** Rate constants k_{IA} of the transition from the inactive to the active state. Symbols in **D-F** cross-reference to the symbols in **C**. Data points in **D-F** represent geometric mean and geometric standard deviation of three experiments.

These results are perfectly in line with the prediction of the working model. Moreover, the degree of reduction can be correctly calculated by equation **(3-32)** as illustrated by the smooth lines in **Figure 3-20E**.

As predicted by the model, the results demonstrate that the blockage or closure of the permeation pathway prevents the channel from inactivation. At this point it is worth mentioning that this finding could also provide an explanation for the deviation of the k_{AI} curve from a simple exponential curve in the range of high negative membrane voltages. As mentioned above, $Kcv_{ATCV\text{-}1}$-like channels exhibit a fast voltage-dependent gating process with closed times in the sub-millisecond range (Rauh et al. 2017b). This gating process becomes visible with increasing negative membrane voltages and causes an apparent reduction of the open-channel amplitude. Hence, this so-called flicker gating leads to a reduction of the open probability similar to the voltage-dependent Ba^{2+} block, even if these two processes take place on different time scales and with different voltage-dependencies. Consequently, on the basis of the proposed working model, it would be expected that the flicker gating causes a slowdown of the inactivation rate at negative membrane voltages and thus a deviation of the k_{AI} curve from a simple exponential course. This prediction fits with the experimental observation. However, a detailed examination of the influence of the flicker gating on the inactivation process is still pending.

3.4. Conclusion

Voltage-dependent gating in potassium channels has classically been attributed to the movement of a positively charged transmembrane helix within a canonical voltage-sensing domain (VSD) (Gandhi & Isacoff 2002). However, several potassium channels such as K2P (Schewe et al. 2016) and modified Kir channels (Yeh, et al. 2005, Kurata et al. 2010) exhibit a pronounced intrinsic voltage-sensitivity without having a canonical VSD. Equally astonishing was the discovery that even potassium channels of the Kcv family, which do not possess either cytoplasmic or extracellular domains, can sense changes in the membrane voltage (Rauh et al. 2017b, Baumeister et al. 2017). In the present study, the voltage-dependence of one of these channels, the outward rectifying $Kcv_{NH\,S77G}$, was examined in detail. This study provided a mechanistic explanation how channels without a canonical VSD can undergo slow voltage-dependent activation and inactivation. It is evident from single-channel experiments in artificial lipid bilayers that $Kcv_{NH\,S77G}$ can enter an ultra-long-lasting inactive state in a voltage-dependent manner: the more negative the applied membrane voltage, the more likely is the transition from the active to the inactive state. Additional single- and multi-channel

measurements performed under various ionic conditions uncovered that the inactivation is sensitive to both the extracellular potassium concentration and the electrochemical gradient. Moreover, it could be demonstrated that the inactivation can be suppressed by introducing a double mutation near the extracellular pore entrance. The combination of all experimental data enabled the development of a mechanistic model, which attributes the voltage-dependence to an ion-flux dependent depletion of the channel pore followed by a conformational change within the selectivity filter that renders the channel non-conductive. It is conceivable that this conformational change might be a partial collapse of the selectivity filter as observed in the low K^+ crystal structure of the prokaryotic KcsA channel (Cordero-Morales et al. 2007). However, since structural data are missing, the true nature of any conformational change that underlies the inactivation in $Kcv_{NH\ S77G}$ remains unknown.

Crucial for the continuous influx of potassium ions is the binding of potassium ions to a binding site in the outer pore entrance. In $Kcv_{NH\ S77G}$, the binding of K^+ to this binding site seems to be impaired in some way. Therefore, it can occur, that this outer binding site remains unoccupied while the ions bound in the selectivity filter are pushed towards the intracellular space by the electrochemical gradient, resulting in a depletion of the selectivity filter. Since most of the membrane voltage drops along the selectivity filter (Contreras et al. 2010), it is reasonable to assume that the voltage-dependence of the inactivation originates from the ions escaping from the selectivity filter immediately before it adopts the ion-depleted, non-conductive conformation.

Ion depletion as a cause of voltage-dependent closure has also been postulated for depolarization activated K2P channels (Schewe et al. 2016) and the hyperpolarization activated MthK channel (Thomson & Rothberg 2010). The voltage-dependent gating observed in K2P channels exhibits remarkable similarities to the voltage-dependent inactivation of $Kcv_{NH\ S77G}$: in both cases inward current gates the channel inactive, while the time constant of activation observed for voltage steps positive to the reversal potential is strikingly voltage-independent (Schewe et al. 2016). However, the authors attribute the voltage-sensitivity of K2P channels to a rapid voltage-dependent refilling of the ion-depleted selectivity filter, rather than to voltage-dependent ion depletion. Nevertheless, it is possible that the inactivation processes observed in K2P channels and $Kcv_{NH\ S77G}$ are governed by a similar mechanism. At least, both processes are mediated by the selectivity filter. Another voltage-dependent gating process that results from conformational changes within or near the selectivity filter is the so-called C-type inactivation (Hoshi & Armstrong 2013). C-type inactivation occurs in a wide range of eukaryotic and prokaryotic potassium channels and plays a crucial role in a large number of physiological processes (McCoy & Nimigean 2012). Simulations and crystallographic studies performed with the prokaryotic potassium channel KcsA suggest that

C-type inactivation reflects the transition from a conductive to a partially collapsed selectivity filter conformation (Cordero-Morales et al. 2007, Zhou et al. 2001). Other studies focusing on C-type inactivation in Kv channels show that the rate of inactivation is regulated by the occupancy of a binding site at the external pore entrance or inside the selectivity filter (Baukrowitz & Yellen 1996, Kiss & Korn 1998). Similar to the voltage-dependent inactivation process found in $Kcv_{NH\ S77G}$, an increase in the extracellular potassium concentration decreases the rate of C-type inactivation at a given voltage (López-Barneo et al. 1993, Baukrowitz & Yellen 1996).

The similarities between the voltage-dependent gating process investigated in the present study and other selectivity filter mediated gating processes support the idea, that all these processes are based on similar mechanistic and molecular principles. Since Kcv channels provide a robust and easy-to-use model system for studies of fundamental potassium channel functions, the further investigation of the voltage-dependent gating process found in $Kcv_{NH\ S77G}$ by means of electrophysiological, computational and structure-resolving techniques will lead to a deeper understanding of the mechanisms that underlie voltage-sensitivity in channels lacking a canonical VSD.

3.5. Material and Methods

3.5.1. Cloning and mutagenesis

The coding sequences of Kcv_{NH} and Kcv_{NTS} were amplified by PCR using a *Taq* polymerase (ThermoFisher Scientific, Waltham, MA, USA). *Taq* polymerase was used to add a single deoxyadenosine (A) to the 3′ ends of the PCR products as required for the subsequent topoisomerase cloning procedure. To express the proteins in their native form without His-Tag, a stop-codon was inserted directly downstream of the coding sequence. The amplified DNA fragments were separated electrophoretically in an agarose gel and then purified by gel extraction using the Zymoclean™ Gel DNA Recovery Kit (Zymo Research, Irvine, CA, USA) following the manufacturer's instructions. For *in vitro* protein expression the coding sequences were cloned into a linearized pEXP5-CT/TOPO-vector using the pEXP5-CT/TOPO TA Expression Kit (Invitrogen), amplified in DH5α cells and purified via a ZR Plasmid Miniprep™-Classic-Kit (Zymo Research, Irvine, CA, USA). The mutations were introduced by PCR-based site-directed mutagenesis using a protocol based on the method described in Papworth et al. (1996). The PCR products were separated electrophoretically in an agarose gel and then purified by gel extraction using the Zymoclean™ Gel DNA Recovery Kit (Zymo Research, Irvine, CA, USA). To minimize the number of false-positive clones, the template DNA was removed by DpnI digestion for 15 minutes at 37°C using FastDigest DpnI (ThermoFisher Scientific, Waltham, MA, USA). 50 μL chemically competent DH5α cells were transformed with 5 μL of the purified PCR products by heat shock at 42°C for 45 seconds and subsequent transfer on ice. Positive colonies were selected after incubation at 37°C over night from LB (10 g/L tryptone, 5 g/L yeast extract, 5 g/L NaCl, 20 g/L agar, pH 7 adjusted with 1M NaOH) agar plates containing 50 μg/mL ampicillin and grown in LB medium at 37°C. The plasmid DNA were finally purified using a ZR Plasmid Miniprep™-Classic-Kit (Zymo Research). The coding region of all constructs were sequenced.

3.5.2. Protein expression and purification

The channel proteins were expressed *in vitro* with the MembraneMaxTM HN Protein Expression Kit (Invitrogen, Karlsbad, CA, USA) following the manufacturer's instructions. The expression was performed in the presence of His-tagged nanolipoproteins (NLPs) (Katzen 2008), which enabled the channel proteins to insert into a lipid environment. The multiple His-tag allowed the purification of the native channel proteins by metal chelate affinity

chromatography using a 0.2 mL HisPur™ Ni-NTA spin column (ThermoFisher Scientific, Waltham, MA, USA). Contrary to the manufacturer's instructions, the column was washed three times with two resin-bed volumes of pure 20 mM imidazole to remove unspecific binders. Subsequently, the channel protein/NLP conjugates were eluted in three fractions with 200 μL pure 250 mM imidazole. The washing and elution steps were done in the absence of additional salts to improve the reconstitution efficiency into the bilayer (Winterstein et al. 2018).

3.5.3. Vertical lipid bilayer experiments

Artificial planar lipid bilayers were formed at room temperature (20-25°C) in a vertical bilayer setup (IonoVation, Osnabrück, Germany) using the monolayer folding technique (Montal & Mueller 1972) or the pseudo painting/air bubble technique (Braun et al. 2014). The preparation of the recording chambers was performed as described in detail by Winterstein et al. (2018). All experiments were performed in pure 1,2-diphytanoyl-sn-glycero-3-phosphocholine (DPhPC, Avanti Polar Lipids, Alabaster, AL, USA) membranes. Experimental solutions were buffered with 10 mM HEPES and adjusted with 1M KOH to pH 7.0. For reconstitution of channel proteins into the DPhPC membrane, a small volume (1 - 2 μL) of the purified channel protein/NLP conjugates were directly administered to the bilayer in the *trans* compartment with a bent 25-μl Hamilton syringe. For insertion of single channels, the first elution fraction of the purified channel protein/NLP conjugates was diluted with pure 250 mM imidazole by a factor of 10^4 - 10^6. For multi-channel experiments, the first elution fraction was diluted by a factor of 10^2 or 10^3. The incorporation of single channels was monitored by applying short (5 seconds) voltage pulses between -120 mV and +120 mV in steps of 20 mV. After insertion of a single channel, the membrane was clamped for periods between 1 minute and 2 hours to a range of voltages between -160 mV and +160 mV in 20 mV steps. The insertion of multiple channels was monitored by clamping the membrane for 10 minutes to a constant voltage of +60 mV or +100 mV. After reaching a constant current, macroscopic current responses were evoked by a pulse protocol as shown in **Figure 3-11A**.
Both compartments of the vertical bilayer setup were connected with Ag/AgCl electrodes to the head stage of a L/M-EPC-7 patch-clamp amplifier (List-Medical, Darmstadt, Germany). Membrane potentials were applied to the electrode in the *cis* compartment. The electrode in the *trans* compartment was connected to the ground. Current responses were filtered with a 1-kHz or 300-Hz four-pole Bessel filter and digitized with a sampling frequency of 5 kHz or 1 kHz, respectively, by a 16-bit LIH 1600 A/D converter (HEKA Elektronik, Lambrecht,

Germany). Experiments with asymmetric ion concentrations were performed with 3 M agar bridges. Ion concentrations were changed by replacing an appropriate volume of the experimental solution with a 500 mM, 1.5 M or 3 M stock solution and thorough mixing with a 1000 μL pipette. Currents were recorded with PatchMaster (HEKA Elektronik, Lambrecht, Germany) and subsequently analyzed with KielPatch (version 3.20 ZBM/2011, CAU Kiel, Germany) and Matlab (MathWorks, Natick, MA, USA).

3.5.4. Dwell-time analysis

To examine the gating of single channels, the open and closed lifetimes obtained by a higher-order Hinkley detector (Schultze & Draber 1993) were used to generate open-time and closed-time histograms. These dwell-time histograms were generated by grouping the lifetimes into bins with exponentially growing width. If the first bin contains all lifetimes between 10^p ms and $10^{p+1/a}$ ms, the right class limit of the *i*-th bin is calculated as follows:

$$t_i = 10^{p+i/a} \tag{3-33}$$

with *p* being a rational integer and *a* a natural number. Therefore, the difference Δt_i between the right and left limit values of the *i*-th bin is given by

$$\Delta t_i = 10^{p+i/a} \cdot \left(1 - 10^{-1/a}\right). \tag{3-34}$$

For the dwell-time analysis of current traces recorded with a filter frequency of 1 kHz and a sampling rate of 5 kHz, *p* has been set to 0 and *a* to 10.

Since the transitions between open and closed states can be represented by a Markov model, the probability density function of lifetimes (*pdf*) is given by a sum of exponential functions (Colquhoun & Sigworth 1983):

$$pdf = \frac{a_1}{\tau_1} \cdot e^{-\frac{t}{\tau_1}} + \frac{a_2}{\tau_2} \cdot e^{-\frac{t}{\tau_2}} + \ldots + \frac{a_n}{\tau_n} \cdot e^{-\frac{t}{\tau_n}} = \sum_{j=1}^{n} \frac{a_j}{\tau_j} \cdot e^{-\frac{t}{\tau_j}} \tag{3-35}$$

with τ_1, τ_2, …, τ_n being the time constants of the various components. The area under this curve in the time interval from 0 to *t* represents the probability, that the lifetime of an event is equal or less than *t*:

$$P(lifetime \le t) = 1 - \sum_{j=1}^{n} a_j \cdot e^{-\frac{t}{\tau_j}} \tag{3-36}$$

with a_1, a_2, …, a_n being the relative contributions of the various components. Since P must be 0 for $t = 0$, the following must apply:

$$\sum_{j}^{n} a_j = 1 \tag{3-37}$$

The mean lifetime is given by

$$\tau = \int_0^{\infty} t \cdot pdf(t)dt = a_1 \cdot \tau_1 + a_2 \cdot \tau_2 + ... + a_n \cdot \tau_n = \sum_{j=1}^{n} a_j \cdot \tau_j \tag{3-38}$$

Therefore, the expected number of events with a lifetime equal or less than t is given by

$$N(lifetime \le t) = N \cdot \left(1 - \sum_{j=1}^{n} a_j \cdot e^{-\frac{t}{\tau_j}} \right) \tag{3-39}$$

with N being the total number of events. The expected number N_i of events in the i-th bin is then

$$N_i = N \cdot \left(\sum_{j=1}^{n} a_j \cdot e^{-\frac{t_i}{\tau_j}} \left(e^{\frac{\Delta t_i}{\tau_j}} - 1 \right) \right). \tag{3-40}$$

The generated open-time and closed-time histograms were fitted with **equation (3-40)** in order to obtain the relative contribution a_j and the mean lifetime τ_j of the various populations of dwell-times. Since the open-time histograms exhibit only one population of lifetimes, only one exponential component had to be considered. Therefore, **equation (3-40)** can be rewritten as follows:

$$N_i(open) = N \cdot e^{-\frac{t_i}{\tau_O}} \cdot \left(e^{\frac{\Delta t_i}{\tau_O}} - 1 \right) \tag{3-41}$$

with τ_0 being the mean open lifetime. The closed-time histograms exhibit two or three populations of lifetimes. Thus, the histograms could be fitted with **equation (3-40)** using n = 2 and n = 3, respectively. The number of free parameters could be reduced by using **equation (3-37)**.

The best fit was obtained by minimizing the squared error sum

$$\chi^2 = \sum_{i=1}^{n} \left(\sqrt{N_i} - \sqrt{N_{i,obs}} \right)^2 \qquad (3\text{-}42)$$

using a 'trust-region-reflective' algorithm (Moré & Sorensen 1983). The deviation between the calculated number of events N_i and the observed number of events $N_{i,obs}$ was weighted by using the square roots of these values.

If each closed time population is interpreted as an individual closed state as shown in **Figure 3-21**, the probability to find a channel in closed state C_j is given by

$$P(C_j) = \frac{a_{Cj} \cdot \tau_{Cj}}{\tau_O + \sum_{j=1}^{n} a_{Cj} \cdot \tau_{Cj}}. \qquad (3\text{-}43)$$

The same considerations give

$$P(O) = \frac{\tau_O}{\tau_O + \sum_{j=1}^{n} a_{Cj} \cdot \tau_{Cj}} \qquad (3\text{-}44)$$

with $P(O)$ being the open probability. **Equations (3-43)** and **(3-44)** were used to calculate the occupation probabilities of the various states.

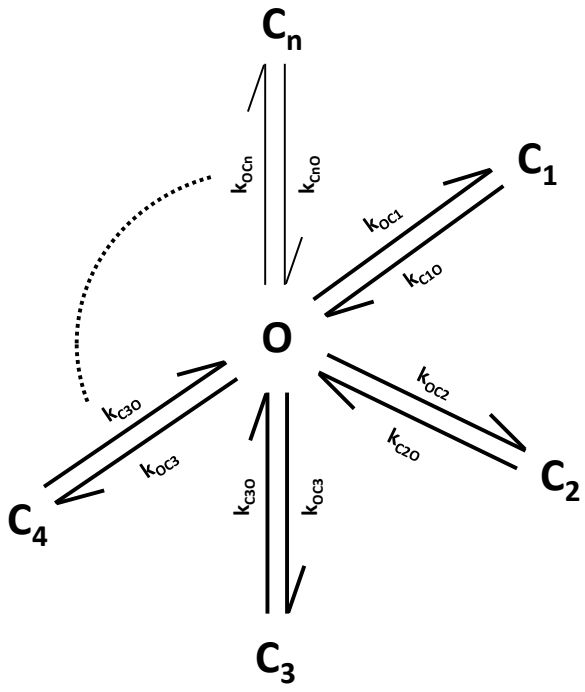

Figure 3-21: Simple Markov model to explain the occurrence of various populations of lifetimes in the closed-time histograms and a single population of lifetimes in the open-time histograms. The open state is depicted as O, the closed states as C_1, C_2, C_3, C_4, ..., C_n. The transitions from the open state to the closed states are given by the rate constants k_{OC1}, k_{OC2}, k_{OC3}, k_{OC4}, ..., k_{OCn}, the transitions from the closed states to the open state by the rate constants k_{C1O}, k_{C2O}, k_{C3O}, k_{C4O}, ..., k_{CnO}.

Because of the limited temporal resolution of the experimental setup a notable number of sub-millisecond closed events were not detected. The underestimation of the number of closed events inevitably resulted in an overestimation of the mean open lifetime τ_0. To obtain an approximation of the true mean open lifetime, a simple missed events correction was applied based on the following considerations: Fitting of a closed-time histogram with **equation (3-40)** provides the total number N of closed events that belong to the various populations of lifetimes found in the histogram. Comparison with the number of observed closed events N_{obs} gives the number of missed events N_m:

$$N_m = N - N_{obs} \tag{3-45}$$

Since the missed closed events have dwell-times in the sub-millisecond range, it is reasonable to assume that the observed total open-time is approximately equal to the true total open time:

$$N_{obs} \cdot \tau_{O,obs} \approx (N_{obs} + N_m) \cdot \tau_O \tag{3-46}$$

with $\tau_{0,\mathrm{obs}}$ being the observed mean open lifetime as obtained by fitting the open-time histogram with **equation (3-41)** and τ_0 the approximated true mean open lifetime. According to **equation (3-46)** the true mean open lifetime can approximately be calculated as follows:

$$\tau_O \approx \frac{1}{\tau_{O,obs}} \cdot \left(1 + \frac{N_m}{N_{obs}}\right) \tag{3-47}$$

All calculations were done with Matlab (MathWorks, Natick, MA, USA).

3.5.5. Burst analysis

In order to analyze the transitions between bursts of activity and interbursts, closed events with dwell-times shorter than 1 s were automatically removed from the reconstructed time series provided by a Hinkley detector, effectively merging the open state O and the short-lived closed states C1 and C2 into the active state A. Both the burst- and interburst-time histograms were fitted with

$$N_i = N \cdot e^{-\frac{t_i}{\tau}} \cdot \left(e^{\frac{\Delta t_i}{\tau}} - 1\right) \tag{3-48}$$

where τ is the mean burst or interburst lifetime. The rate constants k_{AI} and k_{IA} were calculated as described in **section 3.3.3**.

3.5.6. Statistics

Data points are given as arithmetic mean

$$\bar{y} = \frac{1}{n}\sum_{i=1}^{n} y_i \tag{3-49}$$

or geometric mean

$$\bar{y} = \left(\prod_{i=1}^{n} y_i\right)^{1/n} \tag{3-50}$$

with $\bar{y}$ being the mean value and y_i the *i*-th value of the data set $\{y_1, y_2, ..., y_n\}$. If a data point is given as arithmetic mean, the deviation $\Delta\bar{y}$ from this mean is calculated as arithmetic standard deviation:

$$\Delta\bar{y} = \pm\sqrt{\frac{1}{n}\sum_{i=1}^{n}\left(y_i - \bar{y}\right)^2} \tag{3-51}$$

Correspondingly, if a data point is given as geometric mean, the positive and negative deviations from this mean are calculated as follows:

$$\Delta\bar{y}^{+} = \bar{y}\cdot\sigma - \bar{y} \tag{3-52}$$

$$\Delta\bar{y}^{-} = \bar{y} - \frac{\bar{y}}{\sigma} \tag{3-53}$$

with

$$\sigma = \exp\left(\sqrt{\frac{1}{n}\sum_{i=1}^{n}\left(\ln\frac{y_i}{\bar{y}}\right)^2}\right). \tag{3-54}$$

3.6. Supplemental Material

3.6.1. Additional figures

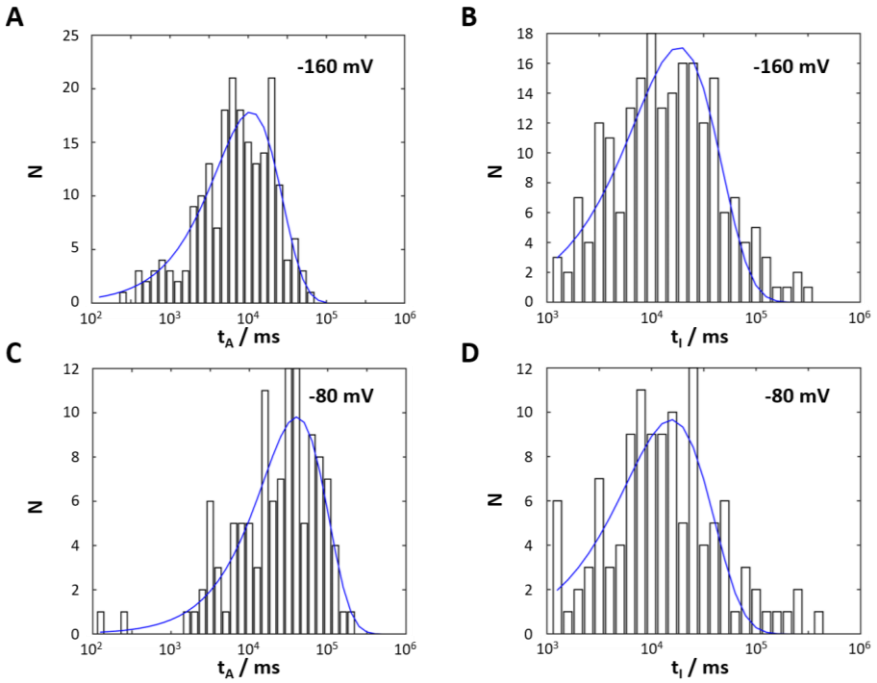

Figure S 3-1: Burst analysis of long-term single-channel traces of the mutant channel Kcv_{NTS} N28Y T29A recorded in symmetrical 100 mM KCl. A,C Exemplary dwell-time histograms for the activated state (bursts of activity) at -160 mV and -80 mV, respectively. **B,D** Exemplary dwell-time histograms for the inactive state (interbursts) at -160 mV and -80 mV, respectively. The dwell-time histograms in **A-D** were fitted with one exponential.

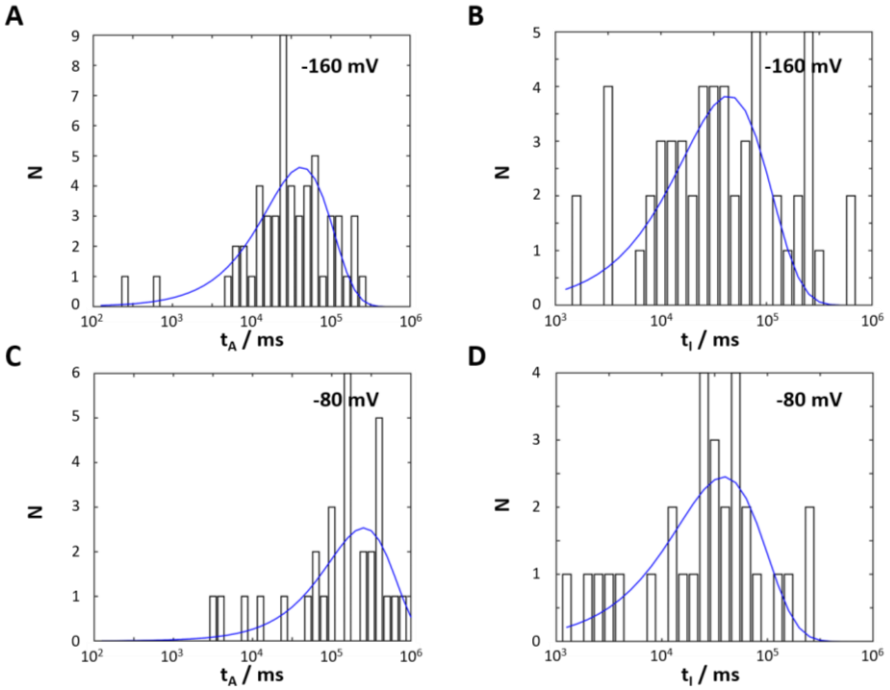

Figure S 3-2: Burst analysis of long-term single-channel traces of $Kcv_{NH\ S77G}$ recorded in symmetrical 250 mM KCl. A,C Dwell-time histograms for the activated state (bursts of activity) at -160 mV and -80 mV, respectively. **B,D** Dwell-time histograms for the inactive state (interbursts) at -160 mV and -80 mV, respectively. The dwell-time histograms in **A-D** were fitted with one exponential.

3.6.2. The Ba^{2+} blocking model

The effect of external Ba^{2+} on the open probability of Kcv_{NTS} was measured in symmetrical 100 mM KCl (Rauh 2014). The relationship between the external barium concentration [Ba^{2+}] and the resulting inhibition (**Figure S 3-3A**) can be described for all examined voltages with a bimolecular reaction:

$$C + Ba^{2+} \underset{k_d}{\overset{k_b}{\rightleftharpoons}} C \cdot Ba^{2+} \qquad \text{(S 3-1)}$$

with C being the channel, Ba^{2+} a barium ion, $C \cdot Ba^{2+}$ the blocked channel, and k_b and k_d the apparent binding and dissociation rate constants, respectively. The law of mass action implies for reaction scheme **(S 3-1)**:

$$\frac{d[C \cdot Ba^{2+}]}{dt} = k_b \cdot [Ba^{2+}] \cdot [C] - k_d \cdot [C \cdot Ba^{2+}]$$

where the square brackets denote the concentration of a reactant. Using the steady-state condition

$$\frac{d[C \cdot Ba^{2+}]}{dt} = 0 \qquad \text{(S 3-2)}$$

and the conservation of the channel

$$[C] + [C \cdot Ba^{2+}] = [C]_t \qquad \text{(S 3-3)}$$

gives

$$\theta = \frac{[C \cdot Ba^{2+}]}{[C]_t} = \frac{[Ba^{2+}]}{[Ba^{2+}] + K_d^{app}} \qquad \text{(S 3-4)}$$

with θ being the inhibition, $[C]_t$ the total number of channels, and $K_d^{app} = k_d / k_b$ the apparent dissociation constant.

The calculated apparent dissociation constants shown in **Figure S 3-3C** exhibit a biphasic voltage-dependence that can be phenomenologically described by a sum of two exponential functions. The decrease in the steepness of the K_d^{app}/V-relationship at negative voltages can be explained by a simple two-barrier, one-site blocking model (**Figure S 3-3B**), that can be written as follows:

$$C + Ba_{ex}^{2+} \underset{k_{d1}}{\overset{k_{b1}}{\rightleftharpoons}} C \cdot Ba^{2+} \underset{k_{b1}}{\overset{k_{d2}}{\rightleftharpoons}} C + Ba_{in}^{2+} \qquad \text{(S 3-5)}$$

with Ba_{ex}^{2+} and Ba_{in}^{2+} being barium ions in the external and internal solution, respectively.

The law of mass action implies

$$\frac{d[C \cdot Ba^{2+}]}{dt} = \left(k_{b1} \cdot [Ba^{2+}]_{ex} + k_{b2} \cdot [Ba^{2+}]_{in}\right) \cdot [C] - \left(k_{d1} + k_{d2}\right) \cdot [C \cdot Ba^{2+}]$$

Using $[Ba^{2+}]_{in} = 0$, the steady-state condition **(S 3-2),** and **equation (S 3-3)** gives

$$\theta = \frac{[C \cdot Ba^{2+}]}{[C]_t} = \frac{[Ba^{2+}]_{ex}}{[Ba^{2+}]_{ex} + \frac{\left(k_{d1} + k_{d2}\right)}{k_{b1}}}. \qquad \text{(S 3-6)}$$

Comparison of **equation (S 3-6)** with **equation (S 3-4)** yields

$$K_d^{app} = \frac{k_{d1} + k_{d2}}{k_{b1}}. \qquad \text{(S 3-7)}$$

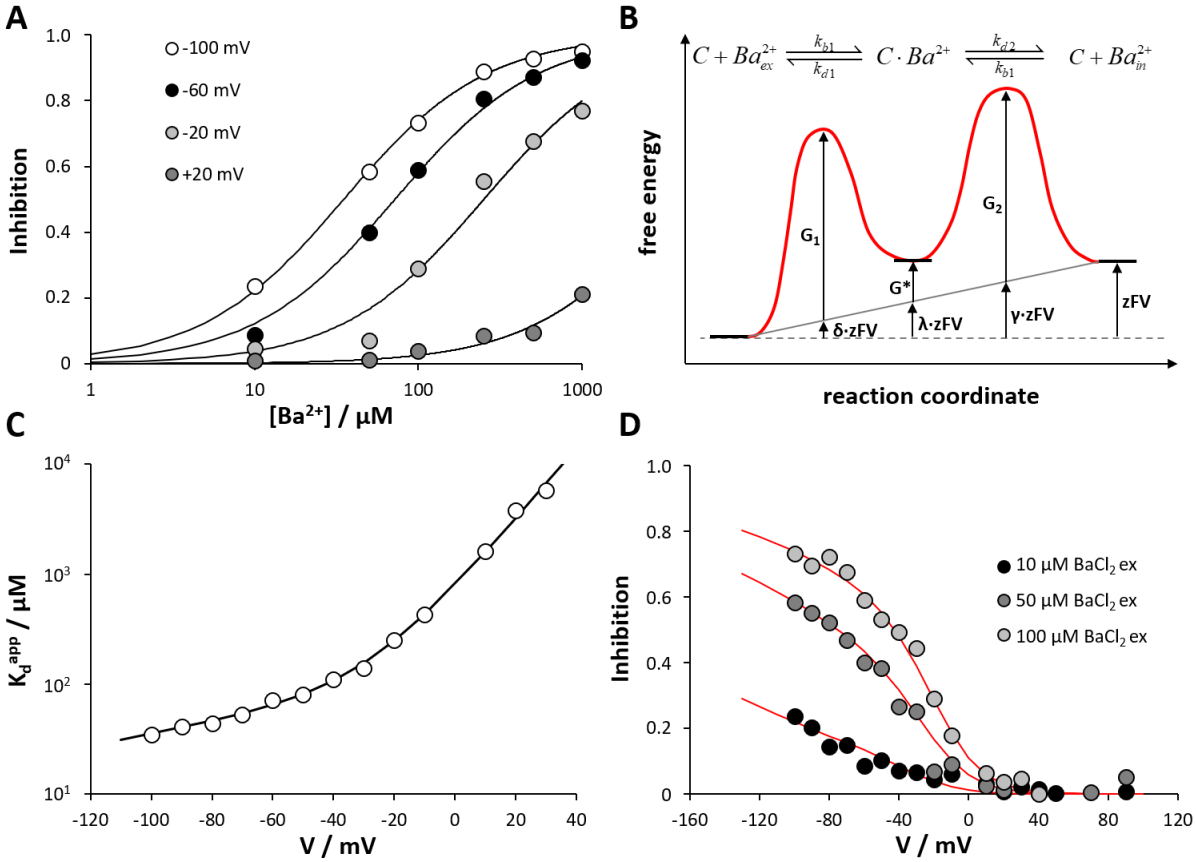

Figure S 3-3: The Ba^{2+} block in Kcv_{NTS} can be described with a two-barrier, one-site model. A Inhibition curves for different membrane voltages in symmetrical 100 mM KCl. Smooth black lines show the best fit with Eqn (S 3-4). **B** Schematic representation of the two-barrier, one-site model. Black bars indicate the possible locations of a barium ion; from left to right: extracellular space, binding site inside the pore, intracellular space. The red line shows a hypothetical two-barrier energy profile. The contribution of the applied electric field to the free energy profile is represented by a gray line. **C** Apparent dissociations constants K_d^{app} values as obtained by Eqn (S 3-4). The black smooth line represents the best fit with Eqn (S 3-11) with $K_d^{app}(0)$ = 696.4 µM, λ = 0.95, (γ -δ) = 0.80, (G_2-G_1)/RT = 1.78. **D** Voltage-dependent inhibition of the Kcv_{NTS} mediated potassium current caused by different $BaCl_2$ concentrations. The smooth red lines show the predicted inhibition on the basis of the two-barrier, one-site blocking model [Eqn (S3-12)]. The experimental data was taken from Rauh 2014.

The rate constants are given, according to Eyring's transition state theory (Tsien & Noble 1969), by the following relations:

$$k_{b1} = \alpha \cdot e^{-(G_1 + \delta \cdot zFV)/RT} \qquad \text{(S 3-8)}$$

$$k_{d1} = \beta \cdot e^{-(G_1 + \delta \cdot zFV - G^* - \lambda \cdot zFV)/RT} = \beta \cdot e^{-(\delta - \lambda) \cdot zFV/RT} \cdot e^{-G_1/RT} \cdot e^{G^*/RT} \qquad \text{(S 3-9)}$$

$$k_{d2} = \beta \cdot e^{-(G_2 + \gamma \cdot zFV - G^* - \lambda \cdot zFV)/RT} = \beta \cdot e^{-(\gamma - \lambda) \cdot zFV/RT} \cdot e^{-G_2/RT} \cdot e^{G^*/RT} \qquad \text{(S3-10)}$$

with α and β being constants, G_1 and G_2 the heights of the energy barriers between the Ba^{2+} binding site and the extra- and intracellular solutions, respectively, G^* the height of the potential well between both energy barriers, z the valence of the ion ($z = +2$ for Ba^{2+}), and δ, λ and γ the fractions of the membrane potential seen when the barium ion is at the location of the first energy barrier, the binding site and the second energy barrier, respectively.

Adding **equations (S 3-8)**, **(S 3-9)** and **(S3-19)** to **equation (S 3-7)** yields:

$$K_d^{app} = K_d^{app}(0) \cdot e^{\lambda \cdot zFV/RT} \cdot \left(1 + e^{-(\gamma - \delta) \cdot zFV/RT} \cdot e^{-(G_2 - G_1)/RT}\right) \qquad \text{(S3-11)}$$

with $K_d^{app}(0) = \frac{\beta}{\alpha} \cdot e^{G^*/RT}$ being a constant. Therefore, the [Ba^{2+}] and voltage-dependent inhibition can be calculated as follows:

$$\theta = \frac{[Ba^{2+}]}{[Ba^{2+}] + K_d^{app}(0) \cdot e^{\lambda \cdot zFV/RT} \cdot \left(1 + e^{-(\gamma - \delta) \cdot zFV/RT} \cdot e^{-(G_2 - G_1)/RT}\right)} \qquad \text{(S3-12)}$$

Fitting the K_d^{app} values shown in **Figure S 3-3C** with **equation (S3-11)** yields $K_d^{app}(0) = 696.4\,\mu M$, $\lambda = 0.95$, $(\gamma - \delta) = 0.80$, and $(G_2 - G_1)/RT = 1.78$.

These parameters were used to predict the voltage-dependent inhibition of the Kcv_{NTS} mediated potassium current for different $BaCl_2$ concentrations. As shown in **Figure S 3-3C**, this prediction is in good agreement with the measured values.

3.7. References

Abenavoli et al. (2009) Fast and slow gating are inherent properties of the pore module of the K^+ channel Kcv. J Gen Physiol. 134(3):219-29

Arnold et al. (2006) The SWISS-MODEL workspace: a web-based environment for protein structure homology modelling. Bioinformatics 22(2):195-201

Atkins & dePaula (2014) Atkins' Physical Chemistry. Oxford University Press Tenth Edition

Baukrowitz & Yellen (1996) Use-dependent blockers and exit rate of the last ion from the multi-ion pore of a K^+ channel. Science 271(5249):653-6.

Baumeister et al. (2017) Conversion of an instantaneous activating K^+ channel into a slow activating inward rectifier. FEBS Letters 591:295–303

Bernèche & Roux (2003) A microscopic view of ion conduction through the K^+ channel. PNAS 100 (15):8644-8648

Bernèche & Roux (2005) A gate in the selectivity filter of potassium channels. Structure 13:591-600

Bichet et al. (2003) Merging functional studies with structures of inward-rectifier K^+ channels. Nature Reviews 4(12):957-67

Biggin et al. (2001) Potassium and sodium ions in a potassium channel studied by molecular dynamics simulations. Biochim Biophys Acta. 1510(1-2):1-9

Braun et al. (2014a) Viral potassium channels as a robust model system for studies of membrane-protein interaction. Biochim Biophys Acta 1838(4):1096-103

Braun et al. (2014b) Pseudo painting/air bubble technique for planar lipid bilayers. J Neurosci Methods. 233:13-7

Bubeck & Pfitzner (2005) Isolation and characterization of a new type of chlorovirus that infects an endosymbiotic Chlorella strain of the heliozoon Acanthocystis turfacea. J Gen Virol 86(Pt 10):2871-7

Chang et al. (2007) charges in the cytoplasmic pore control intrinsic inward rectification and single-channel properties in Kir1.1 and Kir2.1 channels. J. Membrane Biol. 215:181-193

Colquhoun & Hawkes (1983) The principles of the stochastic interpretation of ion-channel mechanisms. Single-Channel Recording: 135-175

Colquhoun & Sigworth (1983) Fitting and statistical analysis of single-channel records. single-channel recording: 191-263

Contreras et al. (2010) Voltage profile along the permeation pathway of an open channel. Biophys J. 99(9): 2863–2869

Cordero-Morales et al. (2007) Molecular driving forces determining potassium channel slow inactivation. Nat Struct Mol Biol. 14(11):1062-9

Deutsch & Chen (1993) Heterologous expression of specific K^+ channels in T lymphocytes: functional consequences for volume regulation. Proc Natl Acad Sci USA 90(21): 10036–10040

Doyle et al. (1998) The structure of the potassium channel: molecular basis of K^+ conduction and selectivity. Science 280(5360):69-77

Gandhi & Isacoff (2002) Molecular Models of Voltage Sensing. J Gen Physiol. 120(4): 455–463

Gazzarini et al. (2009) Chlorella virus ATCV-1 encodes a functional potassium channel of 82 amino acids. Biochemical Journal 420:295-303

Greiner (2011) Characterization of novel potassium transport proteins from Chlorella viruses. Dissertation at the Technische Universität Darmstadt.

Hansen et al. (2016) A simple recipe for setting up the flux equations of cyclic and linear reaction schemes of ion transport with a high number of states: The arrow scheme. Channels (Austin) 10(2): 119–138

Heinemann & Conti (1992) Nonstationary noise analysis and application to patch clamp recordings. Methods Enzymol. 207:131-48.

Hille (2001) Ion channels of excitable membranes. Sinauer Associates, Inc.

Hoshi et al. (1990) Biophysical and molecular mechanisms of shaker potassium channel inactivation. Science 250(4980):533-538

Hoshi & Armstrong (2013) C-type inactivation of voltage-gated K^+ channels: Pore constriction or dilation? JGP 141(2):151-160

Jensen et al. (2012) Mechanism of voltage gating in potassium channels. Science 336(6078):229-33

Kang et al. (2004) Small potassium ion channel proteins encoded by chlorella viruses. Proc Natl Acad Sci USA. 101(15):5318-24

Katzen (2008) Cell-free protein expression of membrane proteins using nanolipoprotein particles. Biotechniques 45(2):190

Kiss & Korn (1998) Modulation of C-type inactivation by K^+ at the potassium channel selectivity filter. Biophys J. 74(4): 1840–1849

Kuang et al. (2015) Structure of potassium channels. Cell. Mol. Life Sci. 72:3677-3693

Kuo et al. (2003) Crystal structure of the potassium channel KirBac1.1 in the closed state. Science 300(5627):1922-6

Kurata & Fedida (2006) A structural interpretation of voltage-gated potassium channel inactivation. Progress in Biophysics and Molecular Biology 92:185-208

Kurata et al. (2010) Voltage-dependent gating in a “voltage sensor-less” ion channel. PLoS 8(2): e1000315

Lockless et al. (2007) Structural and thermodynamic properties of selective ion binding in a K^+ channel. PLoS Biol. 5(5):e121

Long et al. (2005) Voltage Sensor of Kv1.2: structural basis of electromechanical coupling. Science 309(5736):903-908

López-Barneo et al. (1993) Effects of external cations and mutations in the pore region on C-type inactivation of Shaker potassium channels. Receptors Channels. 1(1):61-71

Matsuda (1991) Effects of external and internal K^+ ions on magnesium block of inwardly rectifying K^+ channels in guinea-pig heart cells. J. Physiol. (Lond) 435:83-99

McCoy & Nimigean (2012) Structural correlates of selectivity and inactivation in potassium channels. Biochim Biophys Acta. 1818(2):272-85

Miloshevsky & Jordan (2008) Conformational changes in the selectivity filter of the open-state KcsA channel: an energy minimization study. Biophys J. 95(7): 3239–3251

Montal & Mueller (1972) Formation of bimolecular membranes from lipid monolayers and a study of their electrical properties. Proc Natl Acad Sci USA 69(12):3561-6

Moré & Sorensen (1983) Computing a trust region step. SIAM Journal on Scientific and Statistical Computing 3: 553–572

Morgen & Rubenstein (2013) Proline: the distribution, frequency, positioning, and common functional roles of proline and polyproline sequences in the human proteome. PLoS 8(1): e53785

Nelson & Quayle (1995) Physiological roles and properties of potassium channels in arterial smooth muscle. Am J Physiol. 268(4 Pt 1):C799-822

Neyton & Miller (1988) Potassium blocks barium permeation through a calcium-activated potassium channel. J Gen Physiol. 92(5):549-67

Nichols & Lopatin (1997) Inward rectifier potassium channels. Annu Rev Physiol. 59:171-91.

Nimigean & Miller (2002) Na^+ block and permeation in a K^+ channel of known structure. J. Gen. Physiol. 120:323-335

Oliver et al. (2000) Polyamines as gating molecules of inward-rectifier K^+ channels. Eur. J. Biochem. 267:5824-5829

Pagliuca et al. (2007) Molecular properties of Kcv, a virus encoded K^+ channel. Biochemistry 46:1079-1090

Papworth et al. (1996) Site-directed mutagenesis in one day with >80 % efficiency. Strategies 9:3–4

Piela et al. (1987) Proline-induced constraints in a-helices. Biopolymers 26:1587-1600

Pischalnikova & Sokolova (2009) The domain and conformational organization in potassium voltage-gated ion channels. J Neuroimmune Pharmacol. 4(1):71-82

Pongs (1999) Voltage-gated potassium channels: from hyperexcitability to excitement. FEBS Lett. 452(1-2):31-5

Rauh (2014) Unraveling of structure/function correlates in two viral K^+ channels Kcv_S and Kcv_{NTS} by mutagenesis. Master thesis at the Technische Universität Darmstadt.

Rauh et al. (2017a) Identification of intrahelical bifurcated H-bonds as a new type of gate in K^+ channels. J. Am. Chem. Soc. 139 (22):7494–7503

Rauh et al. (2017b) Extended beta distributions open the access to fast gating in bilayer experiments-assigning the voltage-dependent gating to the selectivity filter. FEBS Lett. 2017 591(23):3850-3860

Roux (2005) Ion conduction and selectivity in K^+ channels. Annu. Rev. Biophys. Biomol. Struct. 34:153–171

Schewe et al. (2016) A non-canonical voltage-sensing mechanism controls gating in K2P K^+ channels. Cell 164(5): 937–949

Schultze & Draber (1993) A nonlinear filter algorithm for the detection of jumps in patch-clamp data. J Membr Biol. 132(1):41-52

Shrivastava et al. (2002) K^+ versus Na^+ ions in a K^+ channel selectivity filter: a simulation study. Biophys J. 83(2): 633–645

Siotto (2017) Mining and analysis of new viral potassium channel proteins. Dissertation at the Technische Universität Darmstadt.

Stojilkovic et al. (2010) Ion channels and signaling in the pituitary gland. Endocr Rev. 31(6):845-915

Thompson & Eisenberg (1999) Transproteomic evidence of a loop-deletion mechanism for enhancing protein thermostability. J. Mol. Biol. 290:595-604

Thomson & Rothberg (2010) Voltage-dependent inactivation gating at the selectivity filter of the MthK K^+ channel. J Gen Physiol. 136(5): 569–579

Thomson et al. (2014) Initial steps of inactivation at the K^+ channel selectivity filter. PNAS 111(17):E1713-22

Tsien & Noble (1969) A transition state theory approach to the kinetics of conductance changes in excitable membranes. J Membr Biol. 1(1):248-73

Winterstein et al. (2018) Reconstitution and functional characterization of ion channels from nanodiscs in lipid bilayers. J Gen Physiol. 150 (4): 637

Yeh et al. (2005) Electrostatics in the cytoplasmic pore produce intrinsic inward rectification in Kir2.1 channels. J Gen Physiol. 126(6):551-62

Yu et al. (2005) Overview of molecular relationships in the voltage-gated ion channel superfamily. Pharmacol Rev. 57(4):387-95

Zhou et al. (2001) Chemistry of ion coordination and hydration revealed by a K^+ channel-Fab complex at 2.0 A resolution. Nature 414(6859):43-8

4. General Discussion

Potassium channels are complex and highly regulated protein structures, which are involved in a large number of cellular and physiological processes in virtually all organisms (Miller 2000). The understanding of these processes and their pathologic dysfunctions comprises necessarily the understanding of the molecular causes and mechanisms underlying the action of potassium channels. In the present work I used $Kcv_{ATCV\text{-}1}$-like potassium channels as robust and easy-to-use model systems for the investigation of gating mechanisms in potassium channels.

4.1. Intrahelical hydrogen-bonds and their implications for ion channel function

Extensive mutation studies conducted on the channel orthologs Kcv_{NTS} and Kcv_{S} led to the discovery of a new type of intracellular gate. Controllable opening and closing of an intracellular gate, referred to as bundle-crossing gate, plays an important role in a large number of potassium channels such as Kv and Kir channels (Yu et al. 2005, Bichet et al. 2003). It is generally believed that the movement of the crucial inner TM helices is facilitated by so-called hinge points located above the actual gate (Labro & Snyders 2012). In the case of the bacterial channels KcsA and MthK as well as the mammalian Kir channels, glycine residues in the middle or near the C-terminal end of the inner, pore-lining transmembrane helix were identified as hinge points (Labro & Snyders 2012, Bichet et al. 2003). In contrast, in voltage-dependent Kv channels the hinge points are presumably formed by proline motifs (PxP or PxG) (Yellen 2002). Various experimental, crystallographic and computational studies have led to the hypothesis that the transition from the closed to the open state of the intracellular gate is caused by rigid body movements of the inner and outer TM helices resulting in a widening of the pore diameter at the bundle-crossing point (e.g. Holmgren et al. 1997, Perozo et al. 1999, Hirano et al. 2009, Bavro et al. 2012). In this scenario it is assumed that a widening of the intracellular pore diameter is facilitated by bending of the pore-lining TM helix at the flexible hinge point. However, there are still doubts if this model can be applied to all potassium channels (Labro & Snyders 2012). A prominent example is the voltage-dependent hERG channel. In contrast to other Kv channels, the inner TM helix of hERG does not contain a proline motif. Moreover, two glycine residues, which could act as possible hinge points, are not essential for voltage-dependent channel gating (Hardmann et al. 2007). This clearly demonstrates that a single mechanism is not sufficient to explain the movements underlying gate opening at the helix bundle crossing. The gating mechanism identified in the first part of the present thesis provides an alternative explanation of how

transmembrane helices that do not have flexible residues can bend. According to the experimental and computational results discussed above, the stochastic closing of the inner gate in Kcv_{ATCV-1}-like potassium channels is facilitated by the formation of an intrahelical hydrogen-bond between the hydroxyl-group of a serine or threonine residue located within the inner TM helix and a carbonyl oxygen in the preceding helix turn. This interaction leads to a slight change in the torsion angles of the peptide backbone and thereby generates a kink in the α-helix. The kink has by itself no impact on gating. The channel only acquires a long-lived closed state when the amino acid downstream of the critical serine has an aromatic or a long hydrophobic side chain that can occlude the ion conduction pathway. In Kcv_{ATCV-1}-like channels this position is usually occupied by phenylalanine (**Figure 2-1B**).

Interestingly, the computational data suggest, that the formation of an intrahelical hydrogen-bond within a TM helix does not move the adjacent phenylamine side chain into the ion conduction pathway, but away from it. This movement gives room for a movement of the neighboring phenylalanine side chains towards the pore center. Consequently, closing and opening of the intracellular gate presumably reflects a close and cooperative interplay between all four monomers. Such a cooperative interplay between the four channel subunits has also been reported for the voltage-dependent opening and closing of the bundle-crossing gate in several Kv channels such as *Shaker* (Bezanilla et al. 1991, Zandany et al. 2008). However, the molecular origin of this cooperativity is still unknown. Since the bundle-crossing gate in *Shaker* is also constituted by hydrophobic amino acid side chains (Hackos et al. 2002), it is conceivable that the concerted pore-opening and closing transitions reflects a direct interaction between the involved blocking residues. These considerations are of course highly speculative.

Even though intrahelical hydrogen bonds have not yet been perceived as important elements of dynamic protein structures, there are some isolated data that already suggest that such serine or threonine mediated intrahelical hydrogen-bonds have an effect on protein function (Deupi et al. 2004, Sansuk et al. 2011). Notably, pairs of serine or threonine together with aromatic or large hydrophobic amino acids are also frequently present in the inner TM helices of K^+ channels. The BK channel for example has a SFF338-340 motive at the cytosolic end of the pore-lining TM helix in which serine and both phenylalanine residues are involved in channel gating (Strutz-Seebohm et al. 2011, Panaghie et al. 2008). Remarkably, the inner TM helix of bacterial voltage-gated sodium channels (BacNavs), which have an architecture similar to that of voltage-dependent potassium channels (Catterall & Zheng 2015), kinks at a threonine residue that corresponds to the glycine hinge of potassium channels (Lenaeus et al. 2017). The authors speculate that the twisting/bending motion of the inner TM helix during

gate opening may be caused by exchange of hydrogen bonds of this threonine from the nearby pore helix to the peptide backbone of the preceding helix turn. At this point it should be mentioned that a bioinformatics analysis of crystal structures of transmembrane proteins has already shown that serine or threonine-mediated intrahelical hydrogen bonds are frequent in these proteins and can cause kinks in α-helices (Ballesteros et al. 2000). The analysis of the crystal structures has also shown that a local intrahelical hydrogen-bond can lead to structural changes over long distances. The local kink on one side of the membrane for example can cause a bending of a helix with the effect of a significant displacement of the residues on the other side of the membrane. Considering the frequency of occurrence and the impact on the global structure of a protein it is reasonable to speculate that the formation of intrahelical hydrogen bonds might play a greater role not only in the function of ion channels but in proteins in general than previously assumed.

4.2. The pore domain of potassium channels exhibits an intrinsic voltage-dependency

The electrophysiological examination of the channel $Kcv_{NH\ S77G}$ uncovered an intrinsic slowly activating, voltage-dependent and outwardly rectifying gating process that is sensitive to both the extracellular potassium concentration and the electrochemical K^+ gradient. These data in combination with mutational experiments support a model in which the voltage-dependent inactivation of $Kcv_{NH\ S77G}$ is caused by an ion-flux dependent depletion of the channel pore. Depletion of ions from the pore causes a conformational change within the selectivity filter that renders the channel non-conductive. However, since structural data are missing, the assumption that the inactivation is caused by a partial collapse of the pore must be considered speculative. Nevertheless, the similarities between the voltage-dependent gating in $Kcv_{NH\ S77G}$ and other selectivity filter mediated gating processes suggest that these processes are - at least partly - based on similar structural rearrangements within or in the proximity of the selectivity filter. Particularly striking is the similarity between the process described here and the voltage-dependent gating in two-pore domain (K2P) channels. Although K2P channels, like Kcv channels, do not have a canonical VSD, nearly all K2P channels show an intrinsic outward rectification (Schewe et al. 2016). Schewe et al. postulated on the basis of electrophysiological and mutational studies that the voltage-dependent closure of the ion conduction pathway is caused by ion depletion of the channel pore, resulting in an inactive filter conformation. Even though voltage-dependent gating is much faster in K2P channels than in $Kcv_{NH\ S77G}$, both processes show a striking common feature: in both cases inward current gates the channel inactive, while the time constant of activation observed for voltage

steps positive to the reversal potential is voltage-independent (Schewe et al. 2016). These findings, together with the fact that both processes are sensitive to the electrochemical K^+ gradient, underscores the idea, that the underlying mechanisms are related.

In order to obtain a more detailed picture of the mechanisms and insights into the structural rearrangements underlying voltage-dependent gating in Kcv channels, additional functional and structure-resolving examinations must be carried out. A first idea of the conformational changes occurring during channel inactivation in the region around the extracellular pore entrance could for example be provided by *electron paramagnetic resonance* (EPR) measurements or Cd^{2+}-binding experiments. Similar experiments have already been conducted to investigate conformal changes during selectivity-filter gating in different potassium channels (e.g. Yellen et al. 1994, Raghuraman et al. 2014). Since all structural information available for Kcv channels so far is mainly based on homology modeling and MD simulations, there is a strong need to gain access to an atomistic structure of a $Kcv_{ATCV\text{-}1}$-like channel through crystallographic or *nuclear magnetic resonance* (NMR) techniques. Such a structure would make it possible to identify the crucial amino acids that are involved in the formation and stabilization of the pore and the selectivity filter. Currently, efforts are being made to chemically synthesize the $Kcv_{ATCV\text{-}1}$ channel using solid-phase peptide synthesis (personal communication Alesia Tietze, Department of Chemistry, TU Darmstadt). This protein could be used in a second step to obtain information on structure and dynamics of $Kcv_{ATCV\text{-}1}$-like channels by means of solid phase NMR. A similar approach has already been used to study the molecular mechanism of proton conduction through the influenza B virus M2 transmembrane proton channel (Williams et al. 2016).

In summary the results presented and discussed here support the view that voltage-sensitivity is not only a property of highly complex proteins such as Kv channels, but an inherent property of some potassium channel pores, which are not linked to a VSD. Furthermore, the fact that the exchange of only two amino acids in the extracellular pore region of $Kcv_{ATCV\text{-}1}$-like channels is sufficient for the establishment of a voltage-dependent gating process suggests that voltage-dependence might be a latent property of the pore-domain of all potassium channels.

4.3. The contribution of small conformational alterations to changes in function and activity

Despite their high sequence identity, $Kcv_{ATCV\text{-}1}$-like potassium channels exhibit a broad spectrum of electrophysiological properties. It could be shown in the present work that crucial

channel properties, for example a low open probability or the occurrence of a voltage-dependent gating process, can be induced or suppressed by the exchange of individual amino acids. Since Kcv_{ATCV-1}-like potassium channels are fully embedded in the lipid membrane and do not possess protein domains that can undergo large conformational motions (Braun et al. 2014), these findings imply that transitions between functional states such as open and closed do not require large conformational changes as for example proposed for the voltage-dependent opening of the bundle-crossing gate in KcsA or Kv channels. Instead, even small changes in the orientation and interaction of a few amino acid side chains can cause dramatic changes in the activity of proteins. The present data therefore support a hypothesis in that the stochastic opening and closing of channels can be explained mainly by simple chemical interactions.

4.4. Kcv channels as building blocks for the design of biosensors or controllable K^+ channels

The profound understanding of the molecular mechanisms underlying the function of viral Kcv channels enables us to specifically modify these proteins and make them usable as biosensors or controllable potassium channels. For this purpose, Kcv channels could be coupled with a variety of sensor domains form other proteins. A proof of principle for introducing new functional properties in Kcv channels has already been successfully demonstrated for Kcv_{PBCV-1}: by fusion of the Kcv_{PBCV-1} pore module with the voltage-sensing domain of a phosphatase from *Ciona intestinales*, Arrigoni et al. (2013) could engineer a voltage-dependent, outward rectifying potassium channel. In a second study Cosentino et al. (2015) were able to show that it is possible to place the Kcv_{PBCV-1} pore under control of the LOV2-Jα photo-switch from *Avena sativa* phototropin 1. In this way they created a blue-light-inducible K^+ channel, referred to as BLINK1. Comparable approaches have also been applied to other potassium channels such as KcsA. For instance, Ohndorf and MacKinnon (2005) were able to construct a cyclic-nucleotide-dependent potassium channel by fusing the pore domain of KcsA with the cyclic nucleotide binding domain (CNBD) of the *Rhodopseudomonas palustris* (RP) channel. These examples clearly demonstrate that the pore domains of potassium channels can serve as building blocks for the rational design of proteins with a broad variety of new properties. In this context, the knowledge about the function of the inner gate obtained in the present thesis could be used to equip Kcv_{ATCV-1}-like channels with new functions by coupling them with sensor domains of other proteins. These could include, for example, pH-, ligand-, redox- and light-sensing domains.

4.5. References

Arrigoni et al. (2013) The voltage-sensing domain of a phosphatase gates the pore of a potassium channel. J Gen Physiol 141(3): 389–395

Ballesteros et al. (2000) Serine and threonine residues bend alpha-helices in the chi(1)=g(-) conformation. Biophys J. 79(5):2754-60

Bavro et al. (2012) Structure of a KirBac potassium channel with an open bundle crossing indicates a mechanism of channel gating. Nat Struct Mol Biol 19(2):158-63

Bezanilla et al. (1991) Molecular basis of gating charge immobilization in Shaker potassium channels. Science 254(5032):679-83

Bichet et al. (2003) Merging functional studies with structures of inward-rectifier K^+ channels. Nature Reviews 4(12):957-67

Braun et al. (2014) Viral potassium channels as a robust model system for studies of membrane-protein interaction. Biochim Biophys Acta 1838(4):1096-103

Catterall & Zheng (2015) Deciphering voltage-gated Na^+ and Ca^{2+} channels by studying prokaryotic ancestors. Trends Biochem Sci 40(9): 526–534

Cosentino et al. (2015) Optogenetics. Engineering of a light-gated potassium channel. Science 348(6235):707-10

Deupi et al. (2004) Ser and Thr residues modulate the conformation of pro-kinked transmembrane alpha-helices. Biophys J 86(1 Pt 1):105-15

Hackos et al. (2002) Scanning the intracellular S6 activation gate in the shaker K^+ channel. J Gen Physiol 119(6): 521–531

Hardmann et al. (2007) Activation gating of hERG potassium channels: S6 glycines are not required as gating hinges. J Biol Chem 282(44):31972-81

Hirano et al. (2010) Rearrangements in the KcsA cytoplasmic domain underlie its gating. J Biol Chem 285(6): 3777–3783

Holmgren et al. (1997) Trapping of organic blockers by closing of voltage-dependent K^+ channels: evidence for a trap door mechanism of activation gating. J Gen Physiol 109(5):527-35

Labro & Snyders (2012) Being flexible: The voltage-controllable activation gate of Kv channels. Front Pharmacol 3:168

Lenaeus et al. (2017) Structures of closed and open states of a voltage-gated sodium channel. Proc Natl Acad Sci USA 114(15):E3051-E3060

Miller (2000) An overview of the potassium channel family. Genome Biol 1(4): reviews0004.1–reviews0004.5

Ohndorf & MacKinnon (2005) Construction of a cyclic nucleotide-gated KcsA K^+ channel. J Mol Biol 350(5):857-65

Panaghie et al. (2008) Voltage-dependent C-type inactivation in a constitutively open K^+ channel. Biophys J 95(6):2759-78

Perozo et al. (1999) Structural rearrangements underlying K^+-channel activation gating. Science 285(5424):73-8

Raghuraman et al. (2014) Dynamics transitions at the outer vestibule of the KcsA potassium channel during gating. Proc Natl Acad Sci USA 111(5): 1831–1836

Sansuk et al. (2011) A structural insight into the reorientation of transmembrane domains 3 and 5 during family A G protein-coupled receptor activation. Mol Pharmacol 79(2):262-9

Strutz-Seebohm et al. (2011) Structural basis of slow activation gating in the cardiac I Ks channel complex. Cell Physiol Biochem 27(5):443-52

Williams et al. (2016) Solid-state NMR investigation of the conformation, proton conduction, and hydration of the influenza B virus M2 transmembrane proton channel. J. Am. Chem. Soc. 138 (26):8143–8155

Yellen et al. (1994) An engineered cysteine in the external mouth of a K^+ channel allows inactivation to be modulated by metal binding. Biophys J 66(4):1068-75

Yellen (2002) The voltage-gated potassium channels and their relatives. Nature 419(6902):35-42

Yu et al. (2005) Overview of molecular relationships in the voltage-gated ion channel superfamily. Pharmacol Rev. 57(4):387-95

Zandany et al. (2008) Direct analysis of cooperativity in multisubunit allosteric proteins. Proc Natl Acad Sci USA 105(33):11697-702

List of abbreviations

A	active state
A/D	analog/digital
ATCV-1	*Acanthocystis turfacea* chlorella virus 12
ATP	adenosine triphosphate
$[Ba^{2+}]$	Ba^{2+} concentration
BK	Big K^+ channel, also known as Maxi-K
C	closed state
CLC	Cl^- channel
δ	fraction of the membrane potential
DH5α	*E. coli* strain useful for recombinant DNA methods
DMEM	Dulbecco's Modified Eagle Medium
DMPC	1,2-dimyristoyl-sn-glycero-3-phosphocholine
DNA	deoxyribonucleic acid
DPhPC	1,2-diphytanoyl-sn-glycero-3-phosphocholine
DTT	dithiothreitol
e	Euler's number ($e \approx 2.718$)
E. coli	*Escherichia coli*
E_r	reversal potential
EPR	electron paramagnetic resonance
ex	extracellular
F	Faraday constant
HEK293	Human embryonic kidney cell line
HEPES	4-(2-hydroxyethyl)-1-piperazineethanesulfonic acid
hERG	human ether-à-go-go-related gene codes for Kv11.1
i	open-channel amplitude
I	macroscopic current or inactive state
in	intracellular

k	rate constant
$[K^+]$	potassium concentration
Kcv	K^+ channel chlorella virus
KcsA	K^+ channel from *Streptomyces lividans*
K_d^{app}	apparent dissociation constant
Kir	inwardly rectifying K^+ channel
KirBac	bacterial inwardly rectifying K^+ channel
Kv	voltage-gated K^+ channel
K2P	two-pore domain K^+ channel
LB medium	lysogeny broth medium
MD	molecular dynamics
N	number of experiments or number of events
Ni-NTA	Ni^{2+}-nitrilotriacetic acid
NLP	nanolipoprotein
NMR	nuclear magnetic resonance
O	open state
P	probability of occupancy
PCR	polymerase chain reaction
PIP_2	phosphatidylinositol-4,5-bisphosphate
PBCV-1	*Paramecium bursaria* chlorella virus 1
pdf	probability densitiy function
pH	potential of hydrogen
R	universal gas constant
rpm	rounds per minute
SUR	sulfonylurea receptor
t	time
T	absolute temperature
TEA^+	tetraethylammonium
TM	transmembrane

τ	time constant
θ	inhibition
V	voltage
$V_{1/2}$	half-activation potential
V-E_r	driving force
VSD	voltage-sensing domain
z	equivalent gating charge or valence of the ion

Amino acids and codes

Alanine	A	Ala
Arginine	R	Arg
Asparagine	N	Asn
Aspartic acid	D	Asp
Cysteine	C	Cys
Glutamine	Q	Gln
Glutamic acid	E	Glu
Glycine	G	Gly
Histidine	H	His
Isoleucine	I	Ile
Leucine	L	Leu
Lysine	K	Lys
Methionine	M	Met
Phenylalanine	F	Phe
Proline	P	Pro
Serine	S	Ser
Threonine	T	Thr
Tryptophane	W	Trp
Tyrosine	Y	Tyr
Valine	V	Val

Own work

Experiments, data analysis and writing were exclusively done by myself, with exception of:

- Section 2.3.7, including text, figures and supplemental material (section 2.6.6, section 2.6.7 and Figs. S2-3 and S2-4), was included in the present work for reasons of completeness and kindly provided by Prof. Dr. Stefan M. Kast, Dr. Leonhard M. Henkes and Martin Urban from the department of physical chemistry III, Technische Universität Dortmund.
- Isolation, sequencing, initial cloning and characterization of viral potassium channels Kcv_S and $Kcv_{NTS,}$ which were used in Rauh et al. (2017) J. Am. Chem. Soc. 139:7494-7503, were performed by Prof. James Van Etten (UNL, Lincoln, USA), Dr. Timo Greiner, Prof. Gerhard Thiel and Prof. Anna Moroni (Università degli Studi di Milano, Italy). Dr. Indra Schröder and Prof. Gerhard Thiel contributed to the design of experiments and interpretation of data. Dr. Indra Schröder, Prof. Gerhard Thiel and Prof. Anna Moroni supported writing of the manuscript.
- The generation of the channel mutants Kcv_S W82C and Kcv_{NTS} W82C by site-directed mutagenesis and their electrophysiological examination (section 2.3.8) were performed by Tobias Winterstein (Master student) under my supervision.
- The single-channel measurements of the viral potassium channel Kcv_{NH} in section 3.2.1 were performed by Daniel Stumpf (Bachelor student) under my supervision.
- The generation of the channel mutants $Kcv_{NH\,S77G}$ Y28N A29T, $Kcv_{NH\,S77G}$ A57P and $Kcv_{NH\,S77G}$ F78A and their electrophysiological examination (section 3.2.4) were performed by Federica D'Arco (Master student) under my supervision.

Declaration - Ehrenwörtliche Erklärung

Ich erkläre hiermit ehrenwörtlich, dass ich die vorliegende Arbeit entsprechend den Regeln guter wissenschaftlicher Praxis selbstständig und ohne unzulässige Hilfe Dritter angefertigt habe.

Sämtliche aus fremden Quellen direkt oder indirekt übernommenen Gedanken sowie sämtliche von Anderen direkt oder indirekt übernommenen Daten, Techniken und Materialien sind als solche kenntlich gemacht. Die Arbeit wurde bisher bei keiner anderen Hochschule zu Prüfungszwecken eingereicht.

Darmstadt, den ……

.....

Oliver Rauh

Curriculum vitae and publications

Personal information

Name	Rauh
Surname	Oliver
Date of Birth	04/02/1989
Place of Birth	Görlitz, Germany
Nationality	German

Education and working experience

1/2017-6/2017	Exchange researcher at the Columbia University Medical Center (New York City, NY) in the Molecular Physiology group of Ph.D. Henry Colecraft
2014-2018	Doctoral degree candidate at the Technische Universität Darmstadt in the Membrane Biophysics Group of Prof. Dr. Gerhard Thiel Doctoral advisor: Dr. Indra Schröder
2014	Master thesis at the TU Darmstadt (Department of Biology) in the Membrane Biophysics Group of Prof. Gerhard Thiel with the title "Mutationsstudien zur Struktur-Funktions-Korrelation der viralen Kaliumkanäle Kcv_S und Kcv_{NTS}" (Unraveling of structure/function correlates in two viral K^+ channels Kcv_S and Kcv_{NTS} by mutagenesis).
2012 to 2014	Study of Biomolecular Engineering (Master) at the TU Darmstadt
2012	Bachelor thesis at the TU Darmstadt (Department of Biology) in the Yeast Membrane Biology Group of Prof. Adam Bertl with the title "Untersuchung der Funktion und Oligomerisierung von Tok1p und Tok1p-Mutanten in Saccharomyces cerevisiae" (Investigation of the function and oligomerisation of Tok1p and Tok1p mutants in Saccharomyces cerevisiae).
2009 to 2012	Study of Biomolecular Engineering (Bachelor) at the TU Darmstadt

2008	Abitur at the Marie-Baum-Schule, Heidelberg

Publications

under revision	**Oliver Rauh**, Ulf Hansen, Deborah-Desiree Scheub, Gerhard Thiel, Indra Schroeder. Site-specific ion occupation in the selectivity filter causes voltage-dependent gating in a viral K^+ channel. Scientific Reports
04/2018	Laura-Marie Winterstein, Kerri Kukovetz, **Oliver Rauh**, Daniel L. Turman, Christian Braun, Anna Moroni, Indra Schroeder, Gerhard Thiel. Reconstitution and functional characterization of ion channels from nanodiscs in lipid bilayers. Journal of General Physiology 150 (4): 637. L.-M. Winterstein, K. Kukovetz and O. Rauh contributed equally to this paper
11/2017	**Oliver Rauh**, Ulf-Peter Hansen, Sebastian Mach, Andreas J. W. Hartel, K. L. Shepard, Gerhard Thiel, Indra Schroeder. Extended beta distributions open the access to fast gating in bilayer experiments-assigning the voltage-dependent gating to the selectivity filter. FEBS Letters 591(23): 3850-3860
10/2017	Andrea Saponaro, Alessandro Porro, Antonio Chaves-Sanjuan, Marco Nardini, **Oliver Rauh**, Gerhard Thiel, Anna Moroni. Fusicoccin Activates KAT1 Channels by Stabilizing their Interaction with 14-3-3- Proteins. The Plant cell 29(19): 2570-2580
06/2017	**Oliver Rauh**, Martin Urban, Leonhard M. Henkes, Tobias Winterstein, Timo Greiner, James L. Van Etten, Anna Moroni, Stefan M. Kast, Gerhard Thiel, Indra Schroeder. Identification of Intrahelical Bifurcated H-Bonds as a New Type of Gate in K^+ Channels. Journal of the American Chemical Society 139(22): 7494-7503
03/2016	Ulf-Peter Hansen, **Oliver Rauh**, Indra Schröder. A simple recipe for setting up the flux equations of cyclic and linear reaction schemes of ion transport with a high number of states: The arrow scheme. Channels (Austin) 10(2): 119–138
01/2017	Patrick Voos, Mehtap Yazar, René Lautenschläger, **Oliver Rauh**, Anna Moroni, Gerhard Thiel. The small neurotoxin apamin blocks not only small

	conductance Ca^{2+} activated K^+ channels (SK type) but also the voltage dependent Kv1.3 channel. European biophysics journal 46(6): 517-523
10/2014	Fenja Siotto, Corinna Martin, **Oliver Rauh**, James L. Van Etten, Indra Schroeder, Anna Moroni, Gerhard Thiel. Viruses infecting marine picoplancton encode functional potassium ion channels. Virology 466-467: 103-111

Acknowledgments - Danksagung

Ich möchte mich an dieser Stelle bei allen Personen bedanken, die mich in den letzten Jahren unterstützt und zum Gelingen dieser Arbeit beigetragen haben.

Mein besonderer Dank gilt…

Herrn Prof. Gerhard Thiel für die Möglichkeit, diese Thesis in seiner Arbeitsgruppe erarbeiten und mich wissenschaftlich frei entfalten zu dürfen. Darüber hinaus möchte ich mich aber auch für die vielen fachlichen Anregungen und Diskussionen sowie unser menschlich sehr gutes Verhältnis bedanken.

Frau Dr. Indra Schröder, für die stete Unterstützung bei Problemen und Fragen jeder Art, das in mich gesetzte Vertrauen und die großartige Chance, als erster Doktorand ihrer noch jungen Arbeitsgruppe promovieren zu dürfen.

Herrn Prof. Dr. Stefan Kast, **Dr. Leonhard Henkes** und **Martin Urban** für die großartige Zusammenarbeit.

Herrn PhD Henry Colecraft für die produktive und einzigartige Zeit, die ich in seiner Arbeitsgruppe in New York verbringen durfte.

Dr. Brigitte Hertel, **Silvia Haase**, **Sylvia Lenz** und **Mirja Manthey** für ihre stete Hilfsbereitschaft sowie das Bereitstellen eines organisierten und funktionierenden Laboralltags.

der gesamten **AG Thiel** für eine einzigartige und wunderbare Arbeitsatmosphäre und die vielen gemeinsamen Aktivitäten.

Christian Braun, **Vera Bandmann**, **Kerri Kukovetz**, **Patrick Voos** (geb. Becker), **Bastian Roth** und **Katja Häupl** für eure Freundschaft und die vielen Stunden, die wir gemeinsam verbracht haben und hoffentlich noch verbringen werden.